

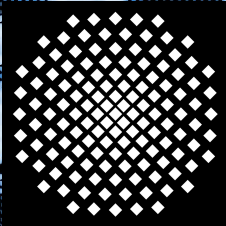
Universität Stuttgart

Germany

Institut für Mechanik (Bauwesen)

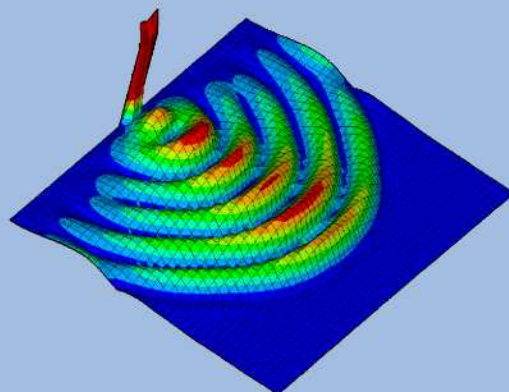
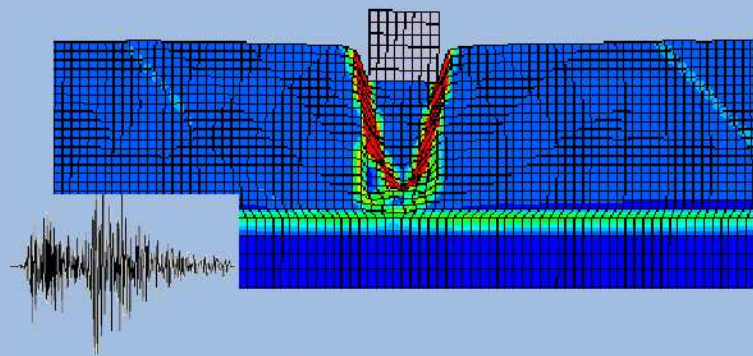
Lehrstuhl für Kontinuumsmechanik

Prof. Dr.-Ing. W. Ehlers



Saturated Porous Media Dynamics with Application to Earthquake Engineering

Yousef Heider



Report No.: II-25 (2012)

Saturated Porous Media Dynamics with Application to Earthquake Engineering

Von der Fakultät Bau- und Umweltingenieurwissenschaften
der Universität Stuttgart zur Erlangung der Würde
eines Doktor-Ingenieurs (Dr.-Ing.)
genehmigte Abhandlung

Vorgelegt von
Yousef Heider
aus
Tartous, Syrien

Hauptberichter: Prof. Dr.-Ing. Wolfgang Ehlers
1. Mitberichter: Prof. Dr.-Ing. Holger Steeb
2. Mitberichter: PD Dr.-Ing. Bernd Markert

Tag der mündlichen Prüfung: 19. Juli 2012

Institut für Mechanik (Bauwesen) der Universität Stuttgart
Lehrstuhl für Kontinuumsmechanik
Prof. Dr.-Ing. W. Ehlers
2012

Report No. II-25
Institut für Mechanik (Bauwesen)
Lehrstuhl für Kontinuumsmechanik
Universität Stuttgart, Germany, 2012

Editor:

Prof. Dr.-Ing. W. Ehlers

© Yousef Heider
Institut für Mechanik (Bauwesen)
Lehrstuhl für Kontinuumsmechanik
Universität Stuttgart
Pfaffenwaldring 7
70569 Stuttgart, Germany

All rights reserved. No part of this publication may be reproduced, stored in a retrieval system, or transmitted, in any form or by any means, electronic, mechanical, photocopying, recording, scanning or otherwise, without the permission in writing of the author.

ISBN 3-937399-22-4
(D 93 - Dissertation, Universität Stuttgart)

Acknowledgements

This thesis was written during my time as a doctoral candidate at the Institute of Applied Mechanics, University of Stuttgart. I owe my gratitude to all those who helped in making this thesis possible, as well as those who supported me in my life. If I have left any name out of the text below please realise that you are only missing from this page, not from my heart or my mind.

I would like to express my sincere gratitude to my supervisor, Professor Wolfgang Ehlers, for giving me the opportunity to do my doctoral study under his guidance and for the kind hospitality at the institute. It has definitely been his invaluable advice, support and encouragement that have made this work possible. His broad knowledge and prominent publications in the fields of continuum mechanics and porous materials modelling were very important foundations of this thesis. My sincere thanks are extended to Professor Holger Steeb, my co-advisor, for his interest in my work, his advice and comments. I am also very grateful to my second co-advisor, Privatdozent Bernd Markert; his constant assistance, precious advice and efforts helped me to improve my critical thinking, research methodology and understanding of different numerical challenges. Additionally, our lengthy discussions and common publications have been essential for this thesis.

My appreciations and sincere thanks also go to my colleagues and friends at the University of Stuttgart, who made my stay here a most pleasant one. I would like to thank my office-mate Seyedmohammad Zinatbakhsh for his goodwill and kindness. Special thanks are due to Dr.-Ing. Nils Karajan, Dr.-Ing. Tobias Graf, Dr.-Ing. Ayhan Acartürk, Dr.-Ing. Hans-Uwe Rempler, Okan Avcı and Andrei Danilov for their friendship, technical and scientific support, as well as helping in solving different programming difficulties especially in the first year of my doctoral study. I would like to convey my gratitude to my colleagues Joffrey Mabuma, Arndt Wagner, Kai Häberle, David Koch, Maik Schenke, Dr.-Ing. Irina Komarova and Arzu Avcı for the warm and friendly working atmosphere as well as for the fruitful discussions we had in the last few years of my stay at the institute.

Special thanks are due to my sincere friend Dr.-Ing. Ayman Abed for his support and constructive comments, which definitely contributed to this thesis. To my friends, Wassim Moussa and Fadi Aldakheel, I would like to extend my gratitude for the nice memories we had in Stuttgart. I am also thankful to my friends at the construction company Züblin for their kindness and encouragement, which helped me to smoothly finalise and defend my doctoral thesis.

I would like to convey my heartfelt thanks to my parents for their everlasting love and constant encouragement. My grateful thanks also go to my wonderful siblings and to their lovely families. I am deeply thankful to my relatives and friends in Syria and abroad, especially to Professor Ahmed Haydar for his continuous care and invaluable advice.

Finally, the financial support for my research work at the Institute of Applied Mechanics was provided through a scholarship by the Syrian Ministry of Higher Education. This generous support is respectfully acknowledged and gratefully appreciated.

Dedicated to my beloved parents in Syria

مهداة مع خالص الحب إلى أبي و أمي

Contents

Contents	I
Deutsche Zusammenfassung	V
Motivation	V
Zielsetzung und Vorgehensweise	VI
Gliederung der Arbeit	VIII
1 Introduction and Overview	1
1.1 Motivation	1
1.2 Basic Features	2
1.3 Thesis Layout	9
2 Theoretical Basics	11
2.1 Theory of Porous Media (TPM)	11
2.2 Kinematics of Multi-phase Continua	13
2.2.1 Basic Definitions	13
2.2.2 Deformation and Strain Measures of Biphasic Continua	15
2.2.3 Geometric Linearisation	17
2.3 Balance Relations	19
2.3.1 Preliminaries	19
2.3.2 General and Specific Balance Relations	20
3 Constitutive Modelling	29
3.1 Saturated Biphasic TPM Model	29
3.1.1 Preliminaries and Assumptions	29
3.1.2 Entropy Inequality Evaluation and Effective Stresses	31
3.1.3 Compressible Fluid Behaviour (Hybrid Model)	35
3.1.4 Different Sets of Governing Balance Relations	36
3.2 Elasto-Viscoplastic Material Behaviour	39

3.2.1	Preface	39
3.2.2	Hyperelastic Material Modelling	41
3.2.3	Plastic Material Modelling	42
3.3	Bulk Waves in Biphase Poroelastic Media	47
4	Numerical Treatment	51
4.1	Finite Element Method	51
4.1.1	Initial-Boundary-Value Problems in Porous Media Dynamics	51
4.1.2	Governing Weak Formulations	54
4.1.3	Spatial Discretisation	55
4.2	The Strongly Coupled Problem of Porous Media Dynamics	60
4.2.1	Pure Differential Coupling	61
4.2.2	Differential and Algebraic Coupling	64
4.3	Time Discretisation	70
4.3.1	Implicit Monolithic Time Integration	71
4.3.2	Semi-Explicit-Implicit Splitting Methods	74
4.4	Treatment of Unbounded Domains	82
4.4.1	Viscous Damping Boundary Method (VDB)	84
5	Liquefaction of Saturated Granular Materials	87
5.1	Preface and Definitions	87
5.1.1	Earthquake-Induced Field Liquefaction	91
5.2	Modelling of Liquefaction Phenomena	92
5.2.1	Elasto-Viscoplastic Material Law for Liquefaction Modelling	93
5.2.2	Simulation of Triaxial Tests under Monotonic Loading	95
5.2.3	Undrained Sand Behaviour under Cyclic Loading	98
5.2.4	Additional Factors Affecting the Dynamic Response of Saturated Granular Media	101
6	Numerical Applications and Solution Schemes	107
6.1	Saturated Poroelastic Half-Space under Harmonic Loading	108
6.1.1	Comparison of Implicit Monolithic and Splitting Schemes	109
6.1.2	Explicit vs. Implicit Monolithic Solutions	113

6.1.3	Verification of the Unbounded Boundary Treatment	115
6.2	Two-dimensional Wave Propagation	119
6.3	Wave Propagation in an Elastic Structure-Soil Half Space	130
6.4	Soil-Structure Interaction under Seismic Loading	135
6.4.1	General Aspects	135
6.4.2	Seismic Input Data	138
6.4.3	Application to Liquefaction Modelling: Structure Founded on Strat- ified Soil	139
7	Summary, Conclusions and Future Aspects	147
7.1	Summary and Conclusions	147
7.2	Future Aspects	149
A	Tensor Calculus	151
A.1	Tensor Algebra	151
A.1.1	Basics of Tensor Calculus	151
A.1.2	Fundamental Tensors	153
A.1.3	The Eigenvalue Problem and Invariants of 2nd-Order Tensors . . .	154
A.1.4	Collected Operators and Rules	154
B	Triaxial Test and Material Parameters	155
	Bibliography	170
	Nomenclature	171
Conventions	171
Symbols	171
Acronyms	176
	List of Figures	180
	List of Tables	181
	Curriculum Vitae	183

Deutsche Zusammenfassung

Der Fokus der vorliegenden Arbeit liegt auf der Entwicklung und Implementierung fortschrittlicher Werkstoffmodelle und numerischer Verfahren zur Analyse und Simulation fluidgesättigter, poröser Medien bei verschiedenen dynamischen Belastungen. Hierbei konzentriert sich die Behandlung auf zwei wichtige Ereignisse in gesättigten Böden, nämlich die Wellenausbreitung in unbegrenzten Gebieten und die seismisch induzierte Verflüssigung.

Motivation

Es ist eine anspruchsvolle Aufgabe für Ingenieure, leistungsfähige Strukturen zu entwerfen. Diese Strukturen sollten u. a. in der Lage sein, allen Arten von zu erwartenden natürlichen oder menschlichen Einflüssen standzuhalten und die Anforderungen einer nachhaltigen und stabilen Konstruktion zu erfüllen. In für Erdbeben anfälligen und seismisch aktiven Ländern werden besonders intensive Bemühungen zur Gestaltung seismisch resistenter Einrichtungen unternommen, um die wirtschaftlichen, sozialen oder ökologischen Probleme, die ein zerstörerisches Erdbeben nach sich ziehen kann, zu reduzieren.

Das Verhalten von Böden bei dynamischer Belastung ist insbesondere in den Bereichen des Bauingenieurwesens und der Seismologie von großer Bedeutung. Nach der Freisetzung von kinetischer Energie im Hypozentrum eines Erdbebens ergeben sich unterschiedliche Arten seismischer Wellen, die sich in der Erdkruste und auf der Erdoberfläche über Tausende von Kilometern fortpflanzen. Die Auswirkungen auf die Strukturen variieren von glatt (nicht zerstörend) oder unauffällig bis zu destruktiv nahe dem Epizentrum. Im schlimmsten Fall können sie durch das Versagen des Baugrundes zum Einstürzen von Gebäuden führen. Dies geschieht meist als Folge von Verflüssigungsphänomenen, die nach plötzlichen Beben oft in losen, gesättigten Böden auftreten können.

Der Einsatz fortschrittlicher Materialmodelle und moderner numerischer Methoden zusammen mit leistungsfähigen Computern verhilft dazu, komplizierte reale Probleme im Rahmen der „Computational Mechanics“ von Materialien und Strukturen nachzustellen und zu verstehen. In diesem Zusammenhang erlauben Simulationstechniken die Quantifizierung und Vorhersage der Leistung bestehender oder geplanter Konstruktionen mit unterschiedlichen Materialeigenschaften und bei verschiedenen Lastbedingungen. Außerdem ermöglichen sie es, optimale Lösungen zu finden, die die vorgegebenen Rahmenbedingungen erfüllen.

Die große Herausforderung besteht aber immer noch in der Einführung effizienter numerischer Werkzeuge, die in der Lage sind, reale Vorgänge genau zu simulieren, wobei die erforderlichen technischen Kapazitäten in einem angemessenen Rahmen bleiben. Der Schwerpunkt dieses Beitrags liegt auf der Entwicklung und Implementierung fortschrittlicher Materialmodelle und numerischer Verfahren, um das Verhalten gesättigter, granularer Materialien bei dynamischer Belastung zu analysieren.

Zielsetzung und Vorgehensweise

Die numerische Modellierung fluidgesättigter, poröser Medien auf der Grundlage der Kontinuumsmechanik ist das ultimative Ziel der vorliegenden Arbeit. Dieses Ziel wird sowohl durch die Anwendung der „Theorie Poröser Medien“ (TPM) als auch durch eine thermodynamisch konsistente Formulierung von Konstitutivgesetzen erreicht. Darüber hinaus wird für die numerische Umsetzung die „Finite-Elemente-Methode“ (FEM) neben verschiedenen monolithischen oder Splitting-Zeitintegrationsverfahren verwendet. Im Rahmen der isothermen und geometrisch linearen Behandlungen liegt der Fokus dieser Monographie auf vollständig gesättigten Materialien mit zwei nicht-mischbaren Phasen. Diese decken zum einen den Fall materiell inkompressibler Aggregate, zum anderen den Fall eines materiell inkompressiblen Festkörpers und eines kompressiblen Porenfluids ab. Außerdem befasst sich die Abhandlung mit zwei wichtigen Ereignissen in porösen Medien, nämlich der dynamischen Wellenausbreitung in unbegrenzten Gebieten und der Bodenverflüssigung.

Modellierung gesättigter, poröser Medien: Fluidgefüllte, poröse Werkstoffe wie wassergesättigter Boden repräsentieren im Wesentlichen ein volumengekoppeltes Festkörper-Fluid-Problem. Mithilfe der „Theorie Poröser Medien“ (TPM) im Rahmen der Mehrphasen-Kontinuumsmechanik können die Bewegungen des Porenfluids und die Deformationen der Festkörpermatrix beschrieben werden. Bei der makroskopischen Behandlung werden die Geometrie der einzelnen Körner und die Struktur der Mikrokanäle ignoriert. Stattdessen wird davon ausgegangen, dass ein statistisch gemittelt „verschmiertes“ Mehrphasen-Kontinuum besteht, bei dem alle Teilkörper gleichzeitig das Gesamtvolumen eines Kontrollraums einnehmen. Diese Art der Behandlung von mehrphasigen Materialien lässt sich auf die „Theorie der Mischung“ (TM) zurückführen, vgl. Bowen [24], Truesdell & Toupin [166] und Truesdell [164].

Die TM wurde später durch das Konzept der Volumenanteile erweitert, um zusätzliche Informationen über die Mikrostruktur des verschmierten Kontinuums zu integrieren, welche für die spätere TPM grundlegend sind. Dieser Ansatz wurde von Drumheller [48] aufgestellt, um einen leeren, porösen Festkörper zu beschreiben. Bowen [25, 26] erweiterte diese Studie hin zu fluidgesättigten, porösen Materialien unter Berücksichtigung sowohl kompressibler als auch inkompressibler Bestandteile. Die späteren Erweiterungen und Beiträge zur TPM, vor allem in den Bereichen der Geomechanik und Biomechanik, sind weitestgehend mit den Arbeiten von de Boer und Ehlers verbunden, für detaillierte Hinweise siehe [17, 18, 21, 57, 58].

Numerische Behandlung stark gekoppelter Probleme: Im Allgemeinen besteht ein gekoppeltes System aus zwei oder mehr interagierenden Subsystemen, in denen eine eigenständige Lösung eines einzelnen Subsystems gleichzeitig eine Behandlung der anderen Subsysteme erfordert. In der Mathematik können gekoppelte Probleme durch interaktive Formulierungen mit abhängigen Feldvariablen, die nicht auf der Gleichungsebene beseitigt werden können, ausgedrückt werden. Die Kopplungsstärke (schwach oder stark) ist abhängig von den gegenseitigen Beziehungen zwischen den Teilsystemen und der nicht-linearen Abhängigkeit der Feldvariablen von den Materialparametern. In diesem Zusammenhang gilt: Je stärker die Kopplung ist, desto weniger mögliche numerische

Verfahren ermöglichen eine robuste Lösung. Für weitere Informationen zu Definitionen und Klassifizierung gekoppelter Probleme wird der interessierte Leser auf die Arbeiten von Zienkiewicz & Taylor [192], Felippa *et al.* [70], Hameyer *et al.* [81], Matthies & Stein-dorf [130] und Markert [125] verwiesen.

Die Modellierung der fluidgesättigten, porösen Medien innerhalb der TPM ergibt stark gekoppelte Formulierungen mit inhärenten Kopplungstermen und Parametern. Dabei sind nur bestimmte numerische Verfahren geeignet, um stabile und präzise Lösungen, besonders für den Fall materiell inkompressibler Bestandteile, zu liefern, vgl. Felippa *et al.* [70], Markert *et al.* [126] und Heider [85]. In dieser Arbeit liegt ein Schwerpunkt auf der Untersuchung von monolithischen und Splitting-Lösungsstrategien und ihrer Algorithmen zur Simulation von Anfangs-Randwertproblemen (ARWP) des porösen Mediums bei dynamischer Belastung.

Bei den impliziten monolithischen Methoden werden die Gleichungen zuerst im Ort mit stabilen Finite-Elementen (FE) diskretisiert, danach wird ein geeignetes Zeitintegrationsverfahren implementiert. Unter Berücksichtigung der Steifigkeit des gekoppelten Systems werden verschiedene Zeitintegrationsverfahren im Rahmen der diagonal-impliziten Runge-Kutta-Ein-Schritt-Methoden (DIRK) diskutiert. Für weitere Details über die Lösung von gekoppelten Systemen im Allgemeinen und dabei in der Dynamik poröser Medien im Besonderen, siehe, z. B. Diebels *et al.* [46], Ellsiepen [66], Hairer & Wanner [80] und Markert *et al.* [126]. Im Splitting-Schema werden die Differenzialgleichungen zuerst in der Zeit diskretisiert, danach mit Zwischenvariablen zerlegt, und zuletzt im Ort mittels linearer FE-Ansatzfunktionen für alle primären Unbekannten diskretisiert, siehe Chorin [37], Prohl [146], Rannacher [150], van Kan [169] und Gresho & Sani [75].

Modellierung dynamischer Wellenausbreitung und Verflüssigung: Betrachtet man die Reaktion von Strukturen, die auf gesättigten Böden gegründet sind, so lassen sich zwei Arten der Beeinflussung des Baugrunds auf das strukturelle Verhalten bei dynamischer Anregung (z. B. während eines Erdbebens) unterscheiden: die Weitertragung der Bodenbewegung in Form einer aufgebrachten dynamischen Belastung (ein Wellenausbreitungsproblem) und das Aufkommen bleibender Verformungen durch das Versagen des Baugrundes (ein Bodenverflüssigungsproblem).

Ein grosser Teil dieser Monographie konzentriert sich auf die Modellierung der dynamischen Wellenausbreitung und die dazugehörigen numerischen Herausforderungen. In diesem Fall wird die Materialreaktion des Festkörpers als linear-elastisch angesehen und vom *Hookeschen* Elastizitätsgesetz bestimmt. Bei der Untersuchung von Verflüssigungsphänomenen in gesättigtem Boden wird die Materialantwort des Festkörpers als elastoviskoplastisch betrachtet. Dies umfasst die Implementierung eines hyperelastischen Modells für das nichtlineare, elastische Verhalten, vgl. Müllerschön [134], Scholz [155] oder Ehlers & Avci [60], und die Anwendung des Einflächenfließkriteriums nach Ehlers [53, 54] zur Beschreibung der inelastischen Reaktion. Die seismisch-induzierte Verflüssigung gesättigter Böden ist durch die Akkumulation des Porenwasserdrucks und die Aufweichung der körnigen Struktur gekennzeichnet. Ein solches Verhalten umfasst mehrere physikalische Ereignisse wie die „Flow-Verflüssigung“ (engl. „flow liquefaction“), die im locker gelagerten Sand stattfindet und die „zyklische Mobilität“ (engl. „cyclic mobility“), welche im mitteldicht bis dicht gelagerten Sand vorkommt, siehe Castro [34], Kramer & Elgamal

[109], Ishihara *et al.* [98], Verdugo & Ishihara [170] oder Zienkiewicz *et al.* [186].

Behandlung unbegrenzter Gebiete: In dem aktuellen Beitrag ist die Simulation der Wellenausbreitung in unbegrenzte Gebiete im Zeitbereich realisiert. Hier wird der semi-infinite Bereich in ein endliches Nahfeld und ein unendliches Fernfeld unterteilt. Das Nahfeld umgibt die Quelle der Schwingung und wird mit der FEM diskretisiert, während die räumliche Diskretisierung des Fernfelds mithilfe der quasi-statischen „Infinite-Elemente-Methode“ (IEM) durchgeführt wird, vgl. Marques & Owen [127] oder Wunderlich *et al.* [182]. Falls die Raumwellen die Schnittstelle zwischen den FE- und den IE-Bereichen erreichen, werden sie mithilfe einer viskosen Dämpfungsbegrenzung (engl. „viscous damping boundary“, Abk. VDB) absorbiert.

Die Idee des VDB-Schemas basiert auf der Arbeit von Lysmer & Kuhlemeyer [120]. Hierin werden geschwindigkeits- und parameterabhängige Dämpfungskräfte eingeführt, um die künstlichen Wellenreflexionen zu vermeiden. Für Anwendungsbeispiele und weitere Informationen siehe Haeggblad & Nordgren [79], Underwood & Geers [168], Wunderlich *et al.* [182] und Akiyoshi *et al.* [2]. Die geschwindigkeitsabhängigen Dämpfungsterme der VDB-Methode treten in der schwachen Formulierung des ARWP in Form von Randintegralen auf. Daher erfordert eine uneingeschränkt stabile numerische Lösung, dass die Dämpfungskräfte implizit behandelt werden (schwache Neumann-Randbedingungen), siehe Ehlers & Acartürk [59] oder Heider *et al.* [87] für weitere Details.

Verifikation und Validierung der numerischen Ergebnisse: Zur Untersuchung der verschiedenen Verhaltensweisen gesättigter poröser Materialien bei dynamischer Anregung werden die bereits genannten Gleichungssysteme, Methoden und Algorithmen auf vier ARWP angewandt. Hierbei werden für die Berechnungen einige numerische Pakete wie das gekoppelte FE-Programm PANDAS und ein FE-Scilab-Code eingesetzt. Die Genauigkeit der Simulationsergebnisse und die Glaubwürdigkeit der Numerik bei der Vorhersage des Verhaltens realer Systeme kann unter Verwendung von Verifikations- und Validierungsverfahren erfolgen, vgl. Oberkampf *et al.* [138] and Taiebat [163]. In diesem Zusammenhang zeigt Abbildung I eine Darstellung der Verifikations- und Validierungsschritte sowie einen allgemeinen Überblick über die folgende Methodik in dieser Arbeit.

Gliederung der Arbeit

Die vorliegende Arbeit ist in sieben Kapitel gegliedert:

Kapitel 1 leitet die Arbeit ein und enthält die in dieser Zusammenfassung aufgeführten Bemerkungen, Zitate, Methoden und Ziele.

Kapitel 2 beschreibt die notwendigen kontinuumsmechanischen Grundlagen für Mehrphasensysteme, die zur Modellierung von zweiphasigen porösen Materialien benötigt werden. Dies beinhaltet einen Überblick über die „Theorie Poröser Medien“, die kinematischen Beziehungen, die allgemeinen Bilanzgleichungen sowie die konstitutiven Annahmen.

Kapitel 3 beschäftigt sich mit thermodynamisch konsistenten Konstitutivgesetzen, die in der Lage sind, verschiedene Verhaltensweisen von porösen Aggregaten zu beschreiben. Dazu gehört die Diskussion der linear-elastischen, der nichtlinearen hyperelastischen und

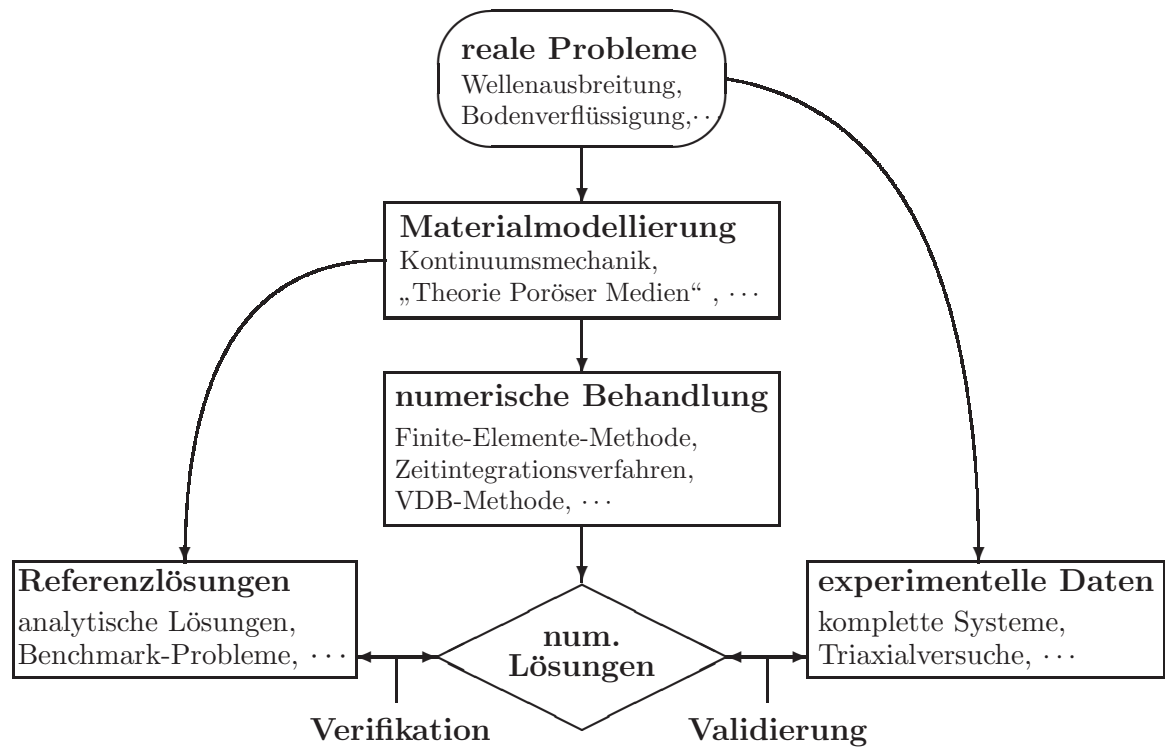


Abbildung I: Verifikations- und Validierungsschritte, vgl. Jeremić *et al.* [100]

der elasto-viskoplastischen Materialmodellierung. Außerdem werden in diesem Kapitel verschiedene Sätze von Bilanzgleichungen sowie die Herleitung der Wellengeschwindigkeiten in poro-elastischen Gebieten eingeführt.

Kapitel 4 erarbeitet die rechnerischen Strategien zur Lösung der ARWP dieser Arbeit. Dazu gehört die Diskussion der verschiedenen Verfahren für die Orts- und Zeitdiskretisierung. Außerdem werden Untersuchungen von steifen Problemen sowie eine Klassifizierung von gekoppelten Systemen in stark oder schwach gekoppelten Problemen durchgeführt. Weiterhin werden in diesem Kapitel die Simulation unbeschränkter Gebiete sowie die Umsetzung der VDB-Methode diskutiert.

Kapitel 5 konzentriert sich auf die Untersuchung und Modellierung der Verflüssigungsphänomene in gesättigten granularen Materialien bei dynamischer Anregung.

Kapitel 6 präsentiert vier numerische Beispiele für die Verifikation und Validierung der numerischen Methoden und Algorithmen in dieser Arbeit. Hierbei werden erhebliche Anstrengungen unternommen, um die Vor- und Nachteile der jeweiligen Lösungsstrategien aufzuzeigen. Weiterhin wird die Fähigkeit des Rechenmodells zur Simulation der realen Antwort diskutiert.

Zum Schluss gibt *Kapitel 7* eine kurze Zusammenfassung und einen Ausblick über zukünftige Entwicklungen der vorgestellten Forschungsarbeit.

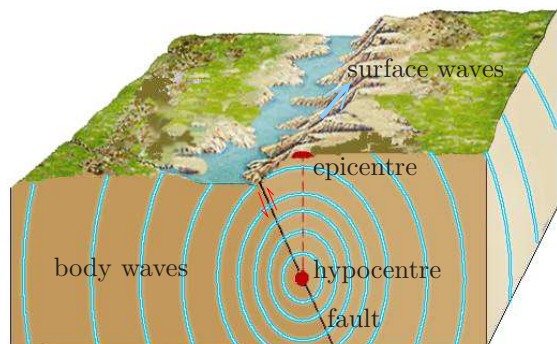
Chapter 1:

Introduction and Overview

1.1 Motivation

A challenging task for today's engineers is to design high performance structures that are able, for instance, to withstand all types of expected natural and human actions, fulfil the requirements of sustainable and healthy constructions, and improve the quality of people's life. In earthquake active and prone countries, intensive efforts are especially paid to designing seismic-resistant facilities in order to eliminate economic, social, and environmental problems that may follow the occurrence of a destructive earthquake.

The behaviour of soil under dynamic loading is of great importance, especially in the fields of civil engineering and seismology. Here, the release of kinetic energy at the hypocentre of an earthquake results in different types of seismic waves that may cross thousands of kilometres in the earth's crust and on the surface (Figure 1.1, left). The impact on structures varies from smooth or unremarkable to destructive near the epicentre of the earthquake. In this connection, Figure 1.1, right, shows overturning of a number of buildings due to the collapse of foundation soil. Such phenomena are known as liquefaction and happen often in loose, saturated soils as a consequence of sudden impacts.



cf. [earthquakesandplates.wordpress.com]



[www.ce.washington.edu]

Figure 1.1: Illustration of earthquake's components and wave propagation (left), and overturning of buildings due to soil liquefaction phenomena followed Niigata earthquake, Japan 1964 (right)

The use of advanced material models and modern numerical methods backed by powerful computers gives the ability to imitate and understand complicated real problems in the field of computational mechanics of materials and structures as well as other branches of applied sciences. In this context, simulation techniques can be used to quantify and predict the performance of an existing or planned engineering system using different material

properties and loading conditions. Moreover, they allow getting an optimal solution of the considered system, which fulfils the predefined constraints.

In earthquake engineering, simulation methods can be used to predict the destructive force of a seismic action with a goal of building safer constructions and protecting people's lives. The big challenge, however, is still in introducing efficient numerical tools, which are able to simulate the real world response accurately and require reasonable technical capacity.

The main focus of this monograph is on the development and implementation of advanced material models and numerical techniques in order to analyse saturated granular material behaviour under dynamic loading conditions.

1.2 Basic Features

The numerical modelling of fluid-saturated porous media dynamics within a continuum-mechanical framework is the ultimate aim of this dissertation. This purpose is achieved by exploiting the Theory of Porous Media (TPM) together with thermodynamically consistent constitutive laws for the material modelling. Additionally, the Finite Element Method (FEM) beside different monolithic or splitting time-stepping schemes are used for the numerical implementation. Within an isothermal and geometrically linear framework, the focus of this monograph is on fully saturated biphasic materials with immiscible phases. This covers the case of materially incompressible solid and fluid aggregates, and the case of a materially incompressible solid but compressible fluid constituent. Moreover, the treatment comprises two important incidents in porous media dynamics, namely, dynamic wave propagation in unbounded domains and liquefaction events.

Modelling of Multiphasic Porous Media

Biphasic porous materials like water-saturated soils essentially represent volumetrically interacting solid-fluid aggregates. Accordingly, they can be properly modelled with the Theory of Porous Media (TPM) on a continuum-mechanical basis accounting for both the solid-matrix deformation and the pore-fluid flow. In the macroscopic treatment, the geometry of the individual grains and the structure of the micro-channels are disregarded, and instead, the aggregates are assumed to be statistically distributed over a representative elementary volume (REV). Applying a homogenisation process to the REV, an averaged continuum model is obtained, in which each spatial point is permanently occupied by all constituents in the sense of superimposed and interacting continua. This way of treating multiphasic porous materials can be traced back to the Theory of Mixture (TM), cf. Bowen [24], Truesdell & Toupin [166] and Truesdell [164].

The absence of microtopology information of the smeared-out continuum in the TM is recovered by incorporating the concept of volume fractions, which is fundamental to the subsequent Theory of Porous Media (TPM). The approach has been employed by Drumheller [48] to describe an empty porous solid, and Bowen [25, 26] extended this study to fluid-saturated porous materials considering compressible as well as incompressible constituents. The later upgrades and contributions to the TPM, especially in the fields

of geomechanics and biomechanics, are substantially related to the works by de Boer and Ehlers, see [17, 18, 21, 57, 58] for detailed references.

Another popular continuum theory to describe the flow of viscous fluids in porous materials is *Biot's Theory* (BT). This macroscopic and phenomenological modelling approach is based on a generalisation of the theory of elasticity to multiphasic aggregates, cf. Biot [12, 13]. In porous media dynamics, BT introduces a critical frequency measure to distinguish between two cases of dynamic response: A low-frequency excitation causing *Poiseuille-type*¹ pore-fluid flow (e. g. seismic waves in water-saturated soil), and a higher-frequency loading with turbulent fluid flow and strong solid-fluid inertia coupling on the micro level. It is worth mentioning in this connection that for extremely high-frequency excitation, wavelengths can be of the same order as the micro-pore diameters, which makes the validity of the macroscopic modelling questionable.

Although BT and the TPM share a number of important features and yield the same results in particular cases, two intrinsic differences between them are important to be mentioned: First, unlike the TPM, BT does not require that the constitutive laws fulfil the thermodynamic constraints. Second, BT treats sealed pores as a part of the solid phase, whereas the TPM assumes that all pores are interconnected. This leads to differences in the definition of constituent volume fractions and the partial densities. Quantitative and detailed comparisons between the two mentioned approaches can be found in the works by Schanz & Diebels [154] or Steeb [159]. In fact, BT, the TM, and the TPM are considered the bases of many research works in the field of porous media dynamics modelling, see Lewis & Schrefler [115], Zienkiewicz *et al.* [185, 186], Breuer [29], Diebels & Ehlers [44] and Li *et al.* [116] among others.

In the current treatment of fluid-saturated biphasic aggregates, the solid constituent is always taken as materially incompressible, whereas two different behaviours of the pore fluid are considered: (1) Materially incompressible as in most parts of the thesis leading to a constant fluid material density. (2) Compressible giving rise to a so-called hybrid biphasic model as introduced by Ehlers *et al.* [62] or Mahnkopf [121]. Here, the introduction of the hybrid model comes in connection with the numerical stability and time-integration schemes discussion.

Numerical Treatment of the Strongly Coupled Problem

In general, a *coupled system* consists of two or more interacting subsystems, where an independent solution of any individual subsystem demands a simultaneous treatment of the others. Mathematically, coupled problems can be expressed by interactive formulations with dependent field variables that cannot be eliminated on the equation level. The coupling strength ranges from *weak* to *strong* depending on the mutual relations between the subsystems and the nonlinear dependency of the material parameters on the field

¹*Hagen-Poiseuille* equation describes the laminar flow of a viscous fluid through a cylindrical tube, which length is significantly larger than its diameter. Such flow is expressed by a linear relation between the pore-pressure gradient and the volume flux (cf. Suter [162]). For tube diameters or flow velocities above certain thresholds (e. g., due to a high frequency excitation and low-viscous fluid), the fluid flow is considered turbulent and the *Poiseuille's* law is not valid (cf. Biot [12]).

variables. Although the aforementioned two classes of coupling are physically motivated, they can only be numerically figured out. Here, the stronger is the coupling, the less are the possible numerical schemes that allow for robust solutions. For more details about the definitions and classification of coupled problems, the interested reader is referred to the works by Zienkiewicz & Taylor [192], Felippa *et al.* [70], Hameyer *et al.* [81], Matthies & Steindorf [130] and Markert [125].

A microscopic investigation of saturated porous materials shows an interaction between the solid and the fluid aggregates with a distinct interface in between. Thus, one has to deal with a *surface-coupled* problem where the pore-fluid pressure is an essential coupling variable. On the macroscopic, continuum level with overlapped constituents at each spatial point of the homogenised medium, the coupling is defined through nonlinear mutual terms of the governing partial-differential balance equations (PDE). This multiphase interaction gives rise to a class of *volume-coupled* or *material-coupled* systems. Indeed, the primary concern of this thesis is on the treatment of this class of problems.

The modelling of fluid-saturated porous media within the TPM implies a volume-coupled formulation over the REV with inherent coupling terms. Here, the coupling is considered strong due to the fact that only specific numerical schemes are eligible to give stable and accurate solutions especially for the case of materially incompressible constituents, cf., e.g., Felippa *et al.* [70], Markert *et al.* [126] and Heider [85] for details. In this monograph, a major focus is laid on the investigation of monolithic and splitting solution strategies and their algorithms for the simulation of initial-boundary-value problems of porous media dynamics.

In the monolithic approach, the system of equations is solved by one common strategy, where the spatial discretisation is carried out first using the finite element method (FEM), and the time integration is applied second via one-step time-stepping schemes. In the case of the materially incompressible biphasic model, the FEM implementation leads to a time-continuous system of differential-algebraic equations (DAE) with singular generalised mass matrix. Thus, only implicit time-integration schemes are appropriate. For hybrid models with materially compressible pore fluids, the spatial discretisation yields a set of space-discrete ordinary differential equations (ODE), where implicit as well as explicit monolithic time-stepping schemes are applicable. However, due to the stiffness of the arising strongly coupled ODE system, implementation of explicit monolithic methods requires the use of very small time steps to obtain a stable solution, cf. Hairer & Wanner [80]. Therefore, implicit schemes are preferable in such cases.

Accounting for the stiffness of the coupled system, different stiffly accurate time-stepping rules are discussed within the framework of one-step, diagonal implicit Runge-Kutta (DIRK) methods. For more details on the solution of coupled systems in general and those arising in porous media dynamics in particular, we refer to the works by Diebels *et al.* [46], Ellsiepen [66], Hairer & Wanner [80], Markert *et al.* [126] and the quotations therein. One of the major challenges of implementing implicit monolithic procedures to the upper mentioned DAE system is the crucial requirement for stable mixed-order finite element formulations in order to avoid oscillations in the pore-pressure field originating from the inherent algebraic volume balance equation. Here, the chosen mixed FEM must fulfil the *Ladyschenskaja-Babuška-Brezzi* (LBB) condition (cf. Brezzi & Fortin [30] or

Braess [27]), which can be verified with the simplified patch test of Zienkiewicz *et al.* [190]. Actually, the latter issue as well as different stabilisation techniques for the monolithic treatment are discussed in details throughout this thesis. Moreover, against the background of an accurate and stable monolithic treatment of multi-field problems, the influence of the chosen primary variables and the governing balance relations is also a subject of investigation.

The other discussed time-stepping strategy in this work belongs to the popular class of operator-splitting techniques, for which several aliases such as the fractional step, the pressure projection, and the pressure correction method are found in the literature. Splitting schemes are applied to the partial differential equations that result from the materially incompressible biphasic model, which gives the possibility to deal with the strongly coupled problem in a weak or loose fashion. The basic idea is to decouple the overall aggregate volume balance (being an algebraic constraint) from the momentum balance equations by advancing each time step via intermediate steps. This allows to separate the pore-pressure solution from the kinematic primary unknowns, and thus, dissolve the necessity to fulfil the LBB condition of mixed-order FEM. Operator-splitting schemes are implemented in a sequence so that the time stepping is applied first, the time partitioning via intermediate velocities second, and the spatial FE discretisation last. This treatment permits to use continuous and equal-order interpolations of all primary variables. Dealing with the coupled equations of porous media dynamics in a decoupled way results in explicit as well as implicit equations. Therefore, this procedure is referred to as a semi-explicit-implicit approach. Here, the aim is to make use of the advantages of the pure-explicit and pure-implicit schemes and to avoid the disadvantages of the monolithic treatment of stiff coupled systems.

In talking about the origin of splitting schemes, Chorin [37] proposed one of the first semi-explicit-implicit methods in order to solve the incompressible *Navier-Stokes* coupled equations in computational fluid dynamics (CFD). Afterwards, different splitting methods and a lot of analysis have been carried out within the CFD, see, e. g., the works by Prohl [146], Rannacher [150], van Kan [169] and Gresho & Sani [75]. Having a comparable mathematical structure to the *Navier-Stokes* equations, several splitting algorithms have been adopted by Zienkiewicz *et al.* [189] to solve the balance relations of saturated soil dynamics. In particular, the various schemes differ in the way that the pore-pressure variable is treated, which could be a conditionally stable explicit or an unconditionally stable implicit treatment, cf. Huang *et al.* [93, 94].

Apart from the aforementioned two solution strategies and for the sake of completeness, we additionally refer to the time- and the coupled space-time discontinuous *Galerkin* (DG) methods, which are widely applied to porous media dynamics, cf., e. g., Chen *et al.* [35, 36]. Such schemes are proved to have a good performance regarding the numerical stability and accuracy. They are also proper for mesh adaptation and parallel computation. However, the application of the DG methods is beyond the scope of this research work.

Dynamic Wave Propagation and Liquefaction Modelling

In talking about the response of structures founded on saturated soils, foundation soil affects the structural behaviour during dynamic excitation (e.g. due to earthquakes) in two significant ways: By transmitting the ground motion in a form of applied dynamic loading (\rightarrow wave propagation problem), and by imposing permanent deformations caused by collapse of the underlying soil (\rightarrow soil liquefaction problem).

A considerable part of this monograph concentrates on the computational modelling of dynamic wave propagation and the accompanying numerical challenges. In this case, the material response of the solid skeleton is considered linear elastic and governed by the *Hookean* elasticity law. Moreover, different monolithic and splitting time-integration schemes are discussed to solve such problems.

The tendency of saturated porous materials to liquefy under the impact of dynamic loading is analysed in detail. Here, the solid constituent response is considered to be elastoviscoplastic. This comprises the implementation of a hyperelastic model for the nonlinear elastic behaviour, cf. Müllerschön [134], Scholz [155] or Ehlers & Avcı [60], and also the application of the single-surface yield function of Ehlers [53, 54] for capturing the inelastic response.

The definitions and terminology of liquefaction-related phenomena throughout this thesis are based on pioneering publications in the field of computational geomechanics and earthquake engineering such as the works by Kramer & Elgamal [109], Castro [34], Ishihara *et al.* [98], Verdugo & Ishihara [170] and Zienkiewicz *et al.* [186]. In this connection, seismic-induced liquefaction tendency in saturated biphasic media is characterised by the build-up of pore-fluid pressure and softening of the solid granular structure. Such behaviour comprises a number of physical events such as the ‘flow liquefaction’ and the ‘cyclic mobility’, which are discussed in detail in Chapter 5. In this context, the attention is paid on investigating the initiation of liquefaction phenomena. However, the post-liquefaction stage, which may include large deformations and requires investigation of the continuous development of the shear strains, is beyond the scope of this work, see, e.g., Wang & Dafalias [174] or Taiebat [163] for more details.

Treatment of Unbounded Domains

Dynamic wave propagation in semi-infinite domains is of great importance, especially in the fields of geomechanics, civil engineering and seismology. As examples, consider the hazardous seismic impacts caused by earthquakes or the wave-induced vibrations of offshore wind turbine’s foundations.

Against the background of an efficient numerical treatment, one has to take into consideration that in unbounded domains, acoustic body waves are supposed to propagate towards infinity. Thus, it is sensible to divide the semi-infinite domain into a finite near field surrounding the source of vibration and an infinite far field accounting for the energy radiation to infinity. In this regard, numerous approaches have been proposed in the literature to efficiently treat unbounded spatial domains, see, e.g., the works by Givoli [71], Lehmann [114] and Heider *et al.* [87] for an overview.

In the current contribution, the simulation of wave propagation into infinity is realised in the time domain. Here, the near field is discretised with the FEM, whereas the spatial discretisation of the far field is accomplished using the mapped infinite element method (IEM) in the quasi-static form as given in the work by Marques & Owen [127]. This insures the representation of the far-field stiffness and its quasi-static response instead of implementing rigid boundaries surrounding the near field, cf. Wunderlich *et al.* [182]. However, when body waves approach the interface between the FE and the IE domains, they partially reflect back to the near field as the quasi-static IE cannot capture the dynamic wave pattern in the far field. To overcome this, the waves are absorbed at the FE-IE interface using the viscous damping boundary (VDB) scheme, which basically belongs to the class of absorbing boundary methods. The idea of the VDB is based on the work by Lysmer & Kuhlemeyer [120], in which velocity- and parameter-dependent damping forces are introduced to get rid of artificial wave reflections. In [120], the verification of the proposed VDB scheme has been carried out by studying the reflection and refraction of elastic waves at the interface between two domains, where the arriving elastic energy should be absorbed. For more information and different applications, see, e. g., the works by Haeggblad & Nordgren [79], Underwood & Geers [168], Wunderlich *et al.* [182] and Akiyoshi *et al.* [2].

The velocity-dependent and with that solution-dependent damping terms of the VDB method enter the weak formulation of the initial-boundary-value problem in form of a boundary integral. Hence, an unconditionally stable numerical solution requires the damping forces to be treated implicitly as weakly imposed Neumann boundary conditions, see Ehlers & Acartürk [59] or Heider *et al.* [87] for more details.

Verification and Validation of the Numerical Results

For investigating several behaviours of saturated porous materials under dynamic excitation, the aforementioned schemes and algorithms are implemented to initial-boundary-value problems (IBVP) using different numerical libraries such as the coupled FE package PANDAS² and a FE splitting Scilab³ code. The accuracy of the simulation results and the credibility of the numerical treatment in foretelling the behaviour of real systems can be assessed using verification and validation procedures, cf. Oberkampf *et al.* [138] and Taiebat [163]. In this connection, Figure 1.2 depicts an illustration of the verification and validation steps as well as a general overview of the methodology followed in this work.

The verification process is carried out to determine that the considered mathematical model, represented by a set of coupled differential equations, is solved correctly in the FE code. This insures that the model implementation accurately represents the developer's conceptual description of the problem. In this regard, code verification covers, for instance, evaluation of the numerical errors and the instability sources and tries to eliminate them.

In the problem of wave propagation in a saturated poroelastic column (Section 6.1), verification of the different computational procedures is carried out by comparing the numerical

²Porous media Adaptive Nonlinear finite element solver based on Differential Algebraic Systems, see [<http://www.get-pandas.com>]

³Scientific free software package for numerical computations, see [<http://www.scilab.org>]

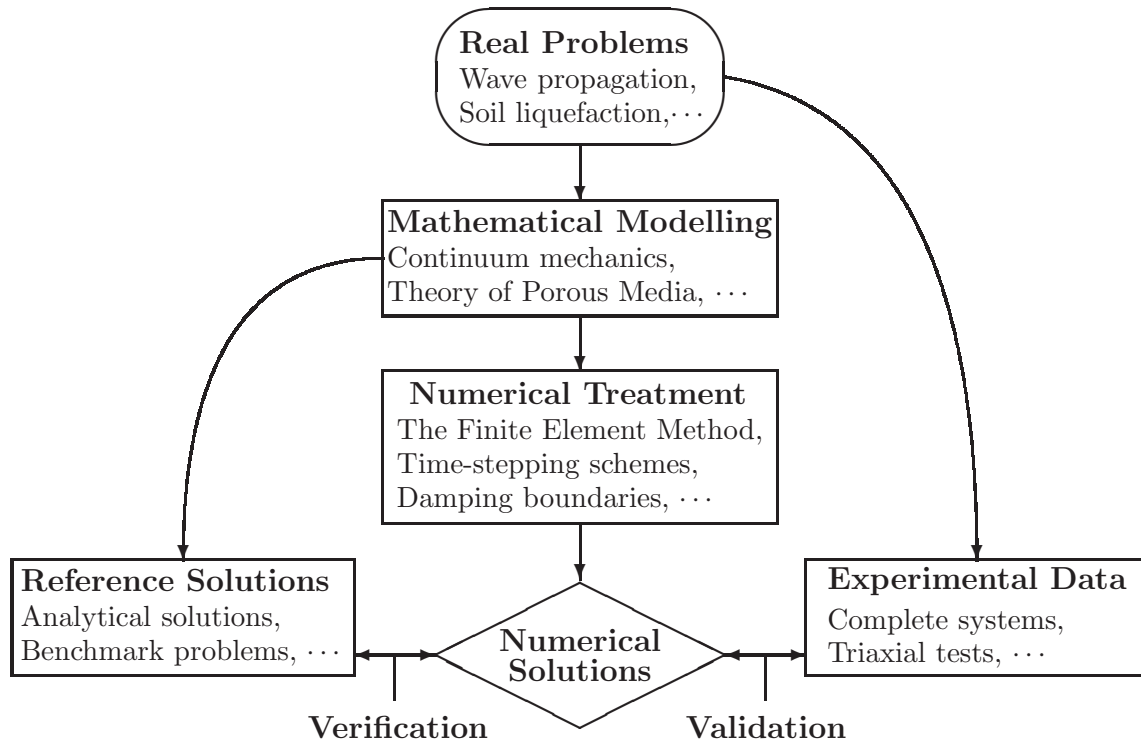


Figure 1.2: Verification and validation of a numerical model, cf. Jeremić *et al.* [100]

results with (semi-)analytical solutions for the solid displacement and the pore-fluid pressure of an infinite half-space under dynamic loading and materially incompressible constituents, cf. de Boer *et al.* [22]. Moreover, a benchmark solution has been numerically generated in Section 6.3 by choosing large dimensions of the IBVP for the verification of the proposed infinite half spaces treatment. In other examples, highly accurate numerical solutions of the coupled PDE using reliable computational procedures have been introduced in order to compare and assess the accuracy and behaviour of the different time-stepping algorithms.

Validation strategies are applied to evaluate the performance of the suggested model and the corresponding computational strategies in simulating the real world behaviour. Comparing numerical results with real experiments helps, on the one hand, to improve both the mathematical model and the physical experiments through identifying and minimising of error sources and, on the other hand, increase the credibility of the computational model in simulating the actual response. An example of material model validation is introduced in Chapter 5. Therein, it is proved that the considered elasto-viscoplastic constitutive model within the numerical treatment is able to simulate saturated granular material behaviour with different initial densities. In particular, the pore-fluid pressure accumulation and the deviatoric stress change in computational triaxial tests (as IBVP) are compared with experimental results of triaxial tests under quasi-static and dynamic loading conditions taken from the literature.

1.3 Thesis Layout

To give a brief overview, *Chapter 2* systematically describes the general framework of continuum-mechanical modelling of multiphasic materials, which includes, for instance, the basics of the Theory of Porous Media and the concept of volume fractions. Moreover, the kinematics of multiphasic continua and the specification of the universal master balance relations are introduced in this part of the thesis.

The formulation of the mathematical model is completed in *Chapter 3*. Therein, thermodynamically consistent constitutive laws, which are able to describe various behaviours of biphasic porous aggregates, are presented. This includes the discussion of the linear elastic, the nonlinear hyperelastic, and the elasto-viscoplastic material modelling. Additionally, this chapter introduces different sets of governing balance equations as well as the derivation of the bulk wave velocities in a poroelastic medium.

The computational strategies to solve initial-boundary-value problems in this thesis are elaborated in *Chapter 4*. Therein, the variational formulation of the governing balance equations and the spatial discretisation using the FEM are discussed in details. Moreover, investigation of stiff problems as well as classification of coupled systems depending on their mathematical structure into strong or weak coupled problems are realised. A considerable part of this chapter is devoted to the time discretisation of strongly coupled problems with detailed description of the monolithic and splitting solution algorithms. Furthermore, simulation of unbounded domains and the implementation of the viscous damping boundary method are figured out in this part of the work.

Chapter 5 concentrates on the investigation of liquefaction phenomena in saturated granular materials under dynamic excitation. This comprises definitions and descriptions of the liquefaction mechanism, factors affecting the saturated soil response, and an *in-situ* earthquake-induced liquefaction example taken from the literature. Moreover, the basic features of liquefaction events like pore-pressure build-up and softening of the granular structure are figured out using a well-formulated elasto-viscoplastic constitutive model with isotropic hardening.

Chapter 6 focuses on the verification and validation of the numerical methods and algorithms in the thesis. Here, the presented formulations and solution schemes are implemented and compared in different initial-boundary-value problems. Furthermore, considerable efforts are made to show the merits and drawbacks of each solution strategy as well as to illustrate the ability of the computational model to simulate the real word response.

Finally, *Chapter 7* introduces a brief summary, conclusions, and proposals for future developments of the presented research work.

Chapter 2:

Theoretical Basics

This chapter is mainly concerned with the description of saturated porous media within a macroscopic framework. Therefore, fundamentals of multiphase continuum theories are briefly introduced. This includes the basic concepts of the TPM, the kinematics of multiphase media, and the balance relations in a general and a specific form. The mathematical modelling is completed in Chapter 3 by introducing thermodynamically consistent constitutive relations, which are able to capture the material response under different loading conditions.

2.1 Theory of Porous Media (TPM)

The TPM provides a comprehensive and excellent framework for the macroscopic modelling of a biphasic porous body consisting of an immiscible solid skeleton saturated by a single interstitial fluid. In this regard, the heterogeneous solid aggregate with a random granular geometry is assumed to be in a state of ideal disarrangement over a representative elementary volume¹ (REV). The dimensions of the chosen REV with respect to the average diameters of the micro-channels or grain sizes play an important role in the validity of the macroscopic approach in describing the flow through the porous space. For detailed information especially about the quantitative evaluation of the REV, we refer to the work by Diebels *et al.* [45] and Du & Ostojca-Starzewski [49] among others.

Applying a homogenisation process to the REV yields a smeared-out continuum φ with overlapped, interacting and statistically distributed solid and fluid aggregates φ^α ($\alpha = S$: solid phase; $\alpha = F$: pore-fluid phase), cf. Figure 2.1. Thus, at any given macroscopic subspace, the following relation holds:

$$\varphi = \bigcup_{\alpha} \varphi^{\alpha} = \varphi^S \cup \varphi^F. \quad (2.1)$$

In order to integrate constituent microscopic information, the introduced ‘Mixture Theory’ model is extended under the assumption of immiscible aggregates by the ‘Concept of Volume Fractions’, which is fundamental to the later Theory of Porous Media, cf., e. g., the works by Bowen [25], de Boer [17, 18], de Boer & Ehlers [20, 21] and Ehlers [57, 58]. Consequently, a volumetric averaging process of all interrelated constituents is prescribed over the REV, and the incorporated physical fields of the microstructure are represented by their volume proportions on the macroscopic level.

¹In some references, representative volume element (RVE) is used instead of REV

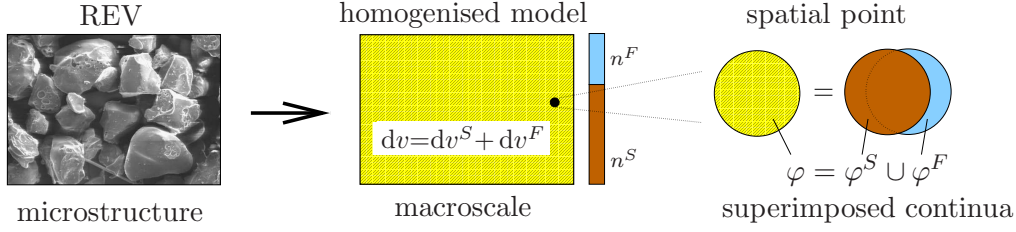


Figure 2.1: REV of saturated sand showing the granular microstructure and the biphasic TPM macro model with overlapped constituents

Applying the concept of volume fractions to a homogenised, fluid-saturated porous body \mathcal{B} within the TPM, the overall volume V of \mathcal{B} results from the sum of the partial volumes V^α of the constituents as

$$V = \int_{\mathcal{B}} dv = \sum_{\alpha} V^\alpha \quad \text{with} \quad V^\alpha = \int_{\mathcal{B}} dv^\alpha =: \int_{\mathcal{B}} n^\alpha dv. \quad (2.2)$$

Following this, the volume fraction n^α of a constituent φ^α is defined over the REV as

$$n^\alpha = \frac{dv^\alpha}{dv} \quad (2.3)$$

with dv^α and dv being the partial and the total volume elements, respectively, cf. Figure 2.1. Thereafter, the saturation condition results from equations (2.2) and (2.3) as

$$\sum_{\alpha} n^\alpha = n^S + n^F = 1 \quad \text{with} \quad \begin{cases} n^S & : \text{solidity,} \\ n^F & : \text{porosity.} \end{cases} \quad (2.4)$$

Under the assumption of a fully saturated medium during the whole deformation process, the saturation constraint (2.4) should always be satisfied. Additionally, in the current treatment of multiphasic materials, it is always assumed that $0 < n^\alpha < 1$, i. e., the transition into a single-phasic material (pure solid or fluid) is not a case of study.

Proceeding from the definition of volume fractions in (2.3), two distinct density functions for each constituent can be specified: The so-called material (or effective) density function $\rho^{\alpha R}$ relating the local mass dm^α to the partial volume element dv^α , and the partial density function ρ^α relating dm^α to the bulk volume element dv :

$$\left. \begin{array}{l} \rho^{\alpha R} := \frac{dm^\alpha}{dv^\alpha}, \\ \rho^\alpha := \frac{dm^\alpha}{dv}, \end{array} \right\} \longrightarrow \begin{cases} \rho = \sum_{\alpha} \rho^\alpha, \\ \rho^\alpha = n^\alpha \rho^{\alpha R}. \end{cases} \quad (2.5)$$

Herein, the overall aggregate density ρ results from the sum of the constituent densities and the partial and material densities are related via n^α . Moreover, $\rho^\alpha = n^\alpha \rho^{\alpha R}$ shows that for the case of materially incompressible constituents ($\rho^{\alpha R} = \text{const.}$) of the biphasic model, the compressibility of the overall medium (bulk compressibility) is only possible under drained conditions through variation of the volume fractions.

2.2 Kinematics of Multi-phase Continua

The kinematic formulations in mixture theories have been originally adopted from the continuum mechanics of single-phase materials, cf. Haupt [83] or Ehlers [50, 52]. Thereafter, they have been used within the TPM to describe the motion of multiphasic continua, cf. Ehlers [57] and de Boer [17]. The purpose of the following section is to give a brief review of the kinematic relations of multiphasic continuum mechanics, which are used in later sections for the treatment of the considered biphasic material in the small deformation regime.

2.2.1 Basic Definitions

The motion of solid and fluid continuum bodies \mathcal{B}^α ($\alpha = S$: solid phase; $\alpha = F$: fluid phase), each of which occupies a considerable physical space of the overall biphasic body \mathcal{B} is studied on the continuum level. Therefore, each constituent φ^α of the homogenised medium is represented by a material point P^α that occupies a unique position \mathbf{X}_α of the reference configuration. In the actual configuration, each spatial position \mathbf{x} is occupied by one material point of each constituent, where the concept of superimposed and interacting continua with an exclusive motion function χ_α for each φ^α should always be maintained, cf. Figure 2.2.

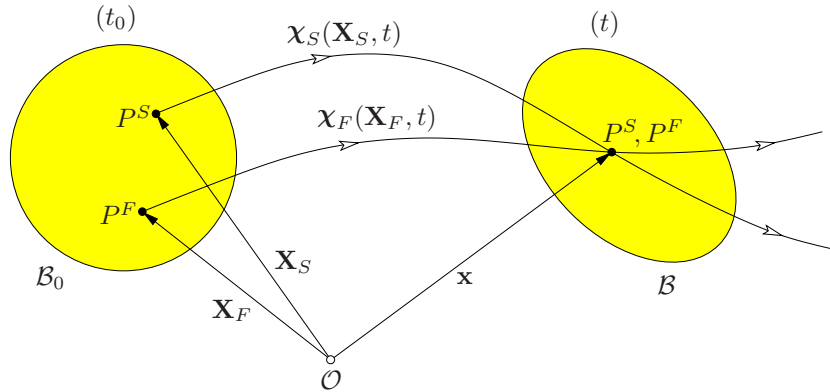


Figure 2.2: Motion of biphasic solid-fluid aggregates

Following this, the *Lagrangian* (material) description of the current position, velocity, and acceleration of each constituent is given, respectively, in terms of unique motion (mapping) functions χ_α as

$$\mathbf{x} = \chi_\alpha(\mathbf{X}_\alpha, t), \quad \mathbf{v}_\alpha := \dot{\mathbf{x}}_\alpha = \frac{d\chi_\alpha(\mathbf{X}_\alpha, t)}{dt}, \quad (\mathbf{v}_\alpha)'_\alpha := \ddot{\mathbf{x}}_\alpha = \frac{d^2\chi_\alpha(\mathbf{X}_\alpha, t)}{dt^2}. \quad (2.6)$$

Continuity allows for an *Eulerian* (spatial) description of the motion, in which χ_α^{-1} is used in order to trace back the location of a material point in the initial configuration. This can only be achieved if the *Jacobian* (J_α) has a value different from zero, i. e.,

$$\mathbf{X}_\alpha = \chi_\alpha^{-1}(\mathbf{x}, t) \quad \text{iff} \quad J_\alpha := \det \frac{d\chi_\alpha(\mathbf{X}_\alpha, t)}{d\mathbf{X}_\alpha} \neq 0. \quad (2.7)$$

Indeed, the existence of χ_α^{-1} guarantees the previously mentioned restriction of an individual motion function for each constituent.

For the sake of completeness, an *Eulerian* description of the velocity and acceleration can be introduced as an alternative to relations (2.6)_{2,3}, i. e.,

$$\dot{\mathbf{x}}_\alpha = \dot{\mathbf{x}}_\alpha(\mathbf{x}, t), \quad \ddot{\mathbf{x}}_\alpha = \ddot{\mathbf{x}}_\alpha(\mathbf{x}, t). \quad (2.8)$$

The local barycentric velocity of the overall medium (mixture velocity) is given in terms of the total and partial densities, cf. (2.5), as

$$\dot{\mathbf{x}} = \frac{1}{\rho} \sum_\alpha \rho^\alpha \dot{\mathbf{x}}_\alpha. \quad (2.9)$$

The relative motion between a constituent φ^α and the overall aggregate φ is described by the diffusion velocity \mathbf{d}_α as

$$\mathbf{d}_\alpha = \dot{\mathbf{x}}_\alpha - \dot{\mathbf{x}} \quad \text{with} \quad \sum_\alpha \rho^\alpha \mathbf{d}_\alpha = \mathbf{0}. \quad (2.10)$$

Here, $(\cdot)'_\alpha$ and $(\cdot)^\cdot$ represent the material time derivatives following the motions of φ^α and φ , respectively. Proceeding with $\Psi(\mathbf{x}, t)$ and $\mathbf{\Psi}(\mathbf{x}, t)$ as scalar- and vector-valued functions, which are arbitrary and sufficiently differentiable, the material time derivatives can be expressed as

$$\begin{aligned} \dot{\Psi}_\alpha &= \frac{d_\alpha \Psi}{dt} = \frac{\partial \Psi}{\partial t} + \text{grad} \Psi \cdot \dot{\mathbf{x}}_\alpha, & \dot{\mathbf{\Psi}}_\alpha &= \frac{d_\alpha \mathbf{\Psi}}{dt} = \frac{\partial \mathbf{\Psi}}{\partial t} + (\text{grad} \mathbf{\Psi}) \dot{\mathbf{x}}_\alpha, \\ \dot{\Psi} &= \frac{d\Psi}{dt} = \frac{\partial \Psi}{\partial t} + \text{grad} \Psi \cdot \dot{\mathbf{x}}, & \dot{\mathbf{\Psi}} &= \frac{d\mathbf{\Psi}}{dt} = \frac{\partial \mathbf{\Psi}}{\partial t} + (\text{grad} \mathbf{\Psi}) \dot{\mathbf{x}}. \end{aligned} \quad (2.11)$$

Herein, $\text{grad}(\cdot) := \partial(\cdot)/\partial \mathbf{x}$ is the gradient operator, which is defined as the partial derivative of (\cdot) with respect to the local position \mathbf{x} .

Following this, equations (2.6)₁ and (2.7)₁ lead to the definitions of the material deformation gradient \mathbf{F}_α and its inverse \mathbf{F}_α^{-1} as fundamental quantities in continuum mechanics. In particular, we have

$$\mathbf{F}_\alpha = \frac{\partial \mathbf{x}}{\partial \mathbf{X}_\alpha} =: \text{Grad}_\alpha \mathbf{x} \quad \text{and} \quad \mathbf{F}_\alpha^{-1} = \frac{\partial \mathbf{X}_\alpha}{\partial \mathbf{x}} =: \text{grad} \mathbf{X}_\alpha \quad (2.12)$$

with $\text{Grad}_\alpha(\cdot) := \partial(\cdot)/\partial \mathbf{X}_\alpha$ denoting the gradient with respect to the reference position. Here, the relation (2.12)₂ requires that \mathbf{F}_α is non-singular, i. e., $\det \mathbf{F}_\alpha := J_\alpha \neq 0$ is always fulfilled. The satisfaction of the latter condition can be proved by utilising a simple argument: Since the motion of any constituent φ^α at any time t is unique and invertible to a unique reference state, cf. (2.7), the deformation gradient is non-singular ($\det \mathbf{F}_\alpha \neq 0$). Additionally, proceeding from the initial (undeformed) state with $\mathbf{F}_\alpha(t_0)$ equal to the second-order identity tensor \mathbf{I} yields that $\det \mathbf{F}_\alpha(t_0) = 1$, such that the

domain of $\det \mathbf{F}$ is restricted to positive values², i. e.,

$$\det \mathbf{F}_\alpha = J_\alpha > 0. \quad (2.13)$$

2.2.2 Deformation and Strain Measures of Biphasic Continua

In porous media theories, it is convenient to proceed from a *Lagrangean* description of the solid matrix via the solid displacement \mathbf{u}_S and velocity \mathbf{v}_S as the kinematical variables. However, the pore-fluid flow is expressed either in a modified *Eulerian* setting via the seepage velocity vector \mathbf{w}_F denoting the fluid motion relative to the deforming skeleton, or by an *Eulerian* description using the fluid velocity \mathbf{v}_F itself. In particular, we have

$$\mathbf{u}_S = \mathbf{x} - \mathbf{X}_S, \quad \mathbf{v}_S = (\mathbf{u}_S)'_S = \dot{\mathbf{x}}_S, \quad \mathbf{v}_F = \dot{\mathbf{x}}_F, \quad \mathbf{w}_F = \mathbf{v}_F - \mathbf{v}_S. \quad (2.14)$$

The solid acceleration vector is derived directly by taking the second time derivative with respect to the solid motion, i. e., $\ddot{\mathbf{x}}_S = (\mathbf{v}_S)'_S$. The fluid acceleration vector is also derived following the motion of φ^S , which requires the use of the material time derivative rule (2.11)₂. In detail, the fluid derivation rule reads

$$\left. \begin{aligned} (\mathbf{v}_F)'_S &= \frac{\partial \mathbf{v}_F}{\partial t} + (\text{grad} \mathbf{v}_F) \mathbf{v}_S \\ (\mathbf{v}_F)'_F &= \frac{\partial \mathbf{v}_F}{\partial t} + (\text{grad} \mathbf{v}_F) \mathbf{v}_F \end{aligned} \right\} \longrightarrow (\mathbf{v}_F)'_S = (\mathbf{v}_F)'_F - \text{grad} \mathbf{v}_F (\mathbf{v}_F - \mathbf{v}_S). \quad (2.15)$$

As the fluid motion is described with respect to the deforming solid phase, the fluid material deformation gradient \mathbf{F}_F will not be required in the later treatment. However, it is clear that the solid material deformation gradient \mathbf{F}_S plays the major role in the kinematical formulation. Thus, exploiting (2.14)₁ and (2.12)₁, \mathbf{F}_S can be expressed as

$$\mathbf{F}_S = \frac{\partial \mathbf{x}}{\partial \mathbf{X}_S} = \frac{\partial (\mathbf{X}_S + \mathbf{u}_S)}{\partial \mathbf{X}_S} = \mathbf{I} + \text{Grad}_S \mathbf{u}_S. \quad (2.16)$$

Having defined \mathbf{F}_S , the deformation and strain tensors as important measures to describe the local behaviour of body deformation are discussed in the following. Here, for better understanding of the deformation mechanism, it is possible to decompose the total deformation into a rotational and a stretch stage using the polar decomposition theorem. Therefore, \mathbf{F}_S is uniquely split into a proper orthogonal rotation tensor \mathbf{R}_S , and a right (material) or a left (spatial) stretch tensor \mathbf{U}_S or \mathbf{V}_S , respectively, viz.:

$$\mathbf{F}_S = \mathbf{R}_S \mathbf{U}_S = \mathbf{V}_S \mathbf{R}_S \quad \text{with} \quad \mathbf{R}_S \mathbf{R}_S^T = \mathbf{R}_S^T \mathbf{R}_S = \mathbf{I}. \quad (2.17)$$

Based on the transport mechanism of a line element between the reference and the actual configuration ($d\mathbf{x} = \mathbf{F}_\alpha d\mathbf{X}_\alpha$), the definitions of the right and the left *Cauchy-Green*

²“The material deformation gradient represents all local properties of the deformation”, cf. Haupt [83]. Thus, $\det \mathbf{F}_\alpha$ serves as a mapping mechanism of a material volume element between the reference and the actual configuration, i. e., $dv = \det \mathbf{F}_\alpha dV_\alpha$. It is clear that negative or zero values of $\det \mathbf{F}_\alpha$ hold no physical meanings.

deformation tensors \mathbf{C}_S and \mathbf{B}_S , which are symmetric, positive definite and have quadratic forms, are respectively given as

$$\begin{aligned} d\mathbf{x} \cdot d\mathbf{x} &= (\mathbf{F}_S d\mathbf{X}_S) \cdot (\mathbf{F}_S d\mathbf{X}_S) = d\mathbf{X}_S \cdot (\mathbf{F}_S^T \mathbf{F}_S) d\mathbf{X}_S = d\mathbf{X}_S \cdot \mathbf{C}_S d\mathbf{X}_S, \\ &\longrightarrow \mathbf{C}_S := \mathbf{F}_S^T \mathbf{F}_S = \mathbf{U}_S \mathbf{U}_S =: \mathbf{U}_S^2 \end{aligned} \quad (2.18)$$

and

$$\begin{aligned} d\mathbf{X}_S \cdot d\mathbf{X}_S &= (\mathbf{F}_S^{-1} d\mathbf{x}) \cdot (\mathbf{F}_S^{-1} d\mathbf{x}) = d\mathbf{x} \cdot (\mathbf{F}_S^{T-1} \mathbf{F}_S^{-1}) d\mathbf{x} = d\mathbf{x} \cdot \mathbf{B}_S^{-1} d\mathbf{x}, \\ &\longrightarrow \mathbf{B}_S := \mathbf{F}_S \mathbf{F}_S^T = \mathbf{V}_S \mathbf{V}_S =: \mathbf{V}_S^2. \end{aligned} \quad (2.19)$$

Due to the orthogonality of \mathbf{R}_S , the following rotational push-forward and pull-back relations between \mathbf{C}_S and \mathbf{B}_S can be defined:

$$\mathbf{B}_S = \mathbf{R}_S \mathbf{C}_S \mathbf{R}_S^T, \quad \text{and} \quad \mathbf{C}_S = \mathbf{R}_S^T \mathbf{B}_S \mathbf{R}_S. \quad (2.20)$$

Proceeding from non-rigid solid matrix motion, strain tensors are introduced as dimensionless measures relating the initial states of the material with the actual ones and enabling to capture body deformations at any time. Among many strain measures in the literature, the *Green-Lagrangean* (\mathbf{E}_S) and the *Almansi* (\mathbf{A}_S) strain tensors are introduced in this discussion. In particular, \mathbf{E}_S is derived as

$$d\mathbf{x} \cdot d\mathbf{x} - d\mathbf{X}_S \cdot d\mathbf{X}_S = d\mathbf{X}_S \cdot \mathbf{C}_S d\mathbf{X}_S - d\mathbf{X}_S \cdot d\mathbf{X}_S = d\mathbf{X}_S \cdot \underbrace{(\mathbf{C}_S - \mathbf{I})}_{2\mathbf{E}_S} d\mathbf{X}_S, \quad (2.21)$$

whereas the derivation of the *Almansi* strain tensor is given as

$$d\mathbf{x} \cdot d\mathbf{x} - d\mathbf{X}_S \cdot d\mathbf{X}_S = d\mathbf{x} \cdot d\mathbf{x} - d\mathbf{x} \cdot \mathbf{B}_S^{-1} d\mathbf{x} = d\mathbf{x} \cdot \underbrace{(\mathbf{I} - \mathbf{B}_S^{-1})}_{2\mathbf{A}_S} d\mathbf{x}. \quad (2.22)$$

For the sake of completeness, the relations between the latter contravariant³ solid strain tensors in the actual and the reference configurations read

$$\boxed{\begin{array}{c} \text{reference configuration} \\ \mathbf{E}_S = \frac{1}{2}(\mathbf{C}_S - \mathbf{I}) \end{array}} \begin{array}{c} \xrightarrow{\mathbf{F}_S^{T-1}(\cdot)\mathbf{F}_S^{-1}} \\ \xleftarrow{\mathbf{F}_S^T(\cdot)\mathbf{F}_S} \end{array} \boxed{\begin{array}{c} \text{actual configuration} \\ \mathbf{A}_S = \frac{1}{2}(\mathbf{I} - \mathbf{B}_S^{-1}) \end{array}} \quad (2.23)$$

For more information about the different strain tensors and transport mechanisms within finite deformation theories, see, e. g., Holzapfel [90] and Ehlers [50, 51].

³Generally, tensors can be formulated within finite deformation theories with respect to curvilinear coordinates (natural basis representation) with co- and contravariant basis vectors, cf. e. g. Ehlers [50]. The transport mechanisms between configurations depend on the type of the variants, i. e., co or contra.

2.2.3 Geometric Linearisation

For practical applications especially in geomechanics, it is convenient to assume that deformations are small, which allows for a geometric linearisation of the kinematic variables. The main advantage of this assumption is that both the model formulations and the numerical implementation are simplified. In this context, Haupt [83] suggested the norm of the displacement gradient as a measure for the smallness of the deformation in the geometric linear theory. In particular, if

$$\Delta = \|\text{Grad}_\alpha \mathbf{u}_\alpha\| = \left\| \frac{\partial \mathbf{u}_\alpha}{\partial \mathbf{X}_\alpha} \right\| \quad (2.24)$$

is agreed to be sufficiently small⁴, this would justify disregarding of higher-order nonlinear terms.

As a starting point, linearisation is applied using *Taylor-series*, cf. Marsden & Hughes [128] or Eipper [65]. Therefore, for a given nonlinear function $f(\mathbf{x})$ such that $f(\bar{\mathbf{x}}) = 0$ with $\mathbf{x} = \bar{\mathbf{x}}$ as a known equilibrium point, *Taylor-series* expansion of $f(\mathbf{x})$ around $\bar{\mathbf{x}}$ reads

$$f(\mathbf{x}) = f(\bar{\mathbf{x}}) + \underbrace{\frac{df}{d\mathbf{x}} \Big|_{\mathbf{x}=\bar{\mathbf{x}}} \cdot (\mathbf{x} - \bar{\mathbf{x}})}_{Df(\bar{\mathbf{x}}) \cdot \Delta \mathbf{x}} + \underbrace{\frac{1}{2} \frac{d^2 f}{d\mathbf{x}^2} \Big|_{\mathbf{x}=\bar{\mathbf{x}}} \cdot (\mathbf{x} - \bar{\mathbf{x}})^2 + \dots}_{R(|\Delta \mathbf{x}|^2)}, \quad (2.25)$$

where $\Delta \mathbf{x} = \mathbf{x} - \bar{\mathbf{x}}$ is the linearisation direction and $R(|\Delta \mathbf{x}|^2)$ includes the higher-order terms. Neglecting $R(|\Delta \mathbf{x}|^2)$ results in the linearised form as

$$f_{\text{lin}} := f(\bar{\mathbf{x}}) + Df(\bar{\mathbf{x}}) \cdot \Delta \mathbf{x}. \quad (2.26)$$

A central role in the linearisation process is the application of the directional derivative (or *Gâteaux* differential), which is given as

$$Df(\bar{\mathbf{x}}) \cdot \Delta \mathbf{x} := D_{\Delta \mathbf{x}} f = \frac{d}{d\epsilon} \left[f(\bar{\mathbf{x}} + \epsilon \Delta \mathbf{x}) \right]_{\epsilon=0}, \quad (2.27)$$

where $\epsilon > 0$ is a small parameter.

Following this, linearisation is applied to several kinematic variables in the direction of the solid deformation increment $\Delta \mathbf{u}_S$. Thus, applying the directional derivative yields

$$\begin{aligned} D_{\Delta \mathbf{u}_S} \mathbf{F}_S &= \frac{d}{d\epsilon} \left[\text{Grad}_S(\mathbf{x} + \epsilon \Delta \mathbf{u}_S) \right]_{\epsilon=0} = \text{Grad}_S \Delta \mathbf{u}_S, \\ D_{\Delta \mathbf{u}_S} J_S &= \frac{d}{d\epsilon} \left[\det(\text{Grad}_S(\mathbf{x} + \epsilon \Delta \mathbf{u}_S)) \right]_{\epsilon=0} = J_S \text{div} \Delta \mathbf{u}_S, \\ D_{\Delta \mathbf{u}_S} \mathbf{E}_S &= D_{\Delta \mathbf{u}_S} \left[\frac{1}{2} (\mathbf{F}_S^T \mathbf{F}_S - \mathbf{I}) \right] \\ &= \frac{1}{2} (\mathbf{F}_S^T \text{Grad}_S \Delta \mathbf{u}_S + \text{Grad}_S^T \Delta \mathbf{u}_S \mathbf{F}_S). \end{aligned} \quad (2.28)$$

⁴If \mathbf{u}_α is a small deformation, then $\|\text{Grad}_\alpha \mathbf{u}_\alpha\| \ll \|\mathbf{u}_\alpha\|$ and, thus, the higher-order nonlinear terms such as $\text{Grad}_\alpha \mathbf{u}_\alpha \text{Grad}_\alpha^T \mathbf{u}_\alpha$ can be neglected (magnitude arguments).

By virtue of (2.28), the linearised forms for the kinematic quantities \mathbf{F}_S , J_S and \mathbf{E}_S are obtained around the undeformed state with $\Delta \mathbf{u}_S = \mathbf{u}_S - \bar{\mathbf{u}}_S = \mathbf{u}_S$, viz.:

$$\begin{aligned}\mathbf{F}_{S\text{lin}} &= \mathbf{I} + \text{Grad}_S \mathbf{u}_S \quad (\text{exact}), \\ J_{S\text{lin}} &= 1 + \text{Div}_S \mathbf{u}_S, \\ \mathbf{E}_{S\text{lin}} &= \frac{1}{2}(\text{Grad}_S \mathbf{u}_S + \text{Grad}_S^T \mathbf{u}_S).\end{aligned}\tag{2.29}$$

The assumption of small strains instead of large strains implies that the *Lagrangean* and the *Eulerian* descriptions are almost identical as there is only a little difference in the material and the spatial coordinates of a given material point in the continuum. Consequently, the integral and the differential operators will be written for the following treatment in the actual configuration style, i. e.,

$$\int_{\Omega_0} (\dots) dV_\alpha \approx \int_{\Omega} (\dots) dv, \quad \text{Grad}_\alpha (\cdot) \approx \text{grad} (\cdot), \quad \text{Div}_\alpha (\cdot) \approx \text{div} (\cdot).\tag{2.30}$$

Here, Ω_0 and Ω represent the domains in the reference and the actual configurations, respectively. Moreover, the linear strain tensor in the subsequent treatment is expressed as

$$\boxed{\boldsymbol{\varepsilon}_S = \frac{1}{2}(\text{grad} \mathbf{u}_S + \text{grad}^T \mathbf{u}_S)}.\tag{2.31}$$

Following this, recall (2.15), the nonlinear convective term $(\text{grad} \mathbf{v}_F) \mathbf{w}_F$ in the fluid acceleration relation can be linearised for the numerical implementation using the directional derivative strategy in two directions $\Delta \mathbf{v}_F = \mathbf{v}_F - \bar{\mathbf{v}}_F$ and $\Delta \mathbf{w}_F = \mathbf{w}_F - \bar{\mathbf{w}}_F$ as

$$\begin{aligned}[\text{grad} \mathbf{v}_F (\mathbf{w}_F)]_{\text{lin}} &= \text{grad} \bar{\mathbf{v}}_F (\bar{\mathbf{w}}_F) + D_{\Delta \mathbf{v}_F} [\text{grad} \Delta \mathbf{v}_F (\bar{\mathbf{w}}_F)] + D_{\Delta \mathbf{w}_F} [\text{grad} \bar{\mathbf{v}}_F (\Delta \mathbf{w}_F)] \\ &= \text{grad} \bar{\mathbf{v}}_F (\bar{\mathbf{w}}_F) + \text{grad} \Delta \mathbf{v}_F (\bar{\mathbf{w}}_F) + \text{grad} \bar{\mathbf{v}}_F (\Delta \mathbf{w}_F) \\ &= -\text{grad} \bar{\mathbf{v}}_F (\bar{\mathbf{w}}_F) + \text{grad} \mathbf{v}_F (\bar{\mathbf{w}}_F) + \text{grad} \bar{\mathbf{v}}_F (\mathbf{w}_F).\end{aligned}\tag{2.32}$$

In earthquake engineering problems with seismic loads of low and moderate frequencies (usually below about 30 Hz), the seepage velocity \mathbf{w}_F and, as consequence, the convective term $(\text{grad} \mathbf{v}_F) \mathbf{w}_F$ are generally considered very small, cf. Zienkiewicz *et al.* [186], i. e.,

$$\|(\text{grad} \mathbf{v}_F) \mathbf{w}_F\| \ll \|\text{grad} \mathbf{v}_F\|.\tag{2.33}$$

Thus, the convective term is regarded as a higher-order term in the geometric linear treatment and can be neglected by magnitude arguments.

For further information about the kinematic formulations and linearisation, the interested reader is referred to the works by, e. g., Ehlers [55], Eipper [65], Ellsiepen [66], Markert [123], Karajan [101] and the quotations therein.

2.3 Balance Relations

This section outlines the balance relations of multiphase continuum mechanics proceeding from the mechanical (mass, momentum and moment of momentum) and the thermodynamical (energy and entropy) conservation laws of classical continuum mechanics of single-phase materials. For this purpose, the general and the specific forms of the balance equations for a deformed multiphase body and its constituents are given in a systematic way. For more detailed and comprehensive introduction of the balance laws, the interested reader is referred to the works by Truesdell & Noll [165], Truesdell & Toupin [166], Truesdell [164], Haupt [83, 84], Ehlers [50, 53, 57], Miehe [131], Göktepe [73] and Karajan [101] among others.

2.3.1 Preliminaries

In general, continuum mechanics is a mathematical theory that aims to investigate the physical phenomena of continuous material body motion in time and space under the effect of forces and temperature differences. Starting from classical continuum mechanics,

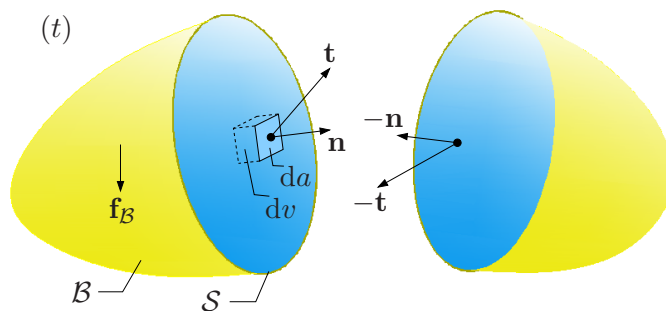


Figure 2.3: Illustration of the spatial body force \mathbf{f}_B and the surface traction vector \mathbf{t}

one considers a certain spatial body \mathcal{B} as a cut of an overall volume and closed by a boundary \mathcal{S} , cf. Figure 2.3. The influence of the outside world on \mathcal{B} is expressed by a force vector \mathbf{f} consisting a body force \mathbf{f}_B and a surface force \mathbf{f}_S :

$$\mathbf{f} = \mathbf{f}_B + \mathbf{f}_S = \int_B \rho \mathbf{b} dv + \int_S \mathbf{t} da. \quad (2.34)$$

Herein, $\rho \mathbf{b}$ (ρ is the density and \mathbf{b} is the mass-specific body force) is a body force that acts on a volume element dv and \mathbf{t} is a surface traction that acts on a surface element da . The *Cauchy* stress theorem states that the spatial stress \mathbf{t} depends linearly on the spatial normal \mathbf{n} of da as

$$\mathbf{t}(\mathbf{x}, t, \mathbf{n}) := \mathbf{T}(\mathbf{x}, t) \mathbf{n}, \quad (2.35)$$

where $\mathbf{T}(\mathbf{x}, t)$ is the *Cauchy* (true) stress tensor that represents the surface force on an area element in the actual configuration (cf. Haupt [84]). In finite deformation theories, $\mathbf{T}(\mathbf{x}, t)$ is exploited to derive several stress tensors in different configurations such as the 1st and the 2nd *Piola-Kirchhoff* stress. However, under the assumption of infinitesimal strains, there is no need to distinguish between the configurations, and thus, $\mathbf{T}(\mathbf{x}, t)$

can be used directly in balance relations for the numerical treatment. In fact, equations (2.34) and (2.35) are considered the bases of *Cauchy's* first and second law of motion, i. e., the linear momentum and moment of momentum balances of single-phasic bodies, cf. Truesdell [164, p. 108] for more details.

Following this, the surface integral of the scalar product of \mathbf{t} and \mathbf{n} can be converted into a volume integral through the *Gauß* integral theorem as

$$\int_S \mathbf{t} \cdot \mathbf{n} \, da = \int_{\mathcal{B}} \operatorname{div}(\mathbf{t}) \, dv. \quad (2.36)$$

Later, the *Gauß* integral theorem is used to recast the general balance equations in a pure volume-integral form over \mathcal{B} . This procedure enables to derive the specific form of the balance relations by assuming that the continuity condition is fulfilled regardless the size of \mathcal{B} , and thus, the integral form of the balance relations is satisfied for an infinitely small \mathcal{B} .

The aim in the following is to investigate the balance relations of multiphasic bodies that consist of identified continuous constituents. Therefore, *Truesdell's* 'metaphysical principles' of mixture theories, cf. Truesdell [164, p. 221], provide a comprehensive and excellent framework.

Truesdell's 'metaphysical principles' of mixture theories

1. *All properties of the mixture must be mathematical consequences of properties of the constituents.*
 2. *So as to describe the motion of a constituent, we may in imagination isolate it from the rest of the mixture, provided we allow properly for the actions of the other constituents upon it.*
 3. *The motion of a mixture is governed by the same equations as is a single body.*
- (2.37)

In other words, proceeding from the principles in box (2.37) together with the kinematics of homogenised multiphasic continua, cf. Section 2.2, each constituent of the overall aggregate follows its unique motion function and undergoes the same balance equations as for a single-phase material, provided that force and energy interactions between the constituents are allowed via production terms. Moreover, the homogenised overall body is treated as a black-box governed by the same laws as for a single body, and its balance equations result from the sum of the balance relations of all related constituents.

2.3.2 General and Specific Balance Relations

The introduction of balance relations for multiphasic materials is accompanied by two statements: The balance laws for each constituent φ^α , and the balance relations for the overall aggregate φ . Following the classical continuum mechanics of single-phase

materials, scalar- and vector-valued general balance formulations for the overall aggregate of multiphase media can be expressed as

$$\begin{aligned} \text{scalar-valued: } \quad & \frac{d}{dt} \int_{\mathcal{B}} \Psi \, dv = \int_S (\boldsymbol{\phi} \cdot \mathbf{n}) \, da + \int_{\mathcal{B}} \sigma \, dv + \int_{\mathcal{B}} \hat{\Psi} \, dv, \\ \text{vector-valued: } \quad & \frac{d}{dt} \int_{\mathcal{B}} \boldsymbol{\Psi} \, dv = \int_S (\boldsymbol{\Phi} \mathbf{n}) \, da + \int_{\mathcal{B}} \boldsymbol{\sigma} \, dv + \int_{\mathcal{B}} \hat{\boldsymbol{\Psi}} \, dv. \end{aligned} \quad (2.38)$$

Therein, the quantities in equations (2.38) can be interpreted as follows:

Ψ , $\boldsymbol{\Psi}$ are, respectively, the volume-specific scalar and the vector-valued densities of the mechanical quantities in \mathcal{B} to be balanced.

$\boldsymbol{\phi} \cdot \mathbf{n}$, $\boldsymbol{\Phi} \mathbf{n}$ are the surface densities of the mechanical quantities, which represent the efflux from the external vicinity with \mathbf{n} as an outward-oriented unit surface normal.

σ , $\boldsymbol{\sigma}$ are the volume densities describing the supply of the mechanical quantities from the external distance.

$\hat{\Psi}$, $\hat{\boldsymbol{\Psi}}$ are the production terms of the mechanical quantities describing a possible coupling of the body with the surrounding.

Following this, the constituent master balance relations are given analogously as

$$\begin{aligned} \text{scalar-valued: } \quad & \frac{d_\alpha}{dt} \int_{\mathcal{B}} \Psi^\alpha \, dv = \int_S (\boldsymbol{\phi}^\alpha \cdot \mathbf{n}) \, da + \int_{\mathcal{B}} \sigma^\alpha \, dv + \int_{\mathcal{B}} \hat{\Psi}^\alpha \, dv, \\ \text{vector-valued: } \quad & \frac{d_\alpha}{dt} \int_{\mathcal{B}} \boldsymbol{\Psi}^\alpha \, dv = \int_S (\boldsymbol{\Phi}^\alpha \mathbf{n}) \, da + \int_{\mathcal{B}} \boldsymbol{\sigma}^\alpha \, dv + \int_{\mathcal{B}} \hat{\boldsymbol{\Psi}}^\alpha \, dv. \end{aligned} \quad (2.39)$$

Here, the mechanical quantities $(\cdot)^\alpha$ of φ^α have the same physical interpretation as for the terms (\cdot) of the overall body balance equations (2.38), except for the constituent production terms $(\hat{\cdot})^\alpha$ that describe in this case the possible interaction of a constituent with the other constituents rather than \mathcal{B} with the surrounding.

In what follows, relations (2.38) and (2.39) are recast into a pure body-integral form under the assumption that the integrands are steady and steadily differentiable (cf. Ehlers [57]). Thus, time differentiation is applied to the left-hand sides of (2.38) and (2.39), and a transformation of the surface integrals into volume ones is performed using the *Gauß* integral theorem, cf. equation (2.36). Consequently, the local master balance relations are obtained provided that all occurring fields are sufficiently continuous over an infinitely small body \mathcal{B} . In particular, one gets

$$\begin{aligned} \underline{\text{the local balance laws of } \varphi} \quad & \underline{\text{the local balance laws of } \varphi^\alpha} \\ \dot{\Psi} + \boldsymbol{\Psi} \operatorname{div} \dot{\mathbf{x}} = \operatorname{div} \boldsymbol{\phi} + \sigma + \hat{\Psi}, \quad & (\Psi^\alpha)'_\alpha + \boldsymbol{\Psi}^\alpha \operatorname{div} \mathbf{v}_\alpha = \operatorname{div} \boldsymbol{\phi}^\alpha + \sigma^\alpha + \hat{\Psi}^\alpha, \\ \dot{\boldsymbol{\Psi}} + \boldsymbol{\Psi} \operatorname{div} \dot{\mathbf{x}} = \operatorname{div} \boldsymbol{\Phi} + \boldsymbol{\sigma} + \hat{\boldsymbol{\Psi}}, \quad & (\boldsymbol{\Psi}^\alpha)'_\alpha + \boldsymbol{\Psi}^\alpha \operatorname{div} \mathbf{v}_\alpha = \operatorname{div} \boldsymbol{\Phi}^\alpha + \boldsymbol{\sigma}^\alpha + \hat{\boldsymbol{\Psi}}^\alpha. \end{aligned} \quad (2.40)$$

Based on *Truesdell's* metaphysical principles, cf. box (2.37), general constraints are added to relations (2.40). Here, the local overall aggregate balances should result from the sum

over all participating constituent balances. Therefore, for the scalar- and the vector-valued balance law entries, the following constraints hold:

$$\begin{aligned} \Psi &= \sum_{\alpha} \Psi^{\alpha}, & \phi \cdot \mathbf{n} &= \sum_{\alpha} (\phi^{\alpha} - \Psi^{\alpha} \mathbf{d}_{\alpha}) \cdot \mathbf{n}, & \sigma &= \sum_{\alpha} \sigma^{\alpha}, & \hat{\Psi} &= \sum_{\alpha} \hat{\Psi}^{\alpha}, \\ \Psi &= \sum_{\alpha} \Psi^{\alpha}, & \Phi \mathbf{n} &= \sum_{\alpha} (\Phi^{\alpha} - \Psi^{\alpha} \otimes \mathbf{d}_{\alpha}) \mathbf{n}, & \sigma &= \sum_{\alpha} \sigma^{\alpha}, & \hat{\Psi} &= \sum_{\alpha} \hat{\Psi}^{\alpha}. \end{aligned} \quad (2.41)$$

Following this, the different quantities of equations (2.40) are specified in Table 2.1 yielding the axiomatically introduced conservation laws of continuum thermodynamics, i. e., the mass, the momentum, the moment of momentum (m. o. m.), the energy, and the entropy balance equations (Ehlers [57]).

φ φ^{α}	Ψ, Ψ $\Psi^{\alpha}, \Psi^{\alpha}$	ϕ, Φ $\phi^{\alpha}, \Phi^{\alpha}$	σ, σ $\sigma^{\alpha}, \sigma^{\alpha}$	$\hat{\Psi}, \hat{\Psi}$ $\hat{\Psi}^{\alpha}, \hat{\Psi}^{\alpha}$
mass	ρ ρ^{α}	$\mathbf{0}$ $\mathbf{0}$	0 0	0 $\hat{\rho}^{\alpha}$
momentum	$\rho \dot{\mathbf{x}}$ $\rho^{\alpha} \mathbf{v}_{\alpha}$	\mathbf{T} \mathbf{T}^{α}	$\rho \mathbf{b}$ $\rho^{\alpha} \mathbf{b}^{\alpha}$	$\mathbf{0}$ $\hat{\mathbf{s}}^{\alpha}$
moment of momentum	$\mathbf{x} \times (\rho \dot{\mathbf{x}})$ $\mathbf{x} \times (\rho^{\alpha} \mathbf{v}_{\alpha})$	$\mathbf{x} \times \mathbf{T}$ $\mathbf{x} \times \mathbf{T}^{\alpha}$	$\mathbf{x} \times (\rho \mathbf{b})$ $\mathbf{x} \times (\rho^{\alpha} \mathbf{b}^{\alpha})$	$\mathbf{0}$ $\hat{\mathbf{h}}^{\alpha}$
energy	$\rho \varepsilon + \frac{1}{2} \dot{\mathbf{x}} \cdot (\rho \dot{\mathbf{x}})$ $\rho^{\alpha} \varepsilon^{\alpha} + \frac{1}{2} \mathbf{v}_{\alpha} \cdot (\rho^{\alpha} \mathbf{v}_{\alpha})$	$\mathbf{T}^T \dot{\mathbf{x}} - \mathbf{q}$ $(\mathbf{T}^{\alpha})^T \mathbf{v}_{\alpha} - \mathbf{q}^{\alpha}$	$\dot{\mathbf{x}} \cdot (\rho \mathbf{b}) + \rho r$ $\mathbf{v}_{\alpha} \cdot (\rho^{\alpha} \mathbf{b}^{\alpha}) + \rho^{\alpha} r^{\alpha}$	0 \hat{e}^{α}
entropy	$\rho \eta$ $\rho^{\alpha} \eta^{\alpha}$	ϕ_{η} ϕ_{η}^{α}	σ_{η} σ_{η}^{α}	$\hat{\eta} \geq 0$ $\hat{\eta}^{\alpha}$

Table 2.1: Identified physical quantities of the master balance relations (2.40)

The hierarchical structure of the balance relation terms in Table 2.1 allows to distinguish between ‘lower’ and ‘higher’ balance equations. For instance, one starts with the mass balance as the ‘lowest’ balance relation before evaluating the ‘higher’ momentum balance. It is also clear from Table 2.1 that the overall and the constituent balance laws are given in similar forms. However, the interactions between the constituents are allowed via the production terms $(\dot{\cdot})^{\alpha}$.

In order to derive a more convenient specific version of the balance relations, the total production terms are decomposed into direct and additional terms governed by the ‘lower’

productions as

$$\begin{aligned}
\hat{\mathbf{s}}^\alpha &= \hat{\mathbf{p}}^\alpha + \hat{\rho}^\alpha \mathbf{v}_\alpha, \\
\hat{\mathbf{h}}^\alpha &= \hat{\mathbf{m}}^\alpha + \mathbf{x} \times (\hat{\mathbf{p}}^\alpha + \hat{\rho}^\alpha \mathbf{v}_\alpha), \\
\hat{e}^\alpha &= \hat{\varepsilon}^\alpha + \hat{\mathbf{p}}^\alpha \cdot \mathbf{v}_\alpha + \hat{\rho}^\alpha \left(\varepsilon^\alpha + \frac{1}{2} \mathbf{v}_\alpha \cdot \mathbf{v}_\alpha \right), \\
\hat{\eta}^\alpha &= \hat{\zeta}^\alpha + \hat{\rho}^\alpha \eta^\alpha.
\end{aligned} \tag{2.42}$$

Herein, the total momentum production $\hat{\mathbf{s}}^\alpha$ is split into a direct term $\hat{\mathbf{p}}^\alpha$ representing the volume-specific local interaction force among the constituents of the overall medium, and an additional production term $\hat{\rho}^\alpha \mathbf{v}_\alpha$ governed by the density production $\hat{\rho}^\alpha$ as a ‘lower’ term. Moreover, the moment of momentum interaction term $\hat{\mathbf{h}}^\alpha$ is also additively split into a direct production term $\hat{\mathbf{m}}^\alpha$ and a further statement of two ‘lower’ productions $\hat{\mathbf{p}}^\alpha$ and $\hat{\rho}^\alpha$. Analogously, the total energy production \hat{e}^α is divided into a direct exchange part $\hat{\varepsilon}^\alpha$ and a secondary statement stemming from the three ‘lower’ production terms. The entropy production $\hat{\eta}^\alpha$ is also split into a volume-specific direct term $\hat{\zeta}^\alpha$ and an indirect part expressed in terms of $\hat{\rho}^\alpha$ and the constituent mass-specific entropy η^α . It is worth mentioning that this split allows to exploit the ‘lower’ balances in order to simplify the ‘higher’ ones.

Inserting the specified terms of Table 2.1 into the local master balances (2.40) results in the well-known specific balance relations for both the overall body and the individual constituents. In what follows, a discussion of the specific local balance laws is briefly introduced.

Balance of Mass

In a closed system as for a spatial body \mathcal{B} with no mass transfer through its surface \mathcal{S} , the total mass remains constant during the deformation process. For a multiphasic body, the axiom of mass conservation is applied to the overall aggregate and to the constituents. Here, incorporating the specific balance terms (Table 2.1) into the local master balances (2.40) yields the local mass balances (continuity equations) of the overall body

$$\dot{\rho} + \rho \operatorname{div} \dot{\mathbf{x}} = 0 \tag{2.43}$$

and the constituents

$$(\rho^\alpha)'_\alpha + \rho^\alpha \operatorname{div} \mathbf{v}_\alpha = \hat{\rho}^\alpha. \tag{2.44}$$

In this connection, taking the constraints (2.41) into account yields the previously introduced relations for the mixture velocity (2.9) and the conservation of mass diffusion (2.10)₂. Moreover, based on (2.41), the sum of all mass exchange terms (mass production or supply terms) due to possible phase transformations or chemical reactions vanishes, viz.:

$$\sum_\alpha \hat{\rho}^\alpha = 0. \tag{2.45}$$

Balance of Linear Momentum

Proceeding with the basics of classical continuum mechanics, the rate of linear momentum of a body \mathcal{B} is equal to the sum of the forces acting on it. In multiphase continua, the overall body is treated as a single phase material with two types of acting forces: The mass-specific body force $\mathbf{b}(\mathbf{x}, t)$ as a distant effect of the surrounding bodies, and the surface traction at the vicinity represented by the *Cauchy* stress tensor $\mathbf{T}(\mathbf{x}, t)$. By virtue of Table 2.1 together with the local master balances (2.40), the overall momentum balance reads

$$\rho \dot{\mathbf{x}} = \operatorname{div} \mathbf{T} + \rho \mathbf{b}. \quad (2.46)$$

Moreover, the constituent momentum balance reads

$$\rho^\alpha \dot{\mathbf{v}}_\alpha = \operatorname{div} \mathbf{T}^\alpha + \rho^\alpha \mathbf{b}^\alpha + \hat{\mathbf{p}}^\alpha. \quad (2.47)$$

Here, $\mathbf{T}^\alpha(\mathbf{x}, t)$ is the partial *Cauchy* stress tensor, $\mathbf{b}^\alpha(\mathbf{x}, t)$ is the partial mass-specific body force, and $\hat{\mathbf{p}}^\alpha$ is the direct momentum supply of φ^α , which represents the influence of the other constituents on φ^α .

Back to the constraints (2.41), the overall and the partial body force densities are related via

$$\rho \mathbf{b} = \sum_\alpha \rho^\alpha \mathbf{b}^\alpha, \quad (2.48)$$

and the *Cauchy* stress tensor is given in terms of the partial stresses and diffusion velocities⁵ as

$$\mathbf{T} = \sum_\alpha (\mathbf{T}^\alpha - \rho^\alpha \mathbf{d}_\alpha \otimes \mathbf{d}_\alpha). \quad (2.49)$$

Moreover, an additional restriction to the overall momentum is introduced in terms of the partial momenta, the diffusion velocities, and the mass productions (de Boer & Ehlers [20]), i. e.,

$$\rho \dot{\mathbf{x}} = \sum_\alpha [\rho^\alpha \dot{\mathbf{v}}_\alpha - \operatorname{div} (\rho^\alpha \mathbf{d}_\alpha \otimes \mathbf{d}_\alpha) + \hat{\rho}^\alpha \mathbf{v}_\alpha]. \quad (2.50)$$

Here, the momentum production vectors should satisfy the following constraint:

$$\sum_\alpha \hat{\mathbf{s}}^\alpha = \sum_\alpha (\hat{\mathbf{p}}^\alpha + \hat{\rho}^\alpha \mathbf{v}_\alpha) = \mathbf{0}. \quad (2.51)$$

Balance of Angular Momentum

The temporal change of the moment of momentum of a body \mathcal{B} equals the sum of all moments of the forces acting on \mathcal{B} with respect to the same original point. The evaluation

⁵For a given fluid-like constituent ($\mathbf{d}_\alpha \neq \mathbf{0}$), the part of the stress tensor \mathbf{T} initiated by the diffusion process is comparable in fluid dynamics to the *Reynolds* stress of a fluid in a turbulent flow situation, cf., e. g., Eipper [65].

of the overall aggregate angular momentum using Table 2.1 and equations (2.40) results in the symmetry constraint of the total *Cauchy* stress tensor, viz.:

$$\mathbf{0} = \mathbf{I} \times \mathbf{T} \quad \longrightarrow \quad \mathbf{T} = \mathbf{T}^T. \quad (2.52)$$

In the constituent moment of momentum balance, the direct production term $\hat{\mathbf{m}}^\alpha$ should be taken into account, i. e.,

$$\mathbf{0} = \mathbf{I} \times \mathbf{T}^\alpha + \hat{\mathbf{m}}^\alpha. \quad (2.53)$$

Following this, the angular momentum production terms (2.42)₂ must fulfil the summation constraints (2.41) yielding

$$\sum_{\alpha} \hat{\mathbf{h}}^\alpha = \mathbf{0}. \quad (2.54)$$

Remark: In this monograph, only the case of symmetric partial stress tensors with $\mathbf{T}^\alpha = (\mathbf{T}^\alpha)^T$ is considered.

Balance of Energy (1st Law of Thermodynamics)

The first axiom of thermodynamics states that the temporal change of the total body energy, i. e. kinetic and internal (stored stress and thermal) power, is equal to the total external supply of mechanical and non-mechanical (heat flux and radiation) energy, cf., e. g., Haupt [83] for more details. Proceeding from the local master equations (2.40) and the specified terms in Table 2.1 together with the ‘lower’ local balance relations, the local energy balance of the overall body is expressed as

$$\rho \dot{\varepsilon} = \mathbf{T} \cdot \mathbf{L} - \operatorname{div} \mathbf{q} + \rho r \quad (2.55)$$

with ε being the internal energy, \mathbf{q} is the heat influx vector, r is the external heat supply, and \mathbf{L} is the spatial velocity gradient defined as $\mathbf{L} = \operatorname{grad} \dot{\mathbf{x}}$. The constituent energy balance is given by

$$\rho^\alpha (\varepsilon^\alpha)'_\alpha = \mathbf{T}^\alpha \cdot \mathbf{L}_\alpha - \operatorname{div} \mathbf{q}^\alpha + \rho^\alpha r^\alpha + \hat{\varepsilon}^\alpha, \quad (2.56)$$

where the quantities ε^α , \mathbf{q}^α , r^α and the spatial velocity gradient $\mathbf{L}_\alpha = \operatorname{grad} \mathbf{v}_\alpha$ correspond to the constituent φ^α . In this case, the direct energy exchange between φ^α and the other constituents is represented by the term $\hat{\varepsilon}^\alpha$.

Evaluation of the summation constraints (2.41) results in the following statements for the internal energy, the heat influx vector and the heat source of the overall medium, respectively, viz.:

$$\begin{aligned} \rho \varepsilon &= \sum_{\alpha} \rho^\alpha (\varepsilon^\alpha + \frac{1}{2} \mathbf{d}_\alpha \cdot \mathbf{d}_\alpha), \\ \mathbf{q} &= \sum_{\alpha} [\mathbf{q}^\alpha - (\mathbf{T}^\alpha)^T \mathbf{d}_\alpha + \rho^\alpha \varepsilon^\alpha \mathbf{d}_\alpha + \frac{1}{2} (\mathbf{d}_\alpha \cdot \mathbf{d}_\alpha) \mathbf{d}_\alpha], \\ \rho r &= \sum_{\alpha} \rho^\alpha (r^\alpha + \mathbf{b}^\alpha \cdot \mathbf{d}_\alpha). \end{aligned} \quad (2.57)$$

Roughly speaking, relations (2.57) show that each energy term of the overall body results from the sum of the corresponding constituent terms and the sum of additional diffusion statements over all constituents. Moreover, the total energy production terms fulfil the following restriction:

$$\sum_{\alpha} \hat{e}^{\alpha} = 0. \quad (2.58)$$

Balance of Entropy (2nd Law of Thermodynamics)

In classical thermodynamics, the entropy axiom postulates that the temporal change of the total entropy of a material body (as a closed system) equals the sum of the entropy supply, the entropy efflux, and the entropy production. Here, the 2nd law of thermodynamics requires that the entropy production term can never be negative, cf. Haupt [83]. Unlike the other balance principles, the entropy is expressed by an inequality, which serves as a mathematical restriction on the constitutive equations governing the reversible (e. g. elastic deformation) and the irreversible (e. g. plastic deformation due to internal dissipative mechanisms) processes in the system.

In the current treatment of a multiphasic medium, the entropy production $\hat{\eta}$ of the overall aggregate should always be positive. However, it is not necessary that the entropy of each constituent in the system satisfies this condition, as this would be a too restrictive treatment (Ehlers [50]). Following this, the local form of the overall entropy based on the local master balances (2.40) and the specifications in Table 2.1 is given by

$$\rho \hat{\eta} \geq \operatorname{div} \phi_{\eta} + \sigma_{\eta}. \quad (2.59)$$

As the overall aggregate is treated as a single-phase material, cf. Truesdell [164], it is reasonable to consider the following thermodynamical *a priori* constitutive relations for the entropy efflux and the external entropy supply:

$$\phi_{\eta} = -\frac{1}{\Theta} \mathbf{q}, \quad \sigma_{\eta} = \frac{1}{\Theta} \rho r, \quad (2.60)$$

where $\Theta > 0$ is the *Kelvin's* temperature, cf. Ehlers [56, 58] for more details. In a similar way, the entropy efflux and the entropy supply of any constituent φ^{α} can be expressed by

$$\phi_{\eta}^{\alpha} = -\frac{1}{\Theta^{\alpha}} \mathbf{q}^{\alpha}, \quad \sigma_{\eta}^{\alpha} = \frac{1}{\Theta^{\alpha}} \rho^{\alpha} r^{\alpha}, \quad (2.61)$$

where, in general, it is possible that each constituent has a distinctive *Kelvin's* temperature Θ^{α} . In analogy to the previously introduced balance relations (2.44), (2.47), (2.53), and (2.56), the local entropy balance of φ^{α} can be expressed as

$$\rho^{\alpha} (\eta^{\alpha})'_{\alpha} = \operatorname{div} \left(-\frac{1}{\Theta^{\alpha}} \mathbf{q}^{\alpha} \right) + \frac{1}{\Theta^{\alpha}} \rho^{\alpha} r^{\alpha} + \hat{\zeta}^{\alpha}. \quad (2.62)$$

By recourse to the summation restrictions (2.41), the following entropy statements be-

tween the overall body and the constituents read:

$$\begin{aligned} \rho \eta &= \sum_{\alpha} \rho^{\alpha} \eta^{\alpha}, & \frac{1}{\Theta} \mathbf{q} &= \sum_{\alpha} \left(\frac{1}{\Theta^{\alpha}} \mathbf{q}^{\alpha} + \rho^{\alpha} \eta^{\alpha} \mathbf{d}_{\alpha} \right), \\ \frac{1}{\Theta} \rho r &= \sum_{\alpha} \frac{1}{\Theta^{\alpha}} \rho^{\alpha} r^{\alpha}, & \hat{\eta} &= \sum_{\alpha} \hat{\eta}^{\alpha} \geq 0. \end{aligned} \quad (2.63)$$

Any thermodynamically consistent treatment requires the fulfilment of the entropy inequality. Therefore, starting with the 2nd law of thermodynamics of non-negative entropy production $\hat{\eta}$, cf. equations (2.63)₄, together with the local form of the constituent entropy balance (2.62) and the total entropy production (2.42)₄, the following overall entropy restriction holds

$$\hat{\eta} = \sum_{\alpha} \hat{\eta}^{\alpha} = \sum_{\alpha} \left[\rho^{\alpha} (\eta^{\alpha})'_{\alpha} + \hat{\rho}^{\alpha} \eta^{\alpha} + \operatorname{div} \left(\frac{1}{\Theta^{\alpha}} \mathbf{q}^{\alpha} \right) - \frac{1}{\Theta^{\alpha}} \rho^{\alpha} r^{\alpha} \right] \geq 0. \quad (2.64)$$

Following this, relation (2.64) is modified using the constituent *Helmholtz* free energy density ψ^{α} , which results from a *Legendre* transformation between the entropy and the temperature as conjugate variables. In particular,

$$\psi^{\alpha} := \varepsilon^{\alpha} - \Theta^{\alpha} \eta^{\alpha} \quad (2.65)$$

together with the ‘lower’ local balances (2.44), (2.47), and (2.56) are incorporated into the entropy inequality (2.64) yielding the well-known *Clausius-Duhem* inequality

$$\begin{aligned} \mathcal{D} = \sum_{\alpha} \frac{1}{\Theta^{\alpha}} \left\{ \mathbf{T}^{\alpha} \cdot \mathbf{L}_{\alpha} - \rho^{\alpha} \left[(\psi^{\alpha})'_{\alpha} + (\Theta^{\alpha})'_{\alpha} \eta^{\alpha} \right] - \hat{\mathbf{p}}^{\alpha} \cdot \mathbf{v}_{\alpha} - \right. \\ \left. - \hat{\rho}^{\alpha} \left(\psi^{\alpha} + \frac{1}{2} \mathbf{v}_{\alpha} \cdot \mathbf{v}_{\alpha} \right) - \frac{1}{\Theta^{\alpha}} \mathbf{q}^{\alpha} \cdot \operatorname{grad} \Theta^{\alpha} + \hat{\varepsilon}^{\alpha} \right\} \geq 0. \end{aligned} \quad (2.66)$$

It is common in practise to additively split \mathcal{D} into local (intrinsic, \mathcal{D}_{loc}) and conductive (thermal, \mathcal{D}_{con}) parts. Consequently, for the case of isothermal treatment with constant and equal *Kelvin’s* temperature for all constituents, i.e. $\Theta^{\alpha} = \Theta = \text{const.}$ and $\hat{\varepsilon}^{\alpha} \equiv 0$, the *Clausius-Duhem* inequality (2.66) is reduced to the local *Clausius-Planck* dissipation inequality, expressed as

$$\mathcal{D}_{loc} = \sum_{\alpha} \left[\mathbf{T}^{\alpha} \cdot \mathbf{L}_{\alpha} - \rho^{\alpha} (\psi^{\alpha})'_{\alpha} - \hat{\mathbf{p}}^{\alpha} \cdot \mathbf{v}_{\alpha} - \hat{\rho}^{\alpha} \left(\psi^{\alpha} + \frac{1}{2} \mathbf{v}_{\alpha} \cdot \mathbf{v}_{\alpha} \right) \right] \geq 0. \quad (2.67)$$

Moreover, as the current monograph mainly focuses on the treatment of saturated geomaterials with immiscible constituents, it is reasonable to exclude the mass production terms from the *Clausius-Planck* inequality. This yields a more simplified thermodynamic restriction:

$$\mathcal{D}_{loc} = \sum_{\alpha} \left[\mathbf{T}^{\alpha} \cdot \mathbf{L}_{\alpha} - \rho^{\alpha} (\psi^{\alpha})'_{\alpha} - \hat{\mathbf{p}}^{\alpha} \cdot \mathbf{v}_{\alpha} \right] \geq 0. \quad (2.68)$$

In what follows, equation (2.68) is used to calibrate the constitutive relations against the thermodynamic consistency.

Chapter 3:

Constitutive Modelling

Within the Theory of Porous Media, the following chapter discusses various thermodynamically consistent constitutive models, which are used to capture the behaviour of saturated porous materials under different loading conditions. Hence, based on the presented continuum-mechanical fundamentals in Chapter 2, the kinematics and different sets of balance relations for biphasic aggregates are discussed. Moreover, the entropy inequality is evaluated in order to provide restrictions for the established constitutive equations. In this connection, an elasto-viscoplastic material model is implemented to simulate liquefaction phenomena, whereas a linear elastic model is applied for the dynamic wave propagation modelling. Additionally, the acoustic wave velocities in poroelastic media are also derived in this chapter.

3.1 Saturated Biphasic TPM Model

Based on the specified balance relations from the preceding chapter, the main focus of this section is laid on the derivation of the governing balance equations for biphasic saturated aggregates and the evaluation of the entropy inequality, which leads to the ‘concept of effective stresses’.

3.1.1 Preliminaries and Assumptions

For the purpose of this monograph, the treatment of saturated porous media proceeds from the following preliminaries:

$$\begin{aligned}
 \text{saturation constraint:} & \quad n^S + n^F = 1 \\
 \text{materially incompressible solid phase:} & \quad \rho^{SR} = \text{const.} \\
 \text{no mass exchange between the constituents:} & \quad \hat{\rho}^\alpha \equiv 0 \\
 \text{non-polar phases:} & \quad \mathbf{T}^\alpha = (\mathbf{T}^\alpha)^T \\
 \text{equal body forces of all constituents:} & \quad \mathbf{b}^\alpha = \mathbf{b} \\
 \text{isothermal process:} & \quad \Theta^\alpha \equiv \Theta = \text{const.}
 \end{aligned} \tag{3.1}$$

It can be seen from the set of relations (3.1) that the model under consideration is both purely mechanical and isotropic. Therefore, the major attention of the later treatment is paid to the mass and the linear momentum balance. The compressibility of the solid constituent is ignored in comparison with that of the solid matrix, cf. Section 2.1. The fluid

phase is treated in most parts of the thesis as materially incompressible ($\rho^{FR} = \text{const.}$). However, for special purposes, the fluid material is considered compressible leading to a so-called hybrid biphasic model, cf., e. g., Ehlers [53] and Mahnkopf [121] for details. In this case, the fluid constituent is assumed to be saturated with ideal gas bubbles yielding a pore-pressure-dependent fluid material density, see Section 3.1.3 for details.

Mass and Volume Balances

Starting with the case of a materially incompressible biphasic aggregate with no mass exchange between the constituents, the partial mass balance (2.44) yields the constituent volume balance, i. e.

$$(\rho^\alpha)'_\alpha = (n^\alpha \rho^{\alpha R})'_\alpha = (n^\alpha)'_\alpha \rho^{\alpha R} \quad \longrightarrow \quad (n^\alpha)'_\alpha + n^\alpha \text{div } \mathbf{v}_\alpha = 0. \quad (3.2)$$

The volume balance of the solid phase is integrated analytically over time yielding an explicit relation for the solidity (n^S) in terms of the solid initial volume fraction n_{0S}^S and the deformation gradient \mathbf{F}_S , viz.:

$$(n^S)'_S = -n^S \text{div } \mathbf{v}_S \quad \longrightarrow \quad n^S = n_{0S}^S (\det \mathbf{F}_S)^{-1} = \frac{1}{J_S} n_{0S}^S. \quad (3.3)$$

In the geometric linear treatment with small strain assumption (Section 2.2.3), equation (3.3) is simplified by formal linearisation of the *Jacobian* (J_S) around the undeformed state. This yields the following linearised solidity relation:

$$n^S = n_{0S}^S (1 - \text{Div}_S \mathbf{u}_S) \approx n_{0S}^S (1 - \text{div } \mathbf{u}_S). \quad (3.4)$$

Herein, the first identity results from the geometric linearisation, whereas the second identity is based on the small strain assumption with no distinction between the actual and the reference configuration. Following this, the volume balance of the overall aggregate results from the sum of the constituent volume balances, i. e., equation (3.2)₂ with $\alpha = \{S, F\}$. In particular, we have

$$\begin{aligned} & (n^S)'_S + n^S \text{div } \mathbf{v}_S + \underbrace{(n^F)'_S + \text{grad } n^F \cdot \mathbf{w}_F}_{(n^F)'_F} + n^F \text{div } \underbrace{(\mathbf{v}_S + \mathbf{w}_F)}_{\mathbf{v}_F} = 0, \\ \longrightarrow & \underbrace{(n^S + n^F)'_S}_{=0} + \underbrace{(n^S + n^F)}_{=1} \text{div } \mathbf{v}_S + \underbrace{\text{grad } n^F \cdot \mathbf{w}_F + n^F \text{div } \mathbf{w}_F}_{\text{div}(n^F \mathbf{w}_F)} = 0. \end{aligned} \quad (3.5)$$

Here, one additionally makes use of the material time derivative rules given in (2.11). As a result, the governing volume balance of the overall aggregate reads

$$\boxed{\text{div}(\mathbf{v}_S + n^F \mathbf{w}_F) = \text{div}(n^S \mathbf{v}_S + n^F \mathbf{v}_F) = 0}. \quad (3.6)$$

For the case of a materially compressible fluid constituent, i. e. $\rho^{FR} = \rho^{FR}(p)$, the fluid mass balance should be considered instead of the volume balance. Therefore, the partial mass balance (2.44) for φ^F reads

$$(n^F)'_F \rho^{FR} + n^F (\rho^{FR})'_F + n^F \rho^{FR} \text{div } \mathbf{v}_F = 0. \quad (3.7)$$

The latter equation can be reformulated by including the solid volume balance (3.3)₁ leading to the overall aggregate mass balance for the case of the hybrid material model. Here, one makes use of the material time derivative rules (2.11), the saturation constraint (3.1)₁, and the grad-div relations from Appendix A. As a result, the overall mass balance reads

$$\boxed{n^F (\rho^{FR})'_S + \operatorname{div}(n^F \rho^{FR} \mathbf{w}_F) + \rho^{FR} \operatorname{div} \mathbf{v}_S = 0}. \quad (3.8)$$

Linear Momentum Balance

The specified linear momentum balance in equation (2.47) can be written in details for the two constituents φ^S and φ^F as

$$\begin{aligned} \rho^S (\mathbf{v}_S)'_S &= \operatorname{div} \mathbf{T}^S + \rho^S \mathbf{b}^S - \hat{\mathbf{p}}^F, \\ \rho^F (\mathbf{v}_F)'_S + \rho^F \operatorname{grad}_{\mathbf{v}_F} (\mathbf{w}_F) &= \operatorname{div} \mathbf{T}^F + \rho^F \mathbf{b}^F + \hat{\mathbf{p}}^F. \end{aligned} \quad (3.9)$$

Therein, the assumption of no mass exchange between the constituents has been used in order to simplify the momentum production summation (2.51), i. e.,

$$\sum_{\alpha} \hat{\mathbf{s}}^{\alpha} = \sum_{\alpha} (\hat{\mathbf{p}}^{\alpha} + \hat{\rho}^{\alpha} \mathbf{v}_{\alpha}) = \sum_{\alpha} \hat{\mathbf{p}}^{\alpha} = \mathbf{0} \quad \longrightarrow \quad \hat{\mathbf{p}}^S + \hat{\mathbf{p}}^F = \mathbf{0}. \quad (3.10)$$

Under the assumption of equal body forces of all φ^{α} (cf. (3.1)₅), the overall momentum balance results from the sum of equations (3.9)₁ and (3.9)₂ as

$$\boxed{\rho^S (\mathbf{v}_S)'_S + \rho^F (\mathbf{v}_F)'_S + \rho^F \operatorname{grad}_{\mathbf{v}_F} (\mathbf{w}_F) = \operatorname{div} (\mathbf{T}^S + \mathbf{T}^F) + (\rho^S + \rho^F) \mathbf{b}}. \quad (3.11)$$

Entropy Inequality

The *Clausius-Planck* inequality (2.68) can be reformulated for the considered case of a biphasic medium where the momentum productions satisfy relation (3.10)₂. Consequently, the overall *Clausius-Planck* entropy inequality reads

$$\mathbf{T}^S \cdot \mathbf{L}_S + \mathbf{T}^F \cdot \mathbf{L}_F - \rho^S (\psi^S)'_S - \rho^F (\psi^F)'_F - \hat{\mathbf{p}}^F \cdot \mathbf{w}_F \geq 0. \quad (3.12)$$

3.1.2 Entropy Inequality Evaluation and Effective Stresses

In saturated biphasic materials, the concept of effective stresses provides an excellent framework for investigating the stress state in a material point, which consists of two coupled components: An ‘extra’ or ‘effective’ stress for which a constitutive relation must be formulated, and a weighted pore-fluid pressure term. The concept of effective stresses is traced back to the early investigations in geomechanics on saturated soils by *Fillunger* and *von Terzaghi* as well as the subsequent studies on unsaturated soils, cf., e. g., *Bishop* [14]. For a historical review, see, e. g., *de Boer & Ehlers* [21]. Thereafter, this concept has been

introduced within the thermodynamically consistent TPM considering, for instance, the cases of materially incompressible biphasic aggregates and materially incompressible solid skeletons with compressible pore-fluid content. For more details, the interested reader is referred to the works by de Boer & Ehlers [21], Eipper [65] and Markert [123] among others.

Making use of the mathematical optimisation strategy of *Lagrangian* multipliers for finding the maxima and minima of a function subjected to constraints, the saturation condition (3.1)₁ is weighted by a *Lagrangian* multiplier \mathcal{P} and added to the entropy inequality (3.12) as

$$\mathbf{T}^S \cdot \mathbf{L}_S + \mathbf{T}^F \cdot \mathbf{L}_F - \rho^S (\psi^S)'_S - \rho^F (\psi^F)'_F - \hat{\mathbf{p}}^F \cdot \mathbf{w}_F - \mathcal{P} (n^S + n^F)'_S \geq 0. \quad (3.13)$$

Herein, the saturation condition, i. e.

$$(n^S + n^F)'_S = 0, \quad (3.14)$$

can be interpreted as a volume balance constraint during the deformation process, and thus, \mathcal{P} can be identified as the pore pressure (p). Following this, the constraint (3.14) is reformulated by specifying the terms $(n^\alpha)'_S$. In particular, $(n^S)'_S$ is given by equation (3.3)₁ and $(n^F)'_S$ is derived by exploiting relation (2.11)₁ as

$$(n^F)'_S = (n^F)'_F - \text{grad } n^F \cdot \mathbf{w}_F. \quad (3.15)$$

Depending on the compressibility of the pore-fluid phase, $(n^F)'_F$ in equation (3.15) can be specified as

$$(n^F)'_F = \begin{cases} -n^F \text{div } \mathbf{v}_F & : \text{ incompressible } \varphi^F \text{ (volume balance),} \\ -n^F \text{div } \mathbf{v}_F - \frac{n^F}{\rho^{FR}} (\rho^{FR})'_F & : \text{ compressible } \varphi^F \text{ (mass balance).} \end{cases} \quad (3.16)$$

Considering, for instance, the case of materially incompressible φ^S and φ^F , equations (3.16)₁, (3.15), and (3.3)₁ are inserted into the dissipation inequality (3.13) with $\mathbf{L}_\alpha = \text{grad } \mathbf{v}_\alpha$ yielding

$$\begin{aligned} \underbrace{\mathbf{T}_E^S}_{(\mathbf{T}^S + n^S \mathcal{P} \mathbf{I})} \cdot \mathbf{L}_S + \underbrace{\mathbf{T}_E^F}_{(\mathbf{T}^F + n^F \mathcal{P} \mathbf{I})} \cdot \mathbf{L}_F - \underbrace{\hat{\mathbf{p}}_E^F}_{(\hat{\mathbf{p}}^F - \mathcal{P} \text{grad } n^F)} \cdot \mathbf{w}_F - \\ - \rho^S (\psi^S)'_S - \rho^F (\psi^F)'_F \geq 0. \end{aligned} \quad (3.17)$$

Herein, \mathbf{T}_E^S , \mathbf{T}_E^F , and $\hat{\mathbf{p}}_E^F$ represent so-called ‘extra’ or ‘effective’ quantities, for which suitable constitutive laws should be formulated. In analogy to the early investigations on soil consolidation in geomechanics by *Fillunger* and *von Terzaghi* (see, de Boer & Ehlers [21]), which presumed that the effective stress is determined by the total stress and the excess pore pressure, the aforementioned effective terms are written as follows:

$$\mathbf{T}_E^S = \mathbf{T}^S + n^S p \mathbf{I}, \quad \mathbf{T}_E^F = \mathbf{T}^F + n^F p \mathbf{I}, \quad \hat{\mathbf{p}}_E^F = \hat{\mathbf{p}}^F - p \text{grad } n^F. \quad (3.18)$$

Following this, appropriate relations for the effective quantities and the energy functions must be formulated such that the entropy inequality (3.17) is fulfilled. In particular, based on the fundamental principles of constitutive modelling¹, i. e., *determinism*, *local action*, *equipresence*, *frame indifference* and *dissipation*, the following response functions have to be defined:

$$\mathcal{R} := \{ \psi^S, \psi^F, \mathbf{T}_E^S, \mathbf{T}_E^F, \hat{\mathbf{p}}_E^F \}. \quad (3.19)$$

Moreover, the *equipresence* principle requires that the response functions (3.19) depend on a set of independent state variables related to the solid and the fluid constituent, i. e.

$$\mathcal{R} = \mathcal{R}(\mathcal{V}) \quad \text{with} \quad \mathcal{V} = \mathcal{V}^S \cup \mathcal{V}^F. \quad (3.20)$$

Please consult Ehlers [50, 53], Markert [123, 124] and Bowen [25] for more details. For a homogeneous solid-fluid biphasic model under isothermal conditions, the set of state variables of a potentially elasto-plastic porous solid matrix φ^S reads

$$\mathcal{V}^S := \{ \mathbf{F}_S, \text{Grad}_S \mathbf{F}_S \}. \quad (3.21)$$

In the finite deformation treatment of elasto-plasticity, cf., e. g., Haupt [82] or Ehlers [51, 52], a stress-free intermediate configuration is introduced, which allows for a multiplicative split of the solid deformation gradient \mathbf{F}_S into an elastic \mathbf{F}_{Se} and a plastic \mathbf{F}_{Sp} part as

$$\mathbf{F}_S = \mathbf{F}_{Se} \mathbf{F}_{Sp}. \quad (3.22)$$

Moreover, the non-polar total strain, e. g. the *Green-Lagrangean* strain \mathbf{E}_S , is additively split into an elastic \mathbf{E}_{Se} and a plastic \mathbf{E}_{Sp} term, i. e.

$$\mathbf{E}_S = \mathbf{E}_{Se} + \mathbf{E}_{Sp}. \quad (3.23)$$

According to the *principle of phase separation* (Ehlers [53]), the free energy function ψ^α of a given constituent depends on the state variables that only influence the process in φ^α itself. Consequently, the second-order gradient terms of the biphasic model can be omitted because they only influence the production terms. Thus, the free energy function of the incompressible solid phase φ^S for a possible elasto-plastic behaviour can be expressed as

$$\psi^S = \psi^S(\mathbf{F}_{Se}, \mathbf{F}_{Sp}) \quad \text{or} \quad \psi^S = \psi^S(\mathbf{E}_{Se}, \mathbf{E}_{Sp}) \quad (3.24)$$

The possibility to represent ψ^S in terms of \mathbf{E}_S instead of \mathbf{F}_S is based on the *principle of material frame indifference*. Moreover, restricting the treatment to a hyperelastic-plastic model, the *Helmholtz* free energy ψ^S can additively be split into an elastic part ψ^{Se} and a plastic part ψ^{Sp} as

$$\psi^S = \psi^{Se}(\mathbf{E}_{Se}) + \psi^{Sp}(\mathbf{E}_{Sp}). \quad (3.25)$$

Following this, the evaluation of the entropy inequality results in the solid extra stress \mathbf{T}_E^S (Cauchy stress) as

$$\mathbf{T}_E^S = \rho^S \mathbf{F}_S \frac{\partial \psi^{Se}}{\partial \mathbf{E}_{Se}} \mathbf{F}_S^T. \quad (3.26)$$

¹For more detailed discussion, see, e. g., Truesdell & Toupin [166], Truesdell & Noll [165], Bowen [25] and Ehlers [50, 53].

Moreover, weighting *Cauchy* stress \mathbf{T}_E^S by $\det \mathbf{F}_{S_e}$ yields the well-known *Kirchhoff* stress tensor $\boldsymbol{\tau}_E^S$ in the actual configuration, which can easily be transformed to the reference configuration yielding the 2nd-*Piola-Kirchhoff* stress \mathbf{S}_E^S . In particular, one gets

$$\boldsymbol{\tau}_E^S = \rho_{0S}^S \mathbf{F}_S \frac{\partial \psi^{S_e}}{\partial \mathbf{E}_{S_e}} \mathbf{F}_S^T, \quad \mathbf{S}_E^S = \rho_{0S}^S \frac{\partial \psi^{S_e}}{\partial \mathbf{E}_{S_e}}. \quad (3.27)$$

In the geometrically linear theory, where no distinction between the aforementioned stress tensors is needed, one introduces the solid effective stress as $\boldsymbol{\sigma}_E^S := \mathbf{T}_E^S \approx \boldsymbol{\tau}_E^S \approx \mathbf{S}_E^S$. More details about the above treatment can be found in the works by Ehlers [50, 53], Eipper [65] and Mahnkopf [121] among others.

The set of constitutive variable of a possibly compressible viscous fluid φ^F reads

$$\mathcal{V}^F := \{n^F, \text{grad } n^F, \rho^{FR}, \text{grad } \rho^{FR}, \mathbf{w}_F, \text{Grad}_F \mathbf{v}_F\}. \quad (3.28)$$

In the considered biphasic material treatment, the terms n^F and $\text{grad } n^F$ can be removed from \mathcal{V}^F as they are directly coupled to \mathbf{F}_S via (3.1)₁ and (3.3)₂. It is worth mentioning that for materially incompressible pore fluids, the terms ρ^{FR} , $\text{grad } \rho^{FR}$ are constants and can also be dropped from the state variables list. The free energy ψ^F of the possible compressible fluid material (isothermal case) can be written as

$$\psi^F = \psi^F(\rho^{FR}). \quad (3.29)$$

Similar to Markert [124], the evaluation of the entropy inequality for this case results in a constitutive relation of the effective pore-fluid pressure p^{FR} (or simply p) of the compressible pore fluid and two additional proportionalities:

$$p = p^{FR} := \mathcal{P} = (\rho^{FR})^2 \frac{\partial \psi^F}{\partial \rho^{FR}}, \quad \mathbf{T}_E^F \propto \mathbf{D}_F, \quad \hat{\mathbf{p}}_E^F \propto -\mathbf{w}_F. \quad (3.30)$$

For a materially incompressible pore fluid, the pore pressure $p^{FR} = p$ is treated in the sense of a constraining force, which has to be determined from the boundary conditions of the boundary-value problem under study, cf. [124]. In the upcoming discussion, the following constitutive relations of \mathbf{T}_E^F and $\hat{\mathbf{p}}_E^F$ will be considered:

$$\mathbf{T}_E^F = \overset{4}{\mathbf{D}} \mathbf{D}_F \quad \text{and} \quad \hat{\mathbf{p}}_E^F = -\mathbf{S}_v \mathbf{w}_F. \quad (3.31)$$

Herein, $\overset{4}{\mathbf{D}}$ is a fourth-order positive definite fluid viscosity tensor, \mathbf{D}_F is the symmetric part of fluid spatial velocity gradient, i. e., $\mathbf{D}_F = \frac{1}{2}(\mathbf{L}_F + \mathbf{L}_F^T)$, and \mathbf{S}_v is a second-order permeability tensor. In the geometrically linear case with isotropic permeability, the constitutive equations of the fluid effective stress and the interaction force can be expressed as

$$\mathbf{T}_E^F = 2 \mu^F \mathbf{D}_F^D \quad \text{and} \quad \hat{\mathbf{p}}_E^F = -\frac{(n^F)^2 \gamma^{FR}}{k^F} \mathbf{w}_F, \quad (3.32)$$

where μ^F is the fluid dynamic viscosity, \mathbf{D}_F^D is the deviatoric part of \mathbf{D}_F , $\gamma^{FR} = \rho^{FR} g$ is the effective fluid weight with the gravity $g = |b| = \text{const.}$, and $k^F > 0$ denotes the conventional hydraulic conductivity (*Darcy's* permeability) in m/s.

The validity of the macroscopic model in describing the fluid flow through a porous space requires that the pore diameters are small with respect to the macroscopic length scale. Here, a big number of capillary tubes are assumed crossing an elemental area of the REV. Following this, under the assumption of *Poiseuille*-type pore-fluid flow, a dimensional analysis based on the comparison between the macroscopic filter (*Darcy*) law that results from the fluid momentum balance (3.9)₂ together with (3.32), and the microscopic *Darcy*'s law that includes information of the microtopolgy and the pore-fluid viscosity is carried out, cf. Markert [124], Diebels *et al.* [45] or Ehlers *et al.* [62]. Therein, it is shown that $\text{div } \mathbf{T}_E^F \ll \hat{\mathbf{p}}_E^F$ yielding that $\text{div } \mathbf{T}_E^F$ can *a priori* be neglected in the fluid momentum balance for the macroscopic treatment. Additionally, the comparison between the macro and micro filter laws shows that the macroscopic parameter k^F includes information about the geometry of the pore-space and the pore-fluid viscosity.

3.1.3 Compressible Fluid Behaviour (Hybrid Model)

Two properties of the pore fluid are considered in this thesis: Firstly, a materially incompressible with constant effective density ($\rho^{FR} = \text{const.}$) and, secondly, a materially compressible as an inseparable mixture of an incompressible liquid phase φ^L and trapped, compressible, ideal gas bubbles φ^G , see, Ehlers *et al.* [62], Diebels [43] and Mahnkopf [121] for details. Within the TPM, a constitutive law for the compressible fluid density is introduced. Here, ρ^{FR} can be expressed in terms of the material densities of the incompressible liquid ($\rho^{LR} = \text{const.}$) and the compressible gas (ρ^{GR}) as

$$\rho^F = n^F \rho^{FR} = n^L \rho^{LR} + n^G \rho^{GR} \quad (3.33)$$

with n^L and n^G being the liquid and gas volume fractions. Assuming that the gas has a barotropic behaviour and is governed by the ideal gas law (*Boyle-Mariotte's* law), a constitutive law that relates the effective density ρ^{GR} to the effective pore-fluid pressure p^{FR} or simply p is provided (see (3.30)₁). Thus, proceeding from an isothermal case and excluding the external influences of p (such as atmospheric pressure²), the ideal gas law (cf. Holbrow *et al.* [89]) is given by

$$\rho^{GR} = p \frac{M}{R\Theta}. \quad (3.34)$$

Herein, R is the universal gas constant, $\Theta = \text{const.}$ is the absolute *Kelvin's* temperature, and M is the molar mass of the gas. The saturation condition (2.4) for this particular case reads

$$n^S + n^F = 1 \quad \text{with} \quad n^F = n^L + n^G. \quad (3.35)$$

Unlike the three-phase material models (cf. Graf [74]), the current treatment assumes that the constituents φ^L and φ^G have the same state of motion as φ^F and, as a consequence, they have the same velocity and material time derivative, i. e., $\mathbf{v}_L = \mathbf{v}_G \equiv \mathbf{v}_F$ and

²In solving initial-boundary-value problems with compressible pore fluid, the external pressure (e. g. atmospheric pressure) is assigned as an initial condition to the problem so that $\rho_{0F}^{GR} \neq 0$.

$(\cdot)'_L = (\cdot)'_G \equiv (\cdot)'_F$, see Mahnkopf [121] for more details. The mass balance equations of φ^L and φ^G under the assumption of no mass exchange read

$$\left. \begin{aligned} (\rho^L)'_F + \rho^L \operatorname{div} \mathbf{v}_F &= 0 \\ (\rho^G)'_F + \rho^G \operatorname{div} \mathbf{v}_F &= 0 \end{aligned} \right\} \longrightarrow \frac{(\rho^L)'_F}{\rho^L} = \frac{(\rho^G)'_F}{\rho^G}. \quad (3.36)$$

Analytical integration of relation (3.36)₂ results in a constant ratio between the partial densities of φ^L and φ^G as

$$\rho^L = C \rho^G. \quad (3.37)$$

Here, C is an integration constant given in terms of the volume fractions and the material densities of φ^L and φ^G at the initial state ($t = t_0$) as

$$C = \frac{n^L \rho^{LR}}{n^G \rho^{GR}} \Big|_{t=t_0} = \frac{n_{0F}^L \rho^{LR}}{n_{0F}^G \rho_{0F}^{GR}}. \quad (3.38)$$

Based on equations (3.33), (3.35), and (3.37), one obtains an implicit relation between ρ^{FR} and the pore-fluid pressure p as

$$\rho^{FR}(p) = \rho^{LR} \frac{1 + C}{C + \frac{\rho^{LR}}{\rho^{GR}(p)}}, \quad (3.39)$$

where ρ^{GR} results from the ideal gas law in (3.34). The case of a materially incompressible fluid corresponds to gas phase absence, i. e., $n^G = 0 \rightsquigarrow C \rightarrow \infty$, yielding that $\rho^{FR} = \rho^{LR}$.

3.1.4 Different Sets of Governing Balance Relations

In order to determine the primary and secondary unknown fields of the arising purely mechanical biphasic model $\varphi = \varphi^S \cup \varphi^F$, the effective stresses (3.18) and the specified momentum production relation (3.32)₂ are inserted into the solid and fluid momentum balances (3.9)₁ and (3.9)₂, respectively. Therefore, under the assumption of materially incompressible φ^S and φ^F with $\operatorname{div} \mathbf{T}_E^F \approx \mathbf{0}$, the governing balance relations of the dynamic biphasic model with primary variables $\{\mathbf{u}_S, \mathbf{v}_F, p\}$ represents a system of nonlinear partial differential equations (PDE) of 2nd order in time and space, viz.:

- Momentum balance of the solid phase:

$$\rho^S (\mathbf{v}_S)'_S = \operatorname{div} (\mathbf{T}_E^S - n^S p \mathbf{I}) + \rho^S \mathbf{b} + \frac{(n^F)^2 \gamma^{FR}}{k^F} \mathbf{w}_F - p \operatorname{grad} n^F, \quad (3.40)$$

- Momentum balance of the pore-fluid phase:

$$\rho^F (\mathbf{v}_F)'_S + \rho^F (\operatorname{grad} \mathbf{v}_F) \mathbf{w}_F = -n^F \operatorname{grad} p + \rho^F \mathbf{b} - \frac{(n^F)^2 \gamma^{FR}}{k^F} \mathbf{w}_F, \quad (3.41)$$

- Volume balance of the overall aggregate:

$$0 = \operatorname{div}(n^S \mathbf{v}_S + n^F \mathbf{v}_F). \quad (3.42)$$

In this case, $(\mathbf{v}_S)'_S = (\mathbf{u}_S)''_S$ represents the 2nd-order time derivative. In the geometric linear treatment (cf. Section 2.2.3) with $\|\operatorname{grad} \mathbf{u}_S\| \ll 1$, one has $n^\alpha(\mathbf{u}_S) \approx n_{0S}^\alpha = \text{const.}$. Thus, the term $\operatorname{grad} n^F$ in equation (3.40) is regarded as a higher-order term and can be omitted in the later discussion. In particular, exploiting the linearised volume fraction relation (3.4), we have

$$\operatorname{grad} n^F = \operatorname{grad} (1 - n^S) \stackrel{\text{lin}}{=} n_{0S}^S \operatorname{grad} \operatorname{div} \mathbf{u}_S \approx \mathbf{0}. \quad (3.43)$$

Moreover, based on the geometric linearisation in Section 2.2.3 and relation (2.33), the nonlinear convective term $(\operatorname{grad} \mathbf{v}_F) \mathbf{w}_F$ can be omitted in the linearised model (see also Zienkiewicz *et al.* [186] for more details). As the volume balance (3.42) is independent of the pore-fluid pressure variable, the relations (3.40)–(3.42) yield in the finite element treatment a set of differential-algebraic equations (DAE) of index higher than one³. This situation corresponds to an ill-posed problem involving a lot of numerical challenges especially with the monolithic implicit time-integration treatment. Therefore, in order to overcome this challenge and improve the numerical stability, equation (3.41) can be solved with respect to $n^F \mathbf{w}_F$ and inserted in (3.42).

In this thesis, only time-integration methods for PDE of first-order in time are considered⁴. Therefore, the relation $\mathbf{v}_S = (\mathbf{u}_S)'_S$ is additionally used to reduce the order of the set of PDE into first order in time. Consequently, the natural set of coupled PDE for the determination of the primary unknowns $\{\mathbf{u}_S, \mathbf{v}_F, p\}$ as well as the secondary variables, e. g., $\mathbf{v}_S(\mathbf{u}_S)$, \mathbf{w}_F , $n^S(\mathbf{u}_S)$ and $n^F(\mathbf{u}_S)$, are introduced in box (3.44) and referred to, according to the related primary unknowns, as $\mathbf{u}_S\text{-}\mathbf{v}_F\text{-}p(1)$ (or $\text{uvp}(1)$) formulation.

Governing uvp (1) formulation, primary unknowns $\{\mathbf{u}_S, \mathbf{v}_F, p\}$	
• Order reduction:	$(\mathbf{u}_S)'_S = \mathbf{v}_S$
• Solid momentum balance:	$\rho^S (\mathbf{v}_S)'_S = \operatorname{div}(\mathbf{T}_E^S - n^S p \mathbf{I}) + \rho^S \mathbf{b} + \frac{(n^F)^2 \gamma^{FR}}{k^F} \mathbf{w}_F$
• Fluid momentum balance:	$\rho^F (\mathbf{v}_F)'_S = -n^F \operatorname{grad} p + \rho^F \mathbf{b} - \frac{(n^F)^2 \gamma^{FR}}{k^F} \mathbf{w}_F$
• Overall volume balance:	$0 = \operatorname{div}\left(\mathbf{v}_S + \underbrace{\frac{k^F}{g} [\mathbf{b} - (\mathbf{v}_F)'_S] - \frac{k^F}{\gamma^{FR}} \operatorname{grad} p}_{n^F \mathbf{w}_F}\right)$

(3.44)

³The classification of DAE systems according to the differentiation index is discussed in Section 4.2, which is based mainly on the works by Hairer & Wanner [80] and Ascher & Petzold [4].

⁴Different Implicit *Runge-Kutta* (IRK) schemes are implemented for the monolithic implicit treatment, which demand that the system of PDE is of first order, cf. Section 4.3 for detailed discussion.

For an easier implementation of the boundary conditions, the overall momentum balance that results from the sum of equations (3.44)₂ and (3.44)₃ is used instead of the pure solid momentum balance (3.44)₂. Moreover, such a modification has positive impacts on the numerical stability of the monolithic implicit treatment due to the elimination of some coupling terms as will be discussed in detail in Section 4.2. As a result, the arising set of coupled PDE is mentioned to, according to the primary unknowns, as $\mathbf{u}_S\text{-}\mathbf{v}_F\text{-}p$ (2) (or uvp (2)) formulation, and summarised in the following box:

Governing uvp (2) formulation, primary unknowns $\{\mathbf{u}_S, \mathbf{v}_F, p\}$	
• Order reduction:	$(\mathbf{u}_S)'_S = \mathbf{v}_S$
• Overall momentum balance:	$\rho^S (\mathbf{v}_S)'_S + \rho^F (\mathbf{v}_F)'_S = \text{div}(\mathbf{T}_E^S - p\mathbf{I}) + (\rho^S + \rho^F) \mathbf{b}$
• Fluid momentum balance:	$\rho^F (\mathbf{v}_F)'_S = -n^F \text{grad} p + \rho^F \mathbf{b} - \frac{(n^F)^2 \gamma^{FR}}{k^F} \mathbf{w}_F$
• Overall volume balance:	$0 = \text{div}\left(\mathbf{v}_S + \underbrace{\frac{k^F}{g} [\mathbf{b} - (\mathbf{v}_F)'_S] - \frac{k^F}{\gamma^{FR}} \text{grad} p}_{n^F \mathbf{w}_F}\right)$

(3.45)

In fact, it is possible to solve the set of equations (3.45) by considering $\{\mathbf{u}_S, \mathbf{w}_F, p\}$ as the primary unknowns. In that case, $\mathbf{v}_F = \mathbf{w}_F + \mathbf{v}_S$ is treated as a secondary variable, and the set of coupled PDE is referred to as $\mathbf{u}_S\text{-}\mathbf{w}_F\text{-}p$ (or uwp) formulation.

Although the governing three-field equations, e.g. (3.45), can be used directly in the numerical treatment, it is convenient under some restrictions to reduce the number of primary variables. This helps to decrease the number of equations that are needed to be solved at each time step, and therefore, accelerate the numerical solution. In this context, for geomechanical problems with applied dynamic loads of low and moderate frequencies⁵ as well as low permeability parameters⁶, it is appropriate to assume that the fluid and solid accelerations are almost identical, i.e., $(\mathbf{v}_F)'_S \approx (\mathbf{v}_S)'_S$ yielding $(\mathbf{w}_F)'_S \approx \mathbf{0}$. This leads to a simpler model based on the primary unknowns $\{\mathbf{u}_S, p\}$, thereby accepting some additional error, cf., e.g., Zienkiewicz *et al.* [186] or Lewis & Schrefler [115] for more details. In this case, the fluid momentum balance (3.45)₃ just serves as an explicit equation for the filter velocity $n^F \mathbf{w}_F$, which is then substituted into the overall volume balance (3.45)₄. In doing so, the system (3.45) is reverted to a simpler set of equations known as ‘up’ formulation, which is in accordance with the primary unknowns \mathbf{u}_S and p .

⁵Seismic excitation is a practical example of low-frequency loading (usually below 30 Hz). In this connection, Biot [12, Eq. (6.11)] introduced a critical frequency relation that takes the geometry of micropores and the pore-fluid properties into account in order to distinguish between the low and the higher frequency ranges. Roughly speaking, the low-frequency range is associated with *Poiseuille*-type flow on the microscale.

⁶For low permeability parameters (k^F in m/s), the relative motion between the solid matrix and the viscous pore-fluid under dynamic loading is very slow. Thus, it is accepted that \mathbf{w}_F has a very small value and the pore fluid is almost trapped in the solid matrix.

In particular, we have

Governing up formulation, primary unknowns $\{\mathbf{u}_S, p\}$	
• Order reduction:	$(\mathbf{u}_S)'_S = \mathbf{v}_S$
• Overall momentum balance:	$(\rho^S + \rho^F)(\mathbf{v}_S)'_S = \text{div}(\mathbf{T}_E^S - p\mathbf{I}) + (\rho^S + \rho^F)\mathbf{b}$
• Overall volume balance:	$0 = \text{div}\left(\mathbf{v}_S - \frac{k^F}{g}[(\mathbf{v}_S)'_S - \mathbf{b}]\right) - \frac{k^F}{\gamma^{FR}}\Delta p$

(3.46)

In (3.46)₃, $\Delta(\cdot) = \text{div grad}(\cdot)$ denotes the *Laplace* operator.

In this monograph, the more general three-field systems are always considered. However, the presented solution procedures can in the same way be applied to the simpler up formulation.

For the case of the biphasic hybrid model with a materially incompressible solid but a compressible fluid constituent, the governing balance relations are similar to the three-field PDE (3.45) except for the overall volume balance (3.45)₄. In this case, the overall mass balance is taken into account (cf. equation (3.8)) after inserting the filter velocity $n^F \mathbf{w}_F$ that results from the fluid momentum balance. In particular, the governing overall mass balance reads

$$n^F (\rho^{FR})'_S = -\rho^{FR} \text{div} \mathbf{v}_S - \text{div}\left(\frac{k^F}{g}[\rho^{FR}(\mathbf{b} - (\mathbf{v}_F)'_S) - \text{grad} p]\right) \quad (3.47)$$

with $\rho^{FR} = \rho^{FR}(p)$ being the pore-pressure-dependent fluid material density.

3.2 Elasto-Viscoplastic Material Behaviour

Constitutive models are represented by mathematical relations, which are ultimately able to describe the stress-strain relationship at each material point under different loading conditions. The aim of this section is to discuss the general settings of an elasto-viscoplastic model for porous materials within the framework of small deformations. Therein, the elastic behaviour of the solid matrix is described via a hyperelastic material model, cf. the works by Eipper [65], Scholz [155] and Ehlers & Avci [60]. The plastic behaviour is captured using the single-surface yield function, which is developed and calibrated in the works by Ehlers [53, 54], Müllerschön [134] and Scholz [155]. Additionally, an introduction to the isotropic and kinematic hardening is given in this part of the work.

3.2.1 Preface

The aim of this preface is to give additional information about the kinematics of elasto-plasticity as well as different elasticity definitions. Throughout this thesis, the convention of positive tension and negative compression is adapted, which is usual in continuum mechanics but contrary to what is often employed in geomechanics.

Additional Kinematic Relations of the Elasto-Plastic Model

In the geometric linear approach with small deformations and rotations, the essential kinematic quantity is the linearised total small strain $\boldsymbol{\varepsilon}_S$, which is, following (3.23), additively decomposed into an elastic and a plastic part, viz.:

$$\boldsymbol{\varepsilon}_S := \mathbf{E}_{S\text{lin}} = \frac{1}{2}(\text{grad } \mathbf{u}_S + \text{grad}^T \mathbf{u}_S) = \boldsymbol{\varepsilon}_{Se} + \boldsymbol{\varepsilon}_{Sp}. \quad (3.48)$$

The multiplicative splitting technique that has been applied to \mathbf{F}_S can also be applied to the solid volume fraction (3.3)₂ as

$$n^S = n_{0S}^S (\det \mathbf{F}_S)^{-1} = n_{0S}^S (\det \mathbf{F}_{Se})^{-1} (\det \mathbf{F}_{Sp})^{-1}. \quad (3.49)$$

Within the geometric linear theory, equation (3.49) can be reformulated by virtue of (3.4) and the definition of the volumetric strain, $\varepsilon_S^V := \boldsymbol{\varepsilon}_S \cdot \mathbf{I} = \text{div } \mathbf{u}_S$, yielding

$$n^S = n_{0S}^S (1 - \varepsilon_{Se}^V) (1 - \varepsilon_{Sp}^V) \quad \text{with} \quad \begin{cases} \varepsilon_{Se}^V = \boldsymbol{\varepsilon}_{Se} \cdot \mathbf{I}, \\ \varepsilon_{Sp}^V = \boldsymbol{\varepsilon}_{Sp} \cdot \mathbf{I}. \end{cases} \quad (3.50)$$

Equation (3.50)₁ can be further simplified by introducing the plastic volume fraction n_p^S as a new variable. In particular, we have

$$n_p^S := n_{0S}^S (1 - \varepsilon_{Sp}^V) \quad \longrightarrow \quad n^S = n_p^S (1 - \varepsilon_{Se}^V), \quad (3.51)$$

where n_p^S can be understood as the solid volume fraction when the material is subjected to purely plastic deformation.

Classical Elasticity Definitions

In the following, several elasticity definitions are briefly reviewed, whereas more details and definitions about elasticity can be found in the works by Houlsby & Puzrin [92], Humrickhouse [96] and Ogden [139] among others. It is important to mention in this regard that the elastic behaviour of the solid matrix in this monograph is described only within the hyperelasticity theory.

A *hyperelastic* material is characterised by the existence of a scalar-valued strain energy function $\psi(\boldsymbol{\varepsilon}_e)$ from which the elastic stress is derived. Such energy functions ensure that the energy is conserved and the elastic strain is entirely reversible. Alternatively, an *elastic* material only requires that the stress is expressed via a tensor-valued function of the elastic strain, i. e., $\boldsymbol{\sigma} = \boldsymbol{\sigma}(\boldsymbol{\varepsilon}_e)$. A third class of elasticity, called *hypoelasticity*, is mentioned, where the strain and the stress increments are related via a fourth-order tensorial function of the strain (sometimes of the stress), i. e., $\overset{4}{\mathcal{C}}_e(\boldsymbol{\varepsilon}_e)$. The use of a hypoelastic formulation to describe the elastic behaviour of a granular material might result in a non-conservative energy model for the case of a non-linear elastic response, cf. Humrickhouse [96] or Borja *et al.* [23].

A hierarchical relation between the three different modes of elasticity as well as details about their derivations are given in Table 3.1.

	Hyperelasticity	Elasticity	Hypoelasticity
Stress	$\boldsymbol{\sigma} = \frac{\partial \psi(\boldsymbol{\varepsilon}_e)}{\partial \boldsymbol{\varepsilon}_e}$	$\boldsymbol{\sigma} = \boldsymbol{\sigma}(\boldsymbol{\varepsilon}_e)$	
Stress increment	$\dot{\boldsymbol{\sigma}} = \frac{\partial^2 \psi(\boldsymbol{\varepsilon}_e)}{\partial \boldsymbol{\varepsilon}_e \otimes \partial \boldsymbol{\varepsilon}_e} \dot{\boldsymbol{\varepsilon}}_e$	$\dot{\boldsymbol{\sigma}} = \frac{\partial \boldsymbol{\sigma}(\boldsymbol{\varepsilon}_e)}{\partial \boldsymbol{\varepsilon}_e} \dot{\boldsymbol{\varepsilon}}_e$	$\dot{\boldsymbol{\sigma}} = \overset{4}{\mathcal{C}}_e(\boldsymbol{\varepsilon}_e) \dot{\boldsymbol{\varepsilon}}_e$
Linear elasticity	$\overset{4}{\mathcal{D}}_e = \frac{\partial^2 \psi(\boldsymbol{\varepsilon}_e)}{\partial \boldsymbol{\varepsilon}_e \otimes \partial \boldsymbol{\varepsilon}_e}$	$\overset{4}{\mathcal{D}}_e = \frac{\partial \boldsymbol{\sigma}(\boldsymbol{\varepsilon}_e)}{\partial \boldsymbol{\varepsilon}_e}$	$\overset{4}{\mathcal{D}}_e = \overset{4}{\mathcal{C}}_e(\boldsymbol{\varepsilon}_e)$

Table 3.1: Different elasticity classes

In Table 3.1, the *elastic* class can be recovered from the *hypoelastic* case if $\overset{4}{\mathcal{C}}_e(\boldsymbol{\varepsilon}_e)$ is integrable with respect to $\boldsymbol{\varepsilon}_e$, and the *hyperelastic* model might be derived from the *elastic* one if $\boldsymbol{\sigma}(\boldsymbol{\varepsilon}_e)$ is integrable with respect to $\boldsymbol{\varepsilon}_e$. If a linear elastic behaviour is considered, then, it is not necessary to distinguish between the three models of elasticity. In that case, the stress and strain are related via a fourth-order elasticity tensor $\overset{4}{\mathcal{D}}_e$, usually called the elastic stiffness matrix.

3.2.2 Hyperelastic Material Modelling

In this monograph, a linear elastic material model is used for the investigation of elastic wave propagation and the different types of waves, whereas a non-linear elastic model is applied when phenomena such as liquefaction are expected to occur.

Linear Elastic Solid Matrix Behaviour

The linear elastic solid behaviour is described using the *Hookean* elasticity law. Herein, the *Cauchy* extra stress tensor can be expressed as

$$\mathbf{T}_E^S := \boldsymbol{\sigma}_E^S = 2\mu^S \boldsymbol{\varepsilon}_{S_e} + \lambda^S (\boldsymbol{\varepsilon}_{S_e} \cdot \mathbf{I}) \mathbf{I} \quad (3.52)$$

with $\boldsymbol{\varepsilon}_{S_e}$ being the elastic strain tensor and μ^S , λ^S are the macroscopic *Lamé* constants of the porous solid matrix. Although the assumption of a materially incompressible solid constituent has been used, the *Lamé* constants in this case should be understood as structural parameters, where the volumetric deformation is allowed through variation of the solid volume fraction.

Non-Linear Elastic Solid Matrix Behaviour

The non-linear elastic behaviour of the solid matrix is captured using a hyperelastic model as given in the works by Avci & Ehlers [5], Eipper [65], Müllerschön [134], Scholz [155] and Ehlers & Scholz [64]. The proposed elasticity model fulfils the thermodynamical

restrictions and shows a very good performance in describing the elastic deformation of isotropic granular porous materials in the framework of the geometric linear theory.

Under the assumption of uncrushable solid particles⁷, a maximum solid volume fraction (n_{\max}^S) is defined, cf. Scholz [155]. The value of n_{\max}^S depends on the granular geometry and adds a restriction to the elastic volumetric strain. Here, the critical elastic volumetric strain $\varepsilon_{Se,crit}^V$ associated with n_{\max}^S can be expressed as

$$\varepsilon_{Se,crit}^V = 1 - \frac{n_{\max}^S}{n_p^S} \quad \text{with} \quad n^S \leq n_{\max}^S < 1. \quad (3.53)$$

Following this, the *Helmholtz* free-energy density function ψ^S can be additively split into a purely elastic ψ^{Se} and a plastic ψ^{Sp} term. In this connection, Avci & Ehlers [5] suggested the following expression to describe the elastic free-energy density:

$$\begin{aligned} \rho_{0S}^S \psi^{Se} = & \mu^S \boldsymbol{\varepsilon}_{Se}^D \cdot \boldsymbol{\varepsilon}_{Se}^D + \frac{1}{2} (k_0^S - k_1^S) (\varepsilon_{Se}^V)^2 - \\ & - k_1^S (\varepsilon_{Se,crit}^V)^2 \left[\ln \left(\frac{\varepsilon_{Se,crit}^V - \varepsilon_{Se}^V}{\varepsilon_{Se,crit}^V} \right) + \frac{\varepsilon_{Se}^V}{\varepsilon_{Se,crit}^V} \right]. \end{aligned} \quad (3.54)$$

Here, ρ_{0S}^S is the initial solid density, k_0^S and k_1^S are material constants determined from the unloading-reloading tests, $\boldsymbol{\varepsilon}_{Se}^D$ is the elastic deviatoric strain, and μ^S is the solid shear modulus. Following this, the solid effective stress reads

$$\boldsymbol{\sigma}_E^S = \rho_{0S}^S \frac{\partial \psi^{Se}}{\partial \boldsymbol{\varepsilon}_{Se}} = 2\mu^S \boldsymbol{\varepsilon}_{Se}^D + \left[k_0^S + k_1^S \left(\frac{\varepsilon_{Se,crit}^V}{\varepsilon_{Se,crit}^V - \varepsilon_{Se}^V} - 1 \right) \right] \varepsilon_{Se}^V \mathbf{I}. \quad (3.55)$$

In this relation, the elastic deviatoric stress is considered to be linear and governed by a constant shear modulus μ^S , whereas the hydrostatic part of $\boldsymbol{\sigma}_E^S$ has been chosen to simulate the physically non-linear unloading-reloading hydrostatic behaviour.

Remark: Based on experimental observations of unloading-reloading triaxial compressional tests, cf. Müllerschön [134], a coupling between the shear strength and the hydrostatic loading can be noticed. This dependency motivates a non-linear relation of the shear modulus as a function of the plastic volumetric strain ε_p^V , i. e.,

$$\mu^S = \mu^S(\varepsilon_{Sp}^V) \quad \text{with} \quad \varepsilon_{Sp}^V = \boldsymbol{\varepsilon}_{Sp} \cdot \mathbf{I}. \quad (3.56)$$

For small deviatoric strain changes, this effect can approximately be ignored, i. e., $\mu^S \approx \text{const.}$

3.2.3 Plastic Material Modelling

In the literature, there exists a great variety of constitutive models, which are able to deal with most of the observed mechanical behaviours of geomaterials. Many problems

⁷Solid grains are assumed to be sufficiently ductile allowing for an elasto-plastic deformation on the micro-level, whereas for brittle particles fracture might occur.

in geomechanics, such as slope stability, bearing capacity of retaining walls, expansive soil phenomena, and saturated soil liquefaction can be efficiently analysed using plasticity models, cf., e. g., Zienkiewicz *et al.* [186] for a general overview.

In the current work, the single-surface plasticity model, which is introduced by Ehlers [53, 54] within the finite elasto-plasticity framework, is discussed and applied to simulate different features of liquefaction phenomena in saturated porous media. Here, in analogy to the works by Müllerschön [134], Scholz [155] and Ehlers & Avci [60], the application of the mentioned plasticity model proceeds from an infinitesimal strain assumption.

Following this, the elements of the considered plasticity model can be recognised as follows: (1) the yield function that encompasses the elastic domain, (2) the flow rule that describes the evolution of the plastic strain and the loading/unloading criterion in order to distinguish between the elastic and the plastic stress steps, and (3) the hardening/softening and the failure state. In this connection, two types of hardening behaviours are reviewed, namely, the isotropic hardening that expresses the expansion/contraction of the yield surface, and the kinematic hardening that describes the shift of the yield surface depending on the plastic strain history through the deviatoric and the hydrostatic plastic strain directions. In the numerical examples, only the isotropic hardening is applied.

Yield Function

For the treatment of plasticity, a yield surface which enfolds the elastic domain is defined in the principle stress space. Inside this surface, stresses are assumed to be elastic whereas on the yield surface, the stress state produces plastic strains. Unlike single-phase non-porous materials (e. g. metals), granular materials exhibit volumetric as well as deviatoric plastic deformations. Therefore, the yield surface which characterises the onset of plastic deformations should be, among others, a closed surface and a function of the first stress invariant I_σ that represents the confining pressure.

Drucker & Prager [47] introduced one of the earliest pressure-dependent yield surfaces to predict the onset of plastic deformations in soil. Such an open-cone yield surface cannot capture the volumetric plastic deformations under purely hydrostatic loading. One of the solutions to tackle this issue is what has been introduced by, e. g., Vermeer [171]. Therein, a cap-type yield surface that accounts for the plastic volumetric strains and the volumetric as well as the shear hardening has been discussed. However, numerical difficulties might arise when the stress state attains the boundary between the cap and the original yield surface. This dilemma has been solved in the class of closed single-surface yield functions, which are differentiable at any point of the surface. A typical shape of such yield surfaces is a closed tear drop with rounded triangle cross sections in the deviatoric plane (Lade [110]). As examples, consider the well-known *Cam-Clay* and the modified *Cam-Clay* models, cf., e. g., Jeremić *et al.* [100], Abed [1] and Müllerschön [134] for a literature review.

In this work, the single-surface yield function (Figure 3.1) developed by Ehlers [53, 54] is used for the treatment of the inelastic granular material behaviour. This yield function is given in terms of the first principal stress invariant I_σ and the second and third deviatoric

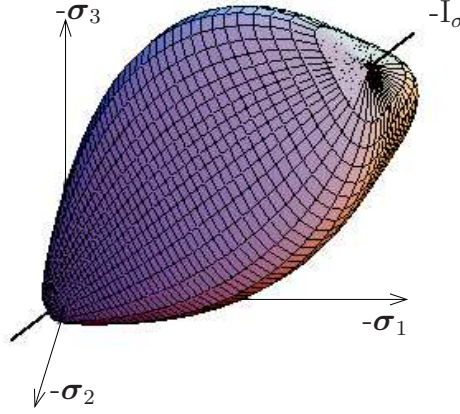


Figure 3.1: Single-surface yield function in the principal stress space, cf. Ehlers [53]

stress invariants $\mathbb{II}_\sigma^D, \mathbb{III}_\sigma^D$ as

$$F(I_\sigma, \mathbb{II}_\sigma^D, \mathbb{III}_\sigma^D) = \sqrt{\mathbb{II}_\sigma^D \left(1 + \gamma \frac{\mathbb{III}_\sigma^D}{(\mathbb{II}_\sigma^D)^{3/2}}\right)^m} + \frac{1}{2} \alpha I_\sigma^2 + \delta^2 I_\sigma^4 + \beta I_\sigma + \epsilon I_\sigma^2 - \kappa = 0 \quad (3.57)$$

with the invariants

$$I_\sigma = \boldsymbol{\sigma}_E^S \cdot \mathbf{I}, \quad \mathbb{II}_\sigma^D = \frac{1}{2} \boldsymbol{\sigma}_E^{SD} \cdot \boldsymbol{\sigma}_E^{SD}, \quad \mathbb{III}_\sigma^D = \frac{1}{3} \boldsymbol{\sigma}_E^{SD} \cdot \boldsymbol{\sigma}_E^{SD} \boldsymbol{\sigma}_E^{SD}. \quad (3.58)$$

Herein, beside the stress invariants, the yield surface is also a function of two sets of material parameters, namely, the hydrostatic parameters $\mathcal{S}_h = \{\alpha, \beta, \delta, \epsilon, \kappa\}$, which control the shape of the yield surface in the hydrostatic plane, and the deviatoric parameters $\mathcal{S}_d = \{\gamma, m\}$, which manage the shape of F in the deviatoric plane, cf. Ehlers [57] and Ehlers & Scholz [64] for more details.

Non-Associative Flow Rule and Loading/Unloading Conditions

Based on experimental evidences on granular materials, adoption of an associative flow rule with plastic flow direction perpendicular to the yield surface obviously leads to an overestimated dilation behaviour. Therefore, a non-associative flow rule needs to be formulated by introducing a plastic potential function different from the yield function. In this connection, the following potential relation as a function of the first principal stress invariant I_σ and the second deviatoric stress invariant \mathbb{II}_σ^D is suggested (cf. Mahnkopf [121]):

$$G(I_\sigma, \mathbb{II}_\sigma^D) = \sqrt{\psi_1 \mathbb{II}_\sigma^D + \frac{1}{2} \alpha I_\sigma^2 + \delta^2 I_\sigma^4} + \psi_2 \beta I_\sigma + \epsilon I_\sigma^2 - \kappa \quad (3.59)$$

with ψ_1, ψ_2 as additional parameters for adjusting the dilation angle. This formulation excludes the third deviatoric invariant \mathbb{III}_σ^D and leads to a circular shape in the deviatoric plane. Following this, a constitutive equation for the temporal evolution of $\boldsymbol{\varepsilon}_{Sp}$ needs to be specified. Therefore, based on the so-called Principle of Maximum Dissipation (PMD), a dissipative optimisation problem is formulated within the potential surface leading to a

canonical formulation for $(\boldsymbol{\varepsilon}_{Sp})'_S$. In particular, the *flow rule* can be expressed as

$$(\boldsymbol{\varepsilon}_{Sp})'_S = \Lambda \frac{\partial G}{\partial \boldsymbol{\sigma}_E^S} \quad (3.60)$$

with Λ being the plastic multiplier. For more details about the PMD, the interested reader is referred to the works by, e. g., Lubliner [119], Simo & Hughes [157] and Miehe [131]. A necessary condition for the solution of the problem in equation (3.60) is the *Karush-Kuhn-Tucker* (KKT) optimality condition, which can be expressed for the case of rate-independent elasto-plasticity as

$$F \leq 0, \quad \Lambda \geq 0, \quad \Lambda F = 0. \quad (3.61)$$

In the numerical implementation of the rate-independent elasto-plasticity, instability and ill-posedness might be encountered during, e. g., shear band localisation, cf. Oka *et al.* [140] and Ehlers *et al.* [63]. A possible method to overcome such a difficulty is to introduce a kind of material rate-dependency by use of elasto-viscoplastic models. According to the overstress concept by Perzyna [143], the following viscoplasticity ansatz can be used:

$$\Lambda = \frac{1}{\eta_r} \left\langle \frac{F}{\sigma_0} \right\rangle^r. \quad (3.62)$$

Here, $\langle \cdot \rangle$ represent the *Macauley* brackets defined as $\langle \cdot \rangle := \frac{1}{2}[(\cdot) + |(\cdot)|]$, σ_0 is a reference stress, r is the viscoplastic exponent, and η_r is the viscoplastic relaxation time. As the aim of the viscosity in this case is to improve the numerical stability, choosing a small value for η_r together with $\sigma_0 > 0$ and $r = 1$ allows for an elasto-viscoplastic model, which behaves very much similar to the elasto-plastic model, but with better stability characters, cf. Haupt [84] or Scholz [155] for more details.

Isotropic Hardening/Softening Evolution Laws

Experiments on dry sand show that isotropic hardening effects appear instantly after loading in triaxial compressional tests, whereas a softening behaviour might be obtained for dense sand after reaching a certain peak stress. Such isotropic hardening and softening attitudes are related to the plastic deformations and can be included in the constitutive model by introducing suitable evolution relations for a subset of the yield function parameters $p_i \in \{\beta, \delta, \epsilon, \gamma\}$. Hence, the parameters p_i are chosen as functions of the dissipative plastic work, cf. de Boer [18].

According to Ehlers & Scholz [64], the evolution relations for the parameters p_i are split into volumetric $(p_i^V)'_S$ and deviatoric $(p_i^D)'_S$ terms, viz.:

$$(p_i)'_S = (p_i^V)'_S + (p_i^D)'_S = (\overset{\star}{p}_i - p_i) (C_{pi}^V (\boldsymbol{\varepsilon}_{Sp}^V)'_S + C_{pi}^D \|(\boldsymbol{\varepsilon}_{Sp}^D)'_S\|) \quad \text{with} \quad p_i(t_0) = p_{i0}. \quad (3.63)$$

Here, $\overset{\star}{p}_i$ and p_{i0} are the maximum and the initial values of p_i , respectively, and C_{pi}^V , C_{pi}^D are material constants. The suggested relation (3.63) allows to distinguish between a deviatoric, positive term $\|(\boldsymbol{\varepsilon}_{Sp}^D)'_S\|$ yielding a plastic hardening behaviour, and a volumetric part that results in positive (hardening) or negative (softening) values. Thus, the densification and the loosening attitudes in the granular structure are represented.

Kinematic Hardening

Due to the kinematic hardening effects, granular materials such as soils show an anisotropic behaviour under cyclic loading conditions. Collins [38] discussed within the critical state framework a kinematic hardening formulation, in which the plastic free energy function ψ^{Sp} is expressed in terms of the volumetric and the deviatoric plastic strain. Therein, the yield locus might be shifted and rotated in the principal stress space leading to an anisotropic hardening general case. Another approach is proposed in the work by Lade & Inelb [112], which allows for rotations and intersections of the yield surfaces in order to achieve a good convergence to the experimental data.

According to, e.g., de Boer & Brauns [19], Ehlers [52] and Brauns [28], porous solid materials exhibit kinematic hardening in the sense of the *Bauschinger* effect. Thus, in order to simulate such behaviours, an appropriate formulation of the back-stress tensor must be specified. As shown in relation (3.25), the free energy function is decoupled for simplicity into an elastic ψ^{Se} and a plastic ψ^{Sp} part. In this, ψ^{Sp} is employed to formulate the back-stress tensor \mathbf{Y}^S (see Ehlers [52]) leading to a $\mathbf{Y}^S - \boldsymbol{\varepsilon}_{Sp}$ relation⁸, which represents a shift of the yield surface. Having $\boldsymbol{\varepsilon}_{Sp}$ symmetric in a simple linear $\mathbf{Y}^S - \boldsymbol{\varepsilon}_{Sp}$ relation, the back-stress tensor \mathbf{Y}^S is also symmetric, and thus, the total effective solid stress tensor $\boldsymbol{\sigma}_E^S$ can additively be split as

$$\boldsymbol{\sigma}_E^S = \bar{\boldsymbol{\sigma}}_E^S + \mathbf{Y}^S. \quad (3.64)$$

Kinematic hardening according to (3.64) can be interpreted geometrically as a translation of the yield locus in the principal stress space $\{\sigma_1, \sigma_2, \sigma_3\}$ to a shifted subspace $\{\bar{\sigma}_1, \bar{\sigma}_2, \bar{\sigma}_3\}$, where both tensors $\boldsymbol{\sigma}_E^S$ and $\bar{\boldsymbol{\sigma}}_E^S$ are symmetric and have the same principal directions.

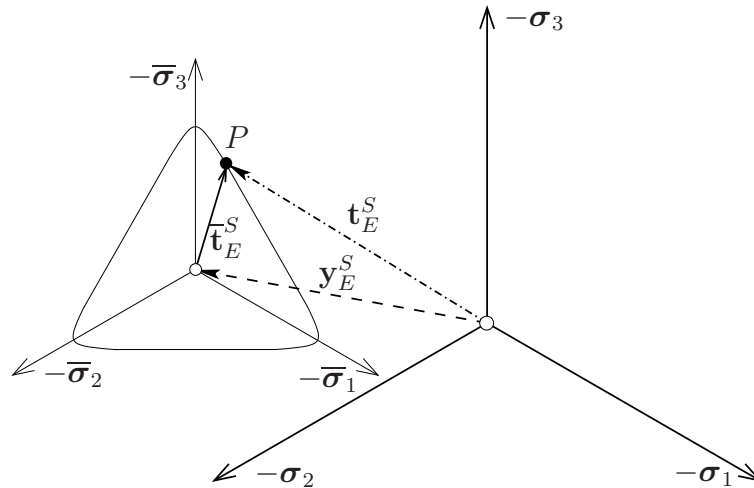


Figure 3.2: Geometrical interpretation of the back-stress in the principal stress space, cf. Brauns [28]

In Figure 3.2, \mathbf{t}_E^S represents the stress state at a point $P(\sigma_1, \sigma_2, \sigma_3)$ of the principal

⁸In the literature, the $\mathbf{Y}^S - \boldsymbol{\varepsilon}_{Sp}$ relation could be linear or nonlinear, rate-dependent or rate-independent, depending on the complexity of the kinematic hardening model, cf. [19].

stress space, whereas $\bar{\mathbf{t}}_E^S$ assigns the same point P in the shifted principal stress subspace as $P(\bar{\boldsymbol{\sigma}}_1, \bar{\boldsymbol{\sigma}}_2, \bar{\boldsymbol{\sigma}}_3)$. The vector \mathbf{y}_E^S (shifting vector) describes the position of the subspace $\{\bar{\boldsymbol{\sigma}}_1, \bar{\boldsymbol{\sigma}}_2, \bar{\boldsymbol{\sigma}}_3\}$ with respect to the original principal stress space.

The yield surface in equation (3.57) can be rewritten in analogy to de Boer & Brauns [19] or Bluhm *et al.* [15] for the case of kinematic hardening as

$$\bar{F}(\bar{\mathbb{I}}_\sigma, \bar{\mathbb{I}}_\sigma^D, \bar{\mathbb{I}}_\sigma^D) = \sqrt{\bar{\mathbb{I}}_\sigma^D \left(1 + \gamma \frac{\bar{\mathbb{I}}_\sigma^D}{(\bar{\mathbb{I}}_\sigma^D)^{3/2}}\right)^m + \frac{1}{2} \alpha \bar{\mathbb{I}}_\sigma^2 + \delta^2 \bar{\mathbb{I}}_\sigma^4 + \beta \bar{\mathbb{I}}_\sigma + \epsilon \bar{\mathbb{I}}_\sigma^2 - \kappa} = 0 \quad (3.65)$$

with $\bar{\mathbb{I}}_\sigma, \bar{\mathbb{I}}_\sigma^D, \bar{\mathbb{I}}_\sigma^D$ being the stress invariants in the shifted principal stress subspace, viz.:

$$\begin{aligned} \bar{\mathbb{I}}_\sigma &= (\boldsymbol{\sigma}_E^S - \mathbf{Y}^S) \cdot \mathbf{I} &= \bar{\boldsymbol{\sigma}}_E^S \cdot \mathbf{I}, \\ \bar{\mathbb{I}}_\sigma^D &= \frac{1}{2} (\boldsymbol{\sigma}_E^S - \mathbf{Y}^S)^D \cdot (\boldsymbol{\sigma}_E^S - \mathbf{Y}^S)^D &= \frac{1}{2} \bar{\boldsymbol{\sigma}}_E^{SD} \cdot \bar{\boldsymbol{\sigma}}_E^{SD}, \\ \bar{\mathbb{I}}_\sigma^D &= \frac{1}{3} (\boldsymbol{\sigma}_E^S - \mathbf{Y}^S)^D \cdot (\boldsymbol{\sigma}_E^S - \mathbf{Y}^S)^D (\boldsymbol{\sigma}_E^S - \mathbf{Y}^S)^D &= \frac{1}{3} \bar{\boldsymbol{\sigma}}_E^{SD} \cdot \bar{\boldsymbol{\sigma}}_E^{SD} \bar{\boldsymbol{\sigma}}_E^{SD}. \end{aligned} \quad (3.66)$$

The values of the material parameters $p_i = \{\beta, \delta, \epsilon, \gamma\}$ are dependent on the dissipative plastic work that defines the isotropic hardening behaviour. For purely kinematic hardening effects, the parameters p_i are taken as constants. Moreover, the plastic potential function in the shifted principal stress subspace is given as

$$\bar{G}(\bar{\mathbb{I}}_\sigma, \bar{\mathbb{I}}_\sigma^D) = \sqrt{\psi_1 \bar{\mathbb{I}}_\sigma^D + \frac{1}{2} \alpha \bar{\mathbb{I}}_\sigma^2 + \delta^2 \bar{\mathbb{I}}_\sigma^4 + \psi_2 \beta \bar{\mathbb{I}}_\sigma + \epsilon \bar{\mathbb{I}}_\sigma^2 - \kappa}. \quad (3.67)$$

Remark: The combination of isotropic and kinematic hardening describes a simultaneous expansion/contraction and a shift of the elastic domain. In the numerical applications in this monograph, only the isotropic hardening effects have been taken into account.

3.3 Bulk Waves in Biphase Poroelastic Media

According to Hadamard [78], acoustic waves in poroelastic continua are assumed to be non-destructive and defined as isolated, non-material surfaces (wave fronts) that move relative to the material constituents. As accelerations but not velocities are considered to be discontinuous across the wave fronts, acoustic waves are also called acceleration waves. For a more detailed discussion, see Hill [88], Wilmański [175] and Mahnkopf [121].

Figure 3.3 illustrates a wave-front surface \mathcal{I} , which divides a domain \mathcal{B} into two subdomains \mathcal{B}^+ and \mathcal{B}^- . Therein, $\mathbf{n}_\mathcal{I}$ is the normal unit vector to \mathcal{I} pointing from \mathcal{B}^- to \mathcal{B}^+ . Assuming that $\mathbf{v}_\mathcal{I}$ is the velocity of \mathcal{I} in the actual configuration, then, the velocity with which the surface \mathcal{I} moves relative to the constituent φ^α and perpendicular to \mathcal{I} is referred to as $\mathbf{w}_{\mathcal{I}\alpha}$ and expressed by

$$\mathbf{w}_{\mathcal{I}\alpha} = w_{\mathcal{I}\alpha} \mathbf{n}_\mathcal{I} \quad \text{with} \quad w_{\mathcal{I}\alpha} := (\mathbf{v}_\mathcal{I} - \mathbf{v}_\alpha) \cdot \mathbf{n}_\mathcal{I}. \quad (3.68)$$

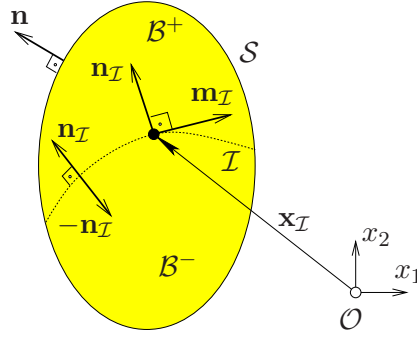


Figure 3.3: Biphase porous body $\mathcal{B} = \mathcal{B}^+ \cup \mathcal{B}^-$ in the actual configuration divided by an immaterial singular surface \mathcal{I}

In this connection, for a scalar-valued field function $\Psi(\mathbf{x}, t)$, which is continuous and sufficiently differentiable over \mathcal{B}^+ and \mathcal{B}^- , the following limits with $\mathbf{x} \in \mathcal{I}$ can be defined:

$$\Psi^+ = \lim_{\varepsilon \rightarrow 0} \Psi(\mathbf{x} + \varepsilon \mathbf{n}_{\mathcal{I}}, t) \quad \text{and} \quad \Psi^- = \lim_{\varepsilon \rightarrow 0} \Psi(\mathbf{x} - \varepsilon \mathbf{n}_{\mathcal{I}}, t), \quad (3.69)$$

where $\varepsilon > 0$ is a small parameter. The jump of Ψ across \mathcal{I} is then given as

$$[[\Psi]] = \Psi^+ - \Psi^-. \quad (3.70)$$

If $[[\Psi]] \neq 0$, a jump exists and the surface \mathcal{I} is called singular with respect to Ψ . Otherwise, it is a jump-free case. The order n of the singular surface is determined by the maximum order m of jump-free spatial derivatives of Ψ via $n = m + 1$, where the order of time derivatives is coupled with that of spatial derivatives. In this work, velocity but not acceleration fields are continuous across \mathcal{I} . Hence, the singular surface is of order two.

Following this, the terms in the balance relations (3.45) for the case of materially incompressible constituents (Section 3.1.4) and linear elastic solid behaviour are tested in regard of their continuity over \mathcal{I} . Starting with the jump-free fields, we have

$$[[\mathbf{v}_\alpha]] = \mathbf{0}, \quad [[p]] = 0, \quad [[\rho^{\alpha R}]] = 0, \quad [[n^\alpha]] = 0. \quad (3.71)$$

Therein, additional to the velocity \mathbf{v}_α and the pore pressure p , the constant material densities $\rho^{\alpha R}$ and the volume fractions n^α are continuous over \mathcal{I} . Unlike the case of a barotropic fluid with $\rho^{FR} = \rho^{FR}(p)$, the pore pressure p is independent of ρ^{FR} in the case of a materially incompressible fluid yielding that $[[\text{grad} p]] = \mathbf{0}$, cf. Kosinski [108].

Next, according to Hadamard's lemma [78], the compatibility condition, and Maxwell's theory for second-order singular surfaces, one finds the following jump expressions:

$$\begin{aligned} [[(\mathbf{v}_\alpha)'_S]] &= (w_{\mathcal{I}\alpha})^2 \boldsymbol{\xi}_\alpha, \\ [[\text{div} \mathbf{v}_\alpha]] &= [[\text{grad} \mathbf{v}_\alpha]] \cdot \mathbf{I} = -w_{\mathcal{I}\alpha} \boldsymbol{\xi}_\alpha \cdot \mathbf{n}_{\mathcal{I}}, \\ [[\text{div} \mathbf{T}_E^S]] &= [[\text{grad} \mathbf{T}_E^S]] \mathbf{I} \\ &= 2\mu^S [[\text{grad} \boldsymbol{\varepsilon}_S]] \mathbf{I} + \lambda^S [[\text{grad}(\boldsymbol{\varepsilon}_S \cdot \mathbf{I})]] \end{aligned} \quad (3.72)$$

with

$$\begin{aligned} \llbracket \text{grad} \boldsymbol{\varepsilon}_S \rrbracket &= \frac{1}{2} (\boldsymbol{\xi}_S \otimes \mathbf{n}_I + \mathbf{n}_I \otimes \boldsymbol{\xi}_S) \otimes \mathbf{n}_I, \\ \llbracket \text{grad}(\boldsymbol{\varepsilon}_S \cdot \mathbf{I}) \rrbracket &= (\mathbf{n}_I \otimes \mathbf{n}_I) \boldsymbol{\xi}_S. \end{aligned} \quad (3.73)$$

Herein, \otimes refers to the dyadic product (tensor product) and $\boldsymbol{\xi}_\alpha$ is an amplitude vector of the discontinuity resulting from the compatibility condition. Following this, applying the continuity condition to the momentum balance of the overall aggregate (3.45)₂ and inserting the resulting jump relations from equations (3.71–3.73) yields

$$\begin{aligned} \rho^S \llbracket (\mathbf{v}_S)'_S \rrbracket + \rho^F \llbracket (\mathbf{v}_F)'_S \rrbracket &= \llbracket \text{div} \mathbf{T}_E^S \rrbracket \\ \longrightarrow \quad & [\rho^S (w_{IS})^2 \mathbf{I} - \mu^S (\mathbf{I} + \mathbf{n}_I \otimes \mathbf{n}_I) - \lambda^S (\mathbf{n}_I \otimes \mathbf{n}_I)] \boldsymbol{\xi}_S + \rho^F (w_{IF})^2 \boldsymbol{\xi}_F = \mathbf{0}. \end{aligned} \quad (3.74)$$

In order to distinguish between the transversal and the longitudinal modes of motion, the rotational and divergence concepts are employed. Therefore, (3.74) is multiplied by the vector \mathbf{m}_I perpendicular to \mathbf{n}_I , i. e. $\mathbf{m}_I \cdot \mathbf{n}_I = 0$, in order to obtain the transversal component of the motion. This yields

$$[\rho^S (w_{IS})^2 - \mu^S] \boldsymbol{\xi}_S \cdot \mathbf{m}_I + \rho^F (w_{IF})^2 \boldsymbol{\xi}_F \cdot \mathbf{m}_I = 0. \quad (3.75)$$

In geomechanical dynamic problems, such as under seismic loading, it is convenient to proceed from moderately small values of k^F associated with negligible relative accelerations of the solid and the fluid, i. e. an insignificant time derivative of the seepage flow in the low frequency range, cf. Zienkiewicz *et al.* [186] and Markert *et al.* [126]. In this case, we may write $\dot{\mathbf{v}}_S \approx \dot{\mathbf{v}}_F$, $w_{IS} \approx w_{IF}$ and $\boldsymbol{\xi}_S \approx \boldsymbol{\xi}_F$. Consequently, relation (3.75) simplifies to

$$[(\rho^S + \rho^F) (w_{IS})^2 - \mu^S] \boldsymbol{\xi}_S \cdot \mathbf{m}_I = 0 \quad (3.76)$$

yielding

$$\boxed{c_s := w_{IS} = \sqrt{\frac{\mu^S}{\rho^S + \rho^F}}} \quad (3.77)$$

as the shear-wave propagation speed.

In analogy, the velocity of the longitudinal waves is obtained by a scalar multiplication of equation (3.74) by a vector \mathbf{n}_I , where $\mathbf{n}_I \cdot \mathbf{n}_I = 1$, yielding

$$[\rho^S (w_{IS})^2 - 2\mu^S - \lambda^S] \boldsymbol{\xi}_S \cdot \mathbf{n}_I + \rho^F (w_{IF})^2 \boldsymbol{\xi}_F \cdot \mathbf{n}_I = 0. \quad (3.78)$$

In the low frequency range with negligible seepage flow acceleration, the pressure-wave speed $c_p := w_{IS} \approx w_{IF}$ can be expressed as

$$\boxed{c_p = \sqrt{\frac{2\mu^S + \lambda^S}{\rho^S + \rho^F}}} \quad (3.79)$$

In this contribution, (3.77) and (3.79) are used in the numerical examples (Section 4) for the treatment of the two modes of wave damping and the application of the viscous damping boundary method.

Remark: For drained porous materials or for complete decoupled motions of the solid and the fluid constituents, ρ^F is taken zero for the calculation of wave speeds in equations (3.77) and (3.79).

In porous materials which are partially saturated or saturated with different fluids, the patterns and behaviours of bulk waves depend on a number of factors, such as the material parameters of the constituents and the frequency of the excitation. In this connection, Steeb *et al.* [160] and Quintal *et al.* [148] studied the attenuation and dispersion of seismic pressure and shear waves at low frequency (1-20 Hz) in partially saturated, double porous materials (e. g. partially saturated rocks). These investigations aimed to find relations between the behaviour of the propagating dynamic waves and the rock-internal oscillations caused by capillary effects. It is found that the compressibility of the interstitial fluids, the oscillations of the fluid bubbles as well as the wave-induced fluid flow in the porous channels play an important role in the attenuation and dispersion of the seismic waves.

Chapter 4:

Numerical Treatment

The following chapter discusses different numerical schemes and challenges that might be faced when implementing the governing sets of coupled balance relations (Section 3.1) to solve initial-boundary-value problems (IBVP). This includes analysis of the Finite Element Method (FEM) for the spatial discretisation, classification of coupled problems depending on the mathematical structure of their governing equations, and discussion of proper time-integration strategies. Additionally, the simulation of bulk wave propagation in unbounded domains is investigated in this chapter.

4.1 Finite Element Method

For the numerical treatment of a given IBVP, the FEM can be implemented in two steps: Firstly, setting the weak or variational statements of the problem's governing equations and, secondly, using the finite element discretisation for the approximate solution of the variational equations. The discussion of the FEM in this section is based on pioneering references such as the works by Hughes [95], Zienkiewicz & Taylor [192] and Brezzi & Fortin [30]. Additionally, for more details about the application of the FEM to porous media problems, the interested reader is referred to the works by, e. g., Ehlers & Ellsiepen [61], Ehlers *et al.* [62], Markert *et al.* [126] and Ellsiepen [66].

4.1.1 Initial-Boundary-Value Problems in Porous Media Dynamics

Mathematically, initial-boundary-value problems are defined in terms of differential equations, which represent the strong or continuous formulations, and additional restraints in time and space. The elements of the strongly formulated IBVP in porous media dynamics with $t \in [0, T]$ (time domain) and $\mathbf{x} \in \Omega$ (spatial domain) can be summarised as follows:

- **Primary variables $\mathbf{u}(\mathbf{x}, t)$:** They represent the major unknowns of the system of equations under investigation. For the different sets of equations in the present treatment, the primary variables can be given as

$$\mathbf{u}_1(\mathbf{x}, t) = \begin{bmatrix} \mathbf{u}_S \\ \mathbf{v}_F \\ p \end{bmatrix}, \quad \mathbf{u}_2(\mathbf{x}, t) = \begin{bmatrix} \mathbf{u}_S \\ \mathbf{w}_F \\ p \end{bmatrix}, \quad \mathbf{u}_3(\mathbf{x}, t) = \begin{bmatrix} \mathbf{u}_S \\ p \end{bmatrix}. \quad (4.1)$$

Herein, \mathbf{u}_1 includes the primary variables for the sets of governing equations uvp (1) and uvp (2) according to the definitions in Section 3.1.4, whereas \mathbf{u}_2 and \mathbf{u}_3 are the primary unknowns for the sets uwp and up, respectively.

- **Secondary variables:** They are considered as functions of the primary variables. Examples of this category are $\mathbf{v}_S(\mathbf{u}_S)$, \mathbf{w}_F , $\boldsymbol{\varepsilon}_S$, $\boldsymbol{\varepsilon}_{Se}$, as well as the deformation-dependent solid volume fraction $n^S(\mathbf{u}_S)$.
- **Balance relations:** These are the different sets of strong equations that have been introduced in Section 3.1.4. They include for the case of materially incompressible solid-fluid aggregates the sets uvp (1), uvp (2), uwp, and up. Additionally, a set of equations is considered for the case of a biphasic hybrid material with materially incompressible solid but compressible fluid constituent.

To convey the different concepts and definitions in a simple case, the basic set of equations (3.40–3.42) is regarded in a linear form. Hence, after neglecting the nonlinear $\text{grad}n^F$ and the convective $(\text{grad}\mathbf{v}_F)\mathbf{w}_F$ terms, the balance equations read:

$$\begin{aligned} \text{solid momentum: } \rho^S (\mathbf{v}_S)'_S &= \text{div}(\mathbf{T}_E^S - n^S p \mathbf{I}) + \rho^S \mathbf{b} + \frac{(n^F)^2 \gamma^{FR}}{k^F} \mathbf{w}_F, \\ \text{fluid momentum: } \rho^F (\mathbf{v}_F)'_S &= -n^F \text{grad} p + \rho^F \mathbf{b} - \frac{(n^F)^2 \gamma^{FR}}{k^F} \mathbf{w}_F, \\ \text{overall volume: } 0 &= \text{div}(n^S \mathbf{v}_S + n^F \mathbf{v}_F). \end{aligned} \quad (4.2)$$

- **Constitutive relations:** As has been discussed in Section 3.2, two types of material behaviour, i. e. linear elastic and nonlinear elasto-viscoplastic, are considered in this monograph:

(1) For the linear elastic case, the *Hookean* elasticity law is used, viz.:

$$\mathbf{T}_E^S := \boldsymbol{\sigma}_E^S(\boldsymbol{\varepsilon}_{Se}) = \boldsymbol{\sigma}_E^S(\mathbf{u}_S). \quad (4.3)$$

(2) For the nonlinear elasto-viscoplastic model with isotropic hardening, the effective solid stress relation can be expressed as

$$\mathbf{T}_E^S := \boldsymbol{\sigma}_E^S(\boldsymbol{\varepsilon}_{Se}) = \boldsymbol{\sigma}_E^S(\boldsymbol{\varepsilon}_S, \boldsymbol{\varepsilon}_{Sp}) = \boldsymbol{\sigma}_E^S(\mathbf{u}_S; \mathbf{q}, p_i) \quad (4.4)$$

with the following evolution relations:

$$\begin{aligned} \text{plastic evolution: } \dot{\boldsymbol{\varepsilon}}_{Sp} &:= (\boldsymbol{\varepsilon}_{Sp})'_S = \Lambda \frac{\partial G}{\partial \boldsymbol{\sigma}_E^S}, \\ \text{viscosity law: } \Lambda &= \frac{1}{\eta_r} \left\langle \frac{F}{\sigma_0} \right\rangle^r, \\ \text{isotropic hardening: } \dot{p}_i &:= (p_i)'_S = h_i \left(\dot{\boldsymbol{\varepsilon}}_{Sp}^V, \|\dot{\boldsymbol{\varepsilon}}_{Sp}^D\| \right). \end{aligned} \quad (4.5)$$

Here, $\mathbf{q} = \begin{bmatrix} \varepsilon_{Sp}^{11} \\ \vdots \\ \Lambda \end{bmatrix}$, $\mathbf{p}_i = \{p_i\} = \begin{bmatrix} \beta \\ \delta \\ \varepsilon \\ \gamma \end{bmatrix}$ represent the internal and the hardening variables, respectively.

For the sake of a simple representation, the linear elastic case is only considered for the discussion of the numerical challenges and solution strategies.

- **Initial conditions** ($t = t_0$, $\mathbf{x} \in \Omega$): To render the pure mechanical IBVP well-posed, initial conditions for the variables \mathbf{u} need to be specified, i. e.,

$$\mathbf{u}(\mathbf{x}, t_0) = \mathbf{u}_0(\mathbf{x}). \quad (4.6)$$

- **Boundary conditions** ($t \in [0, T]$, $\mathbf{x} \in \Gamma$): In boundary-value problems, the surface $\Gamma = \partial\Omega$ is split into *Dirichlet* (essential) and *Neumann* (natural) boundaries allowing for the application of the different external boundary conditions. In particular, these boundaries for the given set of equations (4.2) can be defined in general form as follows:

<i>Dirichlet</i>	<i>Neumann</i>	
$\mathbf{u}_S(\mathbf{x}, t) = \bar{\mathbf{u}}_S(\mathbf{x}, t) \quad \mathbf{x} \in \Gamma_{\mathbf{u}_S}$	$\mathbf{t}^S(\mathbf{x}, t) = \bar{\mathbf{t}}^S(\mathbf{x}, t) = \mathbf{T}^S \mathbf{n} \quad \mathbf{x} \in \Gamma_{\mathbf{t}^S}$	(4.7)
$\mathbf{v}_F(\mathbf{x}, t) = \bar{\mathbf{v}}_F(\mathbf{x}, t) \quad \mathbf{x} \in \Gamma_{\mathbf{v}_F}$	$\mathbf{t}^F(\mathbf{x}, t) = \bar{\mathbf{t}}^F(\mathbf{x}, t) = -n^F p \mathbf{n} \quad \mathbf{x} \in \Gamma_{\mathbf{t}^F}$	
$p(\mathbf{x}, t) = \bar{p}(\mathbf{x}, t) \quad \mathbf{x} \in \Gamma_p$	$v(\mathbf{x}, t) = \bar{v}(\mathbf{x}, t) = n^F \mathbf{w}_F \cdot \mathbf{n} \quad \mathbf{x} \in \Gamma_v$	

Moreover, the boundaries should fulfil the following restrictions:

$$\Gamma = \Gamma_{\mathbf{u}_S} \cup \Gamma_{\mathbf{t}^S} \quad \text{and} \quad \Gamma_{\mathbf{u}_S} \cap \Gamma_{\mathbf{t}^S} = \emptyset \quad : \text{solid momentum balance (4.2)}_1,$$

$$\Gamma = \Gamma_{\mathbf{v}_F} \cup \Gamma_{\mathbf{t}^F} \quad \text{and} \quad \Gamma_{\mathbf{v}_F} \cap \Gamma_{\mathbf{t}^F} = \emptyset \quad : \text{fluid momentum balance (4.2)}_2,$$

$$\Gamma = \Gamma_p \cup \Gamma_v \quad \text{and} \quad \Gamma_p \cap \Gamma_v = \emptyset \quad : \text{overall aggregate volume balance (4.2)}_3.$$

In relations (4.7), $\mathbf{T}^S = \mathbf{T}_E^S - n^S p \mathbf{I}$ defines the solid total stress, $\bar{\mathbf{t}}^S$ and $\bar{\mathbf{t}}^F$ are the external solid and fluid loading vectors acting on the *Neumann* boundaries with outward-oriented unit surface normal \mathbf{n} , and \bar{v} denotes the volume efflux of the incompressible fluid draining through the *Neumann* boundary Γ_v of the overall body. The relation $\bar{\mathbf{t}} = \bar{\mathbf{t}}^S + \bar{\mathbf{t}}^F$ might be used in case of surface tractions $\bar{\mathbf{t}}$ acting on the undrained boundary of the whole body (solid and fluid), whereas for drained boundary the relation $\bar{\mathbf{t}} = \bar{\mathbf{t}}^S$ is spontaneously obtained. If the momentum balance of the overall aggregate is used instead of the solid momentum balance in equation (4.2)₁, the term $\bar{\mathbf{t}}$ appears automatically, which is convenient when monolithic time integration schemes are considered. However, a simple implementation of splitting solution schemes requires that the solid momentum balance is used instead of the overall momentum balance. Thus, the relation $\bar{\mathbf{t}}^S = \bar{\mathbf{t}} - \bar{\mathbf{t}}^F$ can be substituted noting that $\bar{\mathbf{t}}^F = \bar{\mathbf{t}}^F(\mathbf{u}_S, p)$ represents an implicit boundary term, which depends on the solution of the coupled problem.

An analytical solution of the coupled equations is very difficult if not impossible to get, especially for multi-dimensional problems. Therefore, the main concern in the following is to develop numerical schemes for approximate solutions.

4.1.2 Governing Weak Formulations

To define the weak (variational) counterpart of the strong balance equations, a class of independent trial functions¹ needs to be specified. Applying the method of weighted residuals within the principle of virtual work (PVW), the trial functions are multiplied by the balance relations and integrated over the spatial domain Ω in order to get energy-like variational statements. Additionally, the product rule and the *Gaussian Divergence Theorem* (Section 2.3) are applied in order to designate the boundary integrals. Following this, the weak forms of equations (4.2) can be written as

$$\mathcal{G}_{(\mathbf{v}_S)}(\delta \mathbf{u}_S, \mathbf{u}_S, \mathbf{v}_S) \equiv \int_{\Omega} \delta \mathbf{u}_S \cdot [(\mathbf{u}_S)'_S - \mathbf{v}_S] dv = 0, \quad (4.8)$$

$$\begin{aligned} \mathcal{G}_{\mathbf{u}_S}(\delta \mathbf{u}_S, \mathbf{u}_S, \mathbf{v}_S, \mathbf{v}_F, p) &\equiv \int_{\Omega} \text{grad} \delta \mathbf{u}_S \cdot (\mathbf{T}_E^S - n^S p \mathbf{I}) dv - \int_{\Gamma_{\mathbf{t}^S}} \delta \mathbf{u}_S \cdot \bar{\mathbf{t}}^S da + \\ &+ \int_{\Omega} \delta \mathbf{u}_S \cdot \left\{ n^S \rho^{SR} [(\mathbf{v}_S)'_S - \mathbf{b}] - \frac{(n^F)^2 \gamma^{FR}}{k^F} (\mathbf{v}_F - \mathbf{v}_S) \right\} dv = 0, \end{aligned} \quad (4.9)$$

$$\begin{aligned} \mathcal{G}_{\mathbf{v}_F}(\delta \mathbf{v}_F, \mathbf{u}_S, \mathbf{v}_S, \mathbf{v}_F, p) &\equiv - \int_{\Omega} \text{div} \delta \mathbf{v}_F n^F p dv - \int_{\Gamma_{\mathbf{t}^F}} \delta \mathbf{v}_F \cdot \bar{\mathbf{t}}^F da + \\ &+ \int_{\Omega} \delta \mathbf{v}_F \cdot \left\{ n^F \rho^{FR} [(\mathbf{v}_F)'_S - \mathbf{b} + \left(\frac{n^F g}{k^F} \mathbf{I} \right) (\mathbf{v}_F - \mathbf{v}_S)] \right\} dv = 0, \end{aligned} \quad (4.10)$$

$$\mathcal{G}_p(\delta p, \mathbf{v}_S, \mathbf{v}_F) \equiv \int_{\Omega} \delta p \text{div} \mathbf{v}_S dv - \int_{\Omega} \text{grad} \delta p \cdot n^F (\mathbf{v}_F - \mathbf{v}_S) dv + \int_{\Gamma_v} \delta p \bar{v} da = 0. \quad (4.11)$$

Herein, the relation $\mathbf{v}_S = (\mathbf{u}_S)'_S$ has been additionally used to reduce the order of the global set of differential equations into first-order in time. Moreover, $\delta \mathbf{u}_S$, $\delta \mathbf{v}_F$, and δp are the weight functions, which correspond to the primary variables \mathbf{u}_S , \mathbf{v}_F , and p , respectively.

For the sake of a simpler representation, the weak formulations (4.8–4.11) are summarised in a function vector $\mathcal{G}_{\mathbf{u}}$ and the unknown field variables are collected in a vector of unknowns $\mathbf{u} = \mathbf{u}(\mathbf{x}, t)$ yielding

$$\mathcal{G}_{\mathbf{u}} = \begin{bmatrix} \mathcal{G}_{(\mathbf{v}_S)} \\ \mathcal{G}_{\mathbf{u}_S} \\ \mathcal{G}_{\mathbf{v}_F} \\ \mathcal{G}_p \end{bmatrix}, \quad \mathbf{u} = \begin{bmatrix} \mathbf{u}_S \\ \mathbf{v}_S \\ \mathbf{v}_F \\ p \end{bmatrix}, \quad \delta \mathbf{u} = \begin{bmatrix} \delta \mathbf{u}_S \\ \delta \mathbf{v}_F \\ \delta p \end{bmatrix}, \quad (\mathbf{u})'_S = \begin{bmatrix} (\mathbf{u}_S)'_S \\ (\mathbf{v}_S)'_S \\ (\mathbf{v}_F)'_S \\ (p)'_S \end{bmatrix}, \quad \mathbf{u}_0 = \begin{bmatrix} \mathbf{u}_{S0} \\ \mathbf{v}_{S0} \\ \mathbf{v}_{F0} \\ p_0 \end{bmatrix}. \quad (4.12)$$

¹In the context of variational formulation, weight (or test) functions can be looked upon as variations of the real primary fields \mathbf{u} (Ramm [149]). In mathematics, the test functions are introduced in the sense of *Lagrangean* multipliers allowing for a physical interpretation. Moreover, as the test functions represent possible solutions, they are required to vanish at *Dirichlet* boundaries (Hughes [95])

Here, $\delta \mathbf{u}$ additionally represents the vector of test functions, $(\mathbf{u})'_S$ is the time derivative of the vector of unknowns following the solid motion, and $\mathbf{u}_0 = \mathbf{u}(\mathbf{x}, t_0)$ corresponds to the initial values of \mathbf{u} , cf. Markert *et al.* [126] for details.

Following this, the three-field variational problem (4.8–4.11) for linear elastic solid behaviour can be rewritten in an abstract form as

$$\boxed{\text{Find } \mathbf{u} \in \mathcal{S}_u(t) \text{ such that } \mathcal{G}_u(\delta \mathbf{u}, \mathbf{u}) = \mathbf{0} \quad \forall \delta \mathbf{u} \in \mathcal{T}_u, t \in [t_0, T].} \quad (4.13)$$

Herein, $\mathcal{S}_u(t)$ is the trial space for the external variables \mathbf{u} , and \mathcal{T}_u is the test space for the corresponding test functions $\delta \mathbf{u}$. For the case of the elasto-viscoplastic constitutive model, \mathcal{G}_u depends additionally on \mathbf{q} and \mathbf{p}_i , which enter the weak form indirectly via the solid effective stress, i. e. $\mathcal{G}_u(\delta \mathbf{u}, \mathbf{u}; \mathbf{q}, \mathbf{p}_i) = \mathbf{0}$. Moreover, the viscoplastic and isotropic hardening relations (4.5) are strongly fulfilled collected in a local residuum vector as

$$\mathcal{L}_q(\mathbf{q}, \mathbf{p}_i, \mathbf{u}) = \mathbf{A} \begin{bmatrix} \dot{\mathbf{q}} \\ \dot{\mathbf{p}} \end{bmatrix} - \mathbf{r}(\mathbf{q}, \mathbf{p}_i, \mathbf{u}) = \begin{bmatrix} \dot{\boldsymbol{\varepsilon}}_{Sp} \\ 0 \\ \dot{\mathbf{p}}_i \end{bmatrix} - \begin{bmatrix} \Lambda \frac{\partial G}{\partial \boldsymbol{\sigma}_E^S} \\ \Lambda - \frac{1}{\eta_r} \left\langle \frac{F}{\sigma_0} \right\rangle^r \\ \mathbf{h}_i(\dot{\boldsymbol{\varepsilon}}_{Sp}^V, \|\dot{\boldsymbol{\varepsilon}}_{Sp}^D\|) \end{bmatrix} = \mathbf{0} \quad (4.14)$$

with \mathbf{A} being an identity matrix and the vector \mathbf{r} containing the non-differential terms of the local equations, cf., e. g., Scholz [155] for more details.

4.1.3 Spatial Discretisation

The numerical implementation of the FEM requires the transfer of the continuous variational problem (4.13) into a discrete one. Therefore, the continuous spatial domain Ω occupied by the overall body \mathcal{B} is subdivided into N_e finite elements yielding an approximate discrete domain Ω^h . This results in a FE mesh with N_x nodes for the geometry approximation and discrete trial and test functions defined as

$$\begin{aligned} \mathbf{u}^h(\mathbf{x}, t) &= \bar{\mathbf{u}}^h(\mathbf{x}, t) + \sum_{i=1}^{N_u} \mathbf{N}_{u(i)}(\mathbf{x}) \mathbf{u}_{(i)}(t) \in \mathcal{S}_u^h(t), \\ \delta \mathbf{u}^h(\mathbf{x}) &= \sum_{i=1}^{M_u} \mathbf{M}_{u(i)}(\mathbf{x}) \delta \mathbf{u}_{(i)} \in \mathcal{T}_u^h. \end{aligned} \quad (4.15)$$

Herein, $\bar{\mathbf{u}}^h$ represents the approximated *Dirichlet* boundary conditions of the considered problem, N_u is the number of FE nodes used for the approximation of the unknown fields in \mathbf{u} , $\mathbf{N}_{u(i)}$ denotes the space-dependent global basis functions at node i , and $\mathbf{u}_{(i)}$ represents the time-dependent nodal coefficients. Moreover, M_u is the number of FE nodes used for the test functions in $\delta \mathbf{u}$, $\mathbf{M}_{u(i)}$ denotes the corresponding global basis functions, and $\delta \mathbf{u}_{(i)}$ represents the nodal values of the test functions. Furthermore, $\mathcal{S}_u^h(t)$

and \mathcal{T}_u^h are the discrete, finite-dimensional trial and test spaces. In this context, the *Bubnov-Galerkin* procedure² is applied using the same basis functions $\mathbf{N}_{u(i)} \equiv \mathbf{M}_{u(i)}$ for the approximation of \mathbf{u} and $\delta\mathbf{u}$. In this case, the trial and test spaces coincide except for a shift through the *Dirichlet* boundary conditions, i. e., $\mathcal{S}_u^h(t) = \bar{\mathbf{u}}^h + \mathcal{T}_u^h$.

Following this, the semi-discrete FE-*Galerkin* formulation of the variational problem (4.13) in the course of the FE discretisation with linear elastic solid behaviour reads:

$$\boxed{\text{Find } \mathbf{u}^h \in \mathcal{S}_u^h(t) \text{ such that } \mathcal{G}_u^h(\delta\mathbf{u}^h, \mathbf{u}^h) = \mathbf{0} \quad \forall \delta\mathbf{u}^h \in \mathcal{T}_u^h, t \in [t_0, T].} \quad (4.16)$$

For an elasto-viscoplastic solid material model with isotropic hardening, the semi-discrete problem takes the form

$$\mathcal{G}_u^h(\delta\mathbf{u}^h, \mathbf{u}^h; \mathbf{q}^h, \mathbf{p}_i^h) = \mathbf{0} \quad (4.17)$$

with the discrete local system of equations

$$\mathcal{L}_q^h(\mathbf{q}^h, \mathbf{p}_i^h, \mathbf{u}^h) = \mathbf{0}. \quad (4.18)$$

Here, \mathbf{q}^h and \mathbf{p}_i^h additionally represent the internal and the hardening variables in the discrete space. Such variables need to be calculated at the integration points of the numerical quadrature.

Geometry Transformation and Numerical Integration

Geometry mapping approaches provide a simple strategy to perform integration of the weak formulation over finite elements with random geometry (i. e. finite elements with arbitrary dimensions or curved boundaries). Basically, the mapping can be performed in three steps (Ramm [149]):

- (1) A standard finite element with simple geometry is chosen in the parameter space with orthogonal coordinates $\boldsymbol{\xi} := \{\xi_i\} = \{\xi_1, \xi_2, \dots\}^T$, where the relation $-1 \leq \xi_i \leq +1$ is satisfied over the element (cf. Figure 4.1, left).
- (2) The integrations and derivatives are performed in the parameter space over ξ_i .
- (3) Geometrical mapping between the parameter space and the real space is defined, cf. Figure 4.1.

In this regard, one distinguishes between the *isoparametric* case, where the shape functions of the geometry transfer and the ansatz functions of the approximate solution are equal, and the *super-parametric* approach, where the geometry shape functions are of higher order.

The global coordinates $\mathbf{x} := \{x_i\} = \{x_1, x_2, \dots\}^T$ of any point of a finite element are interpolated from the element nodal coordinates in a similar way as for the discrete primary variables interpolation (equation (4.15)). In particular, the geometry mapping

²Unlike *Bubnov-Galerkin* another approach known in literature as *Petrov-Galerkin* considers different interpolation functions for the primary variables and the test functions.

To complete the spatial discretisation procedure, the discrete variables and test functions are specified by choosing appropriate mixed finite element formulations. However, the suitable choice in regard to accuracy and stability depends also on the applied time-stepping algorithm and will, therefore, be discussed in the subsequent sections. In Figure 4.1, an example of the mixed FEM, which is usually suitable for monolithic time-integration schemes, is introduced. For additional particulars on the mixed FE treatment, the reader is referred to the works by Arnold [3], Brezzi & Fortin [30] and Gresho & Sani [75] among others.

Infinite Element Discretisation

For the simulation of wave propagation in unbounded half spaces the usual engineering approach of domain truncation into a finite near field, and an infinite far field is followed in this work. Herein, the FEM is applied to the resulting finite domain and coupled with infinite elements at the truncated infinite boundaries. The applicability of the finite element – infinite element coupling together with the viscous damping boundary approach (VDB) to model the far-field response is discussed in Section 4.4 and assessed by the solutions of one- and two-dimensional problems in Chapter 6.

Following this, a class of quasi-static, mapped infinite elements (IE) is applied, cf. Marques & Owen [127]. Here, one distinguishes between the ansatz functions for the geometry modelling $\mathbf{M}_{\text{inf}(i)}$ (mapping functions), which are multiplied by decay functions in order to extend to infinity and cover the unbounded domain (interpolation from the parameter space ξ_i to the real space x_i), and the shape functions for the primary variables $\mathbf{N}_{\text{inf}(i)}$, which are treated similarly to the FE shape functions ($\mathbf{N}_{\text{inf}(i)} = \mathbf{N}_{\mathbf{u}(i)}$). The significant advantage of using this type of IE treatment is that it leads to integrals over unity elements in the parameter space, on which the Gauß quadrature rule can directly be applied. This entails only minor modifications when using common FE softwares for the numerical treatment, cf. Ehlers *et al.* [62] for exemplary applications.

To illustrate the basic ideas behind the geometry mapping between an infinite real space and a finite parameter space, a one-dimensional infinite element is introduced, cf. Figure 4.2. Therein, an element that extends in the real space from a point ① through ② to a point ③ in the infinity is mapped onto a unity element in the parameter space with natural coordinates that satisfy $-1 \leq \xi_i \leq +1$. The geometry interpolation from the parameter to the real space can be performed following the FE scheme. For instance, the mapping relations in the one-dimensional treatment read

$$x(\xi) = \sum_{i=1}^2 \mathbf{M}_{\text{inf}(i)}(\xi) \bar{x}_{(i)}(t) \quad \text{with} \quad \begin{cases} \mathbf{M}_{\text{inf}(1)} = -2\xi/(1 - \xi), \\ \mathbf{M}_{\text{inf}(2)} = (1 + \xi)/(1 - \xi), \end{cases} \quad (4.23)$$

where $\bar{x}_{(i)}$ represents the nodal coordinates. In (4.23), $\boldsymbol{\xi} = \{-1, 0, +1\}^T$ corresponds to $\mathbf{x} = \{x_1, x_2, \infty\}^T$, and thus, the term $1/(1 - \xi)$ can be interpreted as a decay function. Moreover, the shape functions always satisfy the relation $\mathbf{M}_{\text{inf}(1)} + \mathbf{M}_{\text{inf}(2)} = 1$. For a given field variable (e.g. u) in the one-dimensional problem, the following standard FE

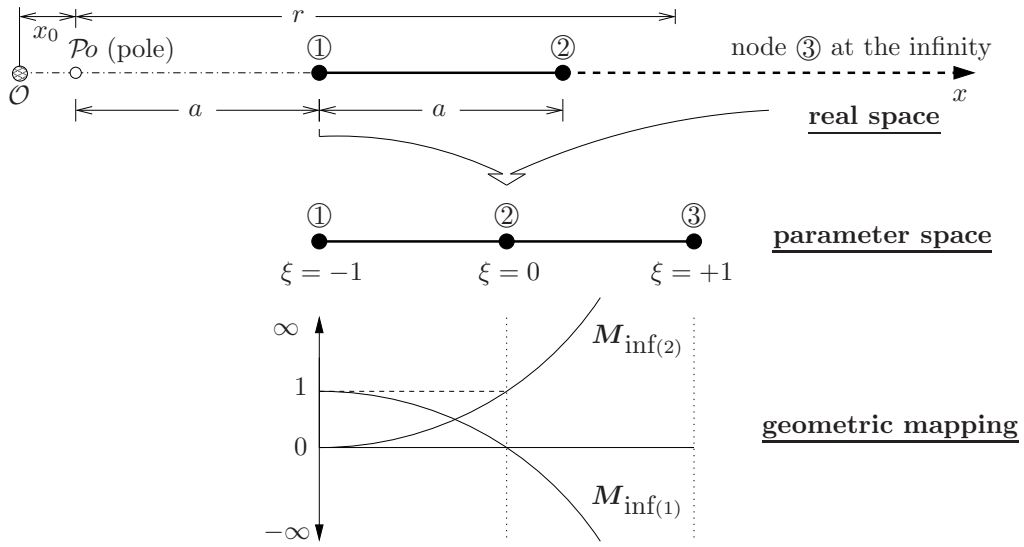


Figure 4.2: Illustration of a one-dimensional infinite element in the real and the parameter space and its geometric mapping functions

interpolation relation can be used:

$$u(\xi) = \sum_{i=1}^3 \mathbf{N}_{u(i)}(\xi) \bar{u}_{(i)}(t) \quad \text{with} \quad \begin{cases} \mathbf{N}_{u(1)} = \frac{1}{2}\xi/(\xi - 1), \\ \mathbf{N}_{u(2)} = (1 - \xi^2), \\ \mathbf{N}_{u(3)} = \frac{1}{2}\xi/(\xi + 1), \end{cases} \quad (4.24)$$

where $\bar{u}_{(i)}$ represents the nodal values. Equation (4.24)₁ can be reformulated by inserting the relation $\xi = 1 - 2a/r$ that results from the reformulation of (4.23) yielding

$$u(r) = \bar{u}_{(3)} + (-\bar{u}_{(1)} + 4\bar{u}_{(2)} - 3\bar{u}_{(3)}) \frac{a}{r} + (2\bar{u}_{(1)} - 4\bar{u}_{(2)} + 2\bar{u}_{(3)}) \frac{a^2}{r^2}. \quad (4.25)$$

Here, r refers to the distance from the pole $\mathcal{P}o$ to a general point within the element and $a = x_2 - x_1$ remarks the infinite element extension (or pole position) as shown in Figure 4.2, top. In (4.25), u attains the values $\{\bar{u}_{(1)}, \bar{u}_{(2)}, \bar{u}_{(3)}\}$ for $r \rightarrow \{a, 2a, \infty\}$, respectively. Moreover, the accuracy of the solution depends on the order of the interpolation functions $\mathbf{N}_{u(i)}$ as well as the position of the pole $\mathcal{P}o$. In this connection, a very small a ($a \rightarrow 0$) leads to an indeterminate case, i. e., $a/r \rightarrow 0/0$, which highlights the role of the pole position (or infinite element extension) in the solution accuracy.

In the current work, two types of singly mapped infinite elements, which extend to infinity in one direction, are implemented [127]. They correspond to linear and quadratic ansatz functions: *5-node isoparametric infinite elements* that utilise five of the shape functions of the 8-node mixed FE and for which five mapping functions $\mathbf{M}_{\text{inf}(i)}$ are derived. *4-node isoparametric infinite elements* that originate from the 6-node Lagrangian FE (linear in ξ_1 and quadratic in ξ_2) with two nodes corresponding to $\xi_2 = +1$ positioned in the infinity (cf. Figure 4.3).

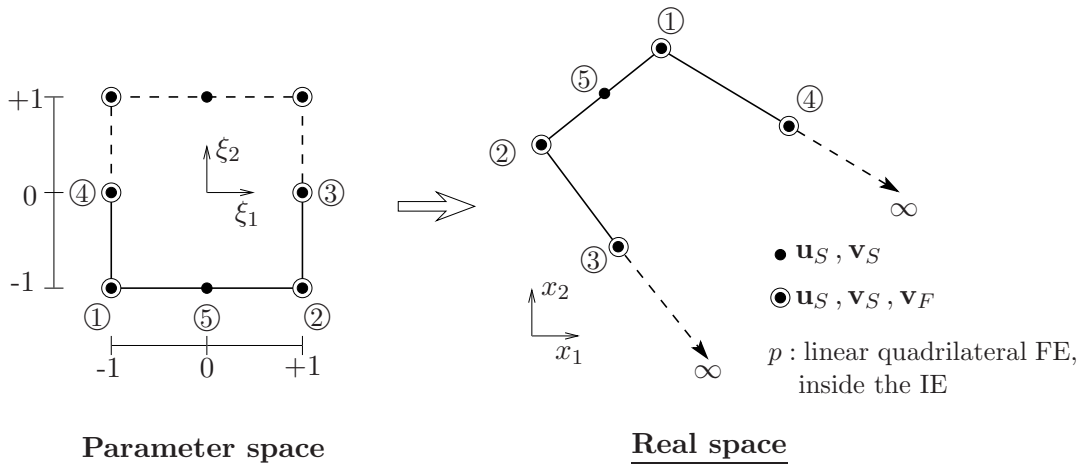


Figure 4.3: Geometric mapping of quadrilateral infinite elements

The infinite elements are assigned to the variables which are defined zero in the infinity, i. e. \mathbf{u}_S , \mathbf{v}_S , and \mathbf{v}_F . For instance, when the mixed FEM is used for the spatial discretisation of the finite domain with quadratic interpolation for \mathbf{u}_S and \mathbf{v}_S , and linear ansatz functions for \mathbf{v}_F and p , the 5-node IE is assigned to \mathbf{u}_S and \mathbf{v}_S , and the 4-node IE is applied to \mathbf{v}_F in the infinite domain. The pore pressure p can be interpolated by quadrilateral linear FE within the infinite element structure as p is not supposed to be zero in the infinity for a materially incompressible biphasic medium. Moreover, such a choice of elements guarantees the continuity across the FE-IE interface.

Additional information and applications of infinite elements can be found in the works by Marques & Owen [127], Heider *et al.* [86, 87] and Wunderlich *et al.* [182].

4.2 The Strongly Coupled Problem of Porous Media Dynamics

In what follows, the space-discrete problem of porous media dynamics (4.16) is analysed with regard to the mathematical structure and the applicable time-discretisation schemes. Such problems belong to the class of strongly coupled systems with interacting solid and fluid subsystems. Hence, they can be represented by coupled formulations with dependent field variables, which cannot be eliminated on the equation level. Therefore, an independent solution of any individual subsystem demands a simultaneous treatment of the other subsystems. For more details about definitions and classification of coupled problems, it is referred to the works by Felippa *et al.* [70], Hameyer *et al.* [81], Matthies & Steindorf [130, 130], Zienkiewicz & Taylor [192] and Markert [125] among others. Following this, abstract settings of coupled problems are introduced following the definitions in the work by Matthies & Steindorf [130] or Matthies *et al.* [129]. Moreover, in order to convey the ideas in a simple way and make the inherent coupling clear, the space-discrete coupled systems are written in descriptive matrix form. Therefore, the following abbreviations for

the approximate fields and the related quantities are introduced:

$$\mathbf{u}^h = \begin{bmatrix} \mathbf{U} \mathbf{u}_S \\ \mathbf{U} \mathbf{v}_S \\ \mathbf{V} \mathbf{v}_F \\ \mathbf{P} \mathbf{p} \end{bmatrix}, \quad (\mathbf{u}^h)'_S = \begin{bmatrix} \mathbf{U} \dot{\mathbf{u}}_S \\ \mathbf{U} \dot{\mathbf{v}}_S \\ \mathbf{V} \dot{\mathbf{v}}_F \\ \mathbf{P} \dot{\mathbf{p}} \end{bmatrix}, \quad \text{grad} \mathbf{u}^h = \begin{bmatrix} \nabla \mathbf{U} \mathbf{u}_S \\ \nabla \mathbf{U} \mathbf{v}_S \\ \nabla \mathbf{V} \mathbf{v}_F \\ \nabla \mathbf{P} \mathbf{p} \end{bmatrix}, \quad (4.26)$$

$$\delta \mathbf{u}^h = \begin{bmatrix} \mathbf{U} \delta \mathbf{u}_S \\ \mathbf{V} \delta \mathbf{v}_F \\ \mathbf{P} \delta \mathbf{p} \end{bmatrix}, \quad \text{grad} \delta \mathbf{u}^h = \begin{bmatrix} \nabla \mathbf{U} \delta \mathbf{u}_S \\ \nabla \mathbf{V} \delta \mathbf{v}_F \\ \nabla \mathbf{P} \delta \mathbf{p} \end{bmatrix}.$$

Herein, $\mathbf{U}, \mathbf{V}, \mathbf{P}$ represent the interpolation functions corresponding to the nodal unknowns of the FE mesh $\mathbf{u}_S, \mathbf{v}_S = \dot{\mathbf{u}}_S, \mathbf{v}_F$ ³, and \mathbf{p} with the related test functions $\delta \mathbf{u}_S, \delta \mathbf{v}_F$, and $\delta \mathbf{p}$. Additionally, the time derivative and divergence operator are defined, respectively, as $(\cdot)' := (\cdot)'_S$ and $\nabla(\cdot) := \text{grad}(\cdot)$. In equation (4.15), the Dirichlet boundary conditions $\bar{\mathbf{u}}^h$ are explicitly fulfilled during the assembling of the FE system and need not to be considered in the sequel.

4.2.1 Pure Differential Coupling

When a time evolution for all the primary variables of the balance relations exists, then the coupled system consists of pure differential equations. An example for this type of coupling is the case of the biphasic hybrid model with a materially incompressible solid but a compressible fluid constituent, cf. Section 3.1.3. Herein, the space-discrete coupled equations can be expressed in a matrix form as

$$\mathcal{G}_u^h = \underbrace{\begin{bmatrix} \mathbf{I} & \mathbf{0} & \mathbf{0} & \mathbf{0} \\ \mathbf{0} & \mathbf{M}_{22} & \mathbf{M}_{23} & \mathbf{0} \\ \mathbf{0} & \mathbf{0} & \mathbf{M}_{33} & \mathbf{0} \\ \mathbf{0} & \mathbf{0} & \mathbf{M}_{43} & \mathbf{M}_{44} \end{bmatrix}}_{\mathbf{M}} \underbrace{\begin{bmatrix} \dot{\mathbf{u}}_S \\ \dot{\mathbf{v}}_S \\ \dot{\mathbf{v}}_F \\ \dot{\mathbf{p}} \end{bmatrix}}_{\dot{\mathbf{y}}} + \underbrace{\begin{bmatrix} \mathbf{0} & -\mathbf{I} & \mathbf{0} & \mathbf{0} \\ \mathbf{K}_{21} & \mathbf{0} & \mathbf{0} & \mathbf{K}_{24} \\ \mathbf{0} & \mathbf{K}_{32} & \mathbf{K}_{33} & \mathbf{K}_{34} \\ \mathbf{0} & \mathbf{K}_{42} & \mathbf{0} & \mathbf{K}_{44} \end{bmatrix}}_{\mathbf{K}} \underbrace{\begin{bmatrix} \mathbf{u}_S \\ \mathbf{v}_S \\ \mathbf{v}_F \\ \mathbf{p} \end{bmatrix}}_{\mathbf{y}} - \underbrace{\begin{bmatrix} \mathbf{0} \\ \mathbf{b}_2 + \mathbf{f}_S \\ \mathbf{b}_3 + \mathbf{f}_F \\ \mathbf{b}_4 + \mathbf{f}_p \end{bmatrix}}_{\mathbf{f}} = \mathbf{0}. \quad (4.27)$$

In (4.27), the 2nd and 3rd rows result from the ‘convectiveless’ overall and fluid momentum balances, given in (3.45)_{2,3}, respectively. The 4th row results from the spatial discretisation of the overall mass balance (3.47). The mass and stiffness submatrices $\mathbf{M}_{ij}, \mathbf{K}_{ij}$ can be easily classified into off-diagonal coupling (highlighted) and diagonal non-coupling terms

³If \mathbf{w}_F is used as a primary variable instead of \mathbf{v}_F , then additionally we have $\mathbf{w}_F = \mathbf{V} \mathbf{w}_F$.

($i = j$). In detail, the mass submatrices are given as

$$\begin{aligned} \mathbf{M}_{22} &= \int_{\Omega^h} \mathbf{U}^T \rho^S \mathbf{U} \, dv, & \mathbf{M}_{23} &= \int_{\Omega^h} \mathbf{U}^T \rho^F \mathbf{V} \, dv, & \mathbf{M}_{33} &= \int_{\Omega^h} \mathbf{V}^T \rho^F \mathbf{V} \, dv, \\ \mathbf{M}_{43} &= \int_{\Omega^h} \nabla \mathbf{P}^T \rho^{FR} \frac{k^F}{g} \mathbf{V} \, dv, & \mathbf{M}_{44} &= \int_{\Omega^h} \mathbf{P}^T n^F h_{pt} \mathbf{P} \, dv. \end{aligned} \quad (4.28)$$

Here, for compressible fluid behaviour, the pressure-dependent fluid material density $\rho^{FR}(p)$ in (3.39) can explicitly be expressed in terms of the pore-fluid pressure as $\rho^{FR}(p) = h_p p$, and the time derivative of $\rho^{FR}(p)$ can be written for simplicity as $(\rho^{FR}(p))'_S = h_{pt}(p)'_S$, where h_p and h_{pt} ⁴ can be understood as the compressibility parameters of the pore fluid. Following this, the stiffness submatrices can be written as

$$\begin{aligned} \mathbf{K}_{21} &= \int_{\Omega^h} \nabla \mathbf{U}^T \mathcal{D}_e \nabla \mathbf{U} \, dv, & \mathbf{K}_{24} &= - \int_{\Omega^h} \nabla \mathbf{U}^T \mathbf{P} \, dv, \\ \mathbf{K}_{32} &= - \int_{\Omega^h} \mathbf{V}^T \frac{(n^F)^2 \gamma^{FR}}{k^F} \mathbf{U} \, dv, & \mathbf{K}_{33} &= \int_{\Omega^h} \mathbf{V}^T \frac{(n^F)^2 \gamma^{FR}}{k^F} \mathbf{V} \, dv, \\ \mathbf{K}_{34} &= - \int_{\Omega^h} \nabla \mathbf{V}^T n^F \mathbf{P} \, dv, & \mathbf{K}_{42} &= \int_{\Omega^h} \mathbf{P}^T \rho^{FR} \nabla \mathbf{U} \, dv, \\ \mathbf{K}_{44} &= \int_{\Omega^h} \nabla \mathbf{P}^T \frac{k^F}{g} \nabla \mathbf{P} \, dv + \int_{\Omega^h} \mathbf{P}^T h_p \operatorname{div} \mathbf{v}_S^h \mathbf{P} \, dv - \int_{\Omega^h} \nabla \mathbf{P}^T \frac{h_p k^F}{g} \dot{\mathbf{v}}_F^h \mathbf{P} \, dv. \end{aligned} \quad (4.29)$$

Herein, $\mathcal{D}_e = \mathcal{D}_e(\mu^S, \lambda^S)$ represents the elasticity matrix for the linear elastic treatment, $\mathbf{v}_S^h := \mathbf{U} \bar{\mathbf{v}}_S$ and $\mathbf{v}_F^h := \mathbf{V} \bar{\mathbf{v}}_F$ are known values of the solid and the fluid velocities.

For the sake of completeness, the space-discrete Neumann boundary terms \mathbf{f}_S , \mathbf{f}_F , \mathbf{f}_p and the body-force vectors \mathbf{b}_2 , \mathbf{b}_3 , \mathbf{b}_4 can be expressed as

$$\begin{aligned} \mathbf{f}_S &= \int_{\Gamma_{\mathbf{t}^S}^h} \mathbf{U}^T \bar{\mathbf{t}} \, da, & \mathbf{f}_F &= \int_{\Gamma_{\mathbf{t}^F}^h} \mathbf{V}^T \bar{\mathbf{t}}^F \, da, & \mathbf{f}_p &= - \int_{\Gamma_{\bar{v}_c}^h} \mathbf{P}^T \bar{v}_c \, da, \\ \mathbf{b}_2 &= \int_{\Omega^h} \mathbf{U}^T \rho^S \mathbf{b} \, dv, & \mathbf{b}_3 &= \int_{\Omega^h} \mathbf{V}^T \rho^F \mathbf{b} \, dv, & \mathbf{b}_4 &= \int_{\Omega^h} \nabla \mathbf{P}^T \rho^{FR} \frac{k^F}{g} \mathbf{b} \, dv, \end{aligned} \quad (4.30)$$

where $\bar{\mathbf{t}}$ and $\bar{\mathbf{t}}^F$ are given in detail in equations (4.7), and $\bar{v}_c := n^F \rho^{FR}(p) \mathbf{w}_F \cdot \mathbf{n}$ for the compressible fluid case.

In preparation for the time discretisation, let $\mathbf{y} = [\mathbf{u}_S, \mathbf{v}_S, \mathbf{v}_F, \mathbf{p}]^T \in \mathbb{R}^m$ with $m = \dim(\mathbf{y})$ represent all nodal degrees of freedom $\mathbf{u}_{(i)}(t)$ of the FE mesh. Then, the coupled system (4.27) takes the general abstract form

$$\mathbf{F}(t, \mathbf{y}, \dot{\mathbf{y}}) \equiv \mathcal{G}_u^h(t, \mathbf{y}, \dot{\mathbf{y}}) \equiv \mathbf{M} \dot{\mathbf{y}} + \mathbf{K} \mathbf{y} - \mathbf{f} \stackrel{!}{=} \mathbf{0}. \quad (4.31)$$

Therein, \mathbf{M} and \mathbf{K} are the global mass and stiffness matrices and \mathbf{f} is the generalised external force vector as illustrated in equations (4.27).

⁴The linearisation is applied using Taylor-series where only the first term has been considered: $h_p \stackrel{lin}{\approx} \frac{\rho^{LR}(1+C)}{C\bar{p}_0 + \frac{R\Theta}{M}\rho^{LR}}$ and $h_{pt} \approx h_p$ with parameters explained in Section 3.1.3.

It is obvious that the structure of the coupled equations and the values of the coupling terms are affected mainly by the permeability and the fluid compressibility parameters. For instance, the coupling stiffness submatrix \mathbf{K}_{32} is proportional to $1/k^F$ so that a decrease in the permeability leads to an increase in the coupling. The remaining coupling terms are not directly affected by rough parameter values and in the geometrically linear regime, they are only subjected to mild changes (cf. Markert *et al.* [126]). The compressibility mainly affects the terms \mathbf{M}_{44} and \mathbf{K}_{44} , so that, for a materially incompressible fluid, the term \mathbf{M}_{44} vanishes and the pure differential equations turn to be differential-algebraic equations (DAE), cf. Section 4.2.2 for a detailed discussion. A more extreme situation is obtained when both the permeability and the fluid compressibility tend to zero values. In that case, one has to deal with a DAE system of an index higher than one as the algebraic volume balance becomes independent of the pore-fluid pressure variable (details in Section 4.2.2).

Restricting our attention to the case of a compressible pore fluid, the system (4.31) can be written explicitly in a form of first-order ordinary differential equations (ODE) as

$$\dot{\mathbf{y}} \stackrel{!}{=} \mathbf{f}_1(t, \mathbf{y}) \quad \text{with} \quad \mathbf{y}(t_0) = \mathbf{y}_0, \quad (4.32)$$

where the vectorial function \mathbf{f}_1 can include some differential operators. In what follows, a number of numerical aspects and time-discretisation approaches are analysed for the treatment of the ODE system (4.32).

Explicit Treatment of Stiff Differential Equations

Based on the absolute stability analysis (A-stability) for ordinary differential equations and without discussing the mathematical particulars, explicit time-integration schemes have bounded stability regions, which impose restrictions on the chosen time-step sizes in order to maintain stable numerical solutions. In contrast, implicit solutions have unbounded stability domains, and therefore, the stability does not apply limits on the time-step size, cf., e. g., Cartwright & Piro [33] for details.

If the maximum time-step size, which is dictated by the boundary of the stability region is much smaller than that demanded due to numerical⁵ or physical⁶ aspects in order to get an accurate solution, then, the problem under consideration is said to be a ‘*stiff problem*’. Thus, one concludes that explicit schemes are best applied to non-stiff or moderate-stiff problems, in which the required time-step sizes for the stability and the accuracy are close to each other.

The system of equations which is summarised in (4.31) includes an inherent non-singular global mass matrix \mathbf{M} as long as the fluid compressibility is guaranteed. Therefore, it is principally possible to solve this system in a monolithic explicit way. Among many

⁵For instance, in order to keep the local truncation error below a desired value, the time-step size must be less than a certain limit noting that the round-off errors, which are related to the computer accuracy, might increase for very small time steps.

⁶In case of dynamic problems, the accuracy of the numerical time-integration implementation demands that the time-step size should not exceed a certain fraction (usually one-tenth) of the minimum period of the applied dynamic load (cf. e. g., Bathe & Wilson [10, chap. 9]).

explicit time-integration schemes in the literature, implementation of the one-step, 1st-order accurate, explicit (forward) *Euler* scheme yields the following space-time-discrete formula:

$$\mathbf{y}_{n+1} = \mathbf{y}_n + \Delta t_n \mathbf{f}_1(t_n, \mathbf{y}_n) \quad \text{or} \quad \mathbf{y}_{n+1} = \mathbf{y}_n - \Delta t_n \mathbf{M}_n^{-1} (\mathbf{K}_n \mathbf{y}_n - \mathbf{f}_n). \quad (4.33)$$

Therein, $\Delta t_n = t_{n+1} - t_n$ is a constant time-step size and $(\cdot)_n := (\cdot)(t_n)$ represent the vector- or tensor-valued quantities at time t_n . Another applied explicit scheme in this work is the 2nd-order accurate explicit *Heun* method, which uses the resulting solution of explicit *Euler* scheme as a predictor (intermediate) solution yielding a more stable scheme. In particular, applying the *Heun* method to the arising ODE system (4.32) yields

$$\begin{aligned} \mathbf{y}_{n+1} &= \mathbf{y}_n + \frac{1}{2} \Delta t_n [\mathbf{f}_1(t_n, \mathbf{y}_n) + \mathbf{f}_1(t_{n+1}, \mathbf{y}_{n+1}^E)] \quad \text{with} \quad \mathbf{y}_{n+1}^E = \mathbf{y}_n + \Delta t_n \mathbf{f}_1(t_n, \mathbf{y}_n) \\ &\longrightarrow \mathbf{y}_{n+1} = \frac{1}{2} (\mathbf{y}_n + \mathbf{y}_{n+1}^E) - \frac{1}{2} \Delta t_n \mathbf{M}_n^{-1} (\mathbf{K}_n \mathbf{y}_{n+1}^E - \mathbf{f}_{n+1}). \end{aligned} \quad (4.34)$$

The performance of the explicit treatment is mainly dependent on the structure and the inverse of the global mass matrix \mathbf{M} . Therefore, an accurate description of the problem behaviour and the stiffness characteristics requires the analysis of the eigenvalues of \mathbf{M} (Cartwright & Piro [33]), which is beyond the scope of the current work.

In this monograph, the stiffness of the problem has been tested in Section 6.1 by solving the coupled equations (4.32) explicitly on an IBVP following the ‘generate and test’⁷ course. The objective is to obtain the maximum Δt_n (critical or Δt_{cr}), which does not violate the stability requirements by trying a range of time steps. According to Matthies *et al.* [129], each subsystem has its own critical time step ($\Delta t_{cr(i)}$) and the Δt_{cr} for the global system is smaller or equal to the minimum of $\Delta t_{cr(i)}$. Moreover, the implementation of the FEM for the pure differential equations succeeds using an equal-order interpolation for all primary variables.

Implicit Treatment

Another possibility for the time discretisation of the ODE system (4.31) is to use implicit monolithic strategies as introduced in Section 4.3.1. In this case, stability does not yield a critical time-step size, and the spatial discretisation of the pure differential equations can be applied using the FEM with no restrictions on the interpolation order of the primary variables.

4.2.2 Differential and Algebraic Coupling

In case of a materially incompressible biphasic aggregate, the resulting overall volume balance initially has no time derivatives and only involves differential operators in space. The other balance equations include terms with temporal evolution of the primary variables.

⁷trial by error: ‘Learning doesn’t happen from failure itself but rather from analysing the failure, making a change, and then trying again’ [www.codinghorror.com].

Consequently, one has to deal with a system of coupled differential-algebraic equations (DAE), where the overall volume balance can be interpreted as an algebraic incompressibility constraint.

Starting with the ‘convectiveless’ basic set of equations (4.2) with its weak forms introduced in equations (4.8)–(4.11), the spatial discretisation yields in matrix form

$$\mathcal{G}_u^h = \underbrace{\begin{bmatrix} \mathbf{I} & \mathbf{0} & \mathbf{0} & \mathbf{0} \\ \mathbf{0} & \mathbf{M}_{22} & \mathbf{0} & \mathbf{0} \\ \mathbf{0} & \mathbf{0} & \mathbf{M}_{33} & \mathbf{0} \\ \mathbf{0} & \mathbf{0} & \mathbf{0} & \mathbf{0} \end{bmatrix}}_{\mathbf{M}} \underbrace{\begin{bmatrix} \dot{\mathbf{u}}_S \\ \dot{\mathbf{v}}_S \\ \dot{\mathbf{v}}_F \\ \dot{\mathbf{p}} \end{bmatrix}}_{\dot{\mathbf{y}}} + \underbrace{\begin{bmatrix} \mathbf{0} & -\mathbf{I} & \mathbf{0} & \mathbf{0} \\ \mathbf{K}_{21} & \mathbf{K}_{22} & \mathbf{K}_{23} & \mathbf{K}_{24} \\ \mathbf{0} & \mathbf{K}_{32} & \mathbf{K}_{33} & \mathbf{K}_{34} \\ \mathbf{0} & \mathbf{K}_{42} & \mathbf{K}_{43} & \mathbf{0} \end{bmatrix}}_{\mathbf{K}} \underbrace{\begin{bmatrix} \mathbf{u}_S \\ \mathbf{v}_S \\ \mathbf{v}_F \\ \mathbf{p} \end{bmatrix}}_{\mathbf{y}} - \underbrace{\begin{bmatrix} \mathbf{0} \\ \mathbf{b}_2 + \mathbf{f}_S \\ \mathbf{b}_3 + \mathbf{f}_F \\ \mathbf{f}_p \end{bmatrix}}_{\mathbf{f}} = \mathbf{0}. \quad (4.35)$$

Here, the 1st–4th rows result from the spatial discretisation of the weak forms (4.8)–(4.11), respectively. The mass submatrices \mathbf{M}_{22} , \mathbf{M}_{33} are non-coupling terms and given in detail in relations (4.28). The stiffness submatrices \mathbf{K}_{ij} consist of diagonal non-coupling and off-diagonal coupling terms (highlighted). In particular, the non-coupling terms read

$$\begin{aligned} \mathbf{K}_{21} &= \int_{\Omega^h} \nabla \mathbf{U}^T \mathcal{D}_e \nabla \mathbf{U} \, dv, & \mathbf{K}_{22} &= \int_{\Omega^h} \mathbf{U}^T \frac{(n^F)^2 \gamma^{FR}}{k^F} \mathbf{U} \, dv, \\ \mathbf{K}_{33} &= \int_{\Omega^h} \mathbf{V}^T \frac{(n^F)^2 \gamma^{FR}}{k^F} \mathbf{V} \, dv, \end{aligned} \quad (4.36)$$

whereas the coupling stiffness submatrices can be expressed as

$$\begin{aligned} \mathbf{K}_{23} &= - \int_{\Omega^h} \mathbf{U}^T \frac{(n^F)^2 \gamma^{FR}}{k^F} \mathbf{V} \, dv, & \mathbf{K}_{24} &= - \int_{\Omega^h} \nabla \mathbf{U}^T n^S \mathbf{P} \, dv, \\ \mathbf{K}_{32} &= - \int_{\Omega^h} \mathbf{V}^T \frac{(n^F)^2 \gamma^{FR}}{k^F} \mathbf{U} \, dv, & \mathbf{K}_{34} &= - \int_{\Omega^h} \nabla \mathbf{V}^T n^F \mathbf{P} \, dv, \\ \mathbf{K}_{42} &= \int_{\Omega^h} \mathbf{P}^T \nabla \mathbf{U} \, dv + \int_{\Omega^h} \nabla \mathbf{P}^T n^F \mathbf{U} \, dv, & \mathbf{K}_{43} &= - \int_{\Omega^h} \nabla \mathbf{P}^T n^F \mathbf{V} \, dv. \end{aligned} \quad (4.37)$$

It is clear that the permeability parameter k^F plays an important role in the subsystem interaction, i. e., the coupling terms \mathbf{K}_{32} and \mathbf{K}_{23} are proportional to $1/k^F$. Therefore, very small values of k^F provoke the coupling and increase the stiffness of the problem. The remaining coupling terms are not directly affected by rough parameter values and in the geometrically linear regime they are only subject to mild changes (Markert *et al.* [126]). The solid *Neumann* boundary term \mathbf{f}_S (cf. (4.30)) depends in this case only on the solid surface traction $\bar{\mathbf{t}}^S$, which requires a special treatment for a surface traction $\bar{\mathbf{t}}$ acting on the whole undrained boundary (solid and fluid) as discussed in Section 4.1.

For the sake of a compact representation, the DAE system (4.35) can be expressed in a general implicit form as

$$\mathbf{F}(t, \mathbf{y}, \dot{\mathbf{y}}) \equiv \mathcal{G}_u^h(t, \mathbf{y}, \dot{\mathbf{y}}) \equiv \mathbf{M} \dot{\mathbf{y}} + \mathbf{K} \mathbf{y} - \mathbf{f} \stackrel{!}{=} \mathbf{0}. \quad (4.38)$$

Therein, $\mathbf{y} = [\mathbf{u}_S, \mathbf{v}_S, \mathbf{v}_F, \mathbf{p}]^T \in \mathbb{R}^m$ with $m = \dim(\mathbf{y})$ again represents all nodal degrees of freedom $\mathbf{u}_{(i)}(t)$ of the FE mesh, \mathbf{M} and \mathbf{K} are the global mass and stiffness matrices, and \mathbf{f} is the generalised external force vector, which includes the body-force terms $\mathbf{b}_2, \mathbf{b}_3$ and the space-discrete *Neumann* boundary terms $\mathbf{f}_S, \mathbf{f}_F$, and \mathbf{f}_p .

In order to discuss the mathematical structure and the different discretisation restrictions, the DAE system (4.38) can be rewritten in a semi-explicit representation. Hence, the resulting formulation consists of ordinary differential equations (ODE) and an algebraic constraint, i. e.,

$$\left. \begin{aligned} \dot{\mathbf{y}}_1 &= \mathbf{h}(t, \mathbf{u}_S, \mathbf{v}_S, \mathbf{v}_F, \mathbf{p}) = \mathbf{h}(t, \mathbf{y}) \\ \mathbf{0} &= \mathbf{g}(t, \mathbf{v}_S, \mathbf{v}_F) \end{aligned} \right\} \quad \text{with} \quad \mathbf{y}(t_0) = \mathbf{y}_0. \quad (4.39)$$

Here, the vector $\mathbf{y}_1 = [\mathbf{u}_S, \mathbf{v}_S, \mathbf{v}_F]^T$ includes the primary variables that are subject to time derivatives, and the vectorial functions \mathbf{g} and \mathbf{h} may contain space-differential operators.

Absence of the pore-fluid pressure variable from the algebraic constraint (volume balance equation) in (4.39) makes the DAE system of an index higher than one (*Hessenberg-index*)⁸. According to Hairer & Wanner [80], the numerical treatment of DAE systems of index-1 is very similar to the treatment of ODE systems. Contrary to this, the implementation of implicit monolithic schemes to solve DAE systems of index higher than one involves a number of numerical challenges such as the need for a mixed finite element method (mixed FEM) or other techniques to maintain the stability. In fact, the higher index problem (4.39) can be classified from a mathematical optimisation viewpoint as a ‘saddle point’ problem. In this regard, the pore-pressure p enters the *Lagrangean* equation as a *Lagrange* multiplier that imposes the incompressibility constraints in order to apply an energy minimisation procedure, i. e., to find the saddle point of the *Lagrangean* argument, cf., e. g., Benzi *et al.* [11] for more details.

A mandatory condition for the solution of the space-discrete ‘saddle point’ problem is that the *Jacobi* matrix resulting from the time discretisation is invertible. Hence, mixed-order of interpolation functions, e. g., quadratic approximation of \mathbf{u}_S and \mathbf{v}_S , and linear approximation of \mathbf{v}_F and p , need to be applied in order to insure that the mentioned *Jacobi* matrix has non-zero eigenvalues due to the application of the FEM. In ‘applied mathematics’, the satisfaction of the so-called *inf-sup* or the *Ladyschenskaja-Babuška-Brezzi* (LBB) condition insures that the chosen shape functions do not lead to a singular *Jacobi* matrix, cf., e. g., Brezzi & Fortin [30], Strang [161] or Wall [172] for details. Alternatively, the ‘patch test’ method (Zienkiewicz *et al.* [190]) provides a simple way of satisfying the essential requirements of the LBB or *inf-sup* condition, and therefore, the stability of the FEM treatment. This test can be performed either on an assembly of several finite elements or on a single element, where on the boundary of the chosen patch the maximum number of enforceable boundary conditions must be prescribed.

⁸The index of a DAE system is remarked by the number of differentiations that are needed to eliminate the algebraic constraints and recover an explicit ODE system (Ascher & Petzold [4]). For instance, the index of the ODE system (4.32) equals zero, whereas the index of the DAE in (4.39) would be equal to one if the relation $(\partial \mathbf{g} / \partial \mathbf{p}) \neq \mathbf{0}$ would be true. However, as $(\partial \mathbf{g} / \partial \mathbf{p}) = \mathbf{0}$, the index is higher than one.

In an attempt to bypass the mixed-FEM restrictions, index reduction procedures can be applied to the DAE system (4.39) in order to recover the index-1 structure. For more details about DAE classes and index reduction schemes, the interested reader is referred to the work by, e.g., Hairer & Wanner [80], Ascher & Petzold [4], Ellsiepen [66] and Markert [125].

Implicit DAE Coupling and Index Reduction

The generalised mass matrix \mathbf{M} of the space-discrete DAE system (4.35) is a singular matrix. Thus, monolithic solutions require the use of implicit time-integration schemes, as the inverse of \mathbf{M} is needed for an explicit treatment.

A reformulation strategy can be applied in order to make the algebraic volume balance (equation (4.35), 4th row) dependent on the pore-fluid pressure variable, and thus, to achieve an index reduction of the DAE system. As has been mentioned in Section 3.1.4, the reformulation can be performed by solving the strong version of the fluid momentum balance (4.2)₂ with respect to $n^F \mathbf{w}_F$ and inserting the result into the volume balance (4.2)₃. The resulting set of differential equations has been referred to as uvp(1)-formulation and summarised in box (3.44). Moreover, the spatial discretisation of the arising uvp(1)-formulation can be expressed in a matrix form as

$$\mathcal{G}_u^h = \underbrace{\begin{bmatrix} \mathbf{I} & \mathbf{0} & \mathbf{0} & \mathbf{0} \\ \mathbf{0} & \mathbf{M}_{22} & \mathbf{0} & \mathbf{0} \\ \mathbf{0} & \mathbf{0} & \mathbf{M}_{33} & \mathbf{0} \\ \mathbf{0} & \mathbf{0} & \mathbf{M}_{43} & \mathbf{0} \end{bmatrix}}_{\mathbf{M}} \underbrace{\begin{bmatrix} \dot{\mathbf{u}}_S \\ \dot{\mathbf{v}}_S \\ \dot{\mathbf{v}}_F \\ \dot{\mathbf{p}} \end{bmatrix}}_{\dot{\mathbf{y}}} + \underbrace{\begin{bmatrix} \mathbf{0} & -\mathbf{I} & \mathbf{0} & \mathbf{0} \\ \mathbf{K}_{21} & \mathbf{K}_{22} & \mathbf{K}_{23} & \mathbf{K}_{24} \\ \mathbf{0} & \mathbf{K}_{32} & \mathbf{K}_{33} & \mathbf{K}_{34} \\ \mathbf{0} & \mathbf{K}_{42} & \mathbf{0} & \mathbf{K}_{44} \end{bmatrix}}_{\mathbf{K}} \underbrace{\begin{bmatrix} \mathbf{u}_S \\ \mathbf{v}_S \\ \mathbf{v}_F \\ \mathbf{p} \end{bmatrix}}_{\mathbf{y}} - \underbrace{\begin{bmatrix} \mathbf{0} \\ \mathbf{b}_2 + \mathbf{f}_S \\ \mathbf{b}_3 + \mathbf{f}_F \\ \mathbf{b}_4 + \mathbf{f}_p \end{bmatrix}}_{\mathbf{f}} = \mathbf{0}. \quad (4.40)$$

Here, the off-diagonal submatrices (highlighted) are the coupling terms and the submatrix \mathbf{K}_{44} is responsible for the index reduction. In fact, the latter reformulation affects only the 4th row in the DAE system (4.35). Hence, the newly emerged submatrices read

$$\begin{aligned} \mathbf{M}_{43} &= \int_{\Omega^h} \nabla \mathbf{P}^T \frac{k^F}{g} \mathbf{V} \, dv, & \mathbf{K}_{42} &= \int_{\Omega^h} \mathbf{P}^T \nabla \mathbf{U} \, dv, \\ \mathbf{K}_{44} &= \int_{\Omega^h} \nabla \mathbf{P}^T \frac{k^F}{\gamma^{FR}} \nabla \mathbf{P} \, dv. \end{aligned} \quad (4.41)$$

As the term \mathbf{K}_{44} is proportional to the permeability parameter k^F , it tends to vanish for very low k^F values, and as a result, the undesired case of a higher index DAE system might be retrieved. Therefore, it is still necessary to use mixed-order finite elements in order to maintain the stability of the implicit monolithic treatment through fulfilment of the *inf-sup* or the LBB condition.

Different Forms of the Coupled DAE System

Alternatively to the uvp(1)-formulation, the set of equations uvp(2) that is given in a strong form in box (3.45) has better stability characteristics and is easier to handle in the numerical applications. Therein, applying the spatial discretisation procedure, the uvp(2)-formulation reads

$$\mathcal{G}_u^h = \underbrace{\begin{bmatrix} I & 0 & 0 & 0 \\ 0 & M_{22} & M_{23} & 0 \\ 0 & 0 & M_{33} & 0 \\ 0 & 0 & M_{43} & 0 \end{bmatrix}}_M \underbrace{\begin{bmatrix} \dot{\mathbf{u}}_S \\ \dot{\mathbf{v}}_S \\ \dot{\mathbf{v}}_F \\ \dot{\mathbf{p}} \end{bmatrix}}_{\dot{\mathbf{y}}} + \underbrace{\begin{bmatrix} 0 & -I & 0 & 0 \\ K_{21} & 0 & 0 & K_{24} \\ 0 & K_{32} & K_{33} & K_{34} \\ 0 & K_{42} & 0 & K_{44} \end{bmatrix}}_K \underbrace{\begin{bmatrix} \mathbf{u}_S \\ \mathbf{v}_S \\ \mathbf{v}_F \\ \mathbf{p} \end{bmatrix}}_{\mathbf{y}} - \underbrace{\begin{bmatrix} \mathbf{0} \\ \mathbf{b}_2 + \mathbf{f}_S \\ \mathbf{b}_3 + \mathbf{f}_F \\ \mathbf{b}_4 + \mathbf{f}_p \end{bmatrix}}_{\mathbf{f}} = \mathbf{0}. \quad (4.42)$$

Here, the 2nd row results from the overall momentum balance rather than the momentum balance of the solid constituent as in the uvp(1)-formulation (4.42). The affected terms, i. e., M_{23} , K_{24} and f_S , are illustrated in detail in equations (4.28) - (4.30).

In comparison with the uvp(1)-formulation, the aforementioned manipulations allow, on the one hand, for an easier implementation of the *Neumann* boundary conditions as the boundary term f_S depends on the overall surface traction $\bar{\mathbf{t}} = \bar{\mathbf{t}}^S + \bar{\mathbf{t}}^F$ that includes the solid traction $\bar{\mathbf{t}}^S$ and the fluid traction $\bar{\mathbf{t}}^F$ rather than $\bar{\mathbf{t}}^S$ alone. On the other hand, this removes the destabilising off-diagonal entry K_{23} containing the factor $1/k^F$, which has a favourable effect on the stability of the system as will be shown in the numerical examples. The uvp(2)-formulation suffers from the same stability problem as uvp(1), where for very low k^F , the index of the DAE system tends to be higher than one. Therefore, stability of the implicit monolithic treatment requires the fulfilment of the *inf-sup* or the LBB condition through using mixed-order interpolations of the primary variables.

Following this, we discuss an alternative approach, which allows the index of the DAE system to be independent from the permeability, and thus, dissolves the requirement to satisfy the *inf-sup* or the LBB restrictions for the case of a very low k^F . This way of treatment is inspired from the hybrid model with materially compressible pore fluid, where the overall volume balance (4.2)₃ is extended by adding some artificial compressibility to the biphasic body. Consequently, the enhanced overall aggregate volume balance with materially incompressible constituents reads

$$\operatorname{div}(n^S \mathbf{v}_S + n^F \mathbf{v}_F) - \epsilon \Delta p = 0 \quad (4.43)$$

with $\Delta(\cdot)$ being the *Laplace* operator and $\epsilon \geq 0$ being a small parameter controlling the influence of the *Laplacean*. This method is comparable to the pressure stabilisation or quasi-compressibility methods used in Computational Fluid Dynamics (CFD), cf. Prohl [146] and Rannacher [150]. Proceeding with (4.43) in the same way as before, the sensitive stiffness term K_{44} , which is essentially responsible for the index order of the DAE system, reads

$$\mathbf{K}_{44} = \int_{\Omega^h} \nabla \mathbf{P}^T \alpha \nabla \mathbf{P} \, dv \quad \text{with} \quad \alpha := \left(\frac{k^F}{\gamma_{FR}} + \epsilon \right) \geq \alpha_{\min}. \quad (4.44)$$

Herein, $\alpha_{\min} > 0$ is associated with a relatively small permeability, which is large enough to prevent oscillations in the pressure variable when equal-order interpolations are used. The magnitude of α_{\min} can be estimated against the poroelastic pressure wave speed in the discretised domain as suggested by Huang *et al.* [94]. It should further be noted that the stabilisation term $\epsilon \Delta p$ also results in an additional boundary term ($\text{grad} p \cdot \mathbf{n}$) which vanishes on impermeable boundaries. A detailed discussion on the choice of the stabilising parameter is presented in the context of the splitting method in Section 4.3. The resulting set of equations, i. e. the DAE system (4.42) with \mathbf{K}_{44} given in (4.44), will be mentioned in the later treatment as uvp (α)-formulation. For further reading on stabilised monolithic schemes in porous media dynamics, we refer to the work by Huang *et al.* [94] and Markert *et al.* [126] among others.

As has been mentioned in Section 3.1.4, another set of equations, namely the uwp-formulation, is obtained if $\{\mathbf{u}_S, \mathbf{w}_F, p\}$ are taken as primary unknowns instead of $\{\mathbf{u}_S, \mathbf{v}_F, p\}$ in the set of equations (3.45). The uwp-formulation is frequently used in the literature, where it provides a new distribution of the coupling and non-coupling mass and stiffness submatrices. This rearrangement of the submatrices influences the solution behaviour under different time-integration schemes, which will be discussed in the numerical examples, cf. Section 6. To clarify this issue, the space-discrete version of the uwp coupled DAE system can be written in details as

$$\mathcal{G}_u^h = \underbrace{\begin{bmatrix} \mathbf{I} & \mathbf{0} & \mathbf{0} & \mathbf{0} \\ \mathbf{0} & \mathbf{M}_{22} & \mathbf{M}_{23} & \mathbf{0} \\ \mathbf{0} & \mathbf{M}_{32} & \mathbf{M}_{33} & \mathbf{0} \\ \mathbf{0} & \mathbf{M}_{42} & \mathbf{M}_{43} & \mathbf{0} \end{bmatrix}}_{\mathbf{M}} \underbrace{\begin{bmatrix} \dot{\mathbf{u}}_S \\ \dot{\mathbf{v}}_S \\ \dot{\mathbf{w}}_F \\ \dot{\mathbf{p}} \end{bmatrix}}_{\dot{\mathbf{y}}} + \underbrace{\begin{bmatrix} \mathbf{0} & -\mathbf{I} & \mathbf{0} & \mathbf{0} \\ \mathbf{K}_{21} & \mathbf{0} & \mathbf{0} & \mathbf{K}_{24} \\ \mathbf{0} & \mathbf{0} & \mathbf{K}_{33} & \mathbf{K}_{34} \\ \mathbf{0} & \mathbf{K}_{42} & \mathbf{0} & \mathbf{K}_{44} \end{bmatrix}}_{\mathbf{K}} \underbrace{\begin{bmatrix} \mathbf{u}_S \\ \mathbf{v}_S \\ \mathbf{w}_F \\ \mathbf{p} \end{bmatrix}}_{\mathbf{y}} - \underbrace{\begin{bmatrix} \mathbf{0} \\ \mathbf{b}_2 + \mathbf{f}_S \\ \mathbf{b}_3 + \mathbf{f}_F \\ \mathbf{b}_4 + \mathbf{f}_p \end{bmatrix}}_{\mathbf{f}} = \mathbf{0}. \quad (4.45)$$

In comparison with the space-discrete uvp (2)-formulation (4.42), the 2nd row of the above system, which represents the overall momentum balance, has been slightly affected by this reformulation. Here, the submatrix \mathbf{M}_{22} is now dependent on the overall density ρ instead of ρ^S alone (cf. equation (4.28)). In the 3rd row, which results from the fluid momentum balance, the term \mathbf{K}_{32} is eliminated and the factor $1/k^F$ occurs solely in the diagonal term \mathbf{K}_{33} . In contrast, the off-diagonal term \mathbf{M}_{32} arises in the generalised mass matrix \mathbf{M} . Moreover, reformulation of the 4th row representing the overall volume balance results in an additional off-diagonal mass submatrix \mathbf{M}_{42} . In the numerical examples in Section 6, the uwp-formulation appears to be more vulnerable to instabilities in the pore-pressure variable especially under high permeability conditions, cf. Markert *et al.* [126] for more details.

The last formulation discussed in this sequence is the reduced up-formulation with primary unknowns $\{\mathbf{u}_S, p\}$. The related strong equations have been introduced in Section 3.1.4

and summarised in Box (3.46). In space-discrete form, the resulting DAE system reads

$$\underbrace{\begin{bmatrix} \mathbf{I} & \mathbf{0} & \mathbf{0} \\ \mathbf{0} & \mathbf{M}_{22} & \mathbf{0} \\ \mathbf{0} & \mathbf{M}_{32} & \mathbf{0} \end{bmatrix}}_{\mathbf{M}} \underbrace{\begin{bmatrix} \dot{\mathbf{u}}_S \\ \dot{\mathbf{v}}_S \\ \dot{\mathbf{p}} \end{bmatrix}}_{\dot{\mathbf{y}}} + \underbrace{\begin{bmatrix} \mathbf{0} & -\mathbf{I} & \mathbf{0} \\ \mathbf{K}_{21} & \mathbf{0} & \mathbf{K}_{23} \\ \mathbf{0} & \mathbf{K}_{32} & \mathbf{K}_{33} \end{bmatrix}}_{\mathbf{K}} \underbrace{\begin{bmatrix} \mathbf{u}_S \\ \mathbf{v}_S \\ \mathbf{p} \end{bmatrix}}_{\mathbf{y}} - \underbrace{\begin{bmatrix} \mathbf{0} \\ \mathbf{b}_2 + \mathbf{f}_S \\ \mathbf{b}_3 + \mathbf{f}_p \end{bmatrix}}_{\mathbf{f}} = \mathbf{0}. \quad (4.46)$$

Therein, the mass and stiffness submatrices can be written in detail as

$$\begin{aligned} \mathbf{M}_{22} &= \int_{\Omega^h} \mathbf{U}^T \rho \mathbf{U} \, dv, & \mathbf{K}_{21} &= - \int_{\Omega^h} \nabla \mathbf{U}^T \mathbf{D}_e \nabla \mathbf{U} \, dv, & \mathbf{K}_{23} &= - \int_{\Omega^h} \nabla \mathbf{U}^T \mathbf{P} \, dv, \\ \mathbf{M}_{32} &= \int_{\Omega^h} \nabla \mathbf{P}^T \frac{k^F}{g} \mathbf{U} \, dv, & \mathbf{K}_{32} &= \int_{\Omega^h} \mathbf{P}^T \nabla \mathbf{U} \, dv, & \mathbf{K}_{33} &= \int_{\Omega^h} \nabla \mathbf{P}^T \frac{k^F}{\gamma^{FR}} \nabla \mathbf{P} \, dv. \end{aligned} \quad (4.47)$$

The coupling characteristics and the structure of the up-formulation are comparable to that of the uvp(2) or uwp relations. Therefore, the same procedures and discussion can also be applied to the simpler up-formulation.

Finally, the time-continuous initial-value problem of the previously mentioned cases, i. e., the hybrid model (4.27), the uvp(1)-formulation (4.40), the uvp(2)-formulation (4.42), the extended uvp(α), the uwp-formulation (4.45), and the reduced up-formulation (4.46) can be summarised in an abstract form as

Find $\mathbf{y}(t) \in \mathbb{R}^m$ such that $\mathbf{F}[t, \mathbf{y}, \dot{\mathbf{y}}] = \mathbf{0}$, $\mathbf{y}(t_0) = \mathbf{y}_0 \quad \forall t \in [t_0, T]$.

(4.48)

Next, a time stepping scheme has to be applied, where the considered time interval is divided into a finite number of subintervals $[t_n, t_{n+1}]$ with time-step size $\Delta t_n = t_{n+1} - t_n > 0$. Conceptually, the solution of the problem (4.48) using a certain time-stepping algorithm (see the following section) starts from an initial point and then takes a time step Δt_n forward to find the next solution point. This process continues with successive steps to cover the entire time domain.

4.3 Time Discretisation

In what follows, a handful of numerical time-integration procedures to solve the time-continuous coupled problem (4.48) is discussed. Such methods can be distinguished into two classes: (1) implicit monolithic schemes, where different diagonally implicit *Runge-Kutta* (DIRK) time-stepping algorithms are applied to the various space-discrete formulations based on *Taylor-Hood*-like equal- or mixed-order interpolations of the respective unknowns, and (2) semi-explicit-implicit splitting schemes, which are realised in the form of predictor-corrector algorithms and proceed from uniform linear FE approximations of the primary variables.

4.3.1 Implicit Monolithic Time Integration

In the course of the numerical integration of stiff DAE and ODE systems, one may distinguish between two major classes of monolithic time-stepping solvers:

1. One-step methods (OSM), such as the implicit *Runge-Kutta* scheme (IRK), which refer only to the information at one previous time step to determine the current values. Higher-order versions of the OSM with better stability and accuracy characteristics can be obtained by considering some temporal intermediate steps. In such cases, all the intermediate information will be discarded when moving to a new time step.
2. Linear multi-step methods (MSM), e. g. the backward differentiation formula (BDF), which try to store and use the values from several previous time steps rather than neglecting them. Consequently, the MSM usually need larger storage capacity in comparison with the OSM.

In talking about the two schemes, the one-step IRK method generally requires the solution of a nonlinear system of DAE at each time step, and therefore, the accuracy is also related to the linearity and the number of function evaluations per time step. Consequently, the local truncation error, which might be needed in case of time adaptivity, is not directly evaluated. In contrast, multi-step schemes, such as the BDF, require one function evaluation per time step, and the accuracy can be improved by increasing the number of dependent previous steps. Therefore, the local truncation error is easier to evaluate. Nevertheless, the time-step control is not an efficient process when implementing the MSM in comparison with the OSM. For instance, the one-step IRK methods allow for different time-step control schemes such as the embedded error estimator, cf., e. g., Diebels *et al.* [46], which usually cannot be implemented to the MSM. For an in-depth discussion about the different numerical schemes, the interested reader is referred to the works by, e. g., Quarteroni *et al.* [147], Ascher & Petzold [4] and Hairer & Wanner [80].

In this monograph, time integration of the arising DAE systems is carried out using one-step schemes, which can be easily recast in the framework of the one-step s -stage diagonally-implicit *Runge-Kutta* (DIRK) methods. This type of treatment allows, on the one hand, to overcome the large memory need and computational costs of the MSM as the solution of the stage equations is performed in a decoupled fashion (Ellsiepen [66]), and, on the other hand, such schemes enable an efficient exploitation of multi-step strategies within a one-step framework. To this end, the applied implicit monolithic time-integration methodology in this work is illustrated in Figure 4.4.

The most basic kind of implicit one-step methods is the backward (implicit) Euler (BE). Although the BE is an A-stable scheme, it is proved to be inappropriate for dynamic problems as it undergoes artificial numerical damping leading to wrong solutions. Thus, very small time steps are needed in order to minimise the numerical damping effects. Another applied scheme in this work is the 2nd-order accurate trapezoidal rule (TR), which shows very slow numerical damping in comparison with the fast-damped BE scheme (Hairer & Wanner [80]). Using the TR to solve stiff DAE problems, instabilities might

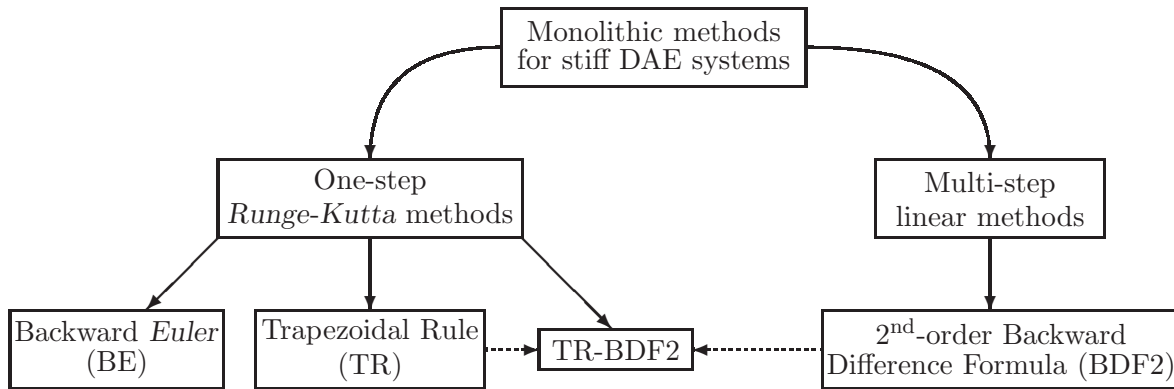


Figure 4.4: Sketch of the considered implicit monolithic time-integration methods in this thesis to solve the coupled problem (4.48)

be observed in the numerical solution due to the fact that this scheme is A-stable but not L-stable. To overcome the mentioned instability problems, the major attention in the following is paid to the TR-BDF2 method (Bank *et al.* [7]), which is A- and L-stable. This scheme has been firstly implemented to the field of porous media dynamics in the work by Markert *et al.* [126], on which the current discussion is based. The one-step TR-BDF2 is a composite integration scheme that benefits from the advantages of both the trapezoidal rule and the 2nd-order backward difference formula (BDF2), and tries to bypass the BDF2 drawbacks of large memory storage and time-step adaptivity, see, e.g., the work by Hosea & Shampine [91] for more details.

The previously mentioned three schemes, i. e., the BE, the TR and the TR-BDF2, can be easily reformulated in the framework of the Runge-Kutta (RK) methods using Butcher tableaus (Butcher [32]), viz.:

$$\begin{array}{c}
 \begin{array}{c|ccc}
 c_1 & a_{11} & \cdots & a_{1s} \\
 \vdots & \vdots & \ddots & \vdots \\
 c_s & a_{s1} & \cdots & a_{ss} \\
 \hline
 & b_1 & \cdots & b_s
 \end{array} &
 \begin{array}{c|c}
 1 & 1 \\
 \hline
 & 1
 \end{array} &
 \begin{array}{c|cc}
 0 & 0 & 0 \\
 \hline
 1 & \frac{1}{2} & \frac{1}{2} \\
 \hline
 & \frac{1}{2} & \frac{1}{2}
 \end{array} &
 \begin{array}{c|ccc}
 0 & 0 & 0 & 0 \\
 \hline
 \theta & \frac{\theta}{2} & \frac{\theta}{2} & 0 \\
 \hline
 1 & \frac{3\theta-\theta^2-1}{2\theta} & \frac{1-\theta}{2\theta} & \frac{\theta}{2} \\
 \hline
 & \frac{3\theta-\theta^2-1}{2\theta} & \frac{1-\theta}{2\theta} & \frac{\theta}{2}
 \end{array}
 \end{array} \quad (4.49)$$

Butcher tableau BE TR TR-BDF2 with $\theta = 2 - \sqrt{2}$

The TR-BDF2, and also the TR, is almost a singly diagonal-implicit Runge-Kutta (SDIRK) method, as the diagonal elements (a_{ss}) are equal except for $a_{11} = 0$. This yields an explicit first stage ($a_{11} = 0$) with no nonlinear equations to be solved, whereas the other stages are implicit. According the work by Hosea & Shampine [91], the TR-BDF2 is considered an optimal choice in the class of 3-stage DIRK, where, beside having strong stability characteristics, there are only two implicit stages per time step, not three. Moreover, it is advantageous to have the SDIRK structure for mildly nonlinear systems. Here, for the considered problem of porous media dynamics, this allows to reuse the linearised matrices in order to evaluate all the implicit stages within the time step, which drastically reduces the required solution time. Hence, applying a stiffly accurate s -stage DIRK method, the

initial-value problem (4.48) can be successively solved according to the following time-integration algorithm:

Time-stepping algorithm of a stiffly accurate s-stage DIRK method	
<i>Given:</i>	coefficients $c_i, a_{ij}, b_j = a_{sj}$ of a s -stage DIRK method, approximate solution $\mathbf{y}_n \approx \mathbf{y}(t_n)$ at time t_n , time-step size Δt_n
<i>Find:</i>	approximate solution $\mathbf{y}_{n+1} \approx \mathbf{y}(t_{n+1})$ at time t_{n+1}
<i>Step 1:</i>	for each <i>Runge-Kutta</i> stage $i = 1, \dots, s$
(a)	set stage time $T_{ni} := t_n + c_i \Delta t_n$ and accumulated stage derivative $\bar{\mathbf{Y}}_{ni} := \Delta t_n \sum_{j=1}^{i-1} a_{ij} \dot{\mathbf{Y}}_{nj}$
(b)	solve nonlinear system for stage increments $\Delta \mathbf{Y}_{ni}$ $\mathbf{R}_{ni}(\Delta \mathbf{Y}_{ni}) \equiv \mathbf{F}\left(T_{ni}, \mathbf{y}_n + \Delta \mathbf{Y}_{ni}, \frac{1}{\Delta t_n a_{ii}} [\Delta \mathbf{Y}_{ni} - \bar{\mathbf{Y}}_{ni}]\right) = \mathbf{0}$
(c)	set stage derivative $\dot{\mathbf{Y}}_{ni} := \frac{1}{\Delta t_n a_{ii}} [\Delta \mathbf{Y}_{ni} - \bar{\mathbf{Y}}_{ni}]$
<i>Step 2:</i>	set $\mathbf{y}_{n+1} := \mathbf{Y}_{ns} = \mathbf{y}_n + \Delta \mathbf{Y}_{ns}$ and $t_{n+1} := T_{ns}$

(4.50)

Following this, the almost SDIRK time-stepping schemes, given in Butcher tableaus (4.49) can be treated following the DIRK algorithm (4.50). In this case, we perform the first explicit RK stage as $c_1 = a_{11} = 0$, and thus, put directly $T_{n1} = t_n$, $\mathbf{Y}_{n1} = \mathbf{y}_n$ and $\Delta \mathbf{Y}_{n1} = \dot{\mathbf{Y}}_{n1} = \mathbf{0}$. Furthermore, it should be noted that for a current time step n , instead of the stage solutions \mathbf{Y}_{ni} , the stage increments $\Delta \mathbf{Y}_{ni} := \mathbf{Y}_{ni} - \mathbf{y}_n$ are used as unknowns to reduce round-off errors during the solution of the time-discrete system in step 1(b) (Hairer & Wanner [80]). In contrast, the accumulated stage derivatives $\bar{\mathbf{Y}}_{ni}$ depend only on previously computed quantities, and thus, are constant for the current *Runge-Kutta* stage i . Apparently, the main computational effort is in the solution of the generally nonlinear system in step 1(b) of the algorithm (4.50). For its efficient solution with the *Newton-Raphson* method, the derivative of the nonlinear vector function $\mathbf{R}_{ni}(\Delta \mathbf{Y}_{ni})$ with respect to the stage increments $\Delta \mathbf{Y}_{ni}$ is required. The *Jacobian* matrix takes the form

$$\mathbf{J}_{ni} := \frac{d\mathbf{R}_{ni}}{d\Delta \mathbf{Y}_{ni}} = \frac{1}{\Delta t_n a_{ii}} \left. \frac{\partial \mathbf{F}}{\partial \dot{\mathbf{y}}} \right|_{\mathbf{z}} + \left. \frac{\partial \mathbf{F}}{\partial \mathbf{y}} \right|_{\mathbf{z}}, \quad (4.51)$$

where $\mathbf{z} = \{T_{ni}, \mathbf{Y}_{ni}, \mathbf{Y}'_{ni}\}$ denotes the current set of arguments of \mathbf{F} in \mathbf{R}_{ni} . Having obtained the *Jacobian* matrix, the current stage increments can be generally calculated via

$$\Delta \mathbf{Y}_{ni}^k = -(\mathbf{J}_{ni}^k)^{-1} \mathbf{R}_{ni}^k, \quad (4.52)$$

where the index k represents the *Newton* iteration step. Herein, a *Newton* iteration procedure can be additionally applied within the current time step n until a suitable convergence criterion, such as $\|\mathbf{R}_{ni}^k\| < TOL_R$ or $\|\Delta \mathbf{Y}_{ni}^k\| < TOL_y$, is met.

Generation of the *Jacobian* Matrix

For problems with linear elastic material response, the partial derivative of the space-discrete global residual vector with respect to \mathbf{y} yields the generalised stiffness matrix \mathbf{K} , and the partial derivative with respect to $\dot{\mathbf{y}}$ yields the generalised mass matrix \mathbf{M} . The biphasic model under study proceeds from geometrical as well as material linearities. Thus, the global mass, stiffness, and *Jacobian* matrices can be given as

$$\left. \frac{\partial \mathbf{F}}{\partial \dot{\mathbf{y}}} \right|_z = \mathbf{M} \approx \text{const.}, \quad \left. \frac{\partial \mathbf{F}}{\partial \mathbf{y}} \right|_z = \mathbf{K} \approx \text{const.} \quad \longrightarrow \quad \mathbf{J}_{ni} = \frac{1}{\Delta t_n a_{ii}} \mathbf{M} + \mathbf{K}. \quad (4.53)$$

Here, the space-discrete system, i. e. $\mathbf{R}_{ni}(\Delta \mathbf{Y}_{ni}) = \mathbf{0}$, is already linear and can be solved by common means.

For a general nonlinear case, such as the system of equations that results from the implementation of the weakly imposed viscous damping boundary (cf. Section 4.4), the derivation of the global mass and stiffness matrices can be carried out numerically. Here, the *Fréchet* scheme is implemented, which allows for an implicit treatment of the boundary terms. In particular, the numerically generated stiffness and mass matrices are expressed via differential quotients as

$$\left. \begin{aligned} \mathbf{K}^k &= \left. \frac{\partial \mathbf{F}}{\partial \mathbf{y}} \right|_z \approx \frac{\mathbf{F}[t_n, \mathbf{y}_n + \epsilon \mathbf{e}_n, \dot{\mathbf{y}}_n] - \mathbf{F}[t_n, \mathbf{y}_n, \dot{\mathbf{y}}_n]}{\epsilon \mathbf{e}_n} \\ \mathbf{M}^k &= \left. \frac{\partial \mathbf{F}}{\partial \dot{\mathbf{y}}} \right|_z \approx \frac{\mathbf{F}[t_n, \mathbf{y}_n, \dot{\mathbf{y}}_n + \epsilon \mathbf{e}'_n] - \mathbf{F}[t_n, \mathbf{y}_n, \dot{\mathbf{y}}_n]}{\epsilon \mathbf{e}'_n} \end{aligned} \right\} \longrightarrow \mathbf{J}_{ni}^k = \frac{1}{\Delta t_n a_{ii}} \mathbf{M}^k + \mathbf{K}^k \quad (4.54)$$

with \mathbf{e}_n and \mathbf{e}'_n as explicit perturbation vectors of \mathbf{y}_n and $\dot{\mathbf{y}}_n$, respectively, k represents the *Newton* iteration step, and $\epsilon > 0$ is a small parameter, which can be determined based on the precision of the computer, cf. Press *et al.* [145] or Lee & Park [113] for additional details.

4.3.2 Semi-Explicit-Implicit Splitting Methods

The application of spitting schemes allows to solve the strongly coupled problem using loose or weak coupling strategies. Such methods include implicit as well as explicit steps, and thus, are subject to a critical (maximum) time-step size for stability reasons. The inclusion of explicit steps is justified in dynamic problems, where the accuracy of the time integration requires that the time-step size does not exceed a certain fraction of the minimum period of the applied dynamic load⁹.

In the current study, splitting strategies (fractional-step or operator-splitting methods) are applied to the biphasic model with materially incompressible constituents. In this case, it is not possible to apply explicit monolithic schemes to the space-discrete DAE systems, e. g. the set (4.35), due to the algebraic coupling that leads to a singular global

⁹According to, e. g., Bathe & Wilson [10, chap.9], it is reasonable that the time-step size does not exceed one-tenth of the minimum period of the applied dynamic load.

mass matrix. Instead, splitting methods can be used, which allow to separate the constituent momentum balances from the algebraic saturation constraint by decoupling the displacement and velocity fields ($\mathbf{u}_S, \mathbf{v}_S$ and \mathbf{v}_F) from the pore-fluid pressure p . This can be accomplished by introducing constituent intermediate velocities \mathbf{v}_α^* , which represent an approximation to the velocities in the next time step. Unlike the monolithic schemes, operator-splitting techniques first demand the time stepping and then the spatial FE discretisation of the decoupled equations.

To convey the different concepts of splitting strategies in a simple case, the material behaviour in the subsequent discussion is taken as linear elastic, cf. Section 3.2. For more details about splitting methods within the TPM, the interested reader is referred to the works by Markert *et al.* [126], Heider [85] and Danilov [40].

Time Discretisation and Splitting

Starting with the basic set of governing balance equations (4.2) and adopting the established splitting algorithms used to solve the incompressible Navier-Stokes equations as given in the work by, e. g., Chorin [37], Gresho & Sani [75], Guermond & Quartapelle [77] and Prohl [146], the splitting is carried out by advancing each time step in multiple steps (fractional-step method), i. e., $\{\mathbf{v}_{\alpha n}, p_n, \mathbf{u}_{S n}\} \rightarrow \mathbf{v}_\alpha^* \rightarrow \{\mathbf{v}_{\alpha n+1}, p_{n+1}, \mathbf{u}_{S n+1}\}$. Similar strategies have already been successfully applied to problems in soil dynamics based on the reduced up formulation, see, e. g., Huang *et al.* [93, 94]. In the current treatment of porous biphasic models with three primary variables, the time discretisation is performed based on a semi-explicit-implicit approach. To this end, we begin with a standard implicit time discretisation of the solid displacement-velocity relation $(\mathbf{u}_S)'_S = \mathbf{v}_S$ by applying the trapezoidal rule:

$$\frac{(\mathbf{u}_{S n+1} - \mathbf{u}_{S n})}{\Delta t_n} = \frac{1}{2} (\mathbf{v}_{S n+1} + \mathbf{v}_{S n}). \quad (4.55)$$

In the solid momentum balance (4.2)₁ with $n^\alpha \approx n_{0S}^\alpha$ and $\text{grad} n^F \approx \mathbf{0}$, the linear elastic solid extra stress is treated explicitly, i. e. $\mathbf{T}_{E n}^S := \mathbf{T}_E^S(\mathbf{u}_{S n})$, the pressure term is considered implicitly, and the seepage velocity is discretised in time with the aid of the intermediate velocities, i. e. $\mathbf{w}_F^* = \mathbf{v}_F^* - \mathbf{v}_S^*$, viz.:

$$\rho^S \frac{(\mathbf{v}_{S n+1} - \mathbf{v}_{S n})}{\Delta t_n} = \text{div} \mathbf{T}_{E n}^S - n^S \text{grad} p_{n+1} + \frac{(n^F)^2 \gamma^{FR}}{k^F} \mathbf{w}_F^* + \rho^S \mathbf{b}_n. \quad (4.56)$$

Exploiting the solid intermediate velocity \mathbf{v}_S^* enables the splitting of equation (4.56) as

$$\rho^S \frac{(\mathbf{v}_S^* - \mathbf{v}_{S n})}{\Delta t_n} = \text{div} \mathbf{T}_{E n}^S - n^S \text{grad} p_n + \frac{(n^F)^2 \gamma^{FR}}{k^F} (\mathbf{v}_F^* - \mathbf{v}_S^*) + \rho^S \mathbf{b}_n, \quad (4.57)$$

$$\rho^S \frac{(\mathbf{v}_{S n+1} - \mathbf{v}_S^*)}{\Delta t_n} = -n^S \text{grad} (p_{n+1} - p_n). \quad (4.58)$$

Applying the same time-stepping procedure to the fluid momentum balance (4.2)₂ yields

$$\rho^F \frac{(\mathbf{v}_{F n+1} - \mathbf{v}_{F n})}{\Delta t_n} = -n^F \text{grad} p_{n+1} - \frac{(n^F)^2 \gamma^{FR}}{k^F} \mathbf{w}_F^* + \rho^F \mathbf{b}_n. \quad (4.59)$$

Following this, the splitting technique is applied using the intermediate velocities, viz.:

$$\rho^F \frac{(\mathbf{v}_F^* - \mathbf{v}_{Fn})}{\Delta t_n} = -n^F \text{grad} p_n - \frac{(n^F)^2 \gamma^{FR}}{k^F} (\mathbf{v}_F^* - \mathbf{v}_S^*) + \rho^F \mathbf{b}_n, \quad (4.60)$$

$$\rho^F \frac{(\mathbf{v}_{Fn+1} - \mathbf{v}_F^*)}{\Delta t_n} = -n^F \text{grad}(p_{n+1} - p_n). \quad (4.61)$$

The remaining overall volume balance (4.2)₃ is treated fully implicitly in time as

$$\text{div}(n^S \mathbf{v}_{Sn+1} + n^F \mathbf{v}_{Fn+1}) = 0. \quad (4.62)$$

The intermediate treatment of the seepage velocity gives equations (4.57) and (4.60) an implicit character in the respective intermediate seepage velocity and makes the choice of the time-step size independent of the actual permeability. If instead \mathbf{w}_F is considered explicitly, additional improvements for the low permeability case are necessary as described by, e. g., Li *et al.* [117]. Moreover, the consideration of $\text{grad} p_n$ in the sense of a predictor in (4.57) and (4.60) is commonly referred to as *Chorin-Uzawa* scheme (Prohl [146]), which is in line with the incremental projection schemes given in the work by, e. g., Goda [72], van Kan [169] and Rannacher [150]. Essentially, inserting (4.58) and (4.61) into the volume balance (4.62) results in a *Poisson*-like equation for the pore-fluid pressure. It is also worth mentioning that a reformulation of equation (4.62) in a similar way as for the monolithic treatment (cf. Section 4.3.1) has no beneficial effect on the solution behaviour.

Weak Formulation

For the sake of the spatial discretisation, the preceding time-discrete relations except for the solid displacement-velocity relation (4.55) are transferred into a variational form. In particular, the weak formulations read:

- Split solid momentum balance:

$$\begin{aligned} \int_{\Omega} \delta \mathbf{u}_S \cdot \left\{ n^S \rho^{SR} \left[\frac{(\mathbf{v}_S^* - \mathbf{v}_{Sn})}{\Delta t_n} - \mathbf{b}_n \right] - \frac{(n^F)^2 \gamma^{FR}}{k^F} (\mathbf{v}_F^* - \mathbf{v}_S^*) \right\} dv + \\ + \int_{\Omega} \text{grad} \delta \mathbf{u}_S \cdot (\mathbf{T}_{En}^S - n^S p_n \mathbf{I}) dv - \int_{\Gamma_{tS}} \delta \mathbf{u}_S \cdot \bar{\mathbf{t}}_n^S da = 0, \end{aligned} \quad (4.63)$$

$$\int_{\Omega} \delta \mathbf{u}_S \cdot \left[\rho^{SR} \frac{(\mathbf{v}_{Sn+1} - \mathbf{v}_S^*)}{\Delta t_n} + \text{grad}(p_{n+1} - p_n) \right] dv = 0. \quad (4.64)$$

- Split fluid momentum balance:

$$\int_{\Omega} \delta \mathbf{v}_F \cdot n^F \rho^{FR} \left[\frac{(\mathbf{v}_F^* - \mathbf{v}_{Fn})}{\Delta t_n} - \mathbf{b}_n + \frac{n^F g}{k^F} (\mathbf{v}_F^* - \mathbf{v}_S^*) + \frac{1}{\rho^{FR}} \text{grad} p_n \right] dv = 0, \quad (4.65)$$

$$\begin{aligned} \int_{\Omega} \delta \mathbf{v}_F \cdot n^F \rho^{FR} \frac{(\mathbf{v}_{Fn+1} - \mathbf{v}_F^*)}{\Delta t_n} dv - \\ - \int_{\Omega} \text{div} \delta \mathbf{v}_F n^F (p_{n+1} - p_n) dv - \int_{\Gamma_{tF}} \delta \mathbf{v}_F \cdot \tilde{\mathbf{t}}_{n+1}^F da = 0. \end{aligned} \quad (4.66)$$

- Overall volume balance:

$$\begin{aligned} & \int_{\Omega} \delta p \operatorname{div} \mathbf{v}_S^* \, dv + \int_{\Gamma_v} \delta p \tilde{v}_{n+1} \, da - \\ & - \int_{\Omega} \operatorname{grad} \delta p \cdot \left[n^F (\mathbf{v}_F^* - \mathbf{v}_S^*) - \Delta t_n \left(\frac{n^F}{\rho^{FR}} + \frac{n^S}{\rho^{SR}} \right) \operatorname{grad} (p_{n+1} - p_n) \right] \, dv = 0. \end{aligned} \quad (4.67)$$

Herein, the weak form of the overall volume balance has been reformulated by substitution of $\mathbf{v}_{S_{n+1}}$ and $\mathbf{v}_{F_{n+1}}$ as given in (4.58) and (4.61), respectively. The resulting time-discrete boundary terms can be expressed in detail as

$$\begin{aligned} \bar{\mathbf{t}}_n^S &= (\mathbf{T}_{E_n}^S - n^S p_n \mathbf{I}) \mathbf{n}, \quad \tilde{\mathbf{t}}_{n+1}^F = -n^F (p_{n+1} - p_n) \mathbf{n}, \\ \tilde{v}_{n+1} &= \left[n^F (\mathbf{v}_{F_{n+1}} - \mathbf{v}_{S_{n+1}}) - \frac{\Delta t_n}{\rho^{SR}} \operatorname{grad} (p_{n+1} - p_n) \right] \cdot \mathbf{n}. \end{aligned} \quad (4.68)$$

It is clear that the treatment of the volume efflux \tilde{v}_{n+1} is not that straightforward as for the monolithic case. However, most of the initial boundary-value problems proceed either from undrained (no-flow) boundaries with $n^F \mathbf{w}_F \cdot \mathbf{n} \equiv 0$ and $\operatorname{grad} p \cdot \mathbf{n} \equiv 0$ or fully permeable conditions with $p \equiv 0$, such that, relations (4.68) simplify accordingly.

Spatial Discretisation

For the spatial discretisation, the strong relation (4.55) and the weak forms (4.63)–(4.67) are treated in the same way as before using the notations (4.26) of Section 4.2. As the splitting procedure requires the approximation of the intermediate velocities on the discrete space, the relations $(\mathbf{v}_S^*)^h = \mathbf{U} \mathbf{v}_S^*$ and $(\mathbf{v}_F^*)^h = \mathbf{V} \mathbf{v}_F^*$ are additionally considered in the following treatment. Here, the nodal values \mathbf{v}_S^* and \mathbf{v}_F^* must not be regarded as intrinsic DOF of the problem as for them no boundary conditions exist, and the associated equations (4.63) and (4.65) just represent fractions of the physical balance relations. Finally, the time-space-discrete equations read:

- Solid displacement-velocity relation:

$$\frac{\mathbf{u}_{S_{n+1}} - \mathbf{u}_{S_n}}{\Delta t_n} - \frac{1}{2} (\mathbf{v}_{S_{n+1}} - \mathbf{v}_{S_n}) = \mathbf{0}. \quad (4.69)$$

- Split solid momentum balance:

$$\mathbf{M}_{22} \frac{\mathbf{v}_S^* - \mathbf{v}_{S_n}}{\Delta t_n} + \mathbf{K}_{21} \mathbf{u}_{S_n} + \mathbf{K}_{22} \mathbf{v}_S^* + \mathbf{K}_{23} \mathbf{v}_F^* + \mathbf{K}_{24} \mathbf{p}_n - \mathbf{b}_{2n} - \mathbf{f}_{S_n} = \mathbf{0}, \quad (4.70)$$

$$\mathbf{M}_{22} \frac{\mathbf{v}_{S_{n+1}} - \mathbf{v}_S^*}{\Delta t_n} + \tilde{\mathbf{K}}_{24} (\mathbf{p}_{n+1} - \mathbf{p}_n) = \mathbf{0}. \quad (4.71)$$

- Split fluid momentum balance:

$$\mathbf{M}_{33} \frac{\mathbf{v}_F^* - \mathbf{v}_{Fn}}{\Delta t_n} + \mathbf{K}_{32} \mathbf{v}_S^* + \mathbf{K}_{33} \mathbf{v}_F^* + \widetilde{\mathbf{K}}_{34} \mathbf{p}_n - \mathbf{b}_{3n} = \mathbf{0}, \quad (4.72)$$

$$\mathbf{M}_{33} \frac{\mathbf{v}_{Fn+1} - \mathbf{v}_F^*}{\Delta t_n} + \mathbf{K}_{34} (\mathbf{p}_{n+1} - \mathbf{p}_n) - \widetilde{\mathbf{f}}_{Fn+1} = \mathbf{0}. \quad (4.73)$$

- Overall volume balance:

$$\mathbf{K}_{42} \mathbf{v}_S^* + \mathbf{K}_{43} \mathbf{v}_F^* + \widetilde{\mathbf{K}}_{44} (\mathbf{p}_{n+1} - \mathbf{p}_n) - \widetilde{\mathbf{f}}_{pn+1} = \mathbf{0}. \quad (4.74)$$

Herein, the mass and stiffness matrices \mathbf{M}_{ik} and \mathbf{K}_{ik} as well as the load vectors \mathbf{b}_i and \mathbf{f}_S coincide with those in (4.35). In addition, the splitting procedure induces the following terms:

$$\begin{aligned} \widetilde{\mathbf{K}}_{24} &= \int_{\Omega^h} \mathbf{U}^T \nabla \mathbf{P} \, dv, & \widetilde{\mathbf{K}}_{34} &= \int_{\Omega^h} \mathbf{V}^T n^F \nabla \mathbf{P} \, dv, \\ \widetilde{\mathbf{K}}_{44} &= \int_{\Omega^h} \nabla \mathbf{P}^T \Delta t_n \left(\frac{n^F}{\rho^{FR}} + \frac{n^S}{\rho^{SR}} \right) \nabla \mathbf{P} \, dv, & (4.75) \\ \widetilde{\mathbf{f}}_{Fn+1} &= \int_{\Gamma_{vF}^h} \mathbf{V}^T \widetilde{\mathbf{t}}_{n+1}^F \, da, & \widetilde{\mathbf{f}}_{pn+1} &= \int_{\Gamma_v^h} \mathbf{P}^T \widetilde{v}_{n+1} \, da. \end{aligned}$$

Following this, we make use of the advantageous property of splitting methods, which permit a continuous and equal-order interpolation to be used for all occurring fields. Thus, proceeding from uniform linear interpolation functions, i.e. $\mathbf{U} = \mathbf{V} = \mathbf{P}$ and $\nabla \mathbf{U} = \nabla \mathbf{V} = \nabla \mathbf{P}$, it is easily concluded that $\mathbf{K}_{22} = -\mathbf{K}_{23} = -\mathbf{K}_{32} = \mathbf{K}_{33} =: \overline{\mathbf{K}}$ and the discrete equations (4.70) and (4.72) simplify accordingly, viz.:

$$\mathbf{M}_{22} \frac{\mathbf{v}_S^* - \mathbf{v}_{Sn}}{\Delta t_n} + \mathbf{K}_{21} \mathbf{u}_{Sn} + \overline{\mathbf{K}} \mathbf{v}_S^* - \overline{\mathbf{K}} \mathbf{v}_F^* + \mathbf{K}_{24} \mathbf{p}_n - \mathbf{b}_{2n} - \mathbf{f}_{Sn} = \mathbf{0}, \quad (4.76)$$

$$\mathbf{M}_{33} \frac{\mathbf{v}_F^* - \mathbf{v}_{Fn}}{\Delta t_n} - \overline{\mathbf{K}} \mathbf{v}_S^* + \overline{\mathbf{K}} \mathbf{v}_F^* + \widetilde{\mathbf{K}}_{34} \mathbf{p}_n - \mathbf{b}_{3n} = \mathbf{0}. \quad (4.77)$$

Exploiting simple algebraic manipulations, equations (4.76) and (4.77) can now be solved with respect to the intermediate velocities yielding the following explicit relations:

$$\begin{aligned} \mathbf{v}_S^* &= \mathbf{v}_{Sn} + \mathbf{h}_1(\mathbf{u}_{Sn}, \mathbf{v}_{Sn}, \mathbf{v}_{Fn}, \mathbf{p}_n, \Delta t_n), \\ \mathbf{v}_F^* &= \mathbf{v}_{Fn} + \mathbf{h}_2(\mathbf{u}_{Sn}, \mathbf{v}_{Sn}, \mathbf{v}_{Fn}, \mathbf{p}_n, \Delta t_n). \end{aligned} \quad (4.78)$$

Herein, for a compact representation, the remainder expressions are collected in the auxiliary functions \mathbf{h}_1 and \mathbf{h}_2 , which only depend on known quantities of time t_n .

Predictor-Corrector Algorithm

In the box below, the semi-explicit-implicit splitting scheme is implemented in form of the predictor-corrector (P-C) algorithm, cf. Markert *et al.* [126].

Predictor-corrector algorithm of the semi-explicit-implicit scheme	
<i>Given:</i> approximate solution $\mathbf{y}_n \approx \mathbf{y}(t_n)$ at time t_n , time-step size Δt_n	
<i>Find:</i> approximate solution $\mathbf{y}_{n+1} \approx \mathbf{y}(t_{n+1})$ at time t_{n+1}	
<i>Step 1:</i> set predictor values	} internal iteration loop
$\mathbf{v}_S^P := \mathbf{v}_{S_n}, \quad \mathbf{v}_F^P := \mathbf{v}_{F_n}, \quad \mathbf{p}^P := \mathbf{p}_n, \quad \mathbf{u}_S^P := \mathbf{u}_{S_n} + \Delta t_n \mathbf{v}_S^P$	
<i>Step 2:</i> compute intermediate velocities	
$\mathbf{v}_S^* = \mathbf{v}_S^P + \mathbf{h}_1(\mathbf{u}_S^P, \mathbf{v}_S^P, \mathbf{v}_F^P, \mathbf{p}^P, \Delta t_n),$ $\mathbf{v}_F^* = \mathbf{v}_F^P + \mathbf{h}_2(\mathbf{u}_S^P, \mathbf{v}_S^P, \mathbf{v}_F^P, \mathbf{p}^P, \Delta t_n)$	
<i>Step 3:</i> calculate the pore-fluid pressure (pressure projection)	
$\mathbf{p}_{n+1} = \mathbf{p}^P - \widetilde{\mathbf{K}}_{44}^{-1} (\mathbf{K}_{42} \mathbf{v}_S^* + \mathbf{K}_{43} \mathbf{v}_F^* - \widetilde{\mathbf{f}}_{p_{n+1}})$	
<i>Step 4:</i> compute velocity correctors and solid displacement	
$\mathbf{v}_{S_{n+1}} = \mathbf{v}_S^* - \Delta t_n \mathbf{M}_{22}^{-1} \widetilde{\mathbf{K}}_{24} (\mathbf{p}_{n+1} - \mathbf{p}^P)$ $\mathbf{v}_{F_{n+1}} = \mathbf{v}_F^* - \Delta t_n \mathbf{M}_{33}^{-1} [\mathbf{K}_{34} (\mathbf{p}_{n+1} - \mathbf{p}^P) - \mathbf{f}_{F_{n+1}}]$ $\mathbf{u}_{S_{n+1}} = \mathbf{u}_{S_n} + \frac{1}{2} \Delta t_n (\mathbf{v}_{S_{n+1}} - \mathbf{v}_{S_n})$	
<i>Step 5:</i> update $\mathbf{y}_n := \mathbf{y}_{n+1}$ and advance in time $t_{n+1} = t_n + \Delta t_n$	

Moreover, Figure 4.5 illustrates the sequence of steps of the P-C algorithm.

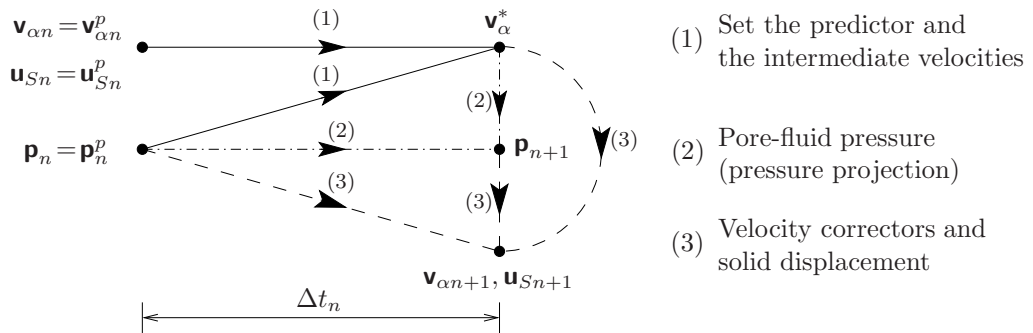


Figure 4.5: Information flow of the predictor-corrector algorithm

The aforementioned algorithm in (4.79) is well-suited for mass matrix lumping, which is recommended as an economical numerical device for matrix inversion, generally paid for by some additional errors. However, it is noticed that the lumping, mass conservation provided, can improve the accuracy of some problems by error cancellation, see, e. g., Wood

[180] or Zienkiewicz & Taylor [191]. Moreover, it is proved that in transient problems, the lumping process introduces some additional dissipation of ‘stiffness matrix form’, which can help in case of numerical oscillations. In the current treatment, the classical row-sum procedure is used to diagonalise the mass matrix by adding all entries in a row to the diagonal element of that row. Thus, the lumped mass matrix can be expressed as

$$\widetilde{\mathbf{M}} = \text{diag}(\widetilde{M}_i) \quad \text{with} \quad \widetilde{M}_i = \sum_{k=1}^m M_{ik}, \quad i = 1, \dots, m, \quad (4.80)$$

where m represents the number of columns (or rows) related to the number of nodal DOF of the FE mesh. In particular, mass lumping is applied to \mathbf{M}_{22} and \mathbf{M}_{33} which need to be inverted in Steps 2 and 4 of the P-C algorithm (4.79).

In this connection, before the update in Step 5, the convergence can be checked by comparing the results of subsequent internal iteration loops (Steps 1 to 4) within the same time step. That is, repeat the iteration loop i of the current time step n until a suitable convergence criterion such as $\|\mathbf{y}_{n+1}^{i+1} - \mathbf{y}_{n+1}^i\| < \text{TOL}_y$ is met. For the numerical examples presented in Section 6, it is found sufficient to pass only once through the internal loop in each time step of the implemented P-C algorithm.

CFL Condition and Time-Step Restrictions

The major drawback of the presented splitting procedure is the restriction to a critical (maximum) time-step size Δt_{cr} due to the arising explicit steps. In particular, the *Courant-Friedrichs-Lewy* (CFL)¹⁰ condition [39] has to be satisfied, which limits the maximal time-step size depending on the minimal discrete-element dimensions and the speed of poroelastic pressure-wave (p-wave) propagation in the solid domain, cf., e. g., Huang *et al.* [94] and Li *et al.* [117] for more details. For 1-d two-node and 2-d four-node linear elements, the critical time-step size can be estimated as

$$\Delta t_{cr}^I = \frac{\Delta x}{c_p^x}, \quad \Delta t_{cr}^{II} = \frac{\Delta x \Delta y}{c_p^x \Delta y + c_p^y \Delta x}. \quad (4.81)$$

Herein, Δx and Δy are the minimal discrete-element dimensions in x and y direction and c_p^x , c_p^y represent the speed of elastic p-wave propagation in x and y direction, respectively. The p-wave speed for the materially incompressible biphasic model has been discussed in Section 3.3. Therein, one distinguishes between the case of negligible relative motion between the solid and fluid phases as $\rho^S + \rho^F$ appears in the p-wave speed relation (3.79) and the case of drained solid skeleton or complete decoupled motion of the fluid and solid phases, where only ρ^S is regarded for the p-wave velocity¹¹.

¹⁰The CFL condition for explicit time integration methods is a necessary but not a sufficient restriction for the stability when treating problems that involve finite-speed propagation of information, i. e. dynamic wave propagation problems. Herein, it is required that the distance travelled by a wave in one time step (Δt) does not exceed one spatial step (Δx) or, equivalently, the numerical wave speed must be at least as fast as the physical wave speed, cf., e. g., [www.cse.illinois.edu/iem/pde/wavecfl].

¹¹In general, there are three apparent types of bulk waves in a saturated porous medium, cf., e. g., Biot [12] and Wilmański & Albers [176]: (1) the fast and only weakly damped longitudinal pressure wave

To be on the safe side, the considered p-wave speed relation in the stability treatment is the one that gives a maximum speed, and accordingly, a minimum critical time-step size, i. e., for a drained, isotropic poroelastic medium, viz.:

$$c_p = \sqrt{\frac{2\mu^S + \lambda^S}{\rho^S}}. \quad (4.82)$$

In general, numerical studies reveal that the stability of the implemented P-C algorithm (4.79) depends very strongly on the chosen time-step size. Although the CFL condition requires that $\Delta t_n \leq \Delta t_{cr}$, an optimal solution is obtained just for $\Delta t_n \approx \Delta t_{cr}$, whereas significant oscillations in the pore-pressure variable can be observed when $\Delta t_n \ll \Delta t_{cr}$. Because of that, the presented algorithm is not feasible in cases where non-uniform FE meshes are required, e. g., when space-adaptive strategies are used, as the whole dynamic problem is governed by one global time step. However, the time-step limitation can be partly avoided by alternatively considering, for instance, the staggered implicit-implicit schemes with stabilising parameters, cf. Gresho & Sani [75] and Huang *et al.* [93, 94] for details.

In the present treatment, the semi-explicit-implicit scheme might undergo instabilities for the case of $\Delta t_n \ll \Delta t_{cr}$. This difficulty becomes apparent from the additional stiffness term $\widetilde{\mathbf{K}}_{44}$ in (4.75)₁, which tends towards zero in the limit of an infinitely small time-step size causing a pressure ‘overshoot’ in the projection step (Step 3) of the P-C algorithm (4.79). As a remedy for this problem, some artificial compressibility can be added to the overall aggregate in analogy to (4.43). This manipulation yields a semi-explicit quasi-compressibility strategy, which in CFD is known as the artificial compressibility method or the modified *Chorin-Uzawa* scheme (Prohl [146]). Applying the latter idea to equation (4.62) yields

$$\operatorname{div}(n^S \mathbf{v}_{S n+1} + n^F \mathbf{v}_{F n+1}) - \epsilon \Delta(p_{n+1} - p_n) = 0, \quad (4.83)$$

where again $\epsilon \geq 0$ is a small parameter and $\Delta(\cdot)$ is the Laplace operator. Then, proceeding through all discretisation steps, one finally obtains

$$\widetilde{\mathbf{K}}_{44} = \int_{\Omega^h} \nabla \mathbf{P}^T \beta \nabla \mathbf{P} \, dv \quad \text{with} \quad \beta := \left[\Delta t_n \left(\frac{n^F}{\rho_{FR}^S} + \frac{n^S}{\rho_{SR}^S} \right) + \epsilon \right] \geq \beta_{\min}, \quad (4.84)$$

where β_{\min} is associated with a critical time-step size. As the CFL condition suggests, the optimal solution is obtained for $\Delta t_n \approx \Delta t_{cr}$, so that it is natural to choose

$$\beta_{\min} = \beta_0 \Delta t_{cr} \left(\frac{n^F}{\rho_{FR}^S} + \frac{n^S}{\rho_{SR}^S} \right). \quad (4.85)$$

It is obvious that the parameter $\beta_0 > 0$ controls the imposed artificial compressibility (see Chapter 6), and thus, adds an additional numerical error to the materially incompressible

(p1-wave or *Biot's* wave of 1st kind) with in-phase motion of the solid and fluid mainly governed by the constituent compressibility, (2) the slow and strongly damped longitudinal pressure wave (p2-wave or *Biot's* wave of 2nd kind) with anti-phase motion of the solid and fluid mainly determined by the solid skeleton deformability, and (3) the even slower transverse shear wave (s-wave) transmitted only in the solid phase and governed by its shear stiffness. In the considered case of materially incompressible constituents, the theoretical speed of the 1st *Biot's* wave is infinite.

biphasic model at the expense of numerical stability. Moreover, the value of β_{\min} is also accepted as a good estimate for α_{\min} (cf. (4.44)₂) to stabilise the monolithic scheme if uniform equal-order elements are used, although α is independent of the FE mesh size, cf. Huang *et al.* [94].

4.4 Treatment of Unbounded Domains

In unbounded domains, acoustic body waves are supposed to propagate towards infinity. Thus, it is reasonable for an efficient numerical treatment to divide the semi-infinite domain into a finite near field surrounding the source of vibration and an infinite far field accounting for the energy radiation to infinity. Applying the finite element method (FEM) for the spatial semi-discretisation of the near field and simply truncating the domain by introducing artificial fixed (hard) or free (soft) boundaries causes the incident waves to be reflected back into the near domain. This might be partly overcome by choosing the dimensions of the near field large enough in order to ensure that the reflected waves will not disturb the progressing ones in the region of interest till the end of the computation. However, this commonly entails a huge number of finite elements followed by uneconomic computational costs.

In this regard, numerous approaches have been proposed in the literature to efficiently treat unbounded spatial domains, see, e. g., the works by Givoli [71] and Lehmann [114] for an overview. In the following, some of the most popular methods used in geomechanics and earthquake engineering are outlined, cf. Heider *et al.* [87]:

(1) The finite element - boundary element coupled scheme (FEM-BEM) as given in the works by, e. g., von Estorff & Firuziaan [69], Schanz [153] and Yazdchi *et al.* [183]. Herein, the near field is modelled with the FEM, whereas the far-field response is captured using the BEM. Although this method exposes a good accuracy by combining the advantages of both mentioned discretisation techniques, the implementation involves a lot of mathematical complexities as it requires the derivation of fundamental solutions including an analytical treatment of the governing differential balance equations.

(2) The combined finite element - infinite element method (FEM-IEM), in which the near field is discretised using the FEM and the far field using the IEM that extends to infinity in one or more directions. The shape functions of the infinite elements towards the infinity, usually called ‘wave propagation functions’ in the dynamic treatment, have exponential form and depend on the frequency of the excitation. Using the FEM-IEM method, the whole problem is solved in the frequency domain. Otherwise, inverse Laplace transformation rules need to be implemented to solve the problem in the time domain, cf. Khalili *et al.* [102] or Wang *et al.* [173]. In this connection, a domain decomposition strategy into a near and a far field can be applied for the time stepping in the time domain as given by Nanning & Schanz [136] and Schanz [153]. Here, the Newmark integration method can be applied directly to the near field to evaluate the temporal behaviour, as it is discretised with the FEM. However, as the IEM is applied to the far field together with the inverse Laplace transformation, the temporal response of the far field can be calculated in the time domain using the convolution quadrature method (CQM).

(3) In the framework of absorbing boundary condition (ABC) schemes, the method of perfectly matched layers (PML) appears as an important strategy to simulate the response of unbounded half-space dynamics, see, e.g., Basu [8], Basu & Chopra [9] and Oskooi *et al.* [141] for details. This method is originally developed for electromagnetic wave problems and then extended to elastic wave propagation in infinite domains. The PML is an unphysical wave absorbing layer, which is placed adjacent to the truncated near-field boundaries that are supposed to extend to infinity. The purpose of the PML is basically to prevent wave reflections back to the near domain. This scheme is applied mostly when solving wave equations in the frequency domain as the solution is based on frequency-dependent stretching functions.

In the current contribution, the simulation of wave propagation into infinity is realised in the time domain. Here, the near field is discretised with the FEM, whereas the spatial discretisation of the far field is accomplished using the mapped IEM in the quasi-static form as given in the work by Marques & Owen [127]. This insures the representation of the far-field stiffness and its quasi-static response instead of implementing rigid boundaries surrounding the near field, cf. Wunderlich *et al.* [182]. This mapped IEM has already been successfully applied by Schrefler & Simoni to simulate the isothermal and the non-isothermal consolidation of unbounded biphasic porous media, see [156, 158]. In particular, they have performed a coupled analysis under quasi-static conditions, where infinite elements with different decay functions are applied to the solid displacement, the pore pressure and the temperature fields. Moreover, they have calibrated the numerical results by comparison with respective analytical reference solutions.

However, in dynamical applications, some additional considerations should be taken into account. Here, when body waves approach the interface between the FE and the IE domains, they partially reflect back to the near field as the quasi-static IE cannot capture the dynamic wave pattern in the far field¹². To overcome this, the waves are absorbed at the FE-IE interface using the viscous damping boundary (VDB) scheme, which basically belongs to the ABC class, cf. Figure 4.6, right.

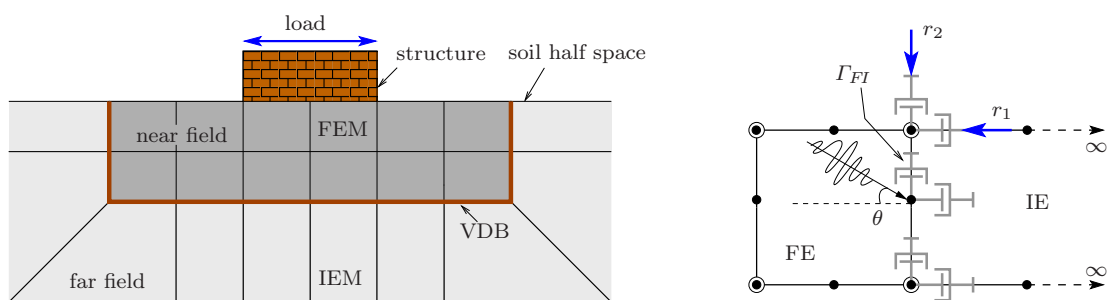


Figure 4.6: Viscous damping boundary method (VDB): FEM-IEM coupling with VDB at the interface (left), and rheological model with applied damping forces (right)

¹²The shape functions (decay functions) of the quasi-static infinite elements towards the infinity, as discussed in Section 4.3.2, are chosen for an easy-to-implement treatment as simple functions of time (polynomials) and not dependent on the frequency of the loading (e.g. exponential) as for dynamic infinite elements (cf. Khalili *et al.* [102]).

4.4.1 Viscous Damping Boundary Method (VDB)

The idea of the VDB is based on the work by Lysmer & Kuhlemeyer [120], in which velocity- and parameter-dependent damping forces are introduced to get rid of artificial wave reflections. In this, the verification of the proposed VDB scheme has been carried out by studying the reflection and refraction of elastic waves at the interface between two domains, where the arriving elastic energy should be absorbed. For more information and different applications, see, e. g., the works by Haeggblad & Nordgren [79], Underwood & Geers [168], Wunderlich *et al.* [182] and Akiyoshi *et al.* [2].

The implementation of the VDB scheme in this work is confined to the case of the materially incompressible biphasic model, where the considered set of equations is the uvp (2) formulation, cf. (3.45). Following this, the weak form of the overall momentum balance is split for the treatment of the far field into two parts: a quasi-static part discretised in space with the mapped IE method and a dynamic part replaced by damping forces integrated over the FE-IE interface Γ_{FI} . In particular, one obtains

$$\underbrace{\int_{\Omega} \text{grad} \delta \mathbf{u}_S \cdot (\mathbf{T}_E^S - p \mathbf{I}) \, dv - \int_{\Omega} \delta \mathbf{u}_S \cdot \rho \mathbf{b} \, dv}_{\text{quasi-static } (\rightarrow \text{IE})} + \underbrace{\int_{\Gamma_{FI}} \delta \mathbf{u}_S \cdot (a_i \rho c_i) \mathbf{v}_S \, da}_{\text{dynamic } (\rightarrow \text{VDB})} = 0. \quad (4.86)$$

In general, three apparent modes of bulk waves, which are two compressional and one shear wave, can be observed in biphasic solid-fluid aggregates, cf. Footnote 11 in Page 80. However, as the treatment of unbounded domains in the current contribution is oriented to geotechnical problems (such as fully saturated silty sand under seismic excitation), only two body waves need to be considered. Here, the low-frequency excitation and the low permeability make the relative motion between the solid matrix and the viscous pore fluid under dynamic loading very slow. Thus, it is accepted that far from the permeable boundary the pore fluid is almost trapped in the solid matrix, and therefore, the fluid can approximately be treated as an incompressible material together with the solid phase. In other words, only biphasic poroelastic media with intrinsically incompressible solid and fluid constituents in the low frequency regime are addressed, which gives rise to only two types of bulk waves that have to be damped out. In particular, these are the longitudinal pressure wave and the transverse shear wave transmitted through the elastic structure of the solid skeleton.

Following this, in order to develop boundary conditions that ensure the absorption of the elastic energy arriving at a certain boundary, Lysmer & Kuhlemeyer [120] developed damping expressions for the boundary conditions. For two-dimensional (2-d) problems, the damping relations read

$$\begin{aligned} \sigma &= (a \rho c_p) \mathbf{v}_{S1} \quad : \text{p-waves}, \\ \tau &= (b \rho c_s) \mathbf{v}_{S2} \quad : \text{s-waves}. \end{aligned} \quad (4.87)$$

These equations are formulated for incident primary (p) and secondary (s) waves that act at an angle θ from the x_1 -axis, cf. Figure 4.6, right. In (4.86) and (4.87), $\rho = \rho^S + \rho^F$

is the density of the overall aggregate, \mathbf{v}_{S1} and \mathbf{v}_{S2} represent the nodal solid velocities in x_1 - and x_2 -direction, c_p and c_s are the velocities of the p- and s-waves given in equations (3.77) and (3.79), and a, b are dimensionless parameters (cf. [79]) given as

$$a = \frac{8}{15\pi} (5 + 5c + 2c^2) \quad , \quad b = \frac{8}{15\pi} (3 + 2c) \quad \text{with} \quad c = \sqrt{\frac{\mu^S}{\lambda^S + 2\mu^S}}. \quad (4.88)$$

The implementation of the method is fairly simple since one adds nothing more than dashpots with damping constants $(a\rho c_p)$ and $(b\rho c_s)$ to the degrees of freedom (DOF) of the FE-IE interface elements (Figure 4.6, right). The effectiveness of the VDB depends strongly on the wave incident angle θ . Indeed, it is shown in the work by Lysmer & Kuhlemeyer [120] that a nearly perfect absorption of the incident waves can only be achieved for $\theta < 60$, whereas some reflections occur for bigger angles. In the weak formulation, the damping terms are written in an integral form over the boundary Γ_{FI} , which for 2-d problems read

$$\mathbf{r} = \begin{bmatrix} r_1 \\ r_2 \end{bmatrix} = \int_{\Gamma_{FI}} \delta \mathbf{u}_S \cdot \begin{bmatrix} a\rho c_p & 0 \\ 0 & b\rho c_s \end{bmatrix} \mathbf{v}_S \, da. \quad (4.89)$$

Due to the dependency on the primary unknown \mathbf{v}_S , the arising damping terms in (4.89) enter the weak formulation of the problem in a form of nonlinear boundary integrals. Thus, an unconditional stability of the numerical solution requires that these terms are treated implicitly by integrating over the boundary at the current time step in the sense of a weakly-imposed *Neumann* boundary, cf. Ehlers & Acartürk [59]. Here, relation (4.54) is employed for the numerical generation of the respective mass, stiffness and *Jacobi* matrices.

Chapter 5:

Liquefaction of Saturated Granular Materials

This chapter is devoted to the investigation of liquefaction phenomena, which usually appear in saturated granular materials after dynamic excitation. This includes definitions and descriptions of liquefaction mechanisms, factors affecting saturated soil behaviour and an *in-situ* example of seismic-induced liquefaction. Moreover, the elasto-viscoplastic constitutive model, as introduced in Section 3.2, is used to capture the basic features of liquefaction events, such as the pore-fluid pressure accumulation and softening of the granular structure.

5.1 Preface and Definitions

Liquefaction events have been observed during earthquakes for a long time. Written records and notices dating back hundreds of years describe earthquake consequences that are now known to be associated with liquefaction. Such phenomena primarily happen in saturated soils, and thus, they are commonly observed in offshore areas and near bodies of water such as rivers, lakes and oceans. It is believed that the term ‘liquefaction’ firstly used in geotechnics by *Hazen* to describe the 1918 collapse of the Calaveras Dam in California. Moreover, early researches and laboratory works in the field of soil liquefaction go back to *Casagrande* in 1936. For a historical review, the interested reader is referred to the works by *Kramer & Elgamal* [109] or *Jefferies & Been* [99] among others.

The stress-strain response of cohesionless, drained granular materials and the related grains rearrangement on the microscale provide an important key to understanding the physics of liquefaction, cf. *de Groot et al.* [76] and *Kramer & Elgamal* [109] for details. In this regards, Figure 5.1, left, shows an exemplary sample of a consolidated, drained granular material, which is subjected to a constant normal stress σ_0 and a monotonic shear stress τ . The applied shear stress leads to a continuous increment of the shear strain γ and two types of volumetric stains ε_S^V (contraction with $\varepsilon_S^V < 0$ and dilation with $\varepsilon_S^V > 0$) due to sliding and rotation of the particles (crash of the grains is excluded). Figure 5.1, right, depicts the stress-strain (τ - γ) behaviour of a sand with two different initial bulk densities (dense and loose) until reaching a critical state (steady state), where the deformation continues at a constant shear stress. Moreover, ε_S^V - γ curves show that the dominant behaviour is contraction in case of a loose sand, whereas medium dense to dense sands undergo contraction at a low stress ratio and dilation at higher stress values. The thresholds at which the behaviours change from contraction to dilation construct a line called the phase transformation line (PTL).

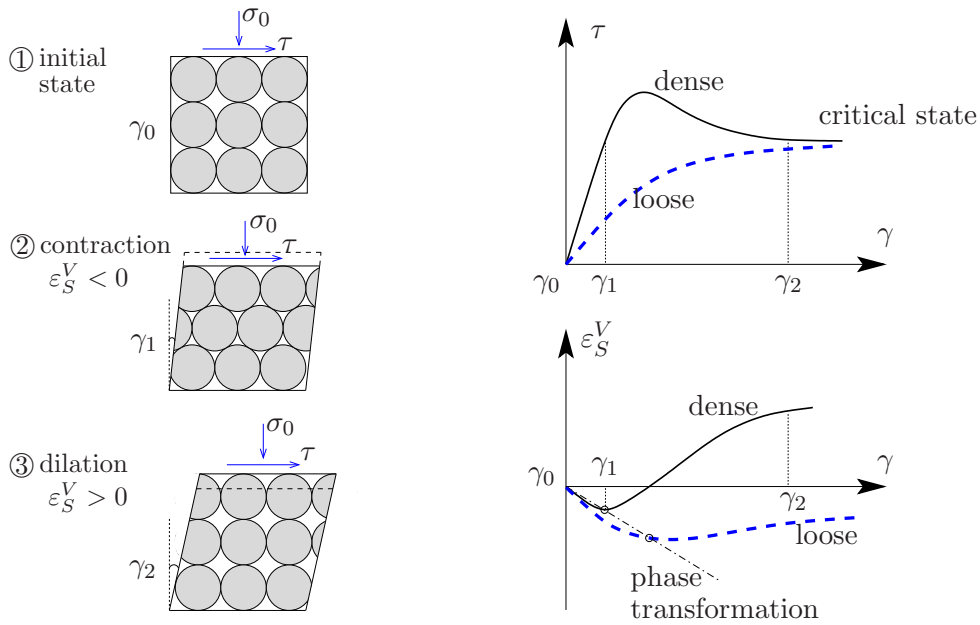


Figure 5.1: Contraction and dilation due reordering of the grains in a shear test of cohesionless dry sand (left) and a schematic illustration of the shear stress τ versus the shear strain γ and the volumetric strain ε_S^V versus γ of a sand in a dense and a loose state (right)

Concerning the undrained behaviour of granular materials, it is assumed in the undrained experiments that the samples are 100% saturated with a materially incompressible fluid and no drainage occurs. Consequently, the volumetric strains almost vanish and become no longer interesting outputs, and instead, the focus is laid on the pore-pressure development. Herein, an increase in the pore pressure is expected if the soil behaviour is contractive, whereas a decrease in the pore pressure occurs for dilative soil behaviour. In order to explain the influence of the initial density (or the initial void ratio) and the initial mean effective stress (after consolidation) on the behaviour of saturated porous media in a schematic way, Figure 5.2 shows the variation of the mean effective stress p' ($p' := -\frac{1}{3} I_\sigma$) and the void ratio e ($e(n^F) := n^F / (1 - n^F)$) in drained and undrained triaxial compression tests (cf. Manzari & Dafalias [122]). In this case, the shear stress (called ‘deviatoric stress’) is applied by varying the principal stresses of the triaxial cell.

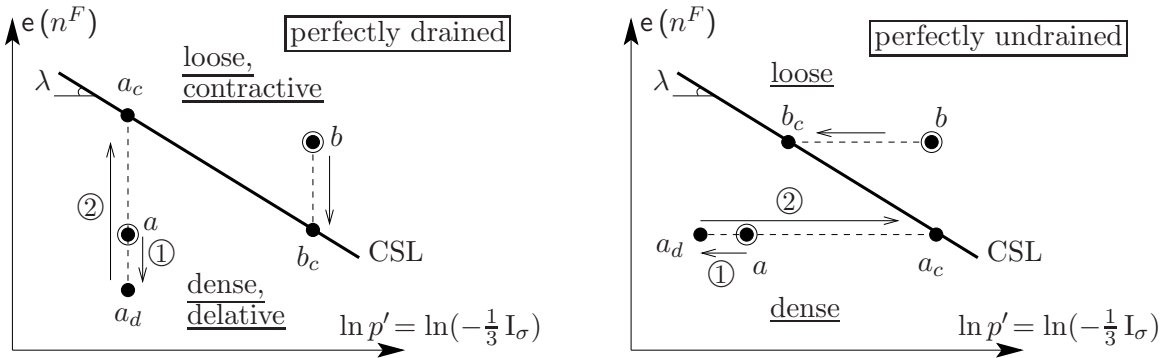


Figure 5.2: A schematic illustration of sand behaviour in drained (right) and undrained (left) triaxial tests with dense and loose initial densities

Within the framework of the Critical State Soil Mechanics (CSSM), the critical state line (CSL) with slope λ defines the state at which the deformations continue for almost fixed shear stress and zero volumetric strain rate. At the CSL, the void ratio of the drained test reaches a critical value (e_c), which meets in the undrained test a critical mean effective stress (p'_c).

In Figure 5.2, one distinguishes between two cases of material density:

(1) A dense material with an initial density higher than a critical value (point a). In the drained case under deviatoric stress (Figure 5.2, left), the specimen initially tends to contract with decreasing void ratio until reaching the state a_d (path ①). Thereafter, the behaviour switches to dilation with increasing void ratio (path ②). Under undrained conditions (Figure 5.2, right), the contractive tendency leads to an increase in the pore pressure and a reduction in the effective stress (path ①). Thereafter, the behaviour changes and the dilative trend causes an increase of the mean effective stress until the state reaches a point a_c with $p' = p'_c$ (path ②), where a critical collapse takes place.

(2) A loose granular material has an initial density less than a critical value, cf. Figure 5.2, point b . Here, the expected drained behaviour under shear stress is contraction, which leads to an increase in the pore pressure under undrained conditions. In this case, the collapse might occur when reaching the state b_c , or alternatively, a further increase in p' leads to cross the CSL to a bounding limit and then the state turns back to b_c to fail, cf. Manzari & Dafalias [122] for more details.

For the treatment of liquefaction mechanisms in this monograph, some basic concepts of soil mechanics are recalled. Here, the effective stress relations (3.18)_{1,2} and the overall volume balance (3.45)₄, which results in the macroscopic filter law can be rewritten as

$$\mathbf{T}^S + \mathbf{T}^F = \mathbf{T}_E^S - p\mathbf{I}, \quad n^F \mathbf{w}_F = -\frac{k^F}{\gamma^{FR}} \text{grad } p + \frac{k^F}{g} [\mathbf{b} - (\mathbf{v}_F)'_S]. \quad (5.1)$$

Herein, (5.1)₁ shows that the total applied stress to a saturated porous medium is carried by the solid skeleton via the effective solid stress \mathbf{T}_E^S and the pore fluid via the pore-fluid pressure p . In the absence of sudden loading (as under quasi-static loads), each grain of the soil particles assemblage is found in a contact with a number of neighbouring particles, which allows for the solid skeleton to carry most of the applied external total stress ($\mathbf{T}^S \approx \mathbf{T}_E^S$ and $p \approx 0$), cf. Figure 5.3, left.

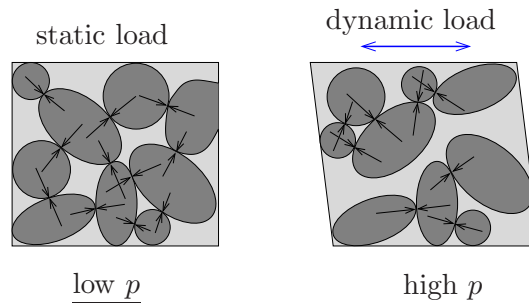


Figure 5.3: Saturated granular assemblage under static and dynamic loadings

Under rapidly applied loading, the pore pressure suddenly increases leading to a collapse in the loose, saturated granular structure, and consequently, solid particles try to move

into a denser configuration, cf. Figure 5.3, right. Thereafter, the excess pore-fluid pressure tends to dissipate, which causes an adverse motion of the solid and the pore fluid phases. This process is governed by relation (5.1)₂ between the seepage velocity \mathbf{w}_F and the pore-pressure gradient, where the permeability k^F in m/s plays a major role in the rapidity of the excess pore-pressure dissipation. If the pore fluid is trapped in the solid matrix, the applied external stress is mostly carried by the pore fluid leading to a poor contact between the solid grains and causes a softening of the granular deposit.

In the following, a number of liquefaction-related definitions and terminologies are given, which are based on pioneering publications in the fields of soil modelling and earthquake engineering, such as the works by Kramer & Elgamal [109], Castro [34], Ishihara [97], Ishihara *et al.* [98], Verdugo & Ishihara [170] and Zienkiewicz *et al.* [186].

General definitions of saturated soil liquefaction

1. *Liquefaction*: A general term used to describe the behaviour of saturated soils, which is characterised by a build-up of the pore pressure and a softening of the granular structure. This comprises a number of physical phenomena such as the ‘flow liquefaction’ and the ‘cyclic mobility’.
2. *Flow liquefaction*: An instability phenomenon that frequently happens in loose soils with low shear strength. Under undrained conditions, the applied load results in an increase of the pore pressure and an incredible reduction of the effective stress until the residual shear strength cannot sustain the static equilibrium. Consequently, saturated soil loses its nature as a solid and flows like a viscous fluid.
3. *Cyclic mobility*: A kind of permanent but limited plastic deformation of saturated soil under cyclic shear loading. Therein, an accumulation of the pore pressure takes place after each applied cycle, however, the mean effective stress can never reach a zero value, and the residual shear strength can always maintain the static equilibrium. (5.2)
4. *Phase transformation*: A threshold character of liquefiable sands. Here, sand initially shows contractive behaviour, but then exhibits dilation after crossing the phase transformation line.
5. *Steady state strength*: A critical state character of sands, which refers to the shear strength at which the shear strain increases continuously under constant shear stress and constant effective confining pressure at constant volume.

Remark: Another related phenomenon, known as ‘dry liquefaction’, is introduced in the literature, see, e. g., Kolymbas [107] and Mira *et al.* [132]. This usually occurs in dry soils of very low density, such as in uncompacted, volcanic fly ashes. In case of sudden loading, the pore air and the soil skeleton coupling plays a paramount role in the stability, where in worst cases, the frictional angle cannot sustain the stability and a collapse might happen.

5.1.1 Earthquake-Induced Field Liquefaction

For a better understanding of the conditions that lead to a seismic-induced saturated soil collapse, an *in-situ* liquefaction example of saturated silty sand is given in the following, where more details can be found in the works by Zeghal & Elgamal [184] or Kramer & Elgamal [109]. Here, the liquefaction-prone Wildlife Refuge area of the Imperial Valley in southern California has been instrumented by the U.S. Geological Survey with the necessary equipments to measure different soil properties during an earthquake. The ultimate aim of this investigation was to analyse the relations among the ground motion, the pore-pressure accumulation and the soil shear strength change.

Figure 5.4, left, shows a cross section in the Wildlife Refuge site, which consists of a clayey silt surface layer (≈ 2.7 m, very low permeability), a liquefiable silty sand (≈ 3.3 m) and a layer of stiff clay (≈ 5.0 m).

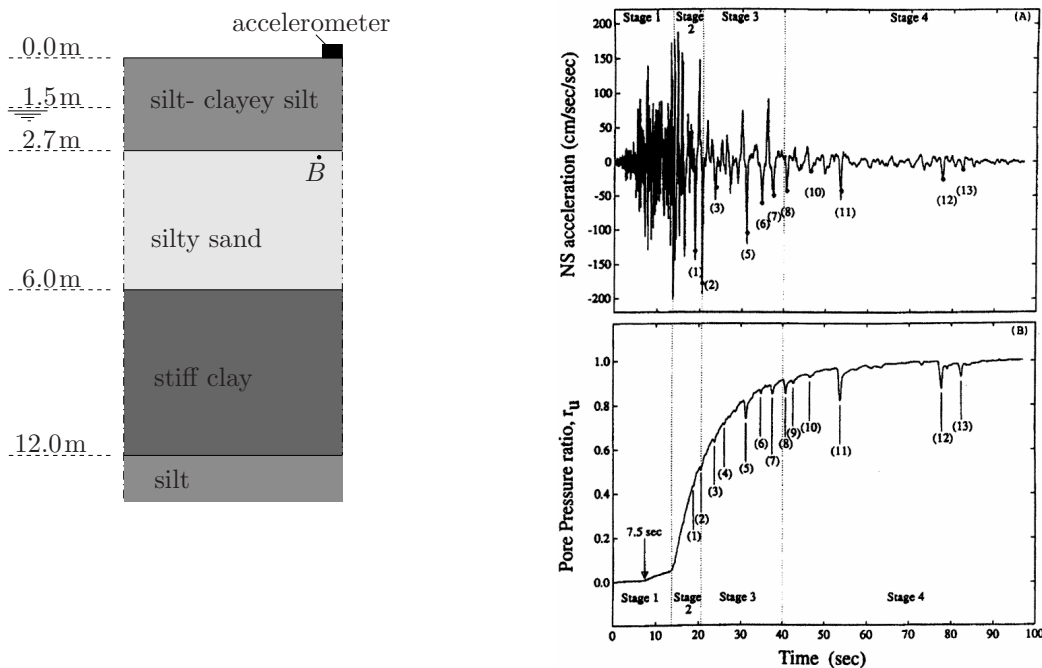


Figure 5.4: Wildlife Refuge site layers (left) and the measured surface acceleration together with the excess pore pressure at point B (right), cf. Zeghal & Elgamal [184]

The ground surface acceleration during Superstition Hills (SH)¹ earthquake is plotted in Figure 5.4, right-top. As an index for the initiation of the *in-situ* liquefaction under seismic shear loading, the excess pore-pressure ratio $|r_u|$ or simply r_u , which is defined as the ratio of the excess pore pressure to the initial effective vertical stress, is used. The value $|r_u| = 1$ is considered as a threshold referring to a decrease of the effective stress until zero value and an increase of the pore pressure until the whole vertical load is carried by the pore fluid upon collapse (cf. Wu *et al.* [181] and Tsuji *et al.* [167]). Figure 5.4, right-bottom, shows the sharp generation of the pore pressure at point B (2.9 m below the ground surface) until the flow liquefaction takes place when r_u attains the value 1.0.

¹Took place on November 24, 1987, with Richter magnitude $M = 6.6$.

In Figure 5.4, right, four stages of seismic response are observed: In stage (1) with $t \in [0 - 13.7 \text{ s}]$, both the ground acceleration and the pore-pressure build-up are low. Stage (2) with $t \in [13.7 - 20.6 \text{ s}]$ coincides with the strongest shocks and the rapid increase of the pore pressure, where $r_{\mathbf{u}}$ reaches the value 0.5. In stage (3) with $t \in [20.6 - 40 \text{ s}]$, lower peak accelerations but rapid increase of the pore pressure can be observed, which indicates a continuous contraction tendency. This behaviour is related to the loose nature of the silty sand layer as will be discussed in details in the following section. In stage (4), $r_{\mathbf{u}}$ attains the value 1.0, which corresponds to a flow liquefaction state. Herein, due to the incredible reduction of the effective stress, the saturated sand layer loses its nature as a solid material and flows like a viscous fluid.

5.2 Modelling of Liquefaction Phenomena

In the literature, liquefaction investigation can roughly be classified into three areas: Field observations and tests, laboratory experiments, and computational modelling. In this connection, *in-situ* tests help to understand different behaviours of soil under realistic material states and boundary conditions. The laboratory experiments, such as the cyclic triaxial and the simple shear stress test, enable to further investigate the liquefaction susceptibility and provide important material parameters for the constitutive models. Additionally, the numerical treatment of porous media dynamics using credible constitutive laws allows to realise the different liquefaction events and enables to extrapolate conditions that cannot be insured in laboratory testing.

In the realm of the plasticity theory, a number of material models have been tuned to simulate liquefaction-related events. For instance, within the critical state framework, the Cam-Clay model (Roscoe & Burland [151]) and the modified version of it are eligible to capture different liquefaction-conjugate soil behaviours such as the shear strength reduction and the plastic volumetric strain increase. The complex and eventually anisotropic response of porous materials under dynamic loading required the development of more advanced material models, which are mostly based on the Cam-Clay model. As examples, see the bounding surface model (cf. Ling *et al.* [118]) and the two-surface plasticity model of Manzari & Dafalias [122].

Another approach to soil liquefaction modelling, which is mainly based on phenomenological observations, is the densification model or the ‘generalised plasticity model’ introduced in the works by Zienkiewicz *et al.* [186, 187]. This model proceeds from giving a direct relation between the stress and the strain increments, where one distinguishes between the loading and the unloading stages, and there is no need to define a yield surface. Beside the densification model, the relatively recent theory of hypoplasticity shows an increasing popularity in the field of soil dynamics modelling among other fields of geomechanics. The hypoplasticity is also an incrementally nonlinear material model, which does not require the existence of a yield surface or the distinction between elastic and plastic strain increments. For details about this theory and its extensions, see, e. g., Kolymbas [106] or Niemunis [137].

The purpose of the following discussion is to investigate the ability and the performance

of the elasto-viscoplastic material model, that has been developed by Ehlers [53] and explained in Section 3.2.3 in capturing undrained porous media behaviours under monotonic and cyclic loading conditions for the sake of liquefaction modelling.

5.2.1 Elasto-Viscoplastic Material Law for Liquefaction Modelling

One of the important features of granular materials that needs to be captured in the modelling is the tendency to undergo volumetric strains under shear stresses. In drained triaxial tests, the total volumetric strain can be seen as a contractive or a dilative overall behaviour, and the total applied stress is equal to the effective stress as there is no pore fluid. Under perfectly undrained conditions, the total volumetric strain is zero for a fully saturated and materially incompressible biphasic medium. In this case, the applied deviatoric stress leads to a variation of the mean effective stress ($p' = -\frac{1}{3}I_\sigma$) and the pore pressure. Hence, according to the principle of effective stresses, the total stress is carried by the effective stress and the excess pore-fluid pressure, see, e.g., Lade [111] for details. Such features can be numerically captured by applying the considered elasto-viscoplastic material law (cf. Section 3.2.3) to simulate triaxial tests as initial-boundary-value problems, cf. Appendix B for details about the geometry and the parameters.

In the following treatment, the triaxial tests are assumed to be carried out in two steps: Firstly, by applying an isotropic, drained consolidation with $\sigma_1 = \sigma_2 = \sigma_3$ causing densification of the porous material specimen (Figure 5.5, segment A-B), and secondly, by imposing a cylindrical deviatoric stress ($\sigma_1 - \sigma_3$) with $\sigma_1 > \{\sigma_2 = \sigma_3\}$, which leads to a shear-induced volumetric strains, cf. Figure 5.5, segment B-C.

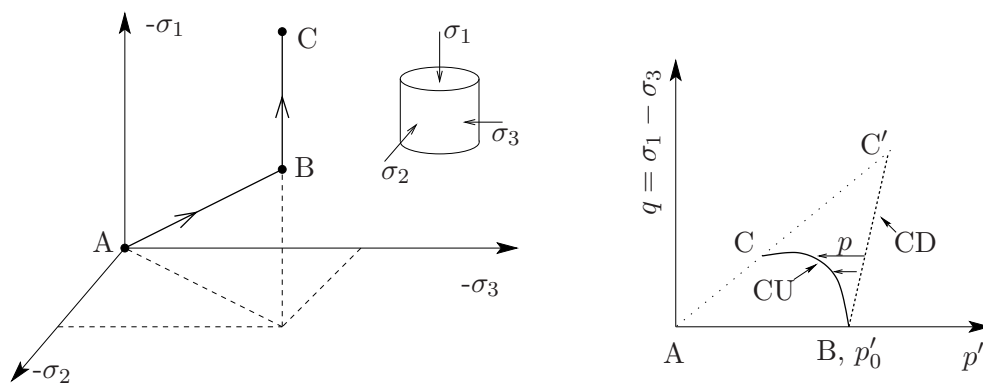


Figure 5.5: Isotropic consolidation (segment A-B) and deviatoric stress (segment B-C) in a triaxial device (left). Consolidated drained (CD) and consolidated undrained (CU) triaxial tests (right)

Moreover, depending on the defined boundary conditions of the triaxial device, two types of triaxial tests are distinguished in this thesis (cf. Figure 5.5, right): The consolidated drained (CD) with drained boundary throughout the whole steps of the experiment, and the consolidated undrained (CU) with drained boundary in the consolidation phase and

undrained boundary in the later deviatoric steps, cf., e. g., Zienkiewicz *et al.* [186]. Liquefaction is mostly considered as an undrained behaviour of saturated soils. Therefore, CU tests are of major interest in the later discussion. The CU test of saturated porous media is performed in two steps: (i) A drained consolidation step where a hydrostatic compression is applied to the specimen. (ii) An undrained deviatoric step where the drainage valve is closed to allow for a pore-pressure build-up. In this case, the test is usually carried out slowly enough to guarantee that the pore-pressure distribution is homogeneous over the specimen. Figure 5.5, right, illustrates how loose porous materials tend to compact under deviatoric stresses leading to an increase of the confining stress p' for the CD test. In the CU test, the compaction tendency is associated with an increase in the pore pressure and, thus, the stress path bends towards the origin of the p' - q diagram (decreasing of p').

Contractive and Dilative Behaviour

As have been discussed in Section 5.1, the behaviour of granular materials depends very much on the initial density. Under shear stress, a dense granular assemblage is expected to compact and then to dilate, whereas a very loose assemblage tends more likely to compact until collapse. In the current modelling, a non-associative flow rule for the plastic material behaviour is applied, cf. Section 3.2.3. Herein, the plastic potential function (3.59) and its parameters ψ_1, ψ_2 play a decisive role in the realisation of the contractive and the dilative behaviours. As a measure for the flow direction, the dilatancy angle ν is introduced, cf. Ehlers [53] or Müllerschön [134]:

$$\tan \nu := \frac{I_{\dot{\epsilon}_p}}{\|\dot{\epsilon}_{Sp}^D\|} = \frac{\dot{\epsilon}_{Sp} \cdot \mathbf{I}}{\sqrt{\dot{\epsilon}_{Sp}^D \cdot \dot{\epsilon}_{Sp}^D}} \xrightarrow{\text{with eq. (3.60)}} \tan \nu = \frac{\sqrt{3}}{\sqrt{2} \Pi_\sigma^D} \frac{\partial G / \partial I_\sigma}{\partial G / \partial \Pi_\sigma^D}. \quad (5.3)$$

Following this, if $\dot{\epsilon}_{Sp} \cdot \mathbf{I} > 0$ then the behaviour is dilative and the volumetric strain increases, whereas if $\dot{\epsilon}_{Sp} \cdot \mathbf{I} < 0$ then the volumetric strain decreases and the behaviour is contractive. If $\dot{\epsilon}_{Sp} \cdot \mathbf{I} = 0$, the material continues deforming at a constant volumetric strain, and the stress state is said to be found on a critical state line (CSL). The latter

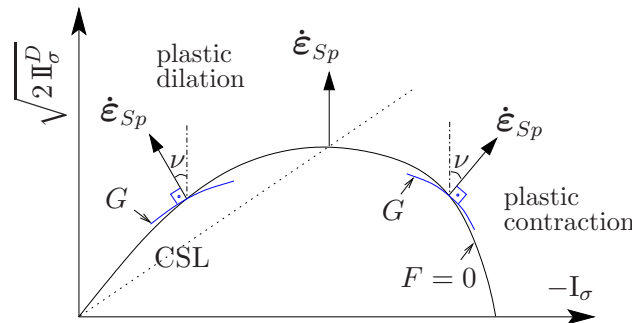


Figure 5.6: Illustration of contractive, dilative, and neutral behaviours of the non-associative flow rule with the help of the plastic potential function G , the yield function $F = 0$ and the critical state line CSL

ideas are illustrated in Figure 5.6, where additional details and similar discussions can be

found in the works by Pastor *et al.* [142] or Lade [111]. In the numerical modelling of a given granular assemblage, it is important for a good approximation of the experimental results to find appropriate values of the parameters ψ_1 and ψ_2 , which are related to the initial density.

5.2.2 Simulation of Triaxial Tests under Monotonic Loading

The triaxial IBVP and the material parameters in Appendix B together with the four cases of parameters in Table 5.1 will be used in the following treatment to simulate the behaviour of sand with various initial densities under drained and undrained conditions.

case	n_{0S}^S	n_{\max}^S	n_{\min}^S	Dr [%]	description w. r. t. Dr [%]		ψ_1	ψ_2
(1)	0.585	0.595	0.38	95	very dense	> 75	1.1	0.64
(2)	0.5	0.595	0.38	56	dense	50 – 75	0.5	0.5
(3)	0.45	0.595	0.38	33	moderate dense	30 – 50	0.5	0.3
(4)	0.4	0.595	0.38	9.5	very loose	< 15	0.4	0.1

Table 5.1: Sand with different initial densities (classifications according to the relative density $Dr := (n_{\max}^S - n_{0S}^S)/(n_{\max}^S - n_{\min}^S) \times 100$, cf. Möller [133]), which requires different plastic potential parameters

Here, cases (1) to (4) refer to the same sand but with different initial densities². In reality, changing the initial density affects the overall sand behaviour, which requires to modify most of the model parameters to capture the accurate response. However, this is beyond the scope of this work, which concentrates on describing the general granular behaviour without calibrating certain sand behaviour.

Drained Sand Behaviour under Monotonic Loading

Figure 5.7 depicts the numerical results of the four cases in Table 5.1 applied to the triaxial IBVP in Appendix B, as well as the experimental results for case (1) of a consolidated drained compression triaxial test.

In case (1) of a very dense sand, a good agreement with the experimental results (exp. (1)) can be obtained. Here, the deviatoric stress increases to a certain peak and then decreases as can be seen in Figure 5.7, left. Moreover, Figure 5.7, right, shows that the first part of the test undergoes a slight contraction until a minimum void ratio is attained. Thereafter, the material exposes a dilative behaviour until collapse. For a very loose sand as in case (4), the contraction tendency is dominant and no peak in the deviatoric stress can be observed. Following this, it is shown that the tendency of the granular assemblage to contract increases by decreasing the initial density. Herein, the influence of the initial

²The parameters in case (1) have been obtained in the laboratory of the Institute of Applied Mechanics, University of Stuttgart, using consolidated drained triaxial compression tests, cf. Avci & Ehlers [5], whereas ψ_1 and ψ_2 for cases (2)-(4) have been chosen by trial.

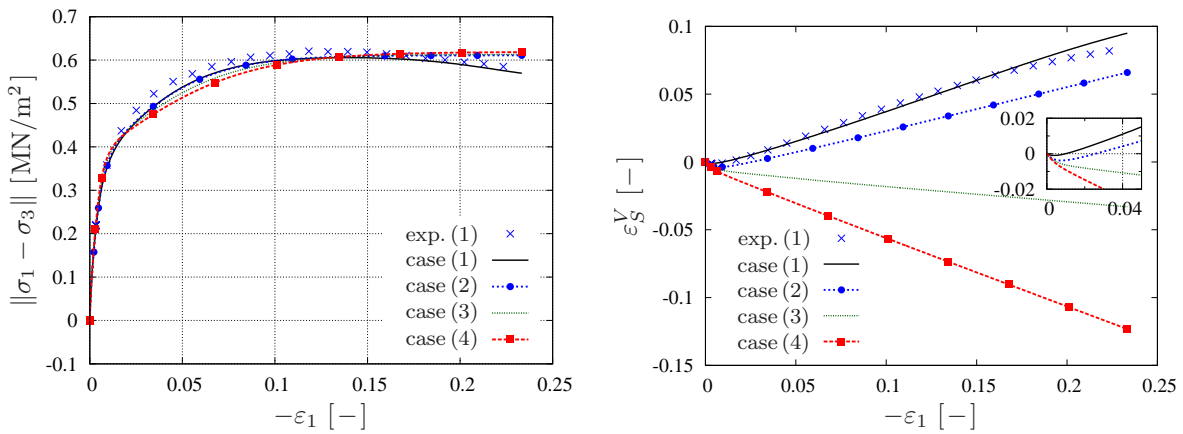
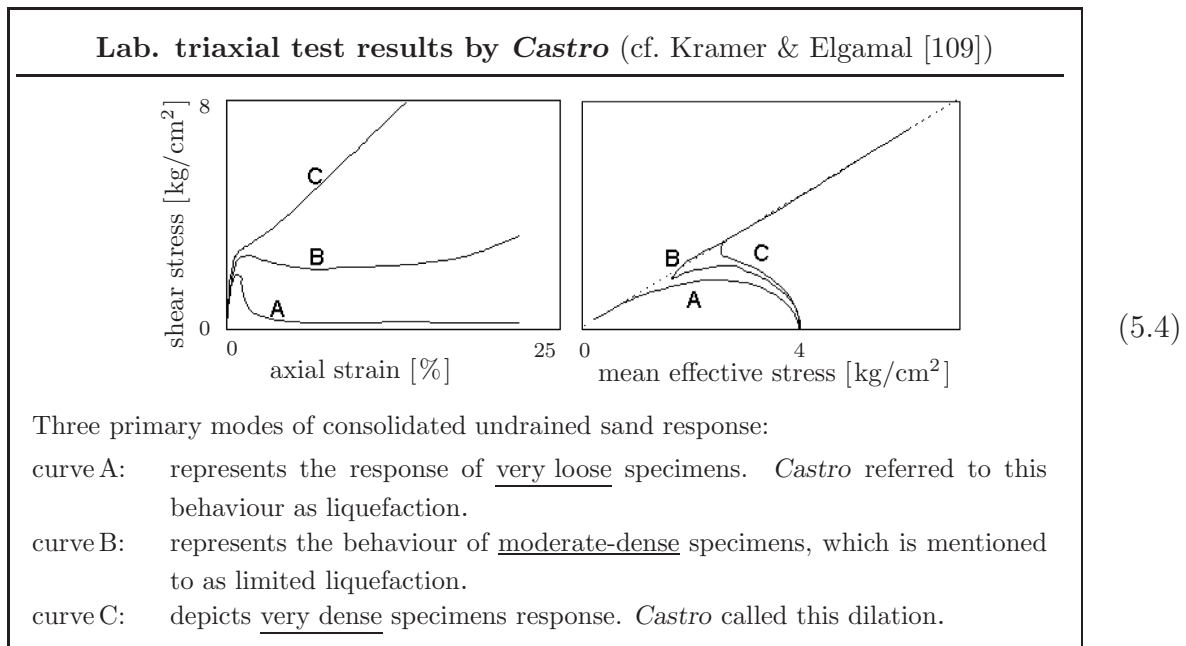


Figure 5.7: Experiment and numerical results of the drained compression triaxial test for the different parameter cases in Table 5.1

density on the behaviour can numerically be encountered by choosing proper ψ_1 and ψ_2 parameters of the plastic potential function as given in Table 5.1.

Undrained Sand Behaviour under Monotonic Loading

The understanding of liquefaction mechanisms primarily stems from laboratory observations. In this connection, Box (5.4) shows early results of CU triaxial tests carried out by *Castro* in the 1960s, who aimed to explain the behaviour of saturated sand during liquefaction events. The experiments were performed considering sands with different initial densities and, as a result, three distinctive modes of response were observed.



In what follows, numerical simulations are performed considering displacement-controlled triaxial tests under undrained conditions and four cases of initial densities, cf. Table 5.1.

The geometry and the other material parameters are given in Appendix B, where the considered behaviour is elasto-viscoplastic with isotropic hardening.

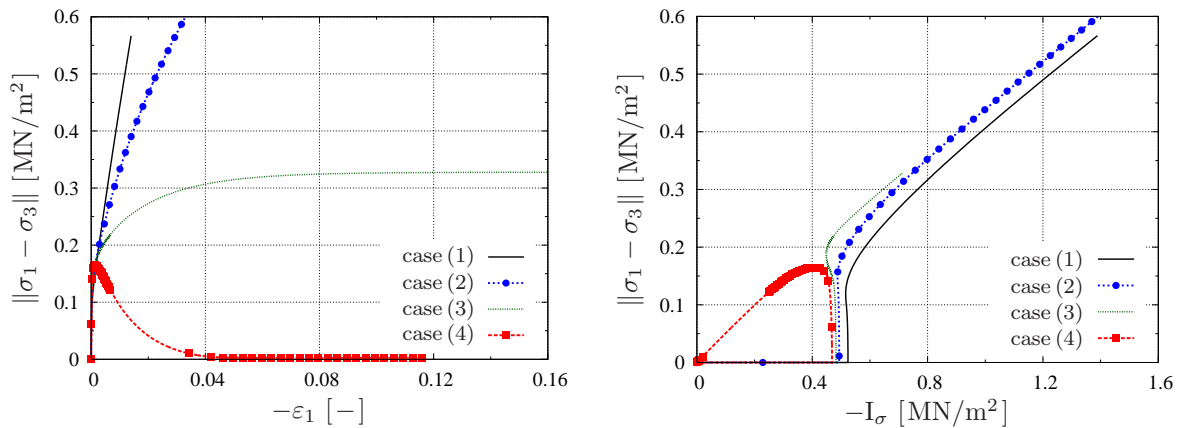


Figure 5.8: Numerical results of undrained triaxial compression tests for the different cases in Table 5.1

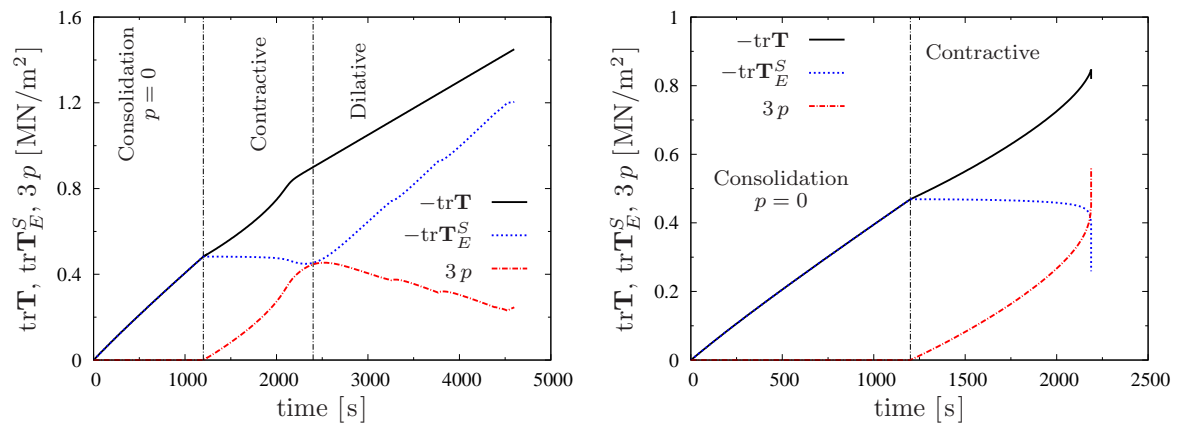


Figure 5.9: Effective stress and pore pressure changes in undrained triaxial compression tests for case (3) of moderate-dense sand (left), and for case (4) of very loose sand (right)

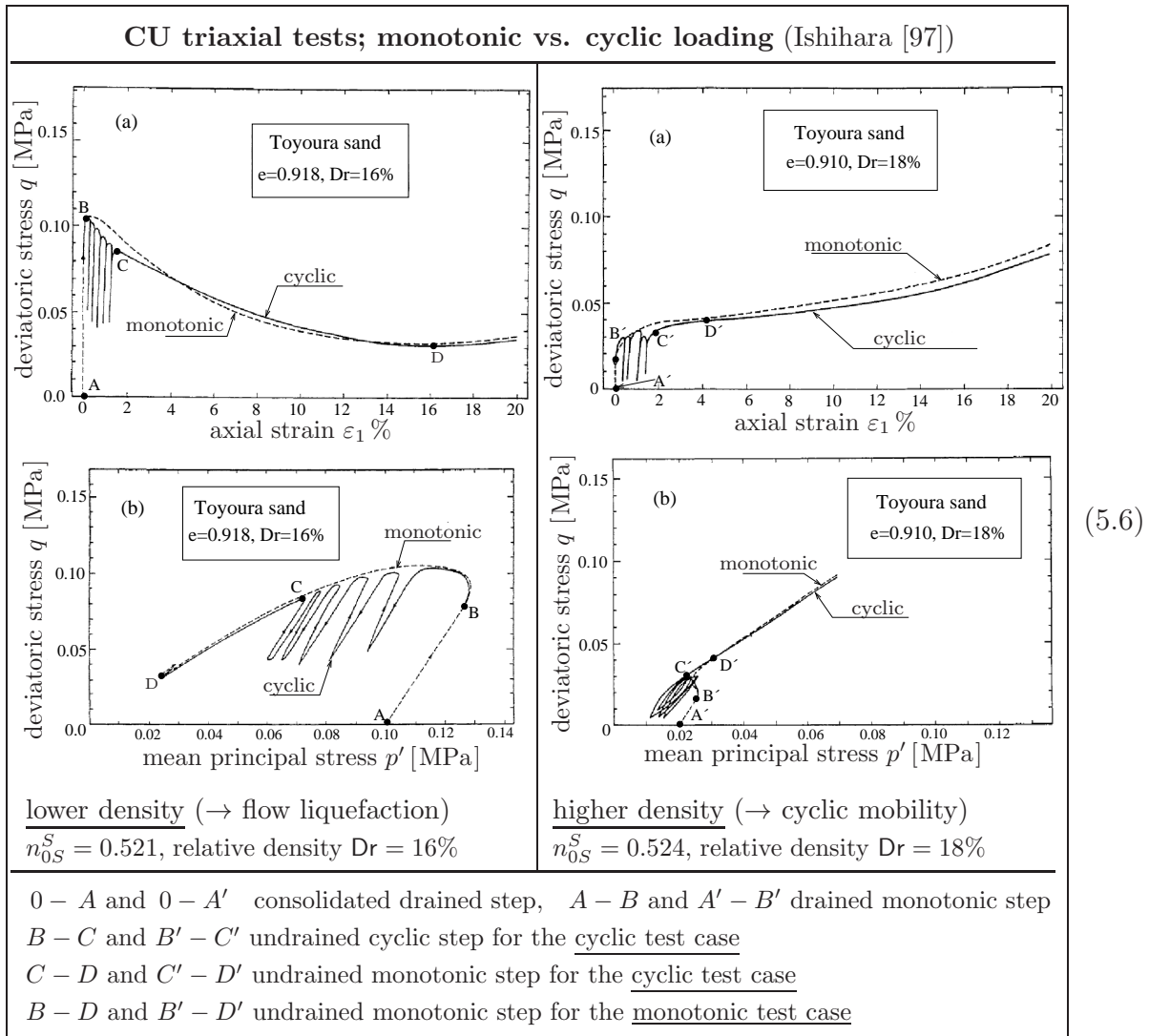
Under monotonic deviatoric stress, Figure 5.8 shows that cases (1) and (2) of very dense to dense specimens experience a short period of contraction, which causes a slight increase of the pore-fluid pressure. This phase is followed by a continuous dilation, leading to a decrease of the pore pressure and an increase of the mean effective stress. Considering the specimens with moderate density in case (3), the initial response is contraction with an accumulation of the pore pressure, which is followed by a phase of immense increase in the axial strain accompanied with a slight change in the shear stress and the mean effective stress until collapse. This type of behaviour corresponds, according to the definitions in Box (5.2), to the cyclic mobility when the applied load is cyclic. In this regard, case (4) in Figure 5.8 represents the flow liquefaction behaviour. Therein, the very loose sample exhibits a peak deviatoric stress followed by a serious decrease in the shearing resistance and a continuous build-up of the pore pressure until the collapse is attained. Kramer & Elgamal [109] indicated that the latter behaviour can be reached when the structure of

the soil skeleton breaks down. The relation between the pore pressure and the volumetric deformations can be explained based on the effective stress principle, viz.:

$$(\mathbf{T}^S + \mathbf{T}^F) \cdot \mathbf{I} = \mathbf{T}_E^S \cdot \mathbf{I} - p \mathbf{I} \cdot \mathbf{I} \quad \longrightarrow \quad \text{tr } \mathbf{T} = \text{tr } \mathbf{T}_E^S - 3p. \quad (5.5)$$

Therefore, the interplay between the mean effective stress and the excess pore pressure for cases (3) and (4) is depicted in Figure 5.9. For case (3) of moderate-dense specimens, Figure 5.9, left, shows a phase transformation state between the contractive and the dilative phases, where the excess pore pressure and the effective stress reverse their behaviours. In the dilative tendency stage, the applied load is increasingly carried by the effective stress, whereas the pore pressure dissipates. Figure 5.9, right, shows how the effective stress reduces and the pore pressure increases until the flow liquefaction takes place. When the effective stress becomes equal to zero, the whole applied stress is carried by the pore fluid.

5.2.3 Undrained Sand Behaviour under Cyclic Loading



Under cyclic loading, saturated sand undergoes liquefaction with patterns similar to that observed under monotonic loading. Using experimental results of anisotropically consolidated undrained triaxial tests, Ishihara [97] showed that the cyclic behaviour of saturated sand (for the sake of seismic-induced liquefaction modelling) can be well understood by comparison with the behaviour under monotonic loading conditions, cf. Box (5.6).

In Box (5.6), the investigation of undrained sand considers two cases of initial density: A low-dense sand, which undergoes flow liquefaction, and a moderate-dense sand that exposes a cyclic mobility behaviour. Under cyclic loading, saturated sand undergoes liquefaction with patterns similar to that observed under monotonic loading.

Employing the elasto-viscoplastic constitutive model as introduced in Section 3.2 with isotropic hardening and in analogy to the works by Ishihara [97] and Ishihara *et al.* [98], it is possible to follow the excess pore-pressure development and the onset of liquefaction events under cyclic loading with irregular amplitudes. If the unloading-reloading process is carried out inside the yield surface of the elasto-viscoplastic model, then the response is governed by the hyperelastic material law. In this case, the reloading process follows the same path as the unloading process and only oscillatory but not accumulative pore-pressure behaviour can be detected. Whenever a plastic yielding occurs, a permanent change in the pore pressure and the effective stress takes place. In particular, the accumulation of the pore pressure and the onset of liquefaction phenomena are mainly governed by the volumetric strains in the plastic range.

In the present work, the flow liquefaction and the cyclic mobility are numerically figured out using an initial-boundary-value problem (IBVP) that represents the triaxial test. Here, the material parameters are chosen for a sand with two different initial densities: A very loose sand as in case (4), Table 5.1, and a sand with moderate density as in case (3), Table 5.1. The geometry of the IBVP and the other material parameters are given in Appendix B, whereas the applied loads are illustrated in Figure 5.10, left, and Figure 5.12, left. The *Neumann* boundary conditions in this investigation are chosen in analogy to those in Box (5.6), viz.:

$$\begin{aligned}
 0 - A & \text{ consolidated drained step,} \\
 A - B & \text{ drained deviatoric step (anisotropic consolidation),} \\
 B - C & \text{ undrained monotonic step for the monotonic CU test,} \\
 B - D & \text{ undrained cyclic step for the cyclic CU test.}
 \end{aligned}
 \tag{5.7}$$

The excess pore pressure in case of a very loose sand is depicted in Figure 5.10, right.

Here, when the unloading-reloading step crosses the yield surface, an accumulation of the pore pressure accompanied by a volumetric plastic deformation can be observed.

Figure 5.11 shows the flow liquefaction behaviour under irregular cyclic loading, where the last loading cycle leads to the same pattern as for the monotonic loading, see, Figure 5.8, case (4). The latter results are comparable with what has been presented in Box (5.6) for a low-dense sand.

In this connection, very loose sand is a highly contractive material under deviatoric stress, which leads to a continuous pore-fluid pressure accumulation until collapse. This happens

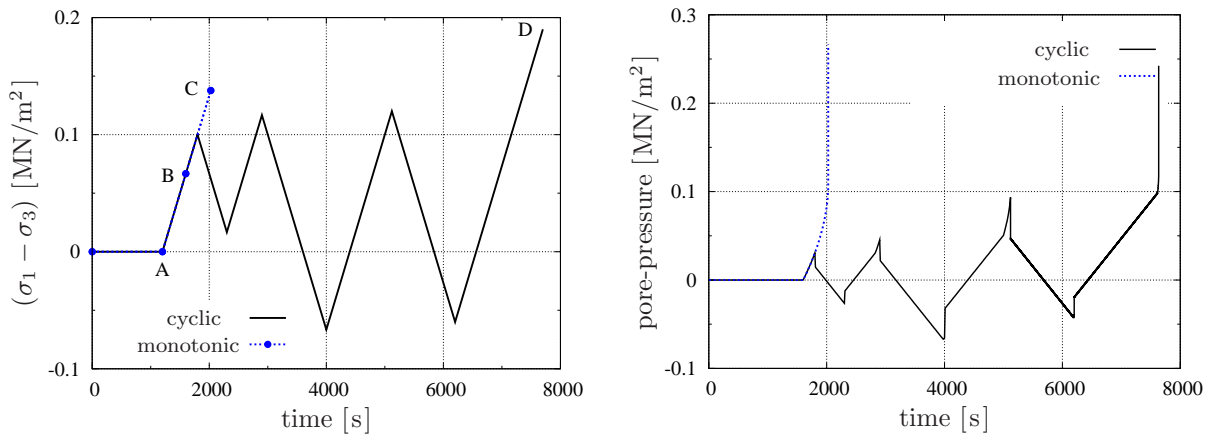


Figure 5.10: Loading path with boundary conditions according to (5.7) (right) and pore-pressure build-up during the cyclic triaxial test (left) for a very loose sand

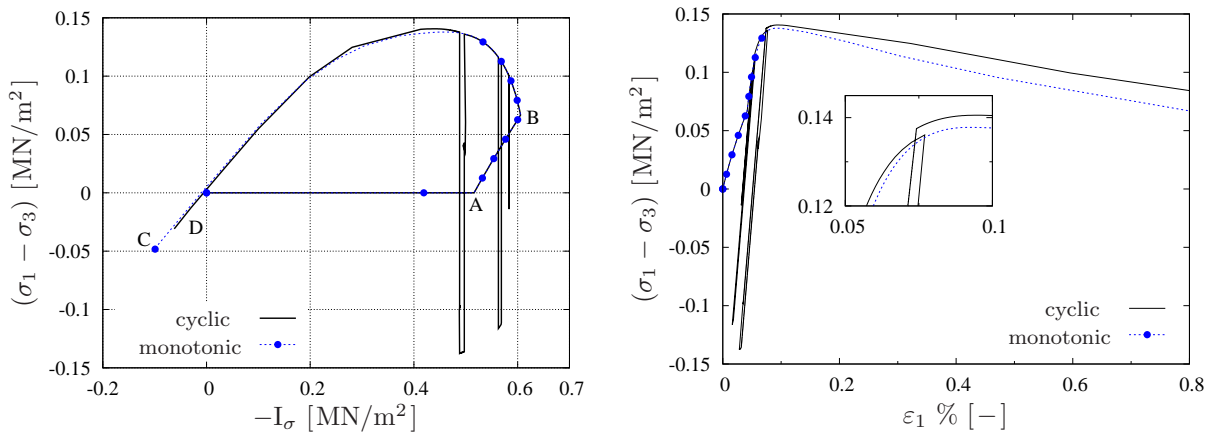


Figure 5.11: Mean effective stress versus deviatoric stress (left) and axial strain versus deviatoric stress (right) under cyclic and monotonic loading for a loose sand

when the stress state is found on the yield surface in both the compression and the extension sides. Here, before the deviatoric stress reaches a peak value, the pore pressure can still be relatively low. After the deviatoric stress attains its maximum value, the pore pressure and the axial strain rapidly increase, which corresponds to a collapse of the solid skeleton.

The pore pressure behaviour for the case of moderate-dense sand under undrained conditions is depicted in Figure 5.12, right. Here, the tendency to contraction under deviatoric stress is limited, which prevents the occurrence of the flow liquefaction. Moreover, Figure 5.12, right, shows that the last cycle causes the pore pressure to increase and then to decrease, which refers to a contractive and then to a dilative behaviour.

Similar to the laboratory-based observations of *Ishihara* in Box (5.6), the numerical results of the considered elasto-viscoplastic model (Figure 5.13) show that at a relatively low stress ratio³, the granular material exposes a contractive tendency allowing for a reduction in the effective stress and a limited plastic strain. Such a behaviour happens when the

³stress ratio = $(\sigma_1 - \sigma_3)/I_\sigma(t_0)$.

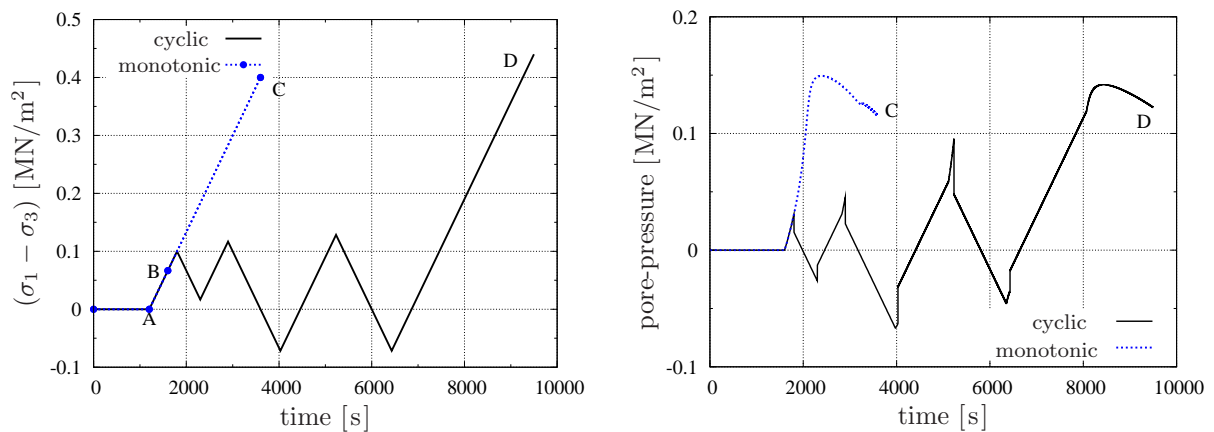


Figure 5.12: Loading path with boundary conditions according to (5.7) (right) and pore-pressure build-up during triaxial shear test (left) for the case of a moderate-dense sand

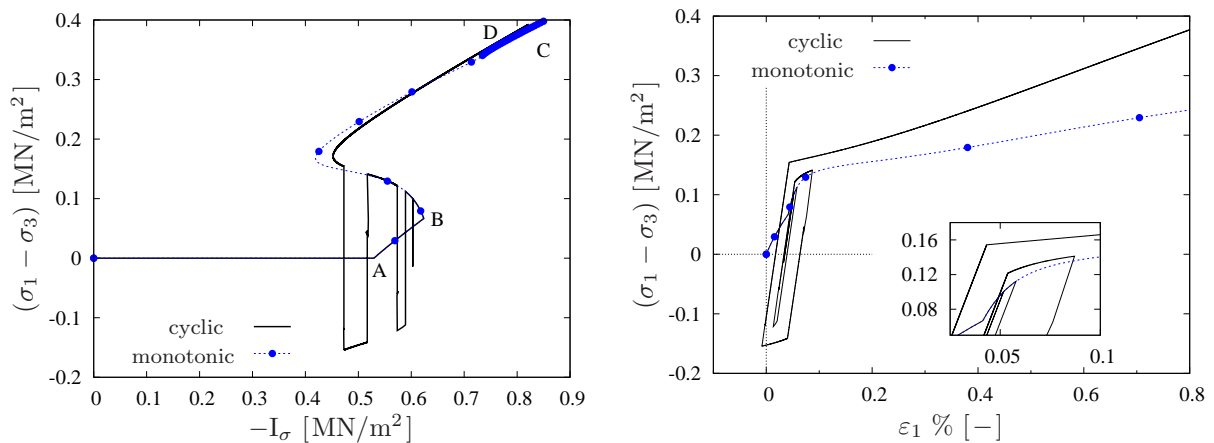


Figure 5.13: Mean effective stress versus deviatoric stress (left) and axial strain versus deviatoric stress (right) under cyclic and monotonic loading for a moderate-dense sand

stress state is found in the extension or the compression sides of the yield surface due to cyclic loading. At a higher stress ratio, the behaviour switches from contractive to dilative. This corresponds to the phase transformation state (Box (5.2)), where significant shear strain occurs at almost constant deviatoric stress.

Remark: The realisation of the unloading-reloading behaviour of saturated porous media under undrained conditions is an important step towards the modelling of seismic-induced liquefaction events, cf. Section 6.4 for an example.

5.2.4 Additional Factors Affecting the Dynamic Response of Saturated Granular Media

In the following, a number of important factors that affect the response of saturated porous media dynamics and can be modelled using the considered material model are discussed. Those factors are tested on an IBVP that lead to a plastic strain localisation and solved

with the coupled FE solver PANDAS. The geometry and the boundary conditions of this problem are illustrated in Figure 5.14, and the balance relations are the coupled PDE (3.45) describing a biphasic medium with materially incompressible constituents. Moreover, the considered solid skeleton response is elasto-viscoplastic with isotropic hardening (Section 3.2). The material parameters are given in Appendix B and only the case of very loose sand (cf. Table 5.1) is taken into account.

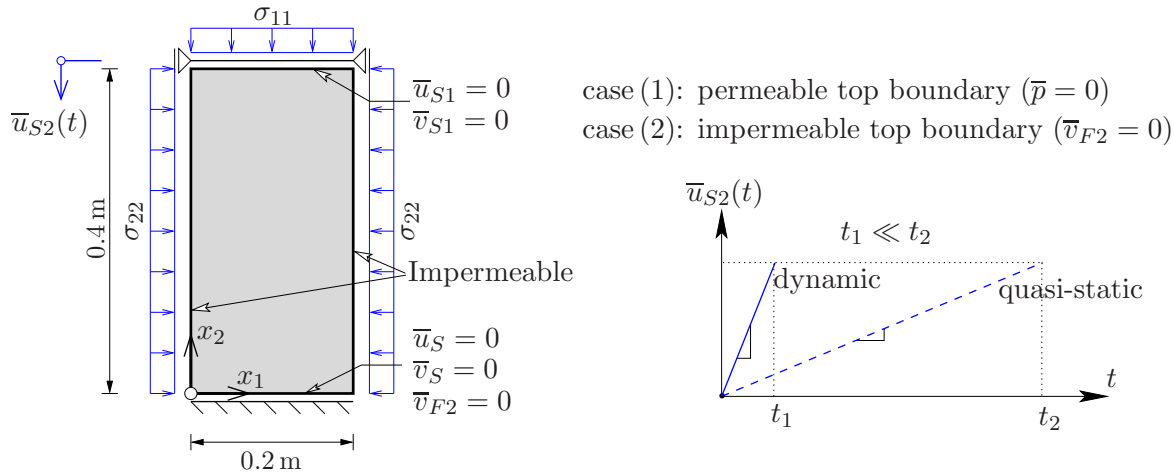


Figure 5.14: The geometry and the boundary conditions (left) and the applied displacements (right) of the strain localisation problem

The first step in the problem is to apply an isotropic consolidation with $\sigma_{11} = \sigma_{22} = 100$ kPa. The consolidation is carried out very slowly and with drained top boundary ($p = 0$) so that no accumulation in the pore pressure can occur. To examine the effect of the loading rate, a fast (dynamic) or a slow (quasi-static) displacement (equation (5.8)) is applied in the second step to the top of the domain until collapse.

$$\bar{u}_{S2}(t) = \begin{cases} -1.0 \times 10^{-6} t \text{ m} & \leftrightarrow \text{quasi-static,} \\ -1.0 \times 10^{-2} t \text{ m} & \leftrightarrow \text{dynamic.} \end{cases} \quad (5.8)$$

The influence of the boundary drainage is tested by varying the permeability of the top boundary under dynamic loading conditions. Additionally, the effect of the microstructure on the response is examined by using different values of the permeability parameter k^F . Details about strain localisation problems can be found in the works by Oka *et al.* [140] and Kimoto *et al.* [105] among others.

Loading Rate Effect: Quasi-Static vs. Dynamic

Most factors affecting soil behaviour are equally important under both dynamic and quasi-static loading conditions. However, the significant character of the dynamic behaviour is the inertia force, which cannot be neglected, and its importance increases with the increase of the loading application rapidity. In Figure 5.15, several events of engineering significance are classified in accordance with the nature of the applied loading, i. e. the

number of cycles per time of loading. For instance, the period for each impulse of seismic loading is within the range of 0.1 to 3.0 seconds (cf. Ishihara [97]), which corresponds to a frequency of 0.3 to 10 Hz.

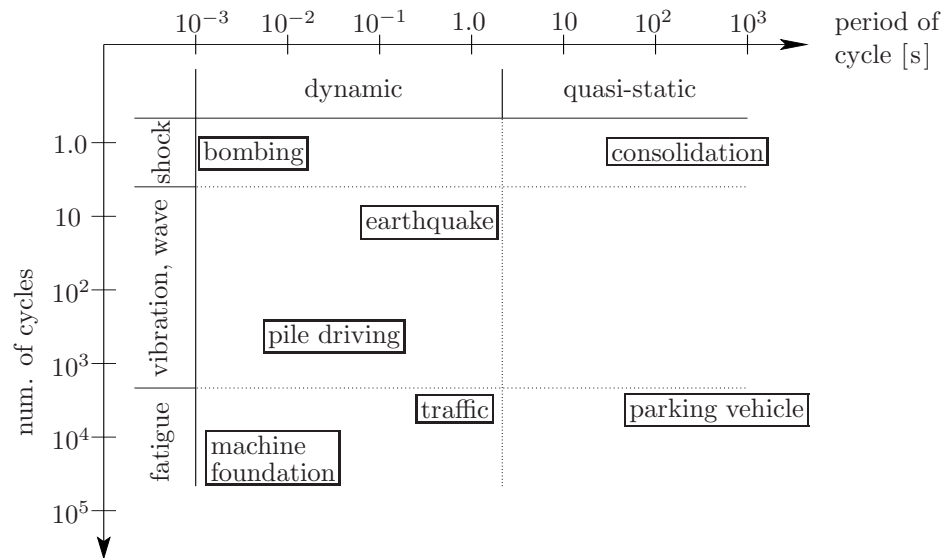


Figure 5.15: Classification of engineering problems in accordance with the loading frequency into dynamic and quasi-static, cf. Ishihara [97]

To understand the dependency of liquefaction occurrence on the rate of the applied displacement (dynamic or quasi-static), the problem which is introduced in Figure 5.14 is analysed using the displacement relations (5.8). Therein, the rate in the dynamic case is $\dot{\bar{u}}_{S2} = -1.0 \times 10^{-2}$ m/s and in the quasi-static case $\dot{\bar{u}}_{S2} = -1.0 \times 10^{-6}$ m/s.

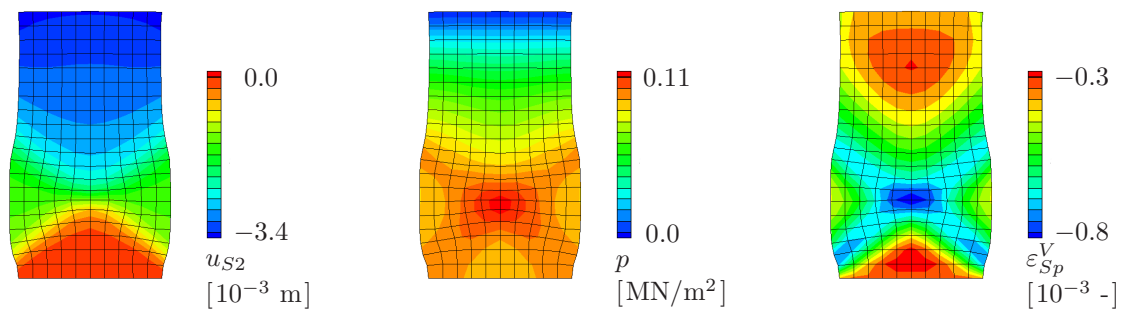


Figure 5.16: Vertical displacement u_{S2} , excess pore pressure p and plastic volumetric strain ϵ_{Sp}^V for a very loose sand and top permeable boundary. The applied deformation is dynamic according to Eq. (5.8) and $k^F = 10^{-6}$ m/s (deformed mesh scale factor 10)

Figure 5.16 shows exemplary contour plots of the computed vertical displacement u_{S2} , excess pore-pressure distribution p and plastic volumetric strain ϵ_{Sp}^V under dynamic loading condition and top permeable boundary. Here, the pore-pressure build-up is accompanied by the plastic volumetric strain (permanent contraction tendency of loose sand), which indicates the probable location of the flow liquefaction event. Under the same boundary conditions except for the applied loading rate, which is now quasi-static, Figure 5.17

shows similar plastic volumetric strain distribution as in Figure 5.16. However, a different pore-pressure distribution is obtained. This is because under quasi-static conditions, the excess pore pressure in a certain location has the time to dissipate through the drained boundary or into neighbouring locations of less accumulated pore pressure.

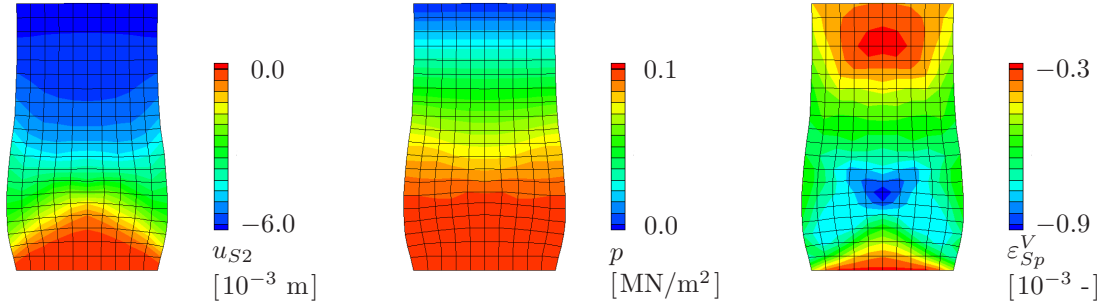


Figure 5.17: Vertical displacement u_{S2} , excess pore-pressure p and plastic volumetric strain ε_{Sp}^V for a very loose sand and top permeable boundary. The applied deformation is quasi-static according to Eq. (5.8) and $k^F = 10^{-6}$ m/s (deformed mesh scale factor 5)

Boundary Drainage Effect

Figure 5.18 shows contour plots of the computed vertical displacement u_{S2} , excess pore-pressure distribution p and plastic volumetric strain ε_{Sp}^V under dynamic loading condition and top impermeable boundary ($\bar{v}_{F2} = 0$). It is obvious from comparing Figure 5.16 with Figure 5.18 that the top impermeable specimen under dynamic loading behaves almost the same like the top permeable specimen under dynamic conditions. However, a shift in the volumetric plastic strain and the excess pore-pressure regions can be observed due to the top boundary drainage.

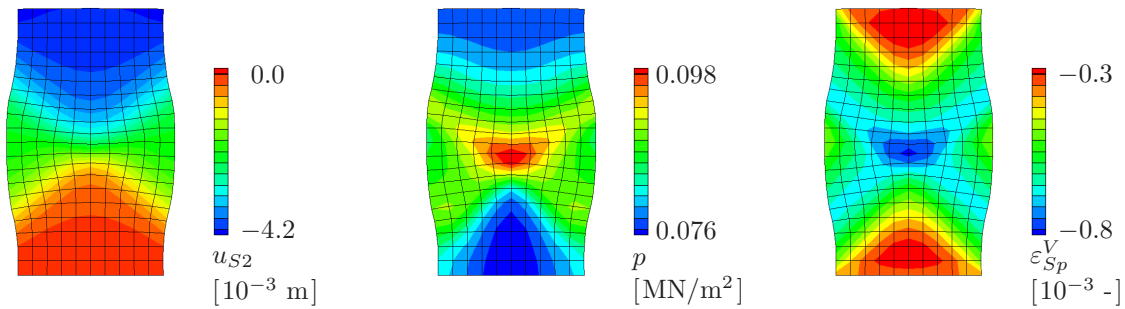


Figure 5.18: Vertical displacement u_{S2} , excess pore-pressure p and plastic volumetric strain ε_{Sp}^V for a very loose sand and top impermeable boundary. The applied deformation is dynamic according to Eq. (5.8) and $k^F = 10^{-6}$ m/s (deformed mesh scale factor 10)

Influence of the Microstructure

The microstructure of a granular material affects liquefaction susceptibility in different ways. For instance, grain sizes play an important role in the response pattern, where

fine and uniform sands are believed to be more liquefaction prone than coarse sands, cf. Prakash [144]. Another factor, which is related to the microstructure, is the length of the micro-channels with respect to the pore diameter. Here, under quickly-applied loading, the long drainage path causes the specimens to behave almost like under perfectly undrained conditions. In the considered macroscopic modelling, the microtopology information of the granular material is included in the permeability parameter. Consequently, the liquefaction susceptibility increases by decreasing the value of the permeability material parameter.

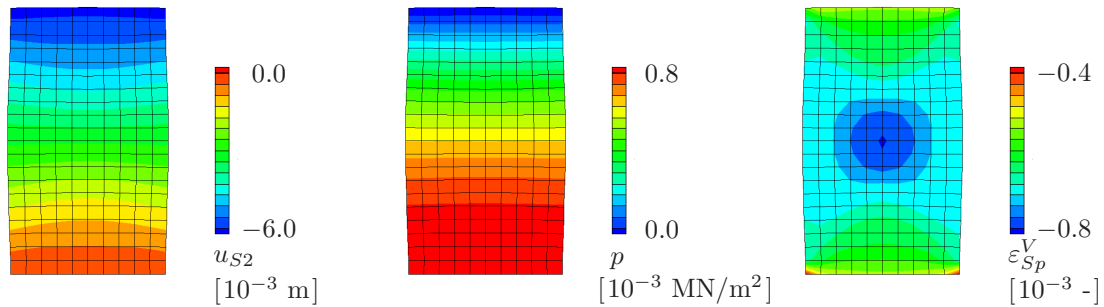


Figure 5.19: Vertical displacement u_{S2} , excess pore-pressure p and plastic volumetric strain ϵ_{Sp}^V for a very loose sand and top permeable boundary. The applied deformation is dynamic according to Eq. (5.8) and $k^F = 10^{-2}$ m/s (deformed mesh scale factor 10)

Back to the numerical example in Figure 5.14, two cases under the same applied dynamic loading but different permeability parameters are compared. Figure 5.19 shows contour plots of the computed quantities u_{S2} , p and ϵ_{Sp}^V with top permeable boundary and permeability parameter of $k^F = 10^{-2}$ m/s. Comparing Figure 5.19 with the lower permeability case ($k^F = 10^{-6}$ m/s) in Figure 5.16, where all the other boundary conditions and parameters are the same, shows that no significant region for the accumulated pore pressure can be seen in Figure 5.19. This is because under higher permeability, the pore fluid can easily escape from the domain. Such behaviour is usually found in coarse saturated grain assemblage or in thin soil layers with short drainage path.

Chapter 6:

Numerical Applications and Solution Schemes

This chapter is devoted to assess the performance of the foregoing discussed computational models with different formulations and solution strategies in representing the developer's conceptual description of dynamic porous media responses and the ability to simulate the real world behaviour (model verification and validation). For this purpose, comparisons and calibrations are carried out by applying the various cases of balance relations, solution algorithms, and constitutive laws to four initial-boundary-value problems. Moreover, considerable efforts are made to show the merits and the drawbacks of the solution schemes and to detect the instability sources in order to avoid them or to suggest stabilisation techniques.

In the numerical examples, certain abbreviations are used for the test cases. Most of those abbreviations are illustrated in Table 6.1.

Abbr.	Prim. variables	Governing equations	Solution algorithm
uvp(1)	$\mathbf{u}_S, \mathbf{v}_F, p$	set (3.44) / DAE (4.40)	implicit monolithic (4.50)
uvp(2)	$\mathbf{u}_S, \mathbf{v}_F, p$	set (3.45) / DAE (4.42)	implicit monolithic (4.50)
uwp	$\mathbf{u}_S, \mathbf{w}_F, p$	set (3.45) / DAE (4.45)	implicit monolithic (4.50)
uvp(α)	$\mathbf{u}_S, \mathbf{v}_F, p$	DAE (4.42) + (4.44)	implicit monolithic (4.50)
up	\mathbf{u}_S, p	set (3.46) / DAE (4.46)	implicit monolithic (4.50)
uvp(pc)	$\mathbf{u}_S, \mathbf{v}_F, p$	equations (4.2)	semi-explicit-implicit (4.79)
uvp(β)	$\mathbf{u}_S, \mathbf{v}_F, p$	equations (4.2)+ (4.85)	semi-explicit-implicit (4.79)

Abbr.	Time integration	Abbr.	Approximation order of primary variables
BE	backward Euler	QL	$\mathbf{u}_S, \mathbf{v}_S$: quadratic; $\mathbf{v}_F/\mathbf{w}_F, p$: linear
TR	trapezoidal rule	LL	$\mathbf{u}_S, \mathbf{v}_S$: linear; $\mathbf{v}_F/\mathbf{w}_F, p$: linear
TB2	TR-BDF2	QQ	$\mathbf{u}_S, \mathbf{v}_S$: quadratic; $\mathbf{v}_F/\mathbf{w}_F, p$: quadratic

Table 6.1: Abbreviations for the different governing equations and numerical schemes. For instance, uvp(2)-TB2-QL stands for the treatment of the \mathbf{u}_S - \mathbf{v}_F - p formulation based on the space-discrete equations (4.42) and using the TR-BDF2 implicit monolithic time-integration scheme together with mixed quadratic-linear finite elements

Different numerical libraries are used for the application of the above mentioned schemes and formulations. For instance, the implicit monolithic DIRK time-stepping algorithm

(4.50) is implemented in the C-based FE package PANDAS¹, whereas a FE Scilab² code is used for the monolithic explicit strategy and the predictor-corrector splitting algorithm (4.79). Due to the differences in the built-in functions between the packages PANDAS and Scilab, the comparisons are mainly confined to the accuracy and the stability attitudes.

6.1 Saturated Poroelastic Half-Space under Harmonic Loading

In this example, an elastic, infinitely long column taken from an unbounded half-space is analysed under plane strain conditions. The top boundary is perfectly drained and the lateral boundaries are impermeable, frictionless, but rigid (cf. Diebels & Ehlers [44]). The applied load and the boundary conditions are illustrated in Figure 6.1, where different cases of spatial discretisation are provided.

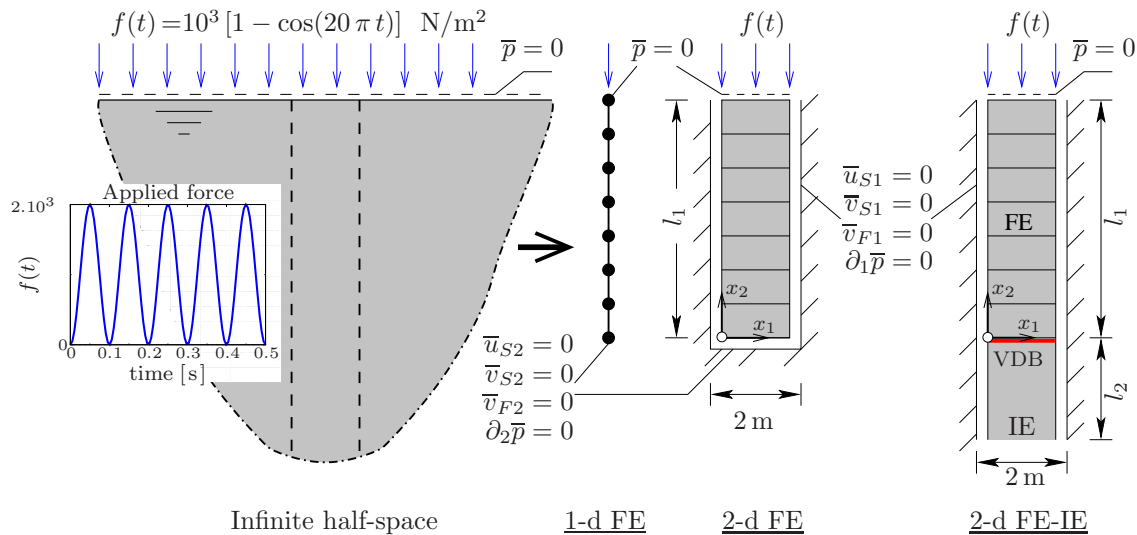


Figure 6.1: From left to right, geometry of the infinite porous media half space, one-dimensional FE discretisation with fixed bottom boundary, two-dimensional FE discretisation with fixed bottom boundary, and two-dimensional FE discretisation with IE at the bottom boundary together with VDB

The material parameters in Table 6.2 are taken from the literature for poroelastic isotropic soil dynamics, cf. de Boer *et al.* [22]. Additionally, in the case of a materially incompressible biphasic medium, an analytical solution for an infinite half space via *Laplace* transform is provided, which is used for the verification of different numerical solutions.

The discussion in this example considers only linear elastic material behaviour and can roughly be divided into three themes: (1) For materially incompressible biphasic aggregates, different implicit monolithic and splitting time-stepping strategies are analysed and

¹Porous media Adaptive Nonlinear finite element solver based on Differential Algebraic Systems, cf. [<http://www.get-pandas.com>].

²Scientific free software package for numerical computations, cf. [<http://www.scilab.org>].

Parameter	Symbol	Value	SI unit
1 st Lamé constant of the solid skeleton	μ^S	$5.583 \cdot 10^6$	N/m ²
2 nd Lamé constant of the solid skeleton	λ^S	$8.375 \cdot 10^6$	N/m ²
effective solid density	ρ^{SR}	2000	kg/m ³
effective fluid density	ρ^{FR}	1000	kg/m ³
initial solidity	n_{0S}^S	0.67	-
Darcy permeability	k^F	$10^{-1}, \dots, 10^{-10}$	m/s

Table 6.2: Material parameters of saturated elastic soil used in the examples [22]

compared, cf. Table 6.1 . (2) For the hybrid biphasic model with a compressible pore fluid, the numerical stiffness of the arising ODE system is discussed through comparing explicit with implicit monolithic schemes. (3) The unbounded boundary domain modelling using the viscous damping boundary (VDB) scheme is investigated in detail.

6.1.1 Comparison of Implicit Monolithic and Splitting Schemes

The objective of this part of the work is to compare the results of the aforementioned different schemes in Table 6.1 with the analytical solutions for the solid displacement and the pore-fluid pressure of an infinite half space under dynamic loading. Here, two values of the Darcy permeability are taken into account, which are the case of high permeability with $k^F = 10^{-2}$ m/s and the case of moderately low permeability with $k^F = 10^{-5}$ m/s. It is worth mentioning that the latter value of k^F is the lowest permeability for which the analytical solutions could be achieved using the build-in integrators of the software Maple. The considered geometry for the IBVP of this part is the 2-d FE, Figure 6.1, where $l_1 = 10$ m and only the FEM is regarded. The results in this section have been published in the works by Markert *et al.* [126] and Heider *et al.* [86].

In the numerical treatment of the considered uniaxial problem, it is noticed that the solutions are not very sensitive to the applied implicit monolithic time-stepping scheme. Therefore, only the TR-BDF2 (TB2) is used for the monolithic time integration. Following this, the main focus is laid on the comparison of uvp(2)-TB2 as the best choice for solving the coupled problem monolithically (see the two-dimensional problem in Section 6.2) with the semi-explicit-implicit solution uvp(pc). Additionally, the results for the monolithic treatment of the reduced \mathbf{u}_S - p formulation up-TB2 are provided. In this context, the solutions proceed from isotropic meshes with uniform and fully integrated quadrilateral elements, where several refinement levels from 1 to 50 elements per meter of problem height are considered. This requires a respective choice of the time-step size ($\Delta t \approx \Delta t_{cr}$) for the semi-explicit-implicit scheme by virtue of the CFL condition (4.81). In particular, the calculated and applied time steps are provided in Table 6.3.

In the semi-explicit-implicit treatment, an exact calculation of Δt_{cr} that fulfils the CFL condition can be obtained using, for instance, the *von Neumann* stability analysis. For our

#elements/meter	1	5	10	15	20	30	40	50
Δt_{cr} (CFL) [10^{-3} s]	5.5	1.5	0.78	0.53	0.4	0.27	0.2	0.16
Δt (pc) [10^{-3} s]	5.0	1.0	0.5	0.25	0.25	0.2	0.1	0.1
#DOFs uvp-LL	154	714	1414	2114	2814	4214	5614	7014
#DOFs uvp-QL	278	1318	2618	3918	5218	7818	10418	13018
#DOFs uvp-QQ	371	1771	3521	5271	7021	10521	14021	17521
#DOFs up-QL	234	1114	2214	3314	4414	6614	8814	11014

Table 6.3: The considered time-step sizes for the splitting scheme and the number of nodal unknowns for different quadrilateral FE discretisations of the 2d-FE, Figure 6.1. Note that uvp(pc)-LL requires additional expenses for the discretisation of the intermediate velocities

particular problem of poroelastic media, Zinatbakhsh [193] showed that the critical time steps, which result from the *von Neumann* analysis agree with that resulting from the approximate relations (4.81) used throughout this thesis (Table 6.3). Here, as mentioned in Section 4.3.2, the CFL condition provides an upper limit for the time-step size as a necessary but not sufficient requirement for the stability, see also Zinatbakhsh *et al.* [194] for additional details.

Starting with the high permeability case ($k^F = 10^{-2}$ m/s), equal-order interpolations can be applied to all the primary variables of the implicit monolithic schemes as well as of the splitting method, cf. Section 4.2.2. Moreover, it is not necessary to use pressure stabilisation of the monolithic strategies for the equal-order ansatz functions. For a point at the top of the domain, Figure 6.2, left, shows that the different formulations yield solid displacement fields that converge to the analytical solution u_{ref} .

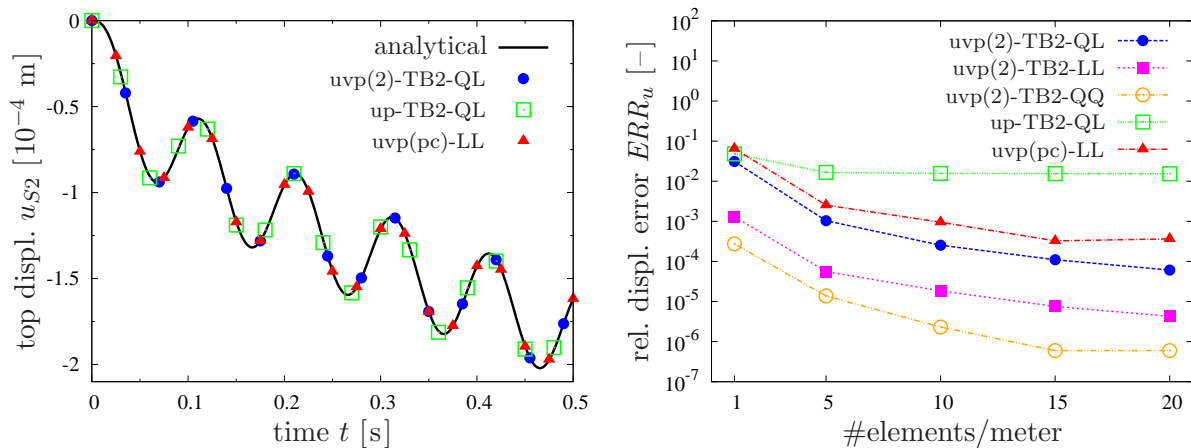


Figure 6.2: Top displacement time history for $k^F = 10^{-2}$ m/s, $t = [0, 0.5]$ s and 5 elem/m (left), and the relative error (right, logarithmic scale) over mesh size at $t = 0.15$ s

A closer look at the results via the relative displacement error $ERR_u := |(u_{S2} - u_{ref})/u_{ref}|$ shows a diversity in the accuracy of the different solutions, cf. Figure 6.2, right. In particular, it is observed that the reduced \mathbf{u}_S - p formulation up-TB2-QL yields the highest

deficiency for large values of k^F , which is expected as the assumption of $(\mathbf{w}_F)'_S \approx \mathbf{0}$ is not valid for the high permeability case. The second scheme in the inaccuracy is the splitting uvp(pc)-LL. Moreover, the use of quadratic-linear Taylor-Hood elements (QL) for the monolithic treatment of uvp(2) formulation results in more errors than the case of applied linear equal-order approximation (LL) to the same formulation.

The latter issue becomes even more prominent for the lower permeability case with $k^F = 10^{-5}$ m/s. Here, comparing again the solid displacement that results from the different numerical schemes with that resulting from the analytical solution of a point at the top of the domain, Figure 6.3, left, shows that only uvp(2)-TB2-LL and uvp(2)-TB2-QQ yield high-accurate results, where still no pressure stabilisation is used. Additionally, the relative displacement errors in Figure 6.3, right, further enhance the preceding findings. It is also noticeable that the solution of the reduced \mathbf{u}_S - p formulation up-QL for lower values of k^F is almost as accurate as the more expensive uvp(2)-QL.

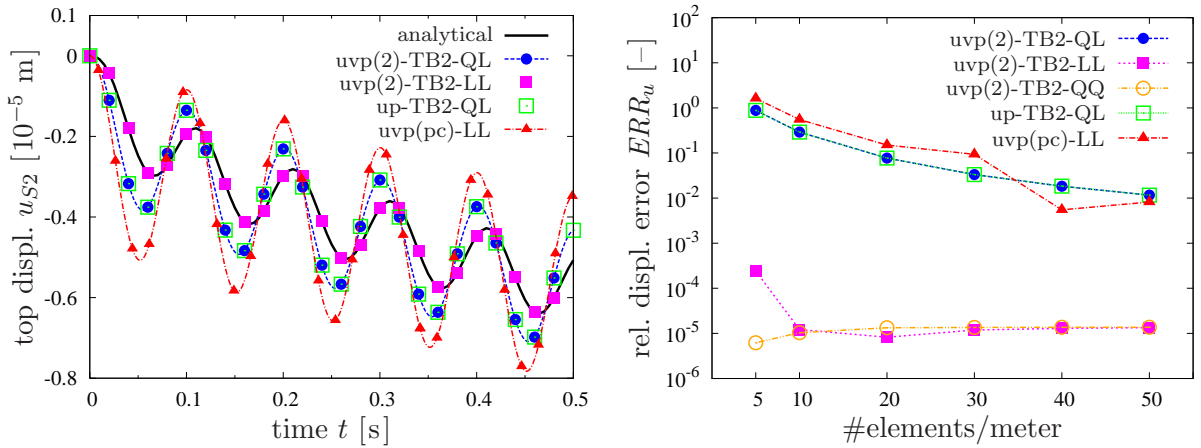


Figure 6.3: Top displacement time history for $k^F = 10^{-5}$ m/s, $t = [0, 0.5]$ s and 10 elem/m (left), and the relative errors (right, logarithmic scale) over mesh size at $t = 0.15$ s

Basically, the emerging challenge lies in the zero pore-pressure boundary condition (perfect drainage) at the loaded top of the domain. According to the principle of effective stresses in (3.18)₁, the applied load is concurrently carried by the solid matrix and the pore fluid. Here, starting with an undeformed initial state of the solid matrix, the equilibrium under sudden loading requires the pore fluid to bear the entire load until the deformation starts in the solid skeleton (consolidation process). However, at the top of the domain, we have the boundary condition $\bar{p} = 0$ leading to an immediate pore-pressure increase in a small layer below the top boundary. In case of a coarse FE discretisation, the apparent steep pressure gradient cannot be resolved accurately, which, consequently, yields an inaccurate displacement solution in the strongly coupled problem. This inaccuracy is even more obvious for mixed quadratic-linear (QL) approximations, where the linear interpolation of p yields unreliable pressure values related to the mid-nodes of the quadratic approximation of \mathbf{u}_S , and thus, further spoils the displacement solution of the neighbouring FE nodes.

To illustrate this, Figure 6.4 depicts the nodal solid displacement and the pore-pressure values in the first half meter below the top of the IBVP for a FE discretisation of 10 elem/m and $k^F = 10^{-5}$ m/s. The quadratic interpolation (QQ) of all variables yields

an adequate approximation of the solid displacement and the pore pressure. Moreover, the solution of uvp(2)-TB2-LL already shows remarkable oscillations, which reveals the necessity to use stabilisation methods for the lower permeability treatment. Following this, despite the inaccurate \mathbf{u}_S solution at the top, the semi-explicit-implicit strategy gives an accurate approximation of \mathbf{u}_S in the domain and even a better pore-pressure solution than uvp-TB2-QQ. To overcome this problem, a feasible way is to provide fine layers of finite elements at loaded permeable boundaries. This seems to be reasonable for the implicit monolithic treatment with no restrictions on the time-step size. However, for the splitting method, the CFL condition might demand a too small global time-step increment.

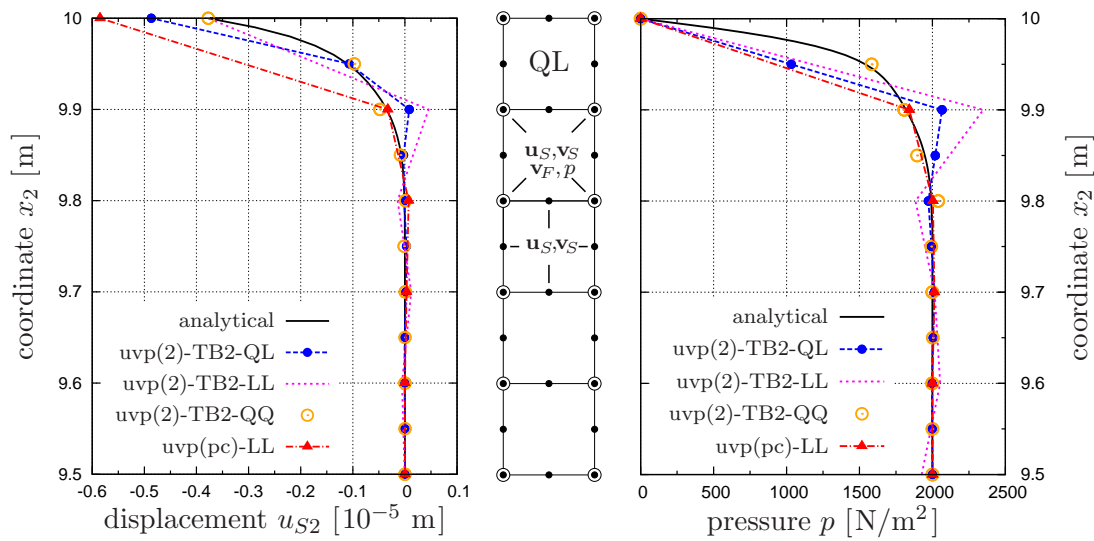


Figure 6.4: Solid displacement (left) and pore-pressure distribution (right) in the first half meter under the loaded top of the IBVP for $k^F = 10^{-5}$ m/s, 10 elem/m at $t = 0.15$ s. In the middle, exemplary mixed quadratic-linear (QL) FE mesh of the uvp(2) test case

In this connection, it is important to mention that although implicit methods allow to apply large time steps, the size of these steps is still limited. Here, beside the need to accurately capture the phase and the amplitude of the applied dynamic load³, using small Δt helps to keep the time discretisation errors small. In Figure 6.5, the relative displacement errors for different time increments of the implicit monolithic strategy TR-BDF2 are compared. Therein, it is clear that Δt influences the accuracy of the different schemes and formulations. For instance, a kind of ‘optimal’ time step close to Δt_{cr} of the CFL condition can be deduced for the linear equal-order approximation (LL).

In dynamical problems, where a finite-speed propagation of information is found, the accuracy of the implicit numerical treatment does not only demand a proper time-step size associated with the highest frequency of the loading, but requires also that the highest

³Under dynamic loading conditions, the maximum time-step size should not exceed half the minimum period, i. e., $\Delta t_{\max} = 0.5 T_{\min} = 5 \cdot 10^{-2}$ s. In practise, it is recommended to use time increments below one-tenth of the minimum period, see, e. g., Bathe & Wilson [10, Sec. 9.3].

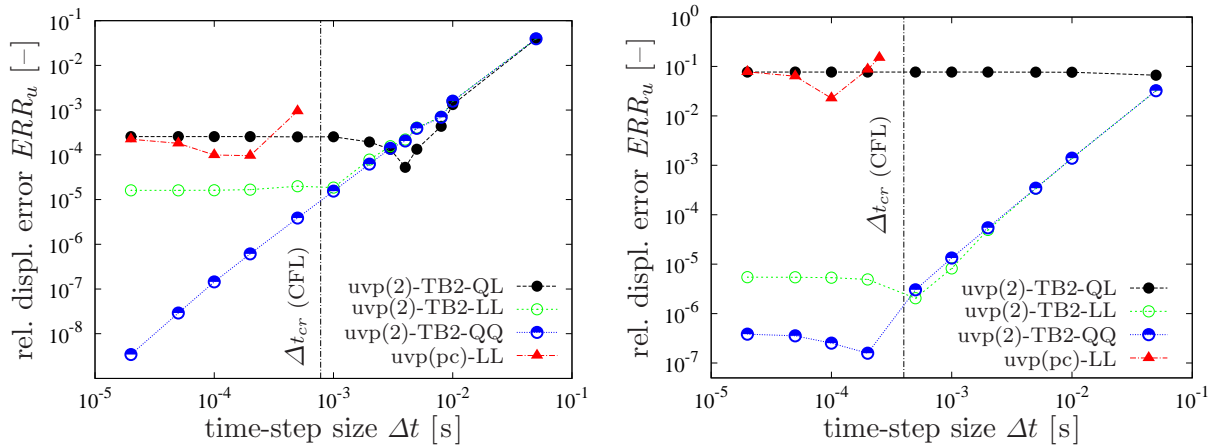


Figure 6.5: Relative displacement error of a point at the top over time-step size (double logarithmic scale) at $t = 0.15$ s for $k^F = 10^{-2}$ m/s and 10 elem/m (left), and $k^F = 10^{-5}$ m/s with 20 elem/m (right)

wave number (reciprocal lowest wave length) be adequately resolved in space. Thus, the so-called pollution effect associated with the dispersion of the FEM solution can be avoided, see, e. g., Deraemaeker *et al.* [42] for details. Here, the lowest wave length should at least be represented by 10 data points (FE nodes), which corresponds to 9 linear elements.

In the considered 2-d FE example in Figure 6.1, the incompressibility of the pore fluid together with a moderately low permeability causes an immediate damping of the propagating pressure waves, which can only appear next to the permeable boundary. Therefore, this example is not well suited to reveal the differences between the various statements and schemes. Alternatively, for further reliable comparisons of the test cases in Table 6.1, a two-dimensional problem is introduced in Section 6.2, which also gives rise to shear and surface wave propagation.

6.1.2 Explicit vs. Implicit Monolithic Solutions

This section focuses on the numerical solution of the hybrid biphasic model with a materially incompressible solid and a compressible pore fluid. The investigation proceeds from the IBVP as given in Figure 6.1, 1-d FE, with $l_1 = 20$ m, where only the one-dimensional FEM is regarded. The behaviour of the solid phase is linear elastic with material parameters given in Table 6.2. Additionally, the parameters of the compressible pore fluid in Table 6.4 are mostly related to the included ideal gas bubbles.

As has been discussed in Section 4.2.1, applying the FEM to the governing differential equations for this case yields a stiff space-discrete ODE system (4.27) with non-singular global mass matrix. Therefore, explicit as well as implicit monolithic strategies are applicable. Moreover, it is not needed to use mixed-order FEM for the spatial discretisation to get a stable solution.

Figure 6.6 depicts equal solid displacement and pore pressure solutions of the arising

Parameter	Symbol	Value	SI unit
initial volume fraction of liquid	n_{0S}^L	0.30	-
initial volume fraction of gas	n_{0S}^G	0.03	-
effective density of liquid	ρ^{LR}	1000	kg/m ³
initial material density of ideal gas	ρ_0^{GR}	1.25	kg/m ³
universal gas constant	R	8.3144	J/K mol
absolute <i>Kelvin's</i> temperature	Θ	273.15	K
molecular mass of dry air	M	$2.897 \cdot 10^{-2}$	kg/mol

Table 6.4: Material parameters for the compressible pore fluid via ideal gas, cf. [123]

ODE system following explicit and implicit monolithic schemes with equal-order linear interpolations (LL) of all primary variables. In the explicit monolithic treatment, the 1st-order accurate explicit *Euler* (expl. Euler) as well as the 2nd-order accurate explicit *Heun* (expl. Heun) scheme have been implemented, see Section 4.2.1. The maximum (critical) time-step size Δt_{cr} , which is required to get a stable solution, has been obtained after trying a range of time steps in the numerical solution. Herein, $\Delta t_{cr} = 5 \times 10^{-5}$ s should not be exceeded for the stability of the explicit *Euler* scheme, whereas the higher order *Heun* method requires time steps smaller than $\Delta t_{cr} = 5 \times 10^{-4}$ s to get a stable solution. The reasonable step size (Δt_{re}) needed to correctly implement the dynamic load is usually chosen one-tenth of the minimum load period, i. e. $\Delta t_{re} \approx T/10 = 10^{-2}$ s. Therefore, for explicit *Euler* $\Delta t_{cr} = 1/200 \Delta t_{re}$ and for *Heun* method $\Delta t_{cr} = 1/20 \Delta t_{re}$.

The implicit monolithic treatment is applied using the 2nd-order accurate TR method with LL interpolations and no restrictions on the time-step size. For the impl. TR-LL implementation, the time-step size Δt_n is chosen equal to 10^{-3} s to ensure the accuracy of the treatment.

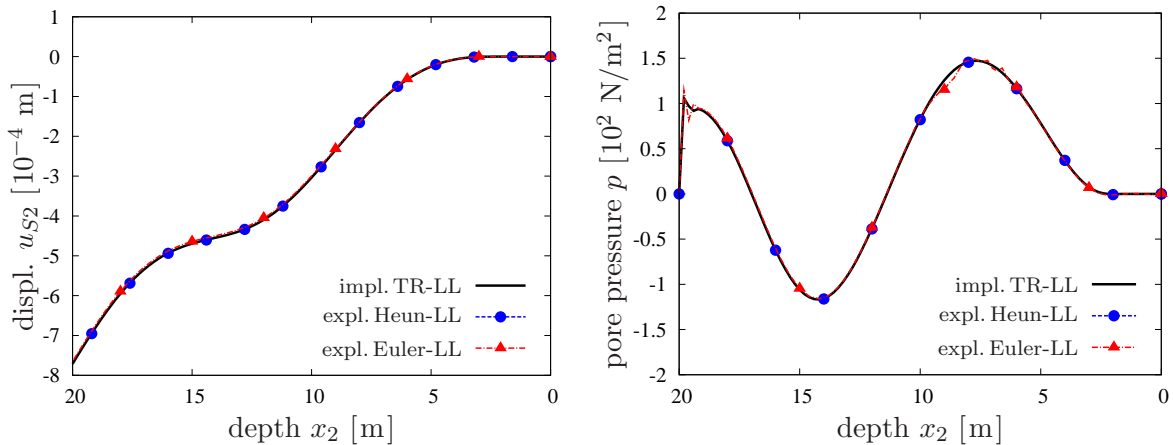


Figure 6.6: Comparison of the explicit and the implicit monolithic treatment via the displacement solution over x_2 (left) and the pore pressure over x_2 (right) at $t = 0.15$ s, $k^F = 10^{-3}$ m/s, and 5 elem/m for the hybrid biphsic model

The finding of Δt_{cr} smaller (or much smaller) than Δt_{re} is in agreement with the definition

of stiff problems, in which very small time steps are required for a stable explicit monolithic treatment, see, e.g., Hairer & Wanner [80] for more details. Based on the preceding results in Figure 6.6, it is often not efficient to apply explicit monolithic schemes to strongly coupled stiff problems, and thus, only implicit strategies are usually applied in the monolithic treatment. Moreover, in order to give a more general statement about the usability of explicit monolithic schemes, it might be important to solve 2-d and 3-d problems with different finite element sizes, which is beyond the scope of this monograph.

6.1.3 Verification of the Unbounded Boundary Treatment

The aim of this section is to test and verify the suggested infinite domain modelling procedure in Section 4.4.1 by comparing the numerical results with analytical solutions of the balance equations. Herein, the investigation is restricted to the materially incompressible biphasic model with linear elastic behaviour of the solid constituent, where for this particular case an analytical solution is available. Moreover, the discussion addresses the efficiency and the challenges of the proposed treatment, cf. Heider *et al.* [87].

In addition to the abbreviations in Table 6.1, this section proceeds from further abbreviations given in Table 6.5 for the sake of a simple and abstract representation of the implemented schemes.

Abbr.	Description
FE-IE	finite element discretisation of the near field and infinite elements for the far field together with VDB scheme, cf. Figure 6.1, 2-d FE-IE
FE-fix	finite element discretisation with finite (fixed) boundaries, cf. Figure 6.1, 2-d FE

Table 6.5: Abbreviations related to the infinite domain modelling

The spatial discretisation with the FE-IE method is carried out using mixed-order (QL) interpolations of both the finite and the infinite elements as discussed in Section 4.4.1. In this regard, the numeration and location of the connecting nodes must coincide in order to insure the continuity across the FE-IE interface. The time discretisation is performed using the implicit monolithic TR-BDF2 scheme with constant time-step size $\Delta t = 10^{-3}$ s for all cases of study.

In order to examine the efficiency of the suggested FE-IE treatment, the domain is truncated at a certain distance l_1 from the top before the propagating pressure waves are damped out. Thus, based on the analytical treatment, it is shown in Figure 6.7 how far the pressure waves can propagate inside the domain for different values of the permeability k^F . Due to the assumed incompressibility of the pore fluid, only one type of p-waves appears, which damps out after a certain distance.

The performance of the proposed infinite domain treatment depends on a number of factors. In addition to the chosen damping relations and parameters (cf. Section 4.4.1), the implementation of the IE for the quasi-static behaviour of the far field and the pore-pressure approximation with the FEM inside the IE directly influence the accuracy of

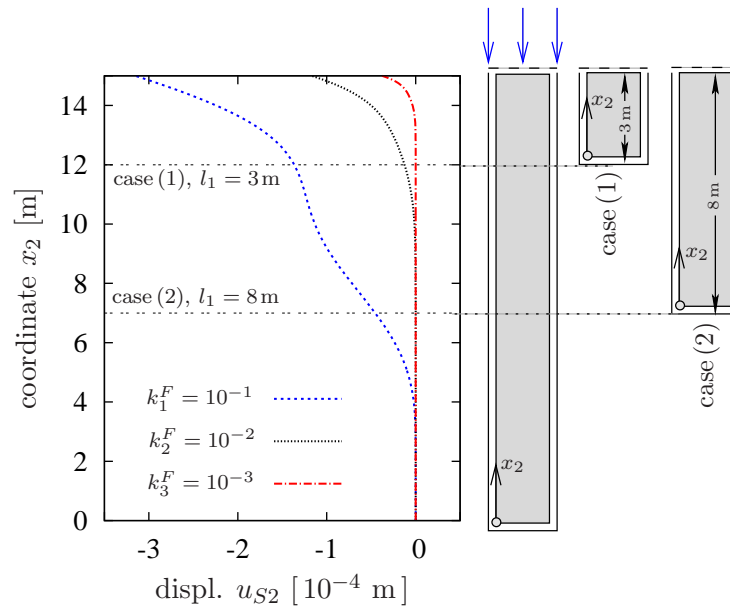


Figure 6.7: Analytical solution of the solid displacement for different values of the permeability k^F at $t = 0.15$ s (left) and the corresponding truncated domains (right)

the results. In this context, the IE extension distance (or the pole of the mapped IE) represented by l_2 in Figure 6.1, 2-d FE-IE, affects the efficiency of the quasi-static IE treatment in an attempt to improve the fit of the far-field response to the considered decay patterns, cf., e.g., Marques & Owen [127] or Zienkiewicz *et al.* [188] for more details. In this connection, a large increase of the IE extension leads to a coarse mesh for the pore-pressure approximation inside the IE, which is undesired especially under low permeability conditions. A comparable situation is found if for the approximation of a steep pore-pressure gradient, a fine FE mesh is required. However, for the shear-wave propagation through the solid skeleton, the influence of the pore-pressure discretisation is of less importance.

In the following discussion, two cases are compared using different values of the permeability k^F and the IE extension l_2 . The specific values are given in Table 6.6.

Case	k^F [m/s]	l_1 [m]	l_2 [m]	Abbr.
(1)	10^{-2}	3	0.15	FE-IE (1) ₁
			3	FE-IE (2) ₁
(2)	10^{-1}	8	1	FE-IE (1) ₂
			8	FE-IE (2) ₂

Table 6.6: Two considered cases with varying permeability and geometry of the infinite domain model

In case (1) with lower permeability, it is clear from Figure 6.8, left, that the FE-IE treatment results in a more accurate solid displacement solution than FE-fix. This situation

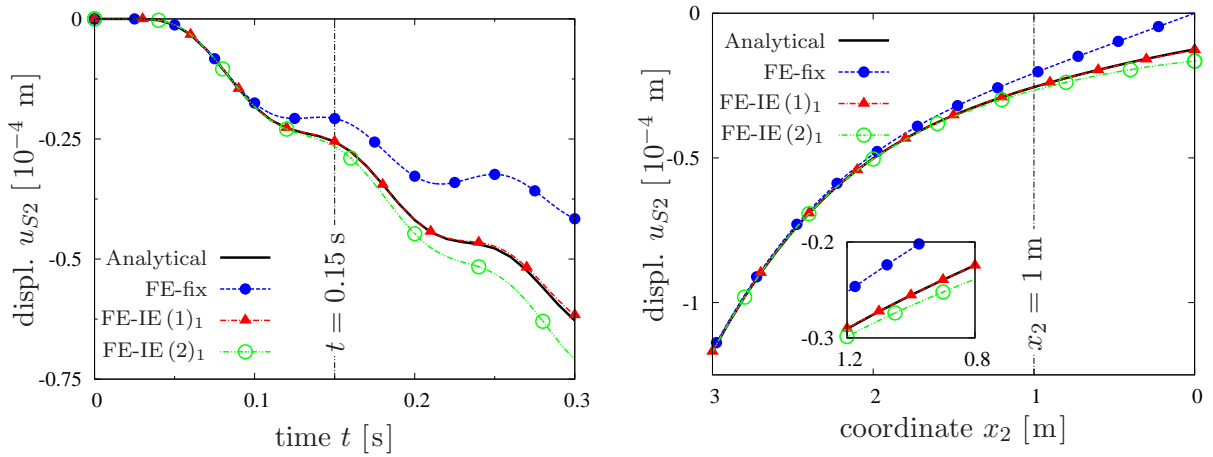


Figure 6.8: Displacement time history u_{S2} at $x_2 = 1$ m (left), and u_{S2} solution over x_2 at $t = 0.15$ s (right) for case (1) and $FE = 20$ elem/m

becomes even more prevalent with the progress of calculation time. In addition, the FE-IE with shorter l_2 yields more accurate approximations than that with longer extension.

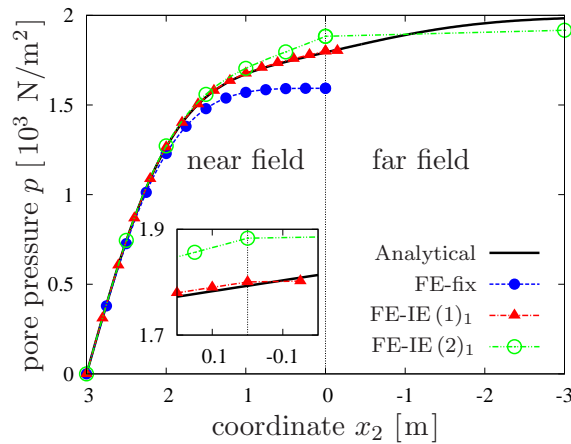


Figure 6.9: Pore-pressure solution p for case (1) with $FE = 20$ elem/m at $t = 0.15$ s

The error can be quantified by calculating, for instance, the relative displacement error⁴ ERR_u at a point with coordinate $x_2 = 1$ m and time $t = 0.15$ s. In this regard, the FE-fix treatment leads to $ERR_u \approx 92\%$, FE-IE (2)₁ yields $ERR_u \approx 4.0\%$, and FE-IE (1)₁ gives the best solution with $ERR_u \approx 0.03\%$. Moreover, it is obvious from Figure 6.8 that ERR_u changes according to the point position and time of observation.

Although increasing the IE extension has a positive impact on the solid displacement solution in the far field (cf. Marques & Owen [127]), the pore-pressure approximation with the FEM inside the IE plays an important role in the overall accuracy of the coupled problem. This coupling between the solid displacement and the pore-pressure solution

⁴ $ERR_u := |(u_{S2} - u_a)/u_a|$ with u_a being the analytical displacement solution and u_{S2} the numerical displacement solution.

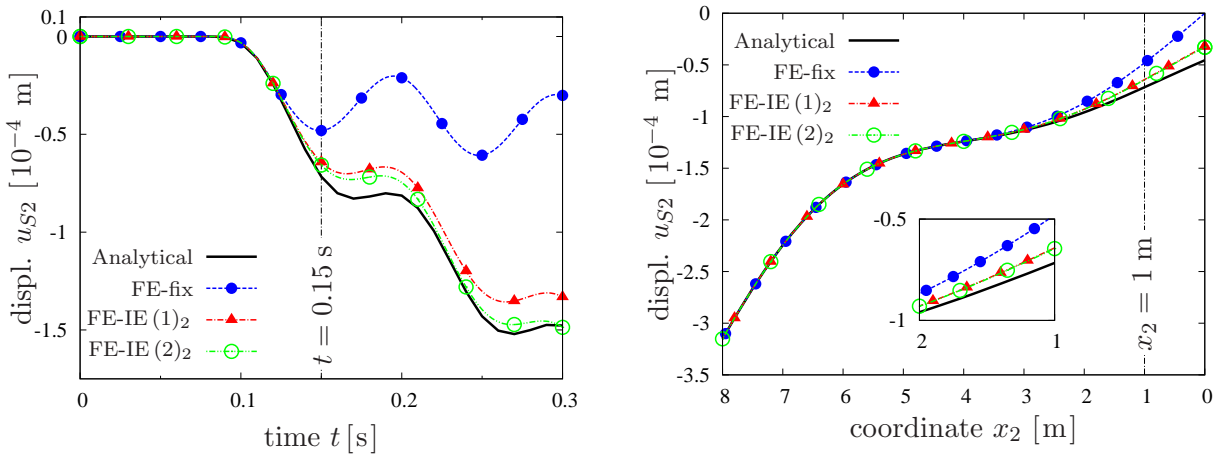


Figure 6.10: Displacement time history u_{S2} at $x_2 = 1$ m (left), and u_{S2} solution over x_2 at $t = 0.15$ s (right) for case (2) and FE = 10 elem/m

becomes more evident for lower values of the permeability. In this connection, Figure 6.9 shows that the FE-IE (1)₁ case with shorter IE extension l_2 , and thus, a denser FE discretisation of the pore pressure is better than the FE-IE (2)₁ case with longer IE extension. Consequently, at the bottom of the truncated domain ($x_2 = 0$ m), Figure 6.8, right, shows that the coarse pore-pressure mesh leads to a poor FE-IE (2)₁ approximation of the solid displacement in the coupled problem.

A similar discussion is performed for case (2) with higher permeability as given in Table 6.6. In this regard, Figures 6.10 and 6.11 show that the FE-IE treatment again leads to better results than the FE-fix treatment for both the solid displacement and the pore-pressure fields.

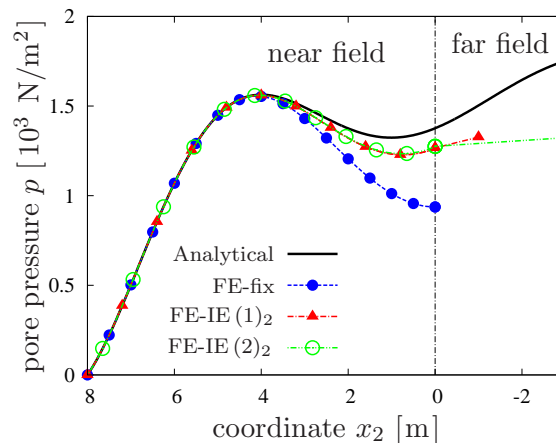


Figure 6.11: Pore-pressure solution p for case (2) with FE = 10 elem/m at $t = 0.15$ s

For a quantitative comparison between the different schemes, the relative displacement error ERR_u is evaluated, for instance, at a point with $x_2 = 1$ m and $t = 0.15$ s. The FE-fix treatment leads to $ERR_u \approx 33\%$, FE-IE (1)₂ results in $ERR_u \approx 10.4\%$, and FE-IE (2)₂ yields the best solution with $ERR_u \approx 9.0\%$. Moreover, Figures 6.10 and 6.11 show that

ERR_u changes as for case (1) according to the point location and time of observation.

In this regard, the FE-IE (2)₂ treatment with relatively long IE extension l_2 yields at different times a better displacement solution than FE-IE (1)₂ with short l_2 , cf. Figure 6.10, left. This finding is in agreement with the quasi-static IE scheme behaviour, where increasing the IE extension distance improves the displacement solution in the far field, cf. Marques & Owen [127]. However, as shown in Figure 6.11, the pore-pressure solution with finer FE discretisation (shorter IE extension) is slightly better than that with longer l_2 . Here, as the permeability parameter k^F is higher in case (2) than in case (1), the influence of the pore pressure on the solid displacement is less important (weaker \mathbf{u}_S - p coupling). Thus, increasing the IE extension distance improves the accuracy of the numerical displacement solution.

Based on the latter results, we conclude that for case (2), the role of the IE extension on the accuracy of the infinite domain treatment is dominant over the influence of the pore-pressure FE approximation within the IE. For the sake of completeness, we mention an additional source of error, which stems from the fact that for high permeabilities, such as in case (2), the assumption of negligible relative accelerations of the solid and the pore-fluid constituents in the far field is somehow violated, cf. Section 4.4.1.

For further analysis of the suggested VDB treatment with different wave types, a two-dimensional wave propagation problem giving rise to shear wave damping in a soil-structure interaction problem is introduced in Section 6.3.

6.2 Two-dimensional Wave Propagation

The simplified soil column problem in Section 6.1 suffers from fast damping of the propagating pressure waves, and thus, is not well-suited to reveal the characteristics of the various cases of Table 6.1. Therefore, the main objective of the following two-dimensional numerical problem is to analyse and illustrate the merits and drawbacks of the different procedures and formulas of Table 6.1. Moreover, this example gives rise to pressure, shear, and surface wave propagation rather than to pure pressure waves as in the previous problem. Analogous to the work by Breuer [29], the dynamical wave propagation in a rectangular symmetric domain (Figure 6.12) under plane-strain conditions is studied, cf. Markert *et al.* [126].

The response of the solid skeleton is considered linear elastic with parameters given in Table 6.2. The applied distributed impulse force is given by

$$f(t) = 10^5 \sin(25 \pi t) [1 - H(t - \tau)] \quad \text{N/m}^2, \quad (6.1)$$

with $H(t - \tau)$ being the Heaviside step function and $\tau = 0.04$ s. Additionally, only the case of a materially incompressible biphasic medium is considered in this treatment.

From the problem setup, two modes of body waves (recall the footnote on page 81) and one mode of surface waves are expected to occur. In particular, the bulk waves are the slow pressure wave (p2-wave) and the transverse shear wave (s-wave) transmitted through the elastic solid matrix. Moreover, at the free top surface, the *Rayleigh* wave (R-wave)

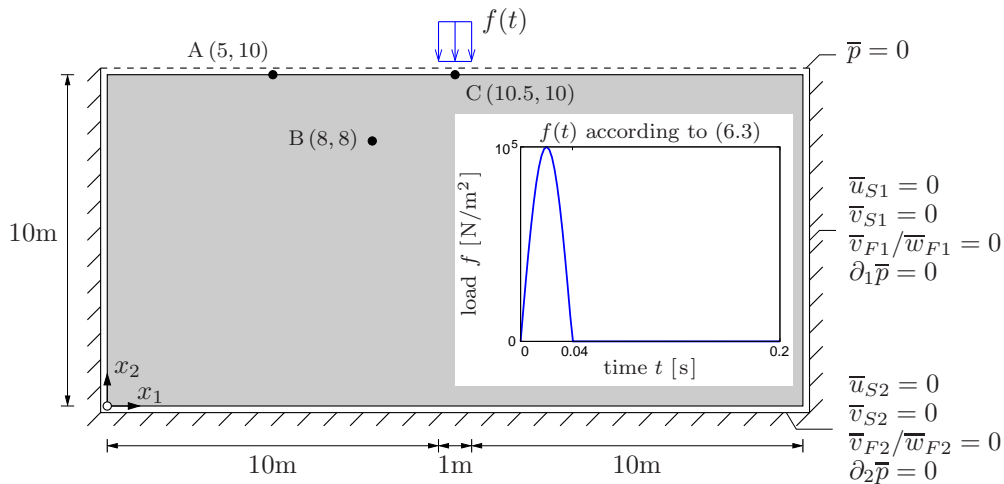


Figure 6.12: Geometry, boundary conditions, and loading path of the 2-d problem

appears as an elastic surface wave with an elliptic in-plane particle movement, commonly noticed as ‘ground rolling’ during earthquake events. In Figure 6.13, exemplary contour plots of the computed solid displacement field and the deformed mesh geometry are given, which helps to make the two-dimensional wave propagation apparent.

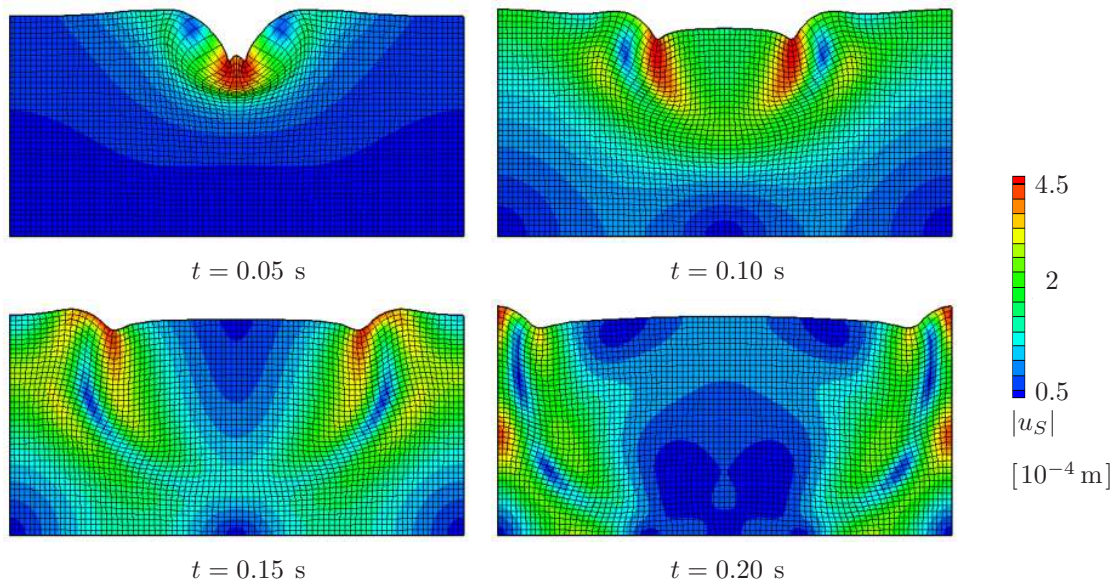


Figure 6.13: Time sequence of solid displacement contour plots ($|u_S| = \sqrt{u_{S1}^2 + u_{S2}^2}$) and deformed mesh (scale $\times 500$) using $uvp(2)$ -TB2-QL, 84–40 elements, and $k^F = 10^{-2}$ m/s

Remark: It is worth mentioning that benchmark solutions of dynamic wave propagation in multiphasic granular materials can be generated experimentally as explained in the work by Bussat *et al.* [31]. Therein, non-destructive tests are applied to reproduce wave transmission in multi-phase concrete samples. The 3-d arrangement of the solid grains is simplified to 2-d by using glassware cylinders with different diameters and equal orientation, cf. Figure 6.14, left. The properties of the mentioned cylinders are comparable with

those of the solid aggregate and the spaces between them are filled afterwards with water and cement in order to emulate the multiphasic characteristics of concrete.

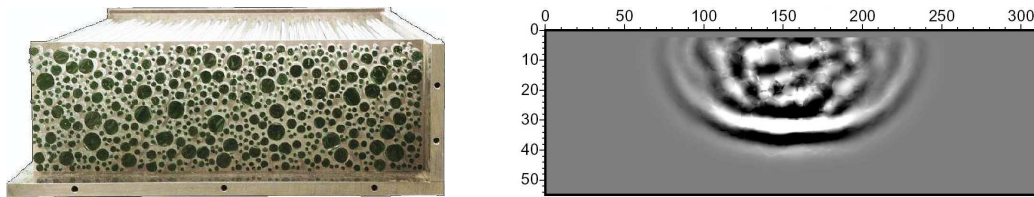


Figure 6.14: Propagation of longitudinal bulk waves at time $t = 20 \mu\text{s}$ inside a concrete sample ($0.3 \times 0.05 \text{ m}$), which represents a multiphasic material (Bussat *et al.* [31])

Back to our problem, the modes of the propagating body waves in Figure 6.14, right, are comparable with the waves that have been depicted in Figure 6.13. However, an exact comparison requires the agreement of the material properties and the different initial and boundary conditions of the experimental and the numerical treatment.

In the current numerical example, the tests and comparisons are carried out considering mainly two cases of permeability (10^{-2} m/s and 10^{-10} m/s) and the spatial discretisation is again based on fully integrated quadrilateral finite elements as given in Table 6.7. Here, the focus is laid on the displacement solution at the free surface (point A) and the pore pressure time history in the domain (point B). In addition, the displacement and the pore-pressure distribution directly under the impulse load (vertical down at point C) are compared for different cases, cf. Figure 6.12.

No. elements (width–height)	21–10	42–20	84–40	168–80
Δt_{cr} (CFL) [10^{-3} s]	4.14	2.07	1.04	0.52
Δt (pc) [10^{-3} s]	2.0	1.0	0.5	–
Δt (monol.) [10^{-3} s]	1.0	1.0	1.0	1.0
α_{\min}/α_0 for $\text{uvp}(\alpha)$	$2.7 \cdot 10^{-6}$	$1.4 \cdot 10^{-6}$	$7.0 \cdot 10^{-7}$	$3.5 \cdot 10^{-7}$
β_{\min}/β_0 for $\text{uvp}(\beta)$	$2.7 \cdot 10^{-6}$	$1.4 \cdot 10^{-6}$	$7.0 \cdot 10^{-7}$	$3.5 \cdot 10^{-7}$

Table 6.7: Mesh sizes and time steps for the problem in Section 6.2, noting that only half of the problem needs to be computed by exploiting the symmetry to $x = 10.5 \text{ m}$

High Permeability Case

Starting with the high permeability case ($k^F = 10^{-2} \text{ m/s}$), equal-order interpolation functions can be applied to the primary variables of the monolithic implicit time integration schemes without the need for special stabilisation techniques. In this connection, the numerical damping and the stability of the monolithic time-stepping rules are examined by comparing the solid displacement solution of point A at the top of the domain⁵. In this,

⁵Noticeable is the elliptic motion of point A at the surface, which represents the R-wave mode.

Figure 6.15, left, depicts the artificial damping of the BE scheme, which can be alleviated by reducing the time-step sizes. Figure 6.15, right, shows that the TR and the TR-BDF2 (TB2) exhibit no numerical damping and lead to stable displacement solutions for all considered formulations. Therefore, we exclude the BE scheme from the later comparisons and focus only on the TR and the TB2 in this example.

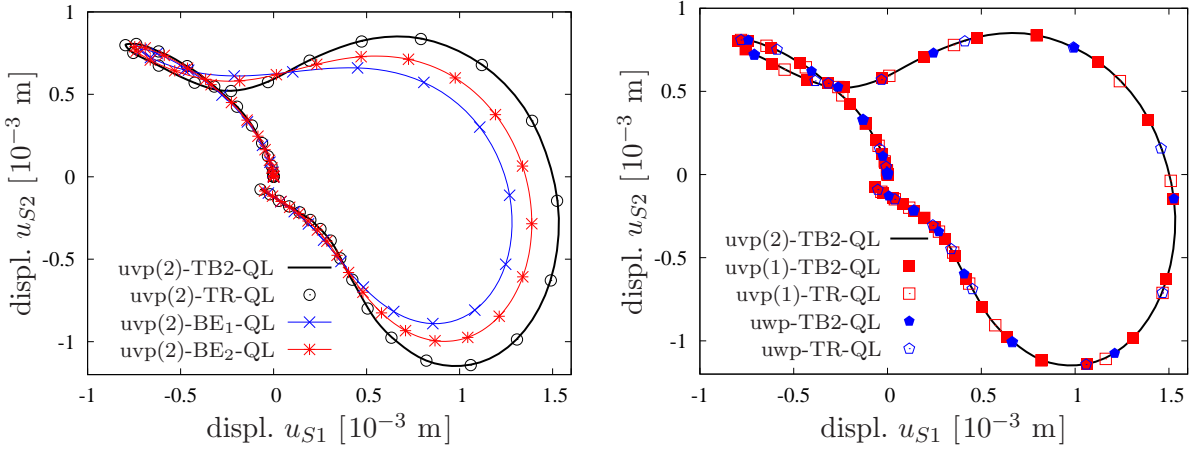


Figure 6.15: Comparison of the elliptic in-plane motion of point A for $k^F = 10^{-2}$ m/s, 42–20 elements, and equal $\Delta t = 10^{-3}$ s except for BE₂ where $\Delta t = 5 \cdot 10^{-4}$ s

Following this, the displacement solution at point A for different mesh and time-step sizes is investigated. Here, the combination uvp(2)-TB2-QL with 84–40 elements is chosen as a reference solution, which yields a very good approximation in comparison with finer mesh results as can be seen in Figure 6.16, left. Moreover, from Figure 6.16, right, it is clear that the implicit monolithic time discretisation is sufficiently accurate for $\Delta t = 10^{-3}$ s, which is the time step of choice for the monolithic strategies.

To continue, we examine the uwp formulation for both implicit time integrators and different interpolation cases in regard to the stability of the pore-pressure solution at

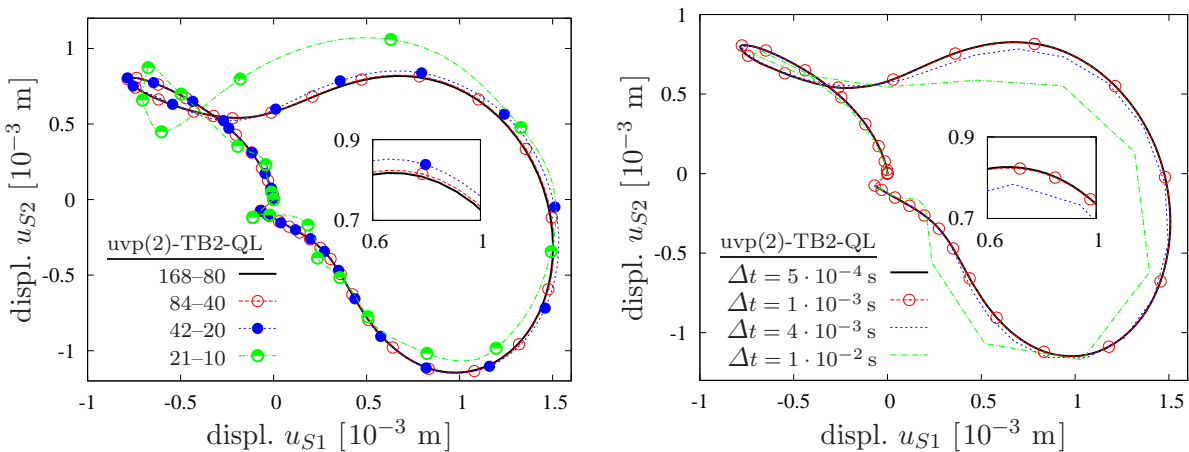


Figure 6.16: Comparison of the elliptic in-plane motion of point A for $k^F = 10^{-2}$ m/s using different mesh sizes and a fixed time step $\Delta t = 10^{-3}$ s (left) and a fixed mesh with 84–40 elements but different time-step sizes (right)

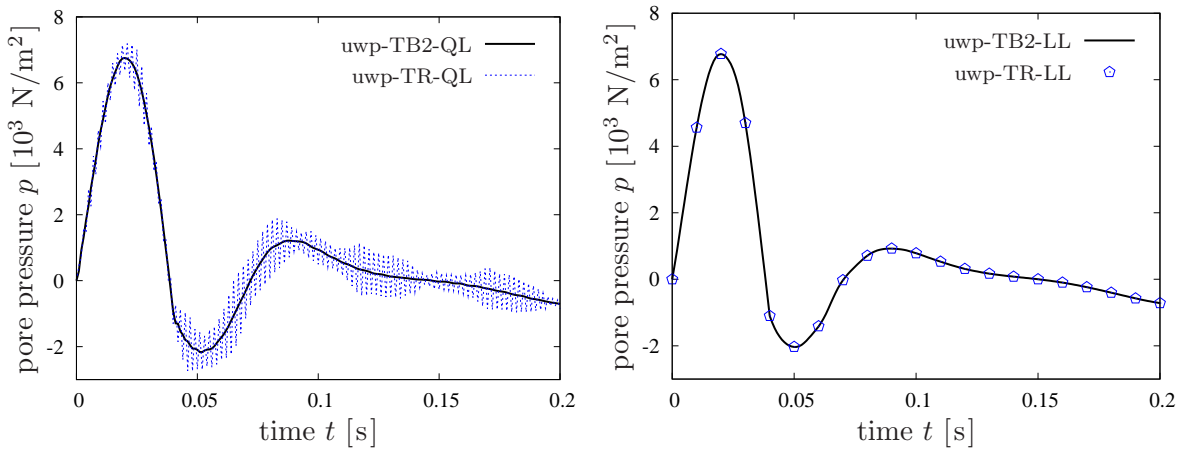


Figure 6.17: Pore pressure time history at point B for $k^F = 10^{-2}$ m/s, 42–20 elements, and $\Delta t = 10^{-3}$ s

point B. As depicted in Figure 6.17, left, the combination uwp-TR-QL yields oscillations in the pressure solution due to the marginal stability of the trapezoidal rule (TR), which, however, can be reduced by using smaller Δt or avoided if TB2 is applied. For linear equal-order elements (LL), the uwp formulation exhibits a stable pressure solution for both TR and TB2, cf., Figure 6.17, right.

The uvp(1) and uvp(2) formulations are compared in the same way as before. In this context, Figure 6.18, left, shows that regardless of the applied formulation, slight oscillations occur when TR in combination with the mixed QL discretisation is used. However, one obtains a stable pressure solution for both cases if TB2 instead of TR is applied or if one proceeds from LL elements for both time-stepping rules (Figure 6.18, right).

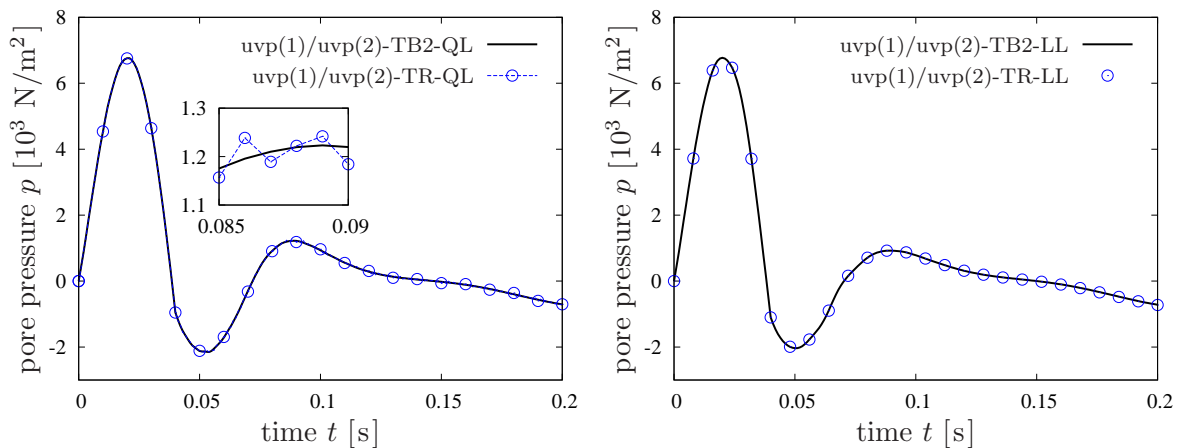


Figure 6.18: Pore pressure time history at point B for $k^F = 10^{-2}$ m/s, 42–20 elements, and $\Delta t = 10^{-3}$ s

Following this, the displacement and the pore pressure solutions of different LL and QQ discretisations are compared with the reference uvp(2)-TB2-QL formulation using 84–40 elements. Figure 6.19 shows the expected convergence of uvp(2)-TB2-LL to the reference solutions as finer meshes are considered, whereas already the coarse 42–20 QQ elements

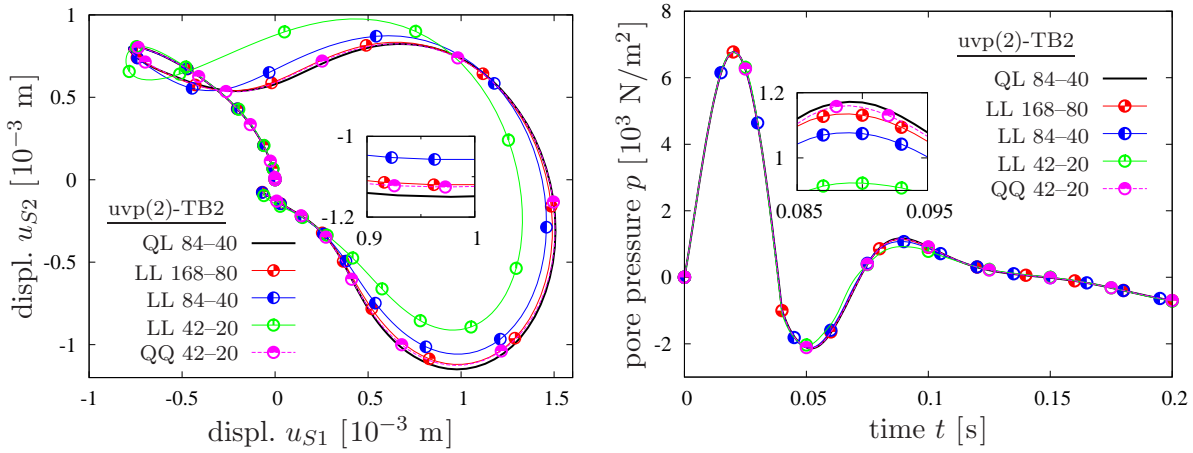


Figure 6.19: In-plane motion of point A (left) and pore-pressure time history at point B (right) for $k^F = 10^{-2}$ m/s and $\Delta t = 10^{-3}$ s

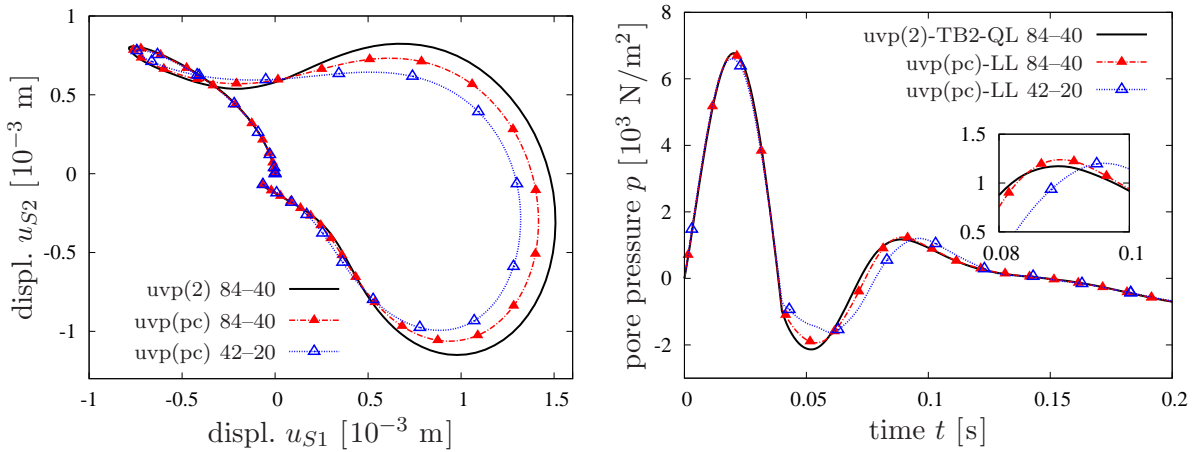


Figure 6.20: In-plane motion of point A (left) and p time history at point B (right) for $k^F = 10^{-2}$ m/s, $\Delta t = 10^{-3}$ s for uvp(2)-TB2, and Δt according to Table 6.7 for uvp(pc)

yield good results.

An almost identical behaviour is observed for uvp(pc)-LL (Figure 6.20) noting that coarse meshes yield an even poorer pressure approximation than uvp(2)-TB2-LL.

The final comparison for the high permeability case reveals the inaccuracy of the reduced up formulation. As illustrated in Figure 6.21, left, the simplifying assumption $(\mathbf{w}_F)'_S \equiv \mathbf{0}$ results in a severe overestimation of the displacement solution. However, one still obtains a good approximation of the pressure field (Figure 6.21, right).

Low Permeability Case

In what follows, the case of a very low permeability is considered, i. e. $k^F = 10^{-10}$ m/s, which further reveals the merits and drawbacks of the considered test cases. The monolithic solution now requires stable mixed FE formulations such as the quadratic-linear Taylor-Hood elements (QL) or some pressure stabilisation as in the uvp(α) formulation

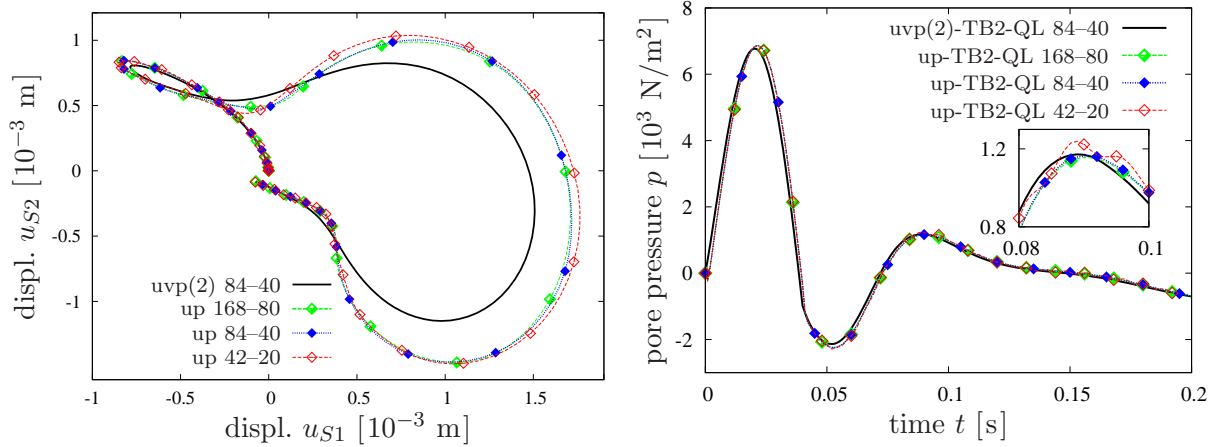


Figure 6.21: In-plane motion of point A (left) and pressure time history at point B (right) for $k^F = 10^{-2}$ m/s and $\Delta t = 10^{-3}$ s

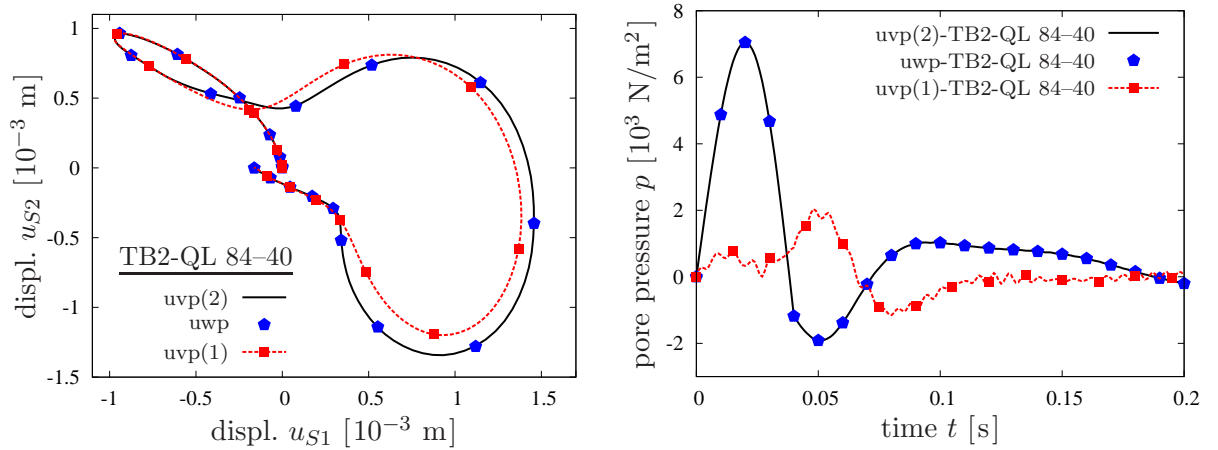


Figure 6.22: In-plane motion of point A (left) and pressure time history at point B (right) for $k^F = 10^{-10}$ m/s and $\Delta t = 10^{-3}$ s

if equal-order elements (LL or QQ) are used.

To begin with, one compares the monolithic solutions of the uvp(1), uvp(2), and uwp formulations. It is apparent from Figure 6.22 that uvp(1) yields an inaccurate displacement solution at point A and a totally wrong pore pressure time history at point B. However, for low values of k^F , the uwp formulation shows the same performance as uvp(2). This becomes also clear from Figure 6.23, where both exhibit instabilities in the pore pressure field if the trapezoidal rule (TR) or a too coarse mesh is used.

The implicit monolithic solution with equal-order finite element interpolations is applied using the stabilised uvp(α) formulation. In this regard, the magnitude of the stabilisation parameter α can reasonably be estimated by recourse to (4.85) as

$$\alpha_{\min} = \alpha_0 \Delta t_{cr} \left(\frac{n^F}{\rho^{FR}} + \frac{n^S}{\rho^{SR}} \right) \quad \text{with} \quad 0 < \alpha_0 \leq 2. \quad (6.2)$$

It follows from Figure 6.24 that the stabilising parameter controls the accuracy of the solution. Here, $\alpha_{0(1)} = 2 \rightarrow \alpha_{\min} = 1.4 \cdot 10^{-6}$ in comparison with $\alpha_{0(2)} = 0.15 \rightarrow$

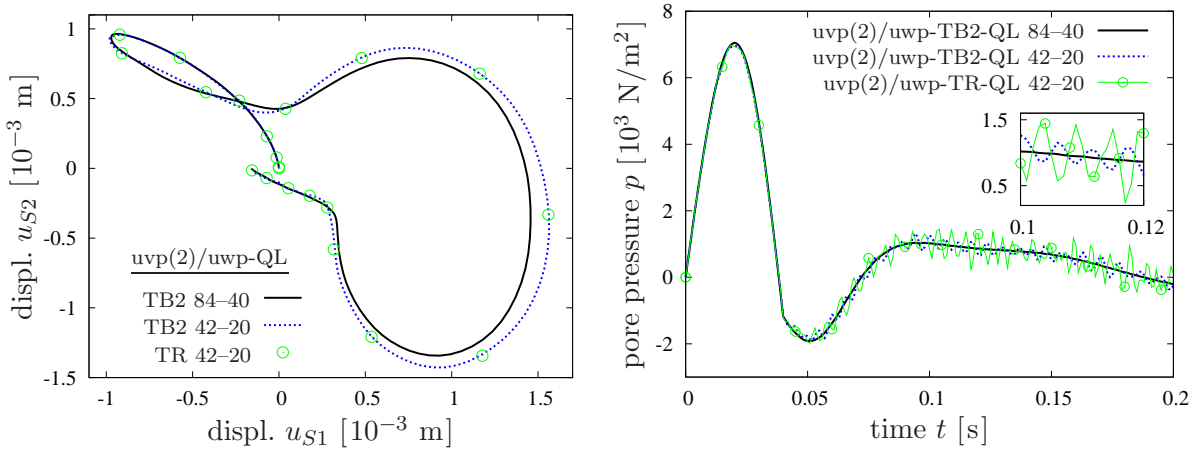


Figure 6.23: In-plane motion of point A (left) and pore pressure time history at point B (right) for $k^F = 10^{-10}$ m/s and $\Delta t = 10^{-3}$ s

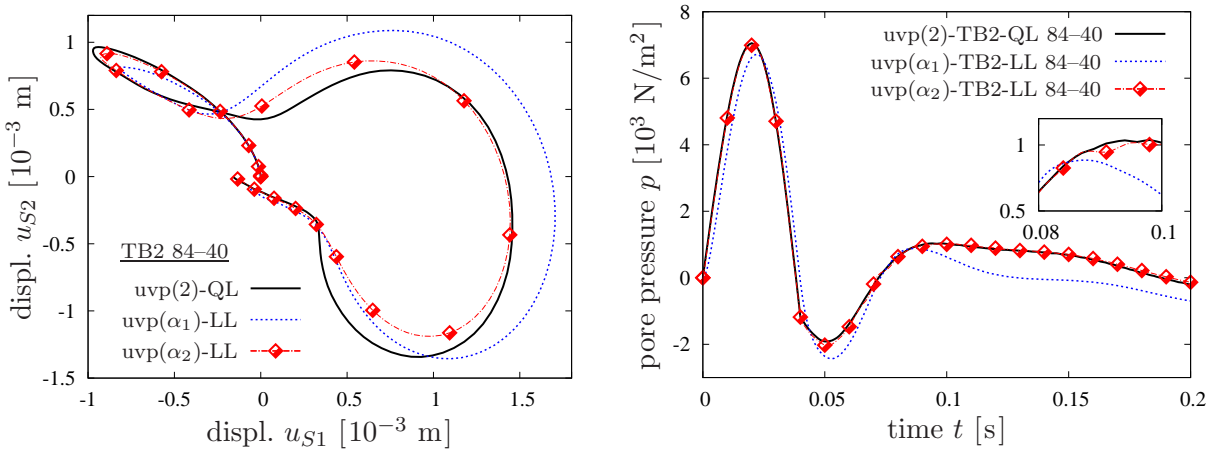


Figure 6.24: In-plane motion of point A (left) and p time history at point B (right) for $k^F = 10^{-10}$ m/s, $\Delta t = 10^{-3}$ s, and parameters $\alpha_{0(1)} = 2$ and $\alpha_{0(2)} = 0.15$ given in (6.2)

$\alpha_{min} = 1.05 \cdot 10^{-7}$ (cf. Table 6.7) yields a faulty ‘weak’ response due to the added artificial compressibility.

Next, the solution behaviour of the splitting scheme is investigated based on the uvp(pc)-LL procedure. Figure 6.25 shows that the formulation converges to the reference solutions, whereas the approximation of the pore-pressure field is better than that of the solid displacement.

Moreover, in the context of the semi-explicit-implicit splitting scheme, the case of using a time step that is much smaller than the critical one ($\Delta t = 5 \cdot 10^{-5} \approx \Delta t_{cr}/20$) is examined. Figure 6.26 shows that in this case only the stabilised uvp(β) formulation yields a reasonable pressure solution, whereas the displacement result is not much affected. Here, two values of the stabilising parameter β as given in (4.85) are used, viz. $\beta_{0(1)} = 1 \rightarrow \beta_{min} = 7 \cdot 10^{-7}$ and $\beta_{0(2)} = 4 \rightarrow \beta_{min} = 2.8 \cdot 10^{-6}$ (cf. Table 6.7). It is also noticeable that the choice of β is independent of the permeability.

For the considered low permeability case, the relative acceleration between the solid and

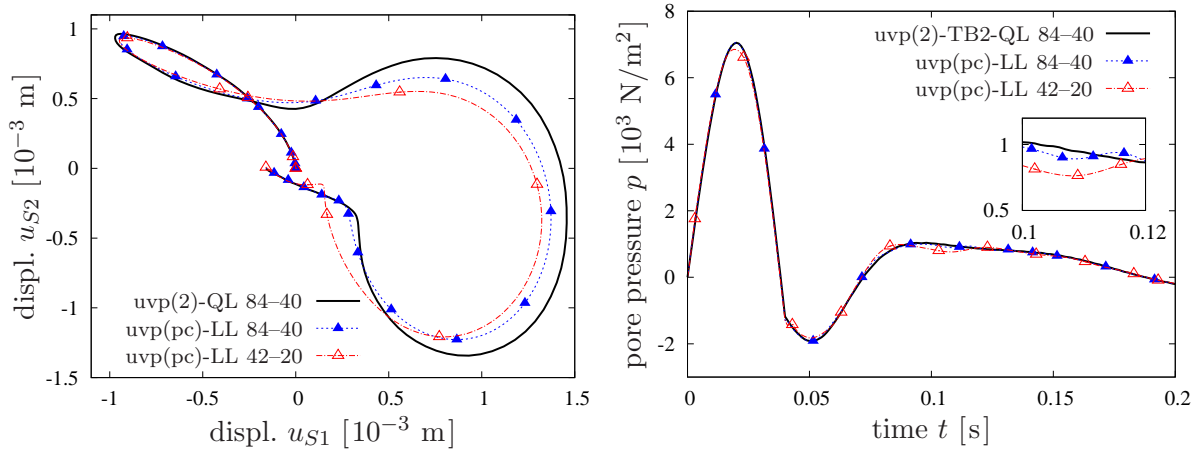


Figure 6.25: In-plane motion of point A (left) and pore pressure time history at point B (right) for $k^F = 10^{-10}$ m/s, $\Delta t = 10^{-3}$ s for uvp(2)-TB2, and Δt according to Table 6.7 for uvp(pc)

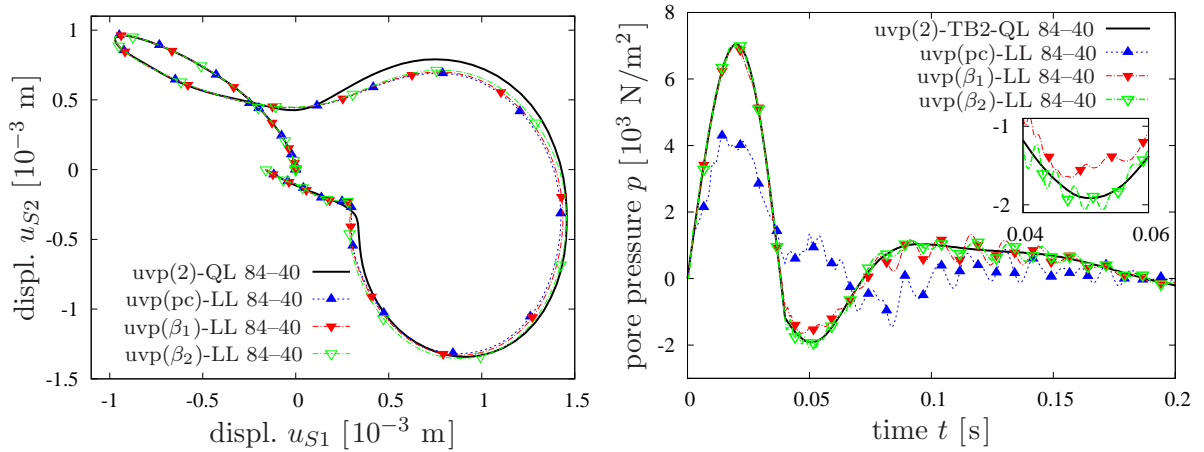


Figure 6.26: In-plane motion of point A (left) and pore pressure time history at point B (right) for $k^F = 10^{-10}$ m/s with $\Delta t = 10^{-3}$ s for uvp(2)-TB2, and with $\Delta t = 5 \cdot 10^{-5}$ s for uvp(pc) and uvp(β) with parameters $\beta_{0(1)} = 1$ and $\beta_{0(2)} = 4$ used in (4.85)

the fluid constituent is negligible, i. e. $(\mathbf{w}_F)'_S \approx \mathbf{0}$. Consequently, the reduced up formulation yields similar results for the displacement and the pore pressure variable as the three-field reference uvp(2), cf. Figure 6.27.

In the simple soil column problem (Section 6.1), an insufficient displacement solution of the mixed QL discretisation at the permeable loaded boundary was observed. The current two-dimensional problem proceeds from permeable boundary conditions under the assigned load, and thus, similar challenges might be observable. Therefore, we zoom into the domain and look what happens with the solid displacement and the pore pressure directly under the applied load below point C. Proceeding from a moderately low permeability with $k^F = 10^{-5}$ m/s as in Section 6.1, we consider the following spatial FE discretisation: 28 elements in x_1 direction (10 for the first 10 m, 8 for the middle 1 m, and 10 for the last 10 m), and uniformly distributed 200 elements (20 elements/meter) in x_2 direction for the QQ reference solution, which is compared to solutions with 50

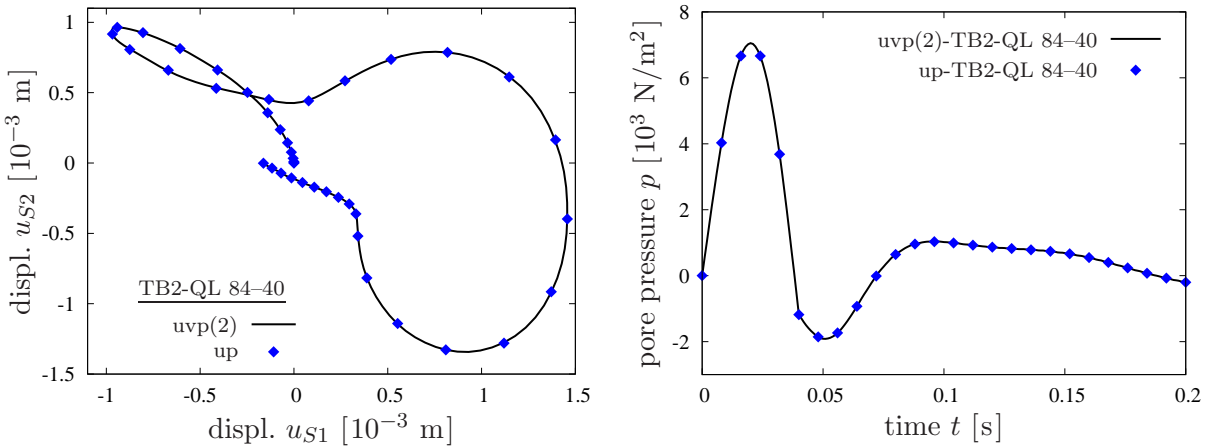


Figure 6.27: In-plane motion of point A (left) and pore pressure time history at point B (right) for $k^F = 10^{-10}$ m/s and $\Delta t = 10^{-3}$ s

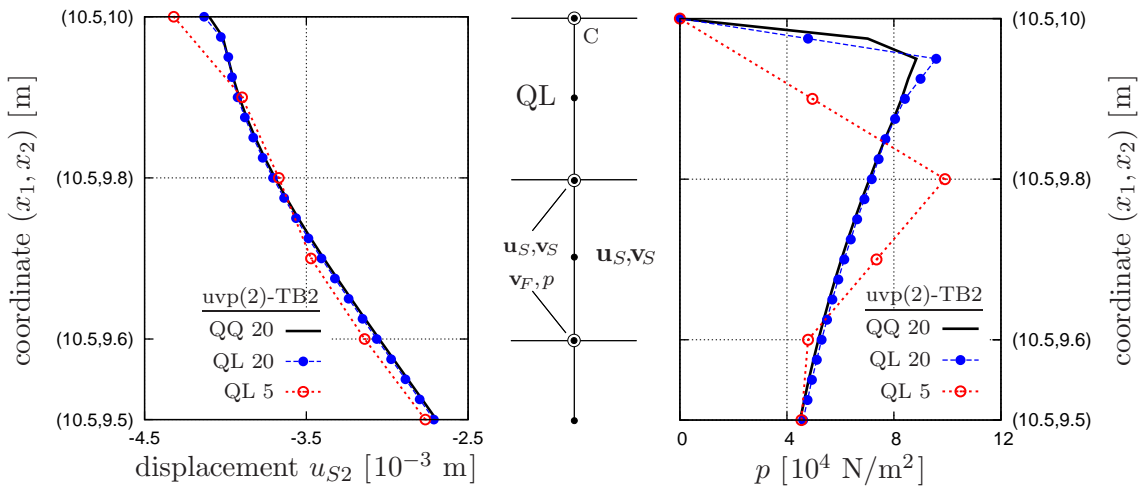


Figure 6.28: Solid displacement (left) and pore pressure distribution (right) in the first half meter under the load vertical down point C for $k^F = 10^{-5}$ m/s at $t = 0.02$ s

elements (5 elements/meter) in x_2 direction. Using uvp(2)-TB2 and the two mesh sizes 28–200 (20) and 28–50 (5), the results of the QQ 20 are compared with that of the QL 5 and QL 20 elementation. Figure 6.28 shows that similarly to the soil column problem, a faulty approximation of \mathbf{u}_S under the applied load is observed when using mixed QL elements. In this case, it is not that much distinctive as in the column problem as the step pore pressure increase is relieved in the horizontal x_1 direction. However, the principle problem is retained and might be overcome by a local mesh refinement at the permeable and loaded boundaries to better resolve the pore-pressure gradients.

Summary and Discussion of Results

For a reliable discussion of our findings, the preceding results of the two-dimensional wave propagation example (Section 6.2) and the first part of the saturated poroelastic column problem (Section 6.1.1) are briefly recapitulated. Therein, the focus is laid on a

dynamic TPM model with materially incompressible constituents in order to determine the primary unknowns, i. e., solid displacement, fluid velocity, and pore-fluid pressure, plus the solid velocity-displacement relation. Moreover, different formulations relying on different primal variables and governing equations are discussed, which are denoted shortly by $\text{uvp}(\dots)$, uwp , and up according to Table 6.1.

A summary of all investigated test cases and their solution behaviour is provided in Table 6.8, where the solid matrix response is governed by a linear elastic model.

Formulation		large k^F (10^{-2} m/s)			small k^F (10^{-10} m/s)		
		BE	TR	TB2	BE	TR	TB2
$\text{uvp}(1)$	LL/QQ	\bigcirc^1	\checkmark	\checkmark	—	—	—
	QL	\bigcirc^1	\checkmark^2	\checkmark	— ⁴	— ⁴	— ⁴
$\text{uvp}(2)$	LL/QQ	\bigcirc^1	\checkmark	\checkmark	—	—	—
	QL	\bigcirc^1	\checkmark^2	\checkmark	\bigcirc^1	\checkmark^2	\checkmark^5
uwp	LL/QQ	\bigcirc^1	\checkmark	\checkmark	—	—	—
	QL	\bigcirc^1	\bigcirc^3	\checkmark	\bigcirc^1	\checkmark^2	\checkmark^5
up	QL	$\bigcirc^{1,7}$	$\bigcirc^{2,7}$	\bigcirc^7	\bigcirc^1	\checkmark^2	\checkmark^5
$\text{uvp}(\alpha)$	LL/QQ	not needed			\bigcirc^1	\checkmark^6	\checkmark^6
$\text{uvp}(\text{pc})$	LL	$\Delta t \approx \Delta t_{cr}$	\checkmark			\checkmark	
		$\Delta t \ll \Delta t_{cr}$	—			—	
$\text{uvp}(\beta)$	LL	$\Delta t \approx \Delta t_{cr}$	not needed			not needed	
		$\Delta t \ll \Delta t_{cr}$	\checkmark^6			\checkmark^6	

¹ artificial numerical damping; reducible by using a smaller Δt

² pressure oscillations; reducible by using a smaller Δt and a finer mesh

³ strong pressure oscillations

⁴ wrong pressure solution

⁵ slight pressure oscillations for coarse meshes

⁶ accuracy depends on stabilising parameter

⁷ inaccurate displacement solution

Table 6.8: Summary of the observed solution behaviour for the distinct test cases. Used symbols: \checkmark : successful computation, \bigcirc : working but not recommended, — : no convergence or computation aborted

For the implicit monolithic solution, the system of equations was firstly discretised in space and secondly in time applying a diagonal implicit Runge-Kutta (DIRK) algorithm using the time-stepping BE, TR, and TR-BDF2 rules. In this regard, TR-BDF2 shows the best performance for solving the dynamic TPM problem, whereas the backward Euler (BE) scheme shows inaccuracy due to its strong damping behaviour, and the trapezoidal rule (TR) only provides marginal stability. The monolithic solution requires a stable mixed FE formulation fulfilling the LBB condition, such as the quadratic-linear (QL) *Taylor-Hood* elements, which is obligatory for low permeability conditions. In those cases, equal-order approximations show instabilities in the pore pressure field unless a pressure stabilisation technique is used, which, however, applies additional numerical errors at the expense of the stability. A major disadvantage of applying monolithic procedures comes

from the higher computational efforts due to the inversion of the *Jacobian* and the larger bandwidth of the system matrices coming along with quadratic interpolations if the stable QL approximation is used.

The semi-explicit-implicit splitting scheme has been implemented in form of the predictor-corrector (P-C) algorithm. In contrast to the monolithic solution, the splitting method demands the time discretisation and the splitting of the equations to be firstly performed, which is followed by the spatial discretisation. Moreover, this scheme allows for a continuous and linear equal-order FE approximation. Due to the included explicit steps, the stability of the splitting method is sensitive to the time-step size Δt but independent of the permeability. In this regard, an optimal solution is obtained for Δt being slightly smaller than the critical time step Δt_{cr} given by the CFL condition. The use of $\Delta t \ll \Delta t_{cr}$ yields pressure oscillations and requires a stabilised formulation. The general drawback that the finest mesh patch or the highest wave speed (CFL condition) dictates the global time step might be overcome by use of multirate time-stepping strategies (Savenco *et al.* [152]). Further demerits of the considered P-C algorithm are the need for finer meshes in order to obtain similar accuracy in the displacement field in comparison with the monolithic solution and the required special treatment of the volume efflux boundary condition.

6.3 Wave Propagation in an Elastic Structure-Soil Half Space

In this example, the dynamic response of an elastic block founded on a soil half space and subjected to horizontal shear loading is discussed. The geometry and the boundary conditions are illustrated in Figure 6.29, and the abbreviations in Table 6.1 and Table 6.5 are still valid here.

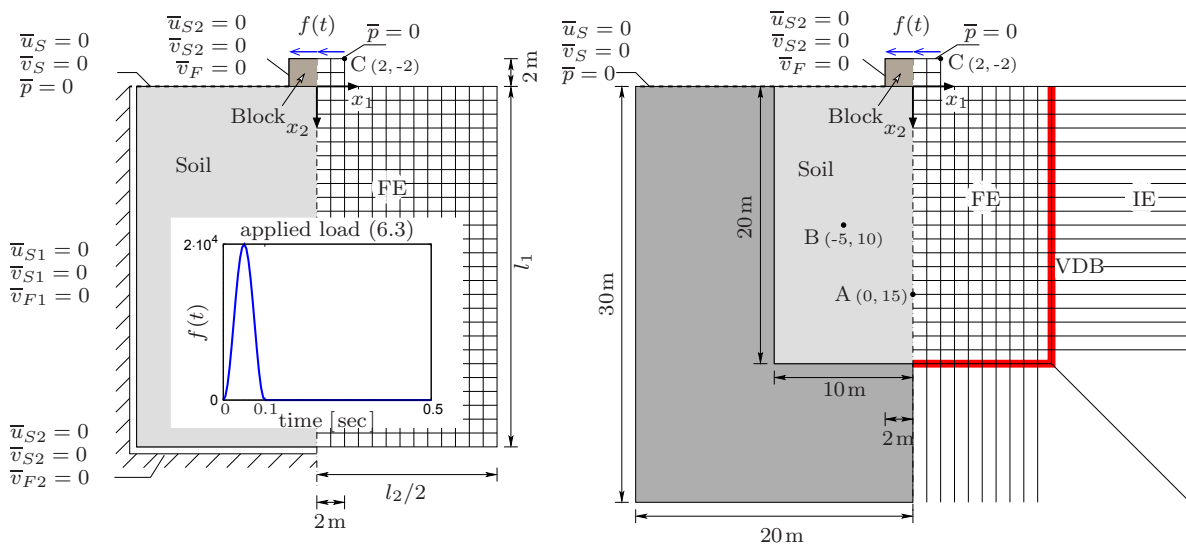


Figure 6.29: Geometry, boundary conditions and loading path of the 2-d structure-soil problem with FE discretisation and fixed boundary (left), and with FE discretisation and IE boundary together with VDB (right)

The modelling of soil is restricted to the case of a materially incompressible biphasic model with linear elastic behaviour of the solid skeleton and using the balance relations and the way of treatment as explained in Section 4.4. Such soil-structure interaction problems have been intensively discussed in the literature, cf. von Estorff [68], von Estorff & Firuziaan [69], Kim & Yun [103] and Heider *et al.* [87] among others. In this regard, the overall behaviour is affected by a number of factors such as the parameters of the subsystems and the structural embedment in the foundation soil.

In the current problem, the block (4×2 m) is considered to be in a welded contact with the soil beneath and discretised with the same type of finite elements as for the soil. The time discretisation is performed using the implicit monolithic TR-BDF2 scheme with unified time-step size $\Delta t = 10^{-3}$ s. The applied shear impulse force is given by

$$f(t) = 10^4 [1 - \cos(20 \pi t)] [1 - H(t - \tau)] \text{ N/m}^2 \quad (6.3)$$

with $H(t - \tau)$ being the Heaviside step function and $\tau = 0.1$ s. As mentioned in Section 4.4, the time-dependent damping terms (4.89) enter the weak formulation of the problem in form of nonlinear boundary integrals. Thus, an unconditional stability of the numerical solution requires that these terms are integrated over the boundary at the current time step in the sense of weakly-imposed *Neumann* boundary conditions. The dynamic response of the soil and the efficiency of the considered infinite boundary treatment are investigated for two cases:

Case (1): the material parameters of the block and the soil are the same (cf. Table 6.2) with $k^F = 10^{-2}$ m/s.

Case (2): the block is considered to be made of concrete⁶ with parameters given in Table 6.9, whereas the soil parameters are taken from Table 6.2 with $k^F = 10^{-2}$ m/s.

Parameter	Symbol	Value	SI unit
1 st Lamé constant	μ^S	$1.25 \cdot 10^{10}$	N/m ²
2 nd Lamé constant	λ^S	$8.30 \cdot 10^9$	N/m ²
effective density	ρ^{SR}	2800	kg/m ³
initial volume fraction	n_{0S}^S	0.99	–
Darcy permeability	k^F	10^{-6}	m/s

Table 6.9: Material parameters of elastic concrete

A benchmark solution, referred to as Ref.FE, is generated by considering $l_1 = l_2 = 40$ m in Figure 6.29, left, where the choice of large dimensions guarantees that no reflected waves propagate back to points A, B and C during the analysis. The efficiency of the proposed boundary treatment is measured by comparing the displacements at different points in the domain (A, B and C) for two types of boundaries, i. e., for FE-IE with VDB as in Figure 6.29, right, and for FE-fix as in Figure 6.29, left, with $l_1 = l_2 = 20$ m.

⁶The numerical simulation of concrete using a multi-phase material model is considered by choosing $n_{0S}^S = 0.99$, i. e., the concrete is treated as an almost single phasic, linear elastic solid skeleton.

In case (1) with unified material parameters, the stiffness ratio of the concrete block to that of soil is $E^B/E^S = 1$, with E^B , E^S being the elasticity moduli⁷ of the concrete and the soil solid skeleton, respectively⁸. In this case, the vibration of the block damps out in a weak manner and results in a successive wave transition into the supporting soil. In this connection, Figure 6.30 shows exemplary contour plots of the computed solid displacement field, which makes the wave propagation and the weak damping behaviour apparent.

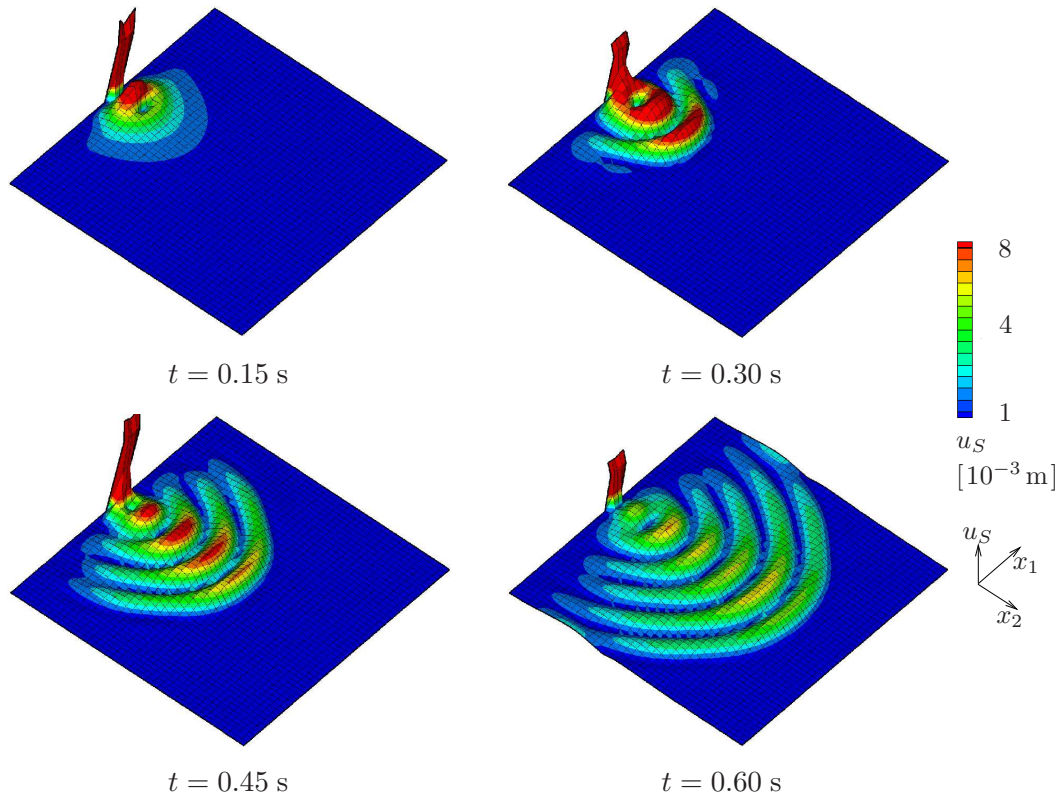


Figure 6.30: Time sequence of solid displacement $u_S = \sqrt{(u_{S1}^2 + u_{S2}^2)}$ contour plots for case (1) with $E^B/E^S = 1$

In Figure 6.31, the time history of the horizontal displacement u_{S1} of point C at the top of the block with weakly damped motion is depicted. Therein, a good agreement among the different solution strategies is obtained as far as the reflected waves do not propagate back to point C. However, the solution with FE-fix deteriorates after a certain time due to the interference of the reflected waves.

For the two points A and B in the soil domain, the time history of the horizontal displacement u_{S1} is plotted in Figure 6.32. The efficiency of the FE-IE scheme in impeding the reflecting waves is obvious by comparison with the reference solution Ref. FE. However, the FE-fix solution violates this agreement due to the overlapping of progressing

⁷The Young's modulus is computed as $E^S = \mu^S (2\mu^S + 3\lambda^S)/(\mu^S + \lambda^S)$.

⁸ $E^B/E^S \ll 1$ represents the case of a soft block founded on a rigid base [68], which is not a case of study in this contribution.

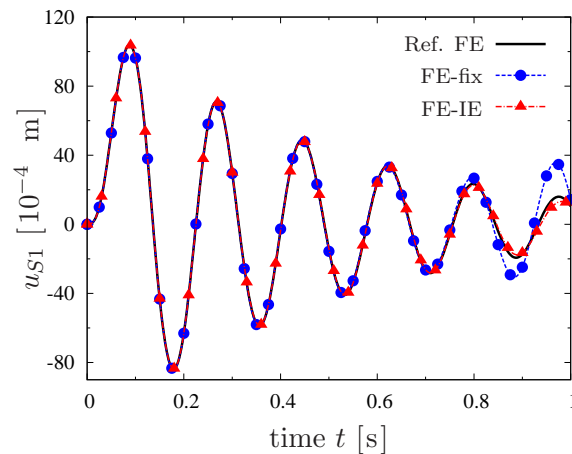


Figure 6.31: Horizontal displacement time history at point C for case (1) with $E^B/E^S = 1$

and reflected waves.

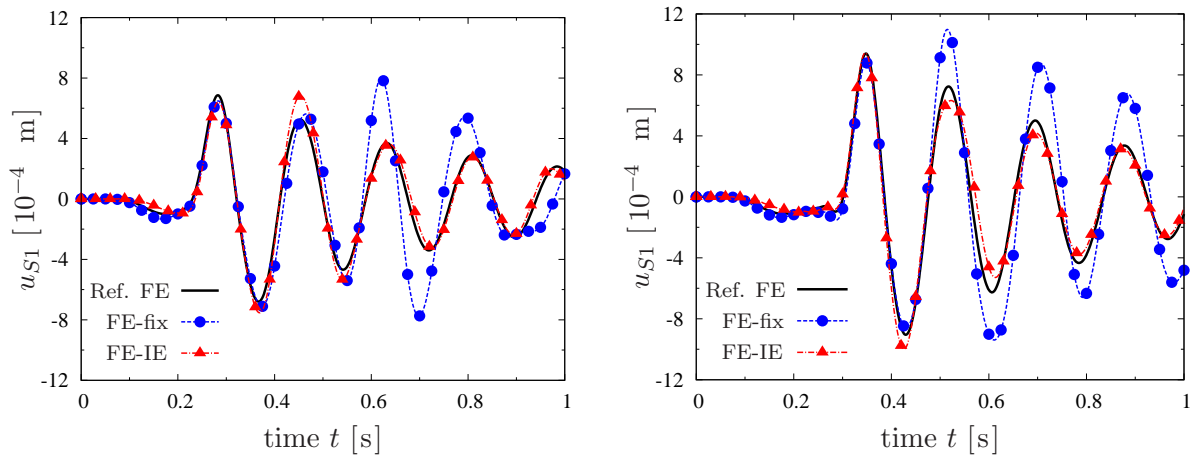


Figure 6.32: Horizontal displacement time history for case (1) with $E^B/E^S = 1$ at point A(0, 15) (left) and at point B(-5, 10) (right)

In case (2), the stiffness of the concrete block is higher than that of soil ($E^B/E^S = 2.1 \times 10^3$), which leads to a strong damping of the block motion. For this case, Figure 6.33 shows exemplary contour plots of the computed horizontal solid displacement for the discussed three different boundary cases, and clearly reveals the influence of the boundary conditions on the reflected waves.

The maximum response of the block decreases in comparison with case (1) and the motion damps out very strongly. Accordingly, only one wave corresponding to the impulse loading appears and radiates towards the infinity. Moreover, Figure 6.34, left, shows that due to the high stiffness difference between the block and the soil beneath, the reflected waves do not propagate into the block as the displacement at point C(2,-2) is not disturbed.

For a point in the domain (here: B(-5,10)), Figure 6.34, right, depicts the time history of the horizontal displacement u_{S1} considering the different boundary treatments. Here, the role of the damping boundary in reducing the effects of the reflecting waves is further

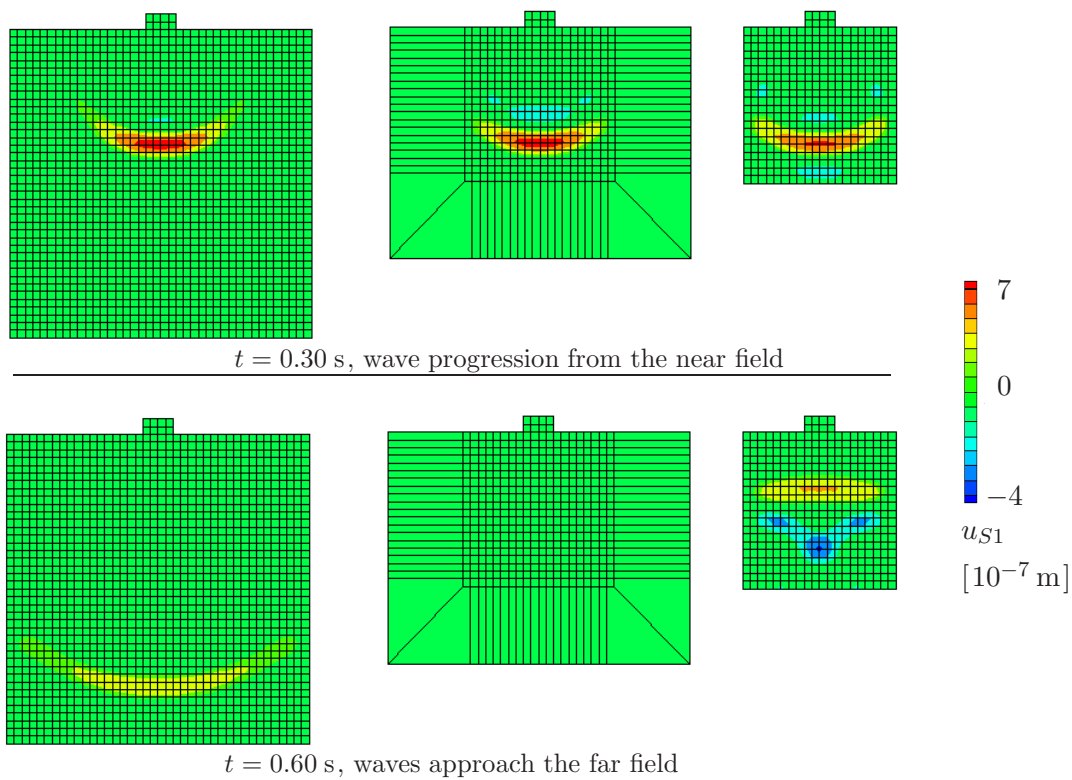


Figure 6.33: Time sequence of displacement u_{S1} contour plots for case (2): Ref. FE (left), FE-IE with VDB (middle) and FE-fix (right)

enhanced by comparing the FE-fix and the FE-IE results with the reference Ref. FE solution.

In conclusion, it is apparent that the proposed VDB method can significantly but not perfectly prevent the wave reflection back to the near field. This is due to the fact that absorption of the approaching waves cannot be made perfect over the whole range of the

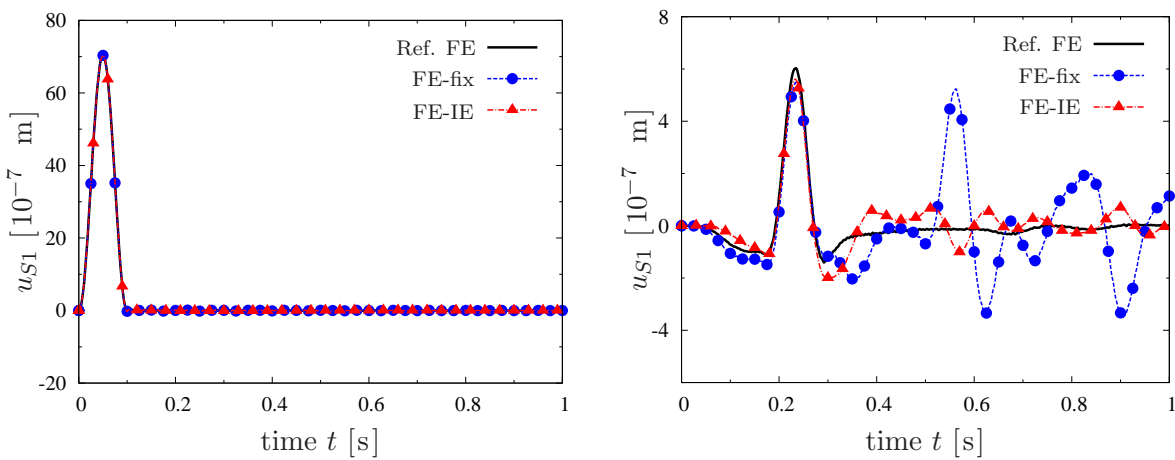


Figure 6.34: Horizontal solid displacement time history for case (2) with $E^B/E^S \gg 1$ at point C(2,-2) (left), and at point B(-5,10) (right)

FE-IE boundary, which is an inherent disadvantage of the VDB treatment originating from the variation of the wave incident angles along the boundary. A possible remedy is to provide curved boundaries, which mimic the shape of the incident wave fronts, and thus, provide small wave incident angles. For a detailed discussion of this issue, one refers to the pioneering work of Lysmer & Kuhlemeyer [120].

6.4 Soil-Structure Interaction under Seismic Loading

The investigation of soil-structure interaction (SSI) under seismic excitation requires the efforts of at least three fields of science, which are the structural engineering to study the structural vibration, the geotechnical engineering to examine the dynamic wave propagation as well as the different behaviours of soil, and the geophysics to determine the earthquake time-history input data, cf. Wolf & Song [179]. The main objective of the following example is to analyse and model the nonlinear elasto-viscoplastic response of soil under seismic loading. Therefore, the treatment of the soil-structure system is carried out in the time domain following a direct method, where the numerical modelling includes the spatial discretisation of the structure and the soil, and the analysis of the whole system is performed in one step for each time step.

6.4.1 General Aspects

In the case of soil-structure interaction under earthquake loading (Figure 6.35, left), the seismic waves that propagate from the hypocentre of the earthquake cause seismically-induced distortions in the soil under the foundations, which in turn lead to deformations in the superstructure. In return, the induced oscillations of the structure lead to structural inertial forces, which add dynamic stresses to the supporting soil. Therefore, it is convenient in the computational analysis to separate the aforementioned behaviours into two successive phenomena, i. e. ‘kinematic interaction’ and ‘inertial interaction’, which in reality occur simultaneously, cf., e. g., Kim & Stewart [104], Wolf [177], and Mylonakis *et al.* [135] for further details.

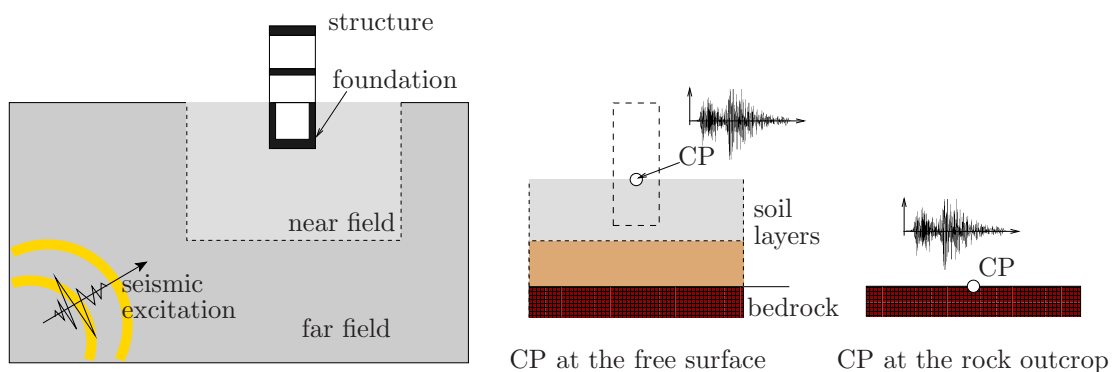


Figure 6.35: Soil-structure interaction under seismic excitation (left), and the ‘control’ point (CP) where the ground motion is specified (right), cf. Wolf [178]

Kinematic Interaction (KI)

The main goal of the KI investigation is to determine the foundation input motion (FIM), which is usually different from the free-field seismic response as it takes the shifts and the rotations of the foundation into consideration⁹. Therefore, the first step is to get the free-field response, which is usually recorded using in-situ accelerographs and represents the spatial and the temporal changes under seismic loadings before the installation of the structure. This includes determining the ‘control’ point (CP) where the ground motion is specified (cf. Figure 6.35, right), and recording the influence of the different body and surface seismic waves.

Having obtained the free-field design motion, the next step is to determine the response across the soil-foundation interface (foundation input motion). Here, the KI analysis accounts for the stiffness of the foundation and the structure, and disregards their masses, cf. Figure 6.36, right. This is because the masses and the resulting inertial loads will be considered in the subsequent inertial interaction analysis. Depending on the considered wave types, the motion of the foundation might include translational and rotational components. This issue can be analysed using linear methods via softwares such as SHAKE (cf. Mylonakis *et al.* [135]), or following nonlinear schemes, where the ‘control’ point is given at the base of the soil profile.

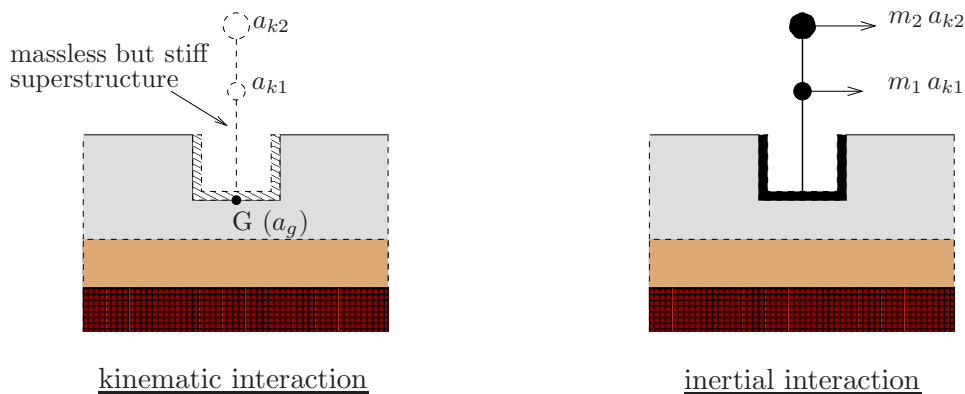


Figure 6.36: Kinematic interaction (KI) (left), and inertial interaction (II) (right), cf. Mylonakis *et al.* [135]

Inertial Interaction (II)

The massless foundation motion, which results from the KI analysis, is used as an input data for the inertial interaction treatment. In most of the structural dynamics problems, the response of the supporting soil is assumed linear elastic or viscoelastic, which is justified for vibrations with small amplitudes, cf. Erxianga *et al.* [67]. In this case, the soil can be replaced by equivalent dynamic springs, dashpots, and masses for each mode of the foundation motion, which take into account small nonlinear behaviours. However,

⁹Generally, six modes of vibration are recorded; three displacements along x_1 , x_2 , and x_3 axes, and three rotations around the mentioned axes.

such a treatment is not well suited to investigate the liquefaction effects associated with a strong nonlinear response, plastic deformations, and accumulation of pore-fluid pressure in the soil layers. Thus, it is essential to apply advanced material models for the soil modelling. The II analysis is usually carried out in two steps: firstly, the modes of the foundation motion as a result of the KI (translations and rotations) are considered, and secondly, the seismic response of the foundation-structure system is determined in order to calculate the cross sections and the reinforcement of the structural elements or to evaluate their performance under a given earthquake.

In practise, the calculation of the inertial forces and the structural deformations under seismic loading can roughly be classified into three methods (Bachmann [6]):

(1) *The equivalent force method*, in which the seismic effect (foundation excitation) is replaced by a static horizontal force acting on the whole structure, whereas the structural behaviour is considered linear elastic. Such methods are usually applied to uniform structures, which can be approximated by single-mass oscillators. Here, seismic building codes (e. g. Eurocode 8) provide parameters that take into consideration different material effects, such as the ground softening, plastic deformations, and damping effects, as well as factors that account for the location and the importance of the facility, cf. Eurocode 8 for full details.

(2) *Response spectrum methods*, which proceed from viscoelastic structural behaviour and apply dynamical linear calculation to the governing balance relations in order to get the maximum responses, i. e. peak displacements, velocities, and accelerations. Here, the structure is replaced by a multi-mass oscillator for the sake of getting the maximum modes of oscillations (independent eigenforms). Then, the total response of the structure is obtained by an overlapping scheme of the different eigenmodes of response.

(3) *The time-history method*, which is mostly applied to assess the performance of a structure under a certain seismic base excitation. The basic idea is to apply time-integration schemes to the governing differential balance equations rather than calculating the response spectra, which yield a more accurate maximum response calculation. For linear systems of equations, simplified methods such as the modal analysis can be applied, which help to decrease the calculation time and the problem complexity. For nonlinear differential balance relations, the treatment becomes more time consuming as linearisation methods have to be applied in each time step.

In the literature, various methods with different levels of complexity are used to investigate SSI problems. In what follows, a brief summary of those schemes is introduced, where more details can be found in the works by, e. g., Jeremić *et al.* [100], Wolf [177, 178] and Mylonakis *et al.* [135].

- **Ignoring the SSI:** In case of a relatively flexible structure founded on a very stiff soil (e. g. bedrock), the seismic-induced motion of the structure leads to negligible deformations in the ground. Thus, the ground motion can be applied directly to the foundation, or alternatively, equivalent loads proportional to the base acceleration can be assigned to the structural masses. However, for structures of higher stiffness founded on soil, the motions that result from the inertial interaction may lead to considerable rocking of the soil under the foundation which has to be taken into

account in the soil half-space analysis.

- **Decoupling methods:** For linear SSI systems, the principle of superposition might be applied. Here, the soil and the structure are investigated separately using the aforementioned KI and II analyses. The total response is then obtained by adding the contributions of the sub-systems at the nodal interface. Such a treatment reduces the size of the problem and allows for a faster calculation in comparison with the direct methods. However, for a non-linear inelastic behaviour of soil, the application of this scheme becomes very sophisticated.
- **Direct methods:** Following the direct methods, the soil-structure system is treated as a whole and the analysis is applied in one step. Here, the finite embedded structure together with a considerable part of the unbounded semi-infinite soil are regarded in the model. Moreover, the free-field motion is applied to fictitious boundaries of the soil (e.g. to the bedrock). In the numerical modelling, the system is treated as an IBVP that incorporates a spatial discretisation of the soil and the structure. Although this way of treatment is time consuming, especially when dealing with nonlinear SSI problems, however, it allows for an accurate analysis of the different behaviours under various loading conditions, cf. Wolf [177].

6.4.2 Seismic Input Data

The data of the seismic excitation in the following numerical example are based on realistic measurements, which are related to the Kobe earthquake¹⁰, FUK station, horizontal north-south (NS) motion. Here, Figures 6.37 and 6.38 depict the NS displacement, velocity and acceleration time histories. These data are taken from the strong motion database of the Pacific Earthquake Engineering Research Center (PEER)¹¹, which are freely available for engineering applications.

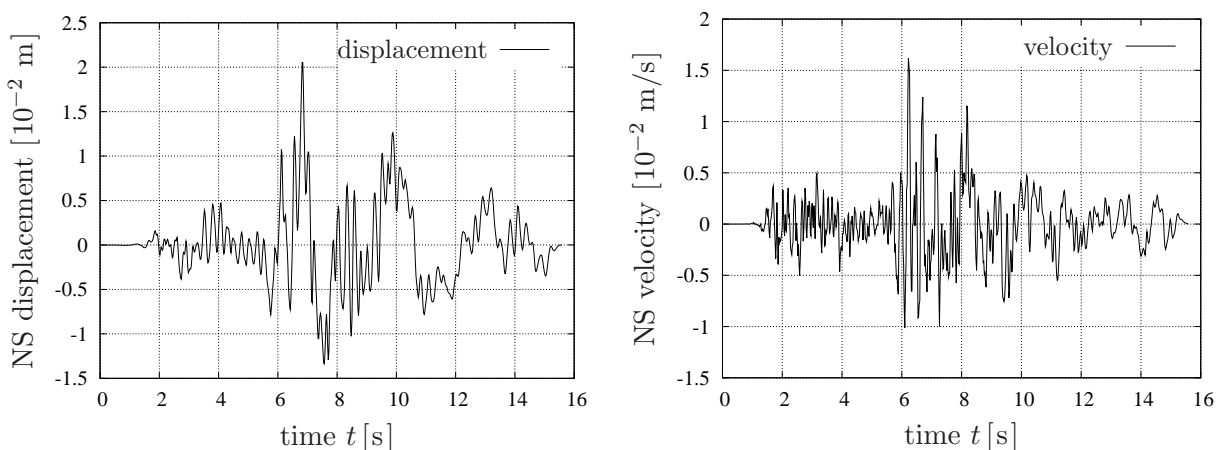


Figure 6.37: Displacement and velocity time history of the Kobe earthquake, FUK station

¹⁰The Kobe earthquake took place in Japan in 1995 with magnitude ≈ 7.2 on the Richter Scale.

¹¹The PEER website [<http://peer.berkeley.edu/smcat>] provides a large variety of reviewed and processed earthquake records, which are useful for the engineering analysis.

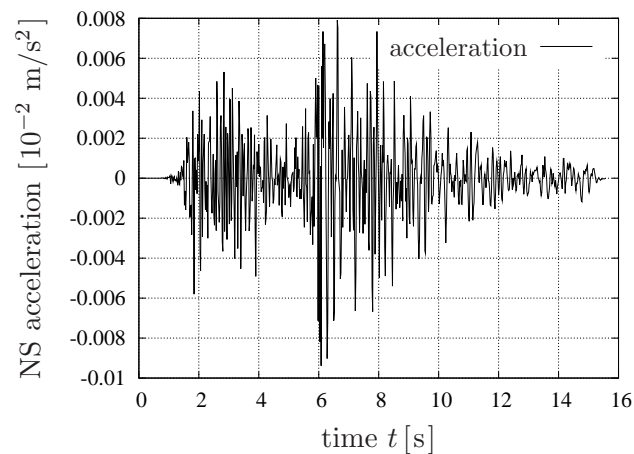


Figure 6.38: Acceleration time history of Kobe earthquake, FUK station

The earthquake time history is usually recorded on a firm ground. Thus, we might apply these data at the bedrock-soil interface of the considered IBVP.

6.4.3 Application to Liquefaction Modelling: Structure Founded on Stratified Soil

In the following, a two-dimensional computational model of a soil-structure system is analysed using the FE package PANDAS. The seismic excitation appears in form of vertically incident shear waves, which is applied at the bottom of the profile, i.e. along the soil-bedrock interface boundary. The geometry and the boundary conditions are illustrated in Figure 6.39, where the abbreviations in Table 6.1 are still valid for this example.

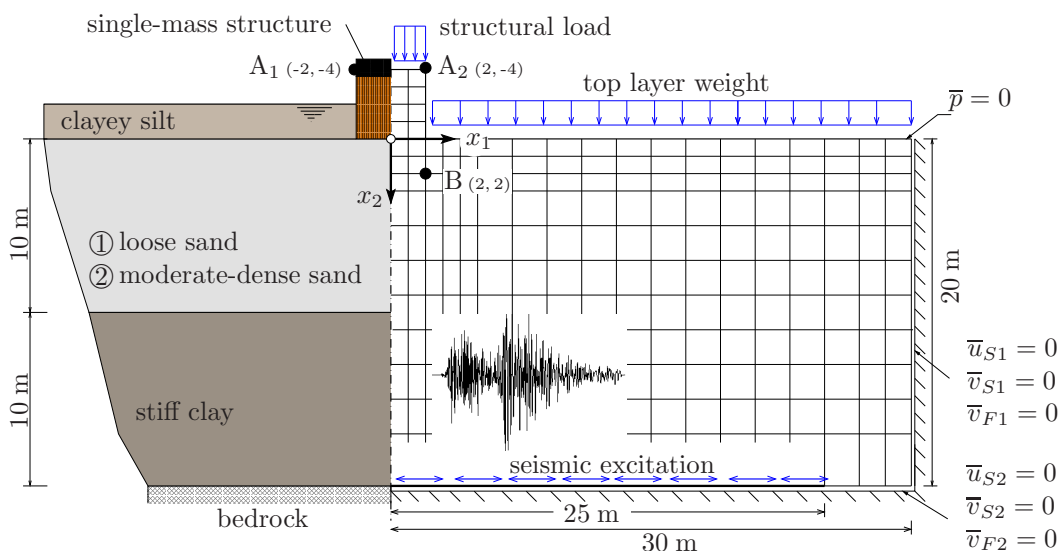


Figure 6.39: Geometry and boundary conditions of the soil-structure interaction problem under seismic loading

In analogy to the liquefaction-prone Wildlife Refuge site strata in Figure 5.4, the chosen

soil layers of the considered problem provide an appropriate environment to liquefaction events. Here, the present layers are illustrated in Figure 6.39 and can briefly be demonstrated as follows: (1) A clayey silt surface layer, which is replaced in the numerical model by a uniformly distributed load (50.0 kN/m^2). This layer provides permeable upper boundaries during the consolidation and the excess pore-pressure dissipation phases. (2) A liquefiable sand layer (10 m thick), on which the structure is installed. The expected behaviour of this layer is nonlinear elastoplastic. Therefore, it is modelled using the elasto-viscoplastic constitutive model with isotropic hardening as introduced in Section 3.2. Here, in order to capture the two significant liquefaction events of flow liquefaction and cyclic mobility, the parameters in Table 5.1 for very loose and moderate-dense sands are exploited. (3) A stiff clay layer (10 m thick) under the sand layer, which is characterised by a low permeability parameter and expected to behave linear elastic. (4) A bedrock that marks the bottom boundary of the considered IBVP, at which the seismic load is applied.

In the current treatment, the modelling of soil is confined to the case of a saturated, materially incompressible solid-fluid aggregate. Moreover, the domain of the boundary-value problem is chosen sufficiently wide in order to avoid the influence of the lateral boundaries on the response of the region of interest under the structure. Herein, the applied loads during the whole numerical treatment are illustrated in Figure 6.40, left.

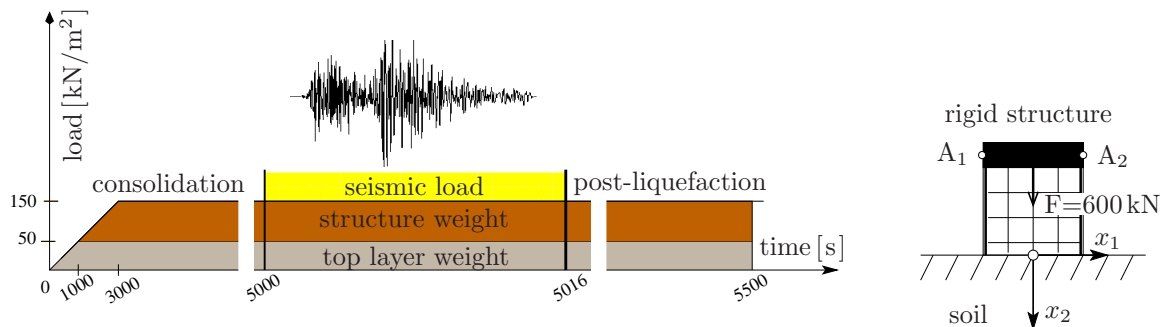


Figure 6.40: Applied loads to the soil-structure interaction problem (left) and illustration of the rigid structure at the top of the soil domain (right)

The structure is assumed to be made of a very stiff material, e. g. concrete with material parameters given in Table 6.9, which can be approximated by a single-mass oscillator with very high stiffness, cf. Figure 6.40, right. Here, depending on the nature of the foundation soil, the structure might undergo settlement, uplifting, or overturning as will be discussed throughout the example. The parameters of the elasto-viscoplastic sand layer are given in Tables B.1 and B.2 with $k^F = 10^{-5} \text{ m/s}$, whereas the parameters of the elastic, stiff clay layer are presented in Table 6.2 with $k^F = 10^{-8} \text{ m/s}$.

In the following investigation, the aim is to reveal the flow liquefaction and the cyclic mobility in saturated soils under extreme dynamic loadings and not to model a particular seismic event. Therefore, the given earthquake excitation is multiplied by amplification factors depending on the initial density of the soil. In this connection, two cases of the initial density and amplification factors are considered for the sand layer under the structure: Firstly, the case of flow-liquefaction-prone very loose sand, where the seismic excitation

is multiplied by a factor of 15. Secondly, the case of moderate-dense sand, where the earthquake data is magnified by a factor of 20 to manifest the cyclic mobility behaviour. In the IBVP, the earthquake velocity (Figure 6.37, right) is used as an input data, which is compatible with the structure of the governing balance relations. In this connection, the treatment proceeds from the set of equations uvp (2) with the primary variables \mathbf{u}_S , \mathbf{v}_S , \mathbf{v}_F , and p , cf. DAE (4.42). Moreover, an implicit monolithic time-stepping algorithm using the Backward *Euler* (BE) scheme is exploited to solve the problem, cf. Box (4.50). The choice of the implicit BE is mainly due to the fact that the BE is easy to implement and needs less calculation time in comparison with the TR or the TR-BDF2 schemes. However, as has been shown in Section 6.2, the BE method suffers from an artificial numerical damping, which can be reduced by choosing smaller time steps. This damping should be taken into account if one compares the numerical solution with reference or benchmark solutions, which is not the case in this treatment.

Case (1): Very Loose Sand Layer \rightarrow Flow Liquefaction

Starting with the case of a very loose sand layer according to the definitions and parameters in Section 5.2, Figure 6.41 shows exemplary contour plots of the solid plastic volumetric strain evolution ε_{Sp}^V .

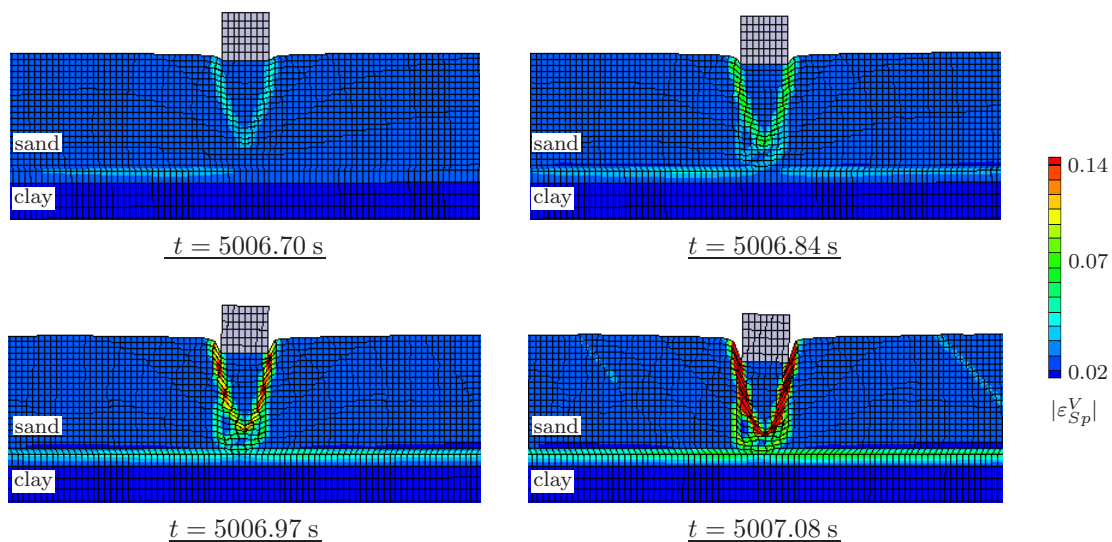


Figure 6.41: Time sequence of solid plastic volumetric strain contour plots for the case of very loose saturated sand layer under the structure (scale factor 10)

This type of soil collapse is known as seismic-induced flow liquefaction, which leads to a punching shear failure in the loose foundation soil¹².

¹²Bearing capacity failure happens when the shear stresses in the soil exceed its shear strength. Herein, depending on the foundation soil properties, three modes of bearing capacity failure can be recognised, cf. Day [41]: (1) *Punching shear failure* which occurs for loose foundation soils. In this case, no general shear surface is generated, and the main deformations happen in the soil directly below the structure's

Unlike the perfectly undrained CU triaxial tests, the behaviour in the considered IBVP is partially undrained with possible excess pore-pressure dissipation during and after the dynamic loading. Herein, the excess pore pressure firstly accumulates in certain sand zones with high plastic volumetric strain and then migrates due to the pore-pressure gradient into neighbouring zones of lower accumulated pore pressure. In this regard, Figure 6.42 shows exemplary time sequence contour plots of the excess pore-water pressure p with deformed mesh (scale factor 10) of the considered 2-d problem.

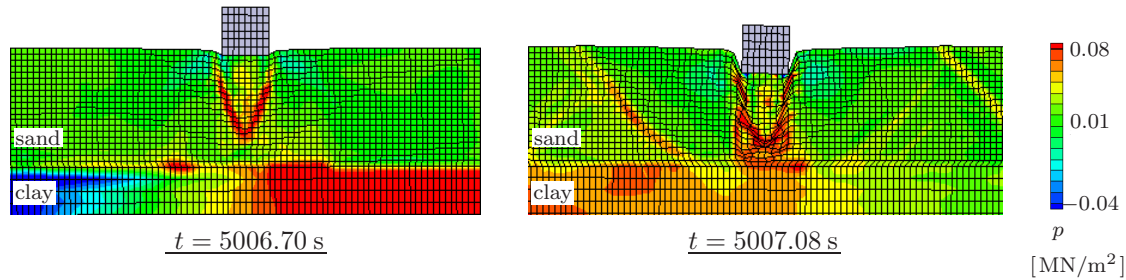


Figure 6.42: Time sequence of pore pressure contour plots for the case of very loose soil layer under the foundation (scale $\times 10$)

Following this, one distinguishes between the oscillatory pore pressure that appears in the elastic clay layer and the accumulative pore pressure in the sand layer under the foundation. In the latter, it is clear that the development of the plastic volumetric strain in certain zones coincides with the pore-pressure build-up. Figure 6.43, left, depicts the interplay between the mean effective stress and the pore pressure (cf. (5.5)) at point B (2,2) in the soil domain.

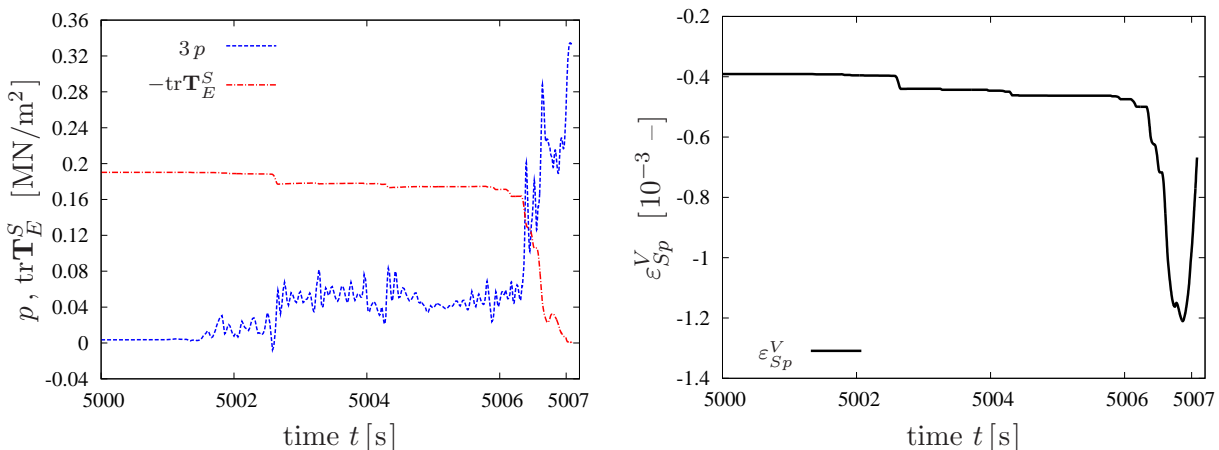


Figure 6.43: Pore pressure and mean effective stress time history at B (2,2) (left), and solid plastic volumetric strain time history at point B (right) during the seismic load, case (1)

footing. (2) *Local shear failure* which is normally seen in soils of medium dense nature. This type of failure is an intermediate state between punching and general shear collapse, where a partial shear surface can be distinguished immediately below the footing. (3) *General shear failure* usually happens in soils of dense or hard state and involves total rupture of the soil with a continuous and distinct shear surface.

Figure 6.43, left, shows that the flow liquefaction takes place due to the reduction of the mean effective stress and the build-up of the pore pressure until most of the applied stress is carried by the pore fluid ($\text{tr}\mathbf{T}_E^S$ tends to become zero). Moreover, the fast increase of the pore pressure at a certain stage of the loading is accompanied by a drastic increase of the plastic volumetric strain. In this case, the continuous increase of the pore-water pressure under deviatoric stress conditions is associated with a contraction tendency of the loose sand layer ($\varepsilon_{Sp}^V < 0$), cf. Figure 6.43, right.

During the seismic excitation, Figure 6.44 illustrates how the structure undergoes vertical as well as horizontal deformations. Moreover, shortly before the collapse, a rapid increase of the horizontal and vertical deformations as well as a small inclination of the structure is demonstrated.

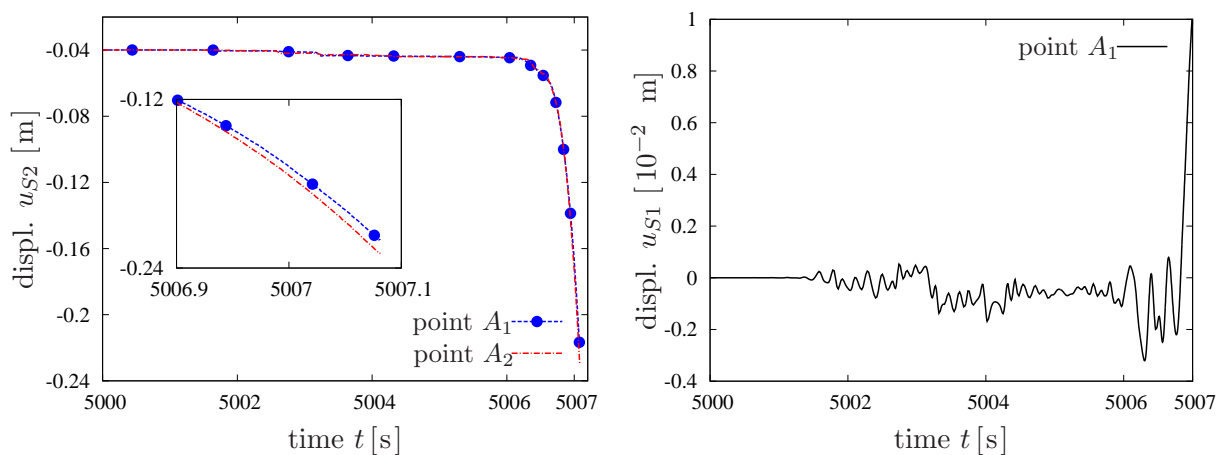


Figure 6.44: Vertical displacement time history at points A_1 (-2,-4) and A_2 (2,-4) (left), and horizontal displacement time history at point A_1 (right) during the seismic load, case (1)

It is worth mentioning that in the case of a very loose foundation sand layer with magnified seismic excitation by a factor of 15, the collapse takes place during the earthquake excitation, and thus, the calculation terminates before the post-liquefaction (dissipation) phase, cf. Figure 6.40, left.

Case (2): Moderate-Dense Sand \rightarrow Cyclic Mobility

For a moderate-dense sand layer underlying the structure (see the classifications in Section 5.2 and the parameters in Table 5.1), Figure 6.45 shows exemplary contour plots of the solid plastic volumetric strain evolution ε_{Sp}^V at different times during the earthquake loading.

The behaviour in Figure 6.45 represents the seismic-induced cyclic mobility, where a limited accumulation of the pore pressure takes place and the effective stress can never reach a zero value. In this connection, Figure 6.46, left, depicts the interplay between the effective stress and the pore pressure at point B (2,2) during the application of the seismic excitation. Here, a slight build-up in the excess pore pressure can be seen till $t \approx 5004$ s, which is followed by a decrease in the pore pressure and an increase in the mean effective

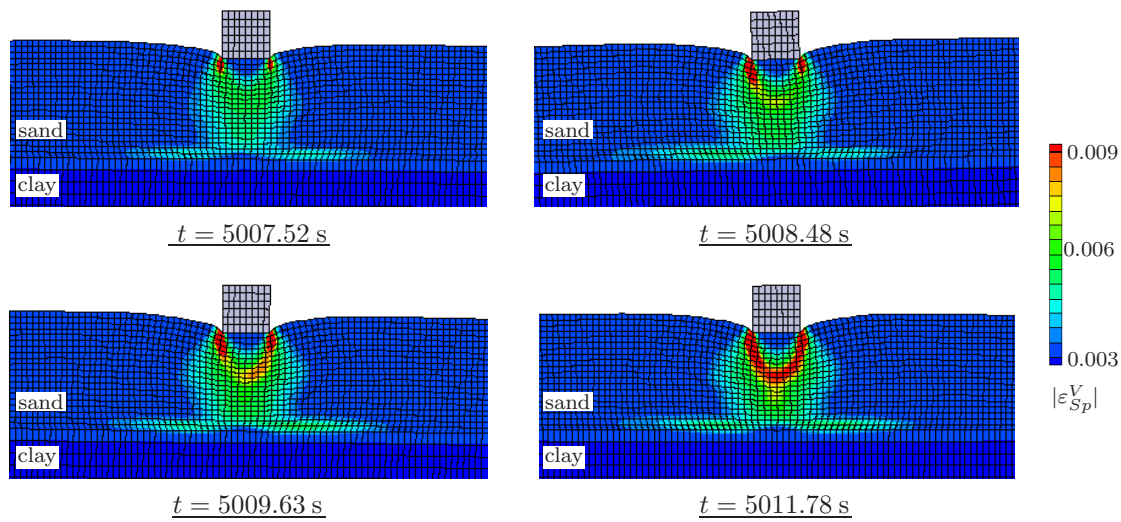


Figure 6.45: Time sequence of solid plastic volumetric strain ε_{Sp}^V contour plots for the case of moderate-dense saturated sand layer under the structure (scale $\times 30$)

stress. Figure 6.46, right, shows that an immense increase in the solid plastic volumetric strain ($\varepsilon_{Sp}^V > 0 \rightarrow$ dilative) occurs when the seismic excitation reaches its peak value at $t \approx 5006.6$ s leading to clear features of the plastic shear band under the structure (cf. Figure 6.45).

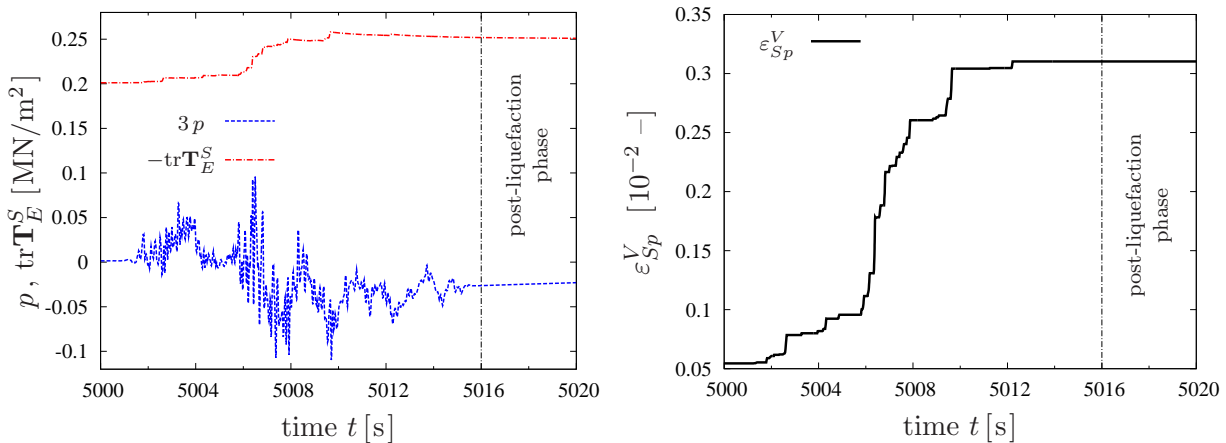


Figure 6.46: Pore-pressure and mean effective stress time history at point $B(2,2)$ (left), and solid plastic volumetric strain time history at B (right) during the seismic excitation and dissipation for case (2) of moderate-dense sand

Figure 6.47, left, depicts the vertical displacement time history at points $A_1(-2,-4)$ and $A_2(2,-4)$ at the top of the structure. It is clear that the vertical settlement in the case of moderate-dense sand is less than that in the very loose sand layer case. Moreover, at the end of the earthquake loading, a small inclination of the structure can be observed. Figure 6.47, right, shows the horizontal motion of the structure during the seismic excitation. Here, a residual horizontal displacement can be detected at the end of the dynamic loading.

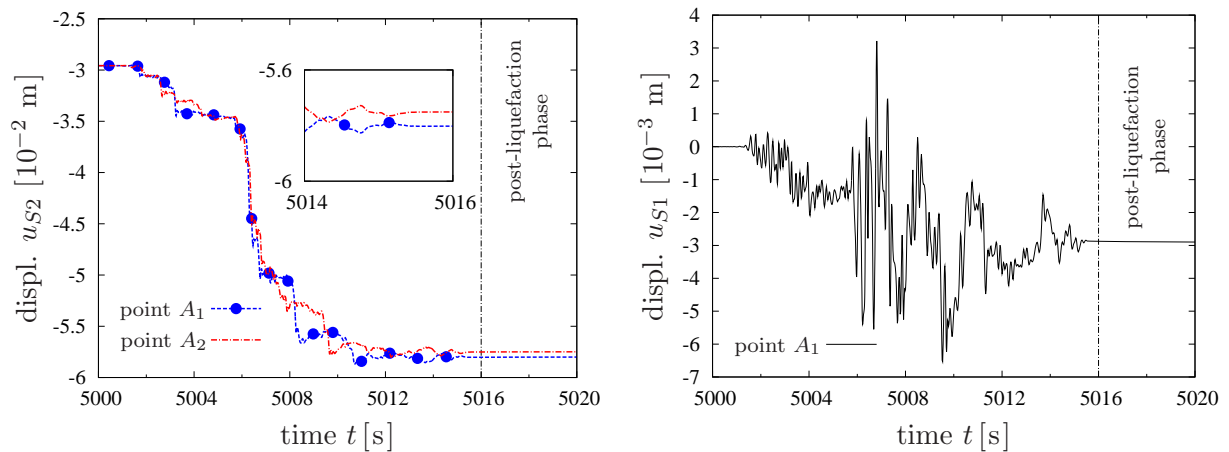


Figure 6.47: Vertical displacement time history at points A_1 (-2,-4) and A_2 (2,-4) (left), and horizontal displacement time history at point A_1 (right) during the seismic excitation and dissipation for case (2) of moderate-dense sand

Remark: In general, the flexibility of the foundation in the SSI system reduces the peak deformations induced by the ground motion. However, under certain circumstances, the natural frequency of the SSI system and that of the excitation are found in a state that leads to a large response (i. e. resonance phenomenon). In such cases, the inertial force due to structural oscillations may lead to large inelastic deformations in both the structure and the foundation soil.

Chapter 7:

Summary, Conclusions and Future Aspects

7.1 Summary and Conclusions

In this monograph, the numerical solution of fluid-saturated porous materials within a continuum-mechanical framework and the related challenges have been investigated. Different thermodynamically consistent material models were used and a special attention has been paid to the behaviour under dynamic loading conditions. This enabled to understand and simulate important phenomena in porous media dynamics, such as the wave propagation in half spaces and the earthquake-induced liquefaction events.

Material modelling using the TPM: The macroscopic material modelling was carried out by exploiting the Theory of Porous Media (TPM). Moreover, the treatment proceeded from saturated biphasic solid-fluid aggregates and was committed to the isothermal and geometrically linear scope, where the main focus was on the case of intrinsically incompressible constituents. Regarding the constitutive modelling, the material response of the solid skeleton for the dynamic wave propagation problems was considered to be linear elastic and governed by the *Hookean* elasticity law. However, for the simulation of liquefaction-related phenomena, an elasto-viscoplastic constitutive model was adopted. This entailed the implementation of a hyperelastic model for the nonlinear elastic behaviour and the exploitation of a single-surface yield function for modelling the inelastic solid response.

The continuum-mechanical treatment of multiphase materials yields a volume-coupled formulation with the coupling inherent in the governing conservation laws. This requires a special investigation to elucidate the characteristics of the balance relations and the appropriate numerical schemes. In the discussion, we have seen that the coupling is defined through distinct terms and material parameters in the set of governing partial-differential balance equations (PDE). For instance, the values of the permeability parameter and the fluid compressibility play decisive roles in determining the scope of coupling, where the most challenging case is for a materially incompressible pore fluid in combination with a very low permeability. Thus, it turned out that only particular numerical schemes are eligible to solve the arising stiff, strongly coupled governing PDE in an efficient way.

Time integration schemes: To solve the initial-boundary-value problems of porous media dynamics in this work, the finite element method (FEM) beside two classes of time integration strategies and their algorithms have been introduced, namely monolithic and splitting solution schemes. In the monolithic treatment, the governing PDE, basically the solid and fluid momentum balances and the overall mass balance, are firstly discretised in space using the FEM and secondly in time. As has been seen, explicit monolithic strategies were only applicable in the case of materially compressible pore-fluid constituents.

However, very small time steps were required to get stable solutions, which gave rise to the *stiffness* of the coupled equations. Therefore, the major attention was on the implicit monolithic treatment, where the stability does not demand a minimum time-step size. Here, different implicit monolithic time-stepping have been introduced and compared in the numerical examples. The semi-explicit-implicit operator-splitting scheme was implemented using a predictor-corrector algorithm. In this regard, the time stepping is applied first, the time partitioning via intermediate velocities second, and the spatial FE discretisation with equal-order interpolations of all primary variables last.

In summary, the following two points, as outcomes of the time-integration schemes and the numerical examples discussion, are mentioned:

- (1) The choice of the primary variables and the corresponding balance relations plays a crucial role for the accuracy and stability of the chosen numerical solution scheme.
- (2) Both the implicit monolithic and the semi-explicit-implicit splitting strategies are basically applicable to the solution of the coupled two-phase problem. However, the implicit monolithic procedure seemed to be more convincing due to its more general suitability, provided that the right multi-field formulation, stable mixed finite elements, and an appropriate time integrator are used.

Unbounded domains modelling using the VDB: For the numerical simulation of wave propagation in porous media infinite half spaces, general absorbing boundary conditions have been discussed. The investigation proceeded from a saturated biphasic solid-fluid aggregate with intrinsically incompressible constituents. As a result, one has to deal with a strongly coupled three-field variational problem, which gives rise to two types of bulk waves, namely, pressure and shear waves. For the treatment of soil-structure interaction problems, the surrounding semi-unbounded domain is split into a near field around the structure (source of vibration) discretised using the FEM, and a far field that extends to infinity, which is discretised in space with the quasi-static, mapped IE. The wave reflection at the near-field/far-field interface is eliminated by introducing a viscous damping boundary (VDB) layer, which entails nonlinear terms in the problem residual. These terms have to be integrated numerically over the FE-IE interface in a weakly imposed manner. Therefore, the use of an implicit monolithic time-stepping scheme is required for an unconditional numerical stability.

Unlike the application to single-phasic elastic materials, the efficiency of the VDB implementation in case of multi-phasic media is affected by additional factors. For instance, it is affected by the accuracy of the FE discretisation of the pore-pressure variable inside the IE, the proper implementation of the mapped IE scheme, and the permeability parameter that governs the solid-fluid interaction, and thus, the strength of the coupling in the multi-field problem. The results of the numerical examples showed that the proposed VDB treatment can significantly suppress the spuriously reflected waves, and therefore, provides a suitable representation of the reference solution at moderate implementation complexity.

Modelling of liquefaction phenomena: A considerable part of this dissertation was devoted to the investigation of liquefaction phenomena, which usually appear in saturated granular materials after dynamic excitation. This included the definitions and the

description of liquefaction mechanisms, the factors affecting saturated soil behaviour, and an *in-situ* example of seismic-induced liquefaction. The modelling of liquefaction events accounted for fluid-saturated granular materials with materially incompressible constituents. Moreover, an elasto-viscoplastic constitutive model was used to capture the basic features of the response, such as the pore-fluid pressure accumulation and softening of the granular structure.

A special attention in the discussion has been paid to the important features of granular materials, such as the tendency to undergo volumetric strains due to the application of shear stresses. Under drained conditions, the volumetric strain can be used as an indicator for a contractive or a dilative behaviour. However, under undrained conditions, the contraction tendency leads to a pore-pressure accumulation and a change in the mean effective stress, which is governed by the principle of effective stresses. The response of granular materials depends very much on the initial density and leads to two significant physical events, which are the ‘flow liquefaction’ and the ‘cyclic mobility’. The flow liquefaction usually happens in loose saturated soils with low shear strength. The applied load in this case results in an increase of the pore pressure and incredible reduction in the effective stress until the soil loses its nature as a solid and flows like a viscous fluid. In the cyclic mobility, the mean effective stress can never reach a zero value, and the residual shear strength can always maintain the static equilibrium. The two aforementioned features have been numerically captured by applying the considered elasto-viscoplastic model to initial-boundary-value problems of saturated soil dynamics.

Numerical examples: Four numerical examples have been finally introduced to validate and to verify the underlying algorithms and procedures using different FE packages. These examples helped in figuring out the merits and the drawbacks of the test cases and in realising the instability or inaccuracy sources, where stabilisation techniques were suggested. Moreover, it has been shown that the suggested formulations, numerical tools and material models can efficiently simulate several behaviours of saturated porous material dynamics, such as the wave propagation in unbounded half spaces and the seismic-induced liquefaction phenomena.

7.2 Future Aspects

The presented findings can serve as a base for future studies and applications in the fields of porous media dynamics and soil-structure interaction. Herein, the methods and constitutive models to describe coupled solid-fluid problems can successfully be used to simulate important phenomena in porous materials, such as the different waves propagation and liquefaction events. Furthermore, the discussed numerical strategies and algorithms provide a good understanding of the solution behaviour and detailed steps for practical applications.

The algorithms and procedures in this work were tested on canonical numerical examples using a Scilab code and the coupled FE solver PANDAS in the two-dimensional space. Therefore, it is very interesting for future implementations to consider three-dimensional problems together with parallel computation using commercial FE codes. In this regard,

a powerful scripting environment for monolithic time integrations can be achieved by introducing a linking interface between the coupled FE solver PANDAS and the ABAQUS commercial FE package, which is an ongoing project at the Institute of Applied Mechanics in Stuttgart.

The next step in the enhancement of the liquefaction modelling is to look at the kinematic hardening for the anisotropic cyclic soil behaviour, which can be applied by introducing appropriate formulations for the back-stress tensor. In this connection, several laboratory experiments, such as the cyclic triaxial test and the simple shear test, have to be performed in order to determine the relevant material parameters.

Appendix A:

Tensor Calculus

This appendix briefly provides a number of important notations and rules of the tensor calculus applied throughout the thesis. For a more comprehensive and detailed discussion, the interested reader is referred to the works by de Boer [16] or Ehlers [55].

A.1 Tensor Algebra

For the statements in the upcoming discussion let $\{\alpha, \beta, a, b, \dots\} \in \mathbb{R}$ be arbitrary scalar quantities, $\{\mathbf{a}, \mathbf{b}, \mathbf{u}, \mathbf{v}, \dots\} \in \mathcal{V}^3$ be arbitrary vectors of the proper *Euklidian* 3-d vector space \mathcal{V}^3 , $\{\mathbf{A}, \mathbf{B}, \mathbf{T}, \dots\} \in \mathcal{V}^3 \otimes \mathcal{V}^3$ be arbitrary 2nd-order tensors, $\{\overset{n}{\mathbf{A}}, \overset{n}{\mathbf{B}}, \overset{n}{\mathbf{C}}, \dots\} \in \mathcal{V}^3 \otimes \mathcal{V}^3 \otimes \dots \otimes \mathcal{V}^3$ (n-times) be arbitrary n-th order tensors in the corresponding n-th order dyadic product space and the indices $\{i, j, k, l\} = 1, 2, \dots, n \in \mathbb{N}$ be natural numbers.

A.1.1 Basics of Tensor Calculus

Linear mapping and dyadic product

A 2nd-order tensor \mathbf{T} is a linear mapping, which transforms a vector \mathbf{u} uniquely in a vector \mathbf{w} :

$$\mathbf{w} = \mathbf{T} \mathbf{u}. \quad (\text{A.1})$$

In other words, a simple 2nd-order tensor $\mathbf{A} := \mathbf{a} \otimes \mathbf{b}$ maps a vector \mathbf{c} onto a vector $\mathbf{d} = (\mathbf{b} \cdot \mathbf{c}) \mathbf{a}$ as

$$(\mathbf{a} \otimes \mathbf{b}) \mathbf{c} =: (\mathbf{b} \cdot \mathbf{c}) \mathbf{a}. \quad (\text{A.2})$$

Linear mapping in basis notation

In the following, one makes use of the summation convention of *Einstein*, which states that whenever the same index occurs twice in a term, a summation over that index has to be carried out. Therefore, a vector \mathbf{a} can be expressed in terms of its coefficients a_i and basis \mathbf{e}_i as $\mathbf{a} := a_i \mathbf{e}_i = a_1 \mathbf{e}_1 + a_2 \mathbf{e}_2 + a_3 \mathbf{e}_3 = \sum_{i=1}^3 (a_i \mathbf{e}_i)$. The simple tensor \mathbf{A} reads

$$\mathbf{A} = \mathbf{a} \otimes \mathbf{b} = (a_i \mathbf{e}_i) \otimes (b_j \mathbf{e}_j) = a_i b_j (\mathbf{e}_i \otimes \mathbf{e}_j) =: A_{ij} (\mathbf{e}_i \otimes \mathbf{e}_j), \quad (\text{A.3})$$

with A_{ij} being the coefficients and $(\mathbf{e}_i \otimes \mathbf{e}_j)$ being the basis of \mathbf{A} .

Following this, the linear mapping can be given as

$$\mathbf{w} = \mathbf{A} \mathbf{u} = (A_{ij} \mathbf{e}_i \otimes \mathbf{e}_j) (u_k \mathbf{e}_k) = A_{ij} u_k (\mathbf{e}_j \cdot \mathbf{e}_k) \mathbf{e}_i = A_{ij} u_k \delta_{jk} \mathbf{e}_i = \underbrace{A_{ij} u_j}_{w_i} \mathbf{e}_i. \quad (\text{A.4})$$

Here, δ_{jk} is the *Kronecker* symbol, with $\delta_{jk} = 1$ for $j = k$ and $\delta_{jk} = 0$ for $j \neq k$.

Collected product operations

In the linear mapping, a number of tensorial operations have been used, which, among others, will be explained in the following. The scalar product (inner product) of two tensorial quantities results in a scalar value:

$$\alpha = \mathbf{a} \cdot \mathbf{b} = a_i b_i, \quad \beta = \mathbf{A} \cdot \mathbf{B} = a_{ij} b_{ij}. \quad (\text{A.5})$$

Following this, a number of relations related to the tensor product of tensors are given:

$$\begin{aligned} \mathbf{c} &= \mathbf{A} \mathbf{b} = A_{ij} b_j \mathbf{e}_i, \\ \mathbf{C} &= \mathbf{A} \mathbf{B} = A_{ij} B_{jk} (\mathbf{e}_i \otimes \mathbf{e}_k), \\ \mathbf{D} &= \overset{4}{\mathbf{A}} \mathbf{B} = A_{ijkl} B_{kl} (\mathbf{e}_i \otimes \mathbf{e}_j). \end{aligned} \quad (\text{A.6})$$

The vector or cross product (outer product) of two vectors yields a vector:

$$\mathbf{d} = \mathbf{u} \times \mathbf{w} = |\mathbf{u}| |\mathbf{w}| \sin[\angle(\mathbf{u}, \mathbf{w})] \mathbf{n} \quad (\text{A.7})$$

with \mathbf{n} being a unit vector $\perp (\mathbf{u}, \mathbf{w})$ and $|\cdot|$ is the norm (positive square root) of the vector (\cdot) . The outer tensor product of tensors (double cross product) yields

$$\begin{aligned} (\mathbf{A} \otimes \mathbf{B})(\mathbf{u}_1 \times \mathbf{u}_2) &:= \mathbf{A} \mathbf{u}_1 \times \mathbf{B} \mathbf{u}_2 - \mathbf{A} \mathbf{u}_2 \times \mathbf{B} \mathbf{u}_1, \\ \mathbf{A} \otimes \mathbf{B} &= (\mathbf{a} \otimes \mathbf{b}) \otimes (\mathbf{c} \otimes \mathbf{d}) = (\mathbf{a} \times \mathbf{c}) \otimes (\mathbf{b} \times \mathbf{d}). \end{aligned} \quad (\text{A.8})$$

Specific tensors and rules

The transposed tensor \mathbf{A}^T related to \mathbf{A} shows the following property

$$\mathbf{w} \cdot (\mathbf{A} \mathbf{u}) = (\mathbf{A}^T \mathbf{w}) \cdot \mathbf{u}. \quad (\text{A.9})$$

In basis notation, the transposition of $\mathbf{A} = A_{ij} (\mathbf{e}_i \otimes \mathbf{e}_j)$ can be applied by an exchange of the subscripts of the tensor coefficients as $\mathbf{A}^T = A_{ji} (\mathbf{e}_i \otimes \mathbf{e}_j)$ or by an exchange of the tensor basis as $\mathbf{A}^T = A_{ij} (\mathbf{e}_j \otimes \mathbf{e}_i)$.

The inverse of a 2nd-order tensor \mathbf{A} with $\det \mathbf{A} \neq 0$ is expressed using the adjoint (adj) and the cofactor (cof) operators as

$$\mathbf{A}^{-1} = (\det \mathbf{A})^{-1} \text{adj } \mathbf{A} \quad \text{or} \quad \mathbf{A}^{-1} = (\det \mathbf{A})^{-1} \text{cof } \mathbf{A}^T, \quad (\text{A.10})$$

where $\mathbf{A} \mathbf{A}^{-1} = \mathbf{A}^{-1} \mathbf{A} = \mathbf{I}$, with \mathbf{I} being the 2nd-order identity tensor.

An orthogonal tensor \mathbf{A} exhibits the following property

$$\mathbf{A}^{-1} = \mathbf{A}^T \quad \longleftrightarrow \quad \mathbf{A} \mathbf{A}^T = \mathbf{I}. \quad (\text{A.11})$$

The trace (tr) of a tensor \mathbf{A} is given by a scalar product as

$$\text{tr } \mathbf{A} = \mathbf{A} \cdot \mathbf{I}. \quad (\text{A.12})$$

A tensor \mathbf{A} is called symmetric if $\mathbf{A} = \mathbf{A}^T$ and skew-symmetric if $\mathbf{A} = -\mathbf{A}^T$. Moreover, a tensor \mathbf{A} can be additively split into a symmetric and a skew-symmetric part as

$$\mathbf{A} = \text{sym } \mathbf{A} + \text{skw } \mathbf{A}, \quad (\text{A.13})$$

$$\text{where: } \text{sym } \mathbf{A} := \frac{1}{2}(\mathbf{A} + \mathbf{A}^T), \quad \text{skw } \mathbf{A} := \frac{1}{2}(\mathbf{A} - \mathbf{A}^T).$$

An arbitrary tensor \mathbf{A} can be additively split into a spherical and a deviatoric parts as

$$\mathbf{A} = \mathbf{A}^V + \mathbf{A}^D, \quad (\text{A.14})$$

$$\text{where: } \mathbf{A}^V := \frac{1}{3}(\mathbf{A} \cdot \mathbf{I}) \mathbf{I}, \quad \mathbf{A}^D := \mathbf{A} - \frac{1}{3}(\mathbf{A} \cdot \mathbf{I}) \mathbf{I}.$$

In this, the deviatoric part \mathbf{A}^D is a traceless tensor, i. e. $\mathbf{A}^D \cdot \mathbf{I} = 0$

A.1.2 Fundamental Tensors

Tensors which are built from basis vectors are called fundamental tensors.

The 2nd-order fundamental tensor (or identity tensor) \mathbf{I} leads to an identical mapping of vectors or tensors, viz.:

$$\mathbf{a} = \mathbf{I} \mathbf{a}, \quad \mathbf{A} = \mathbf{I} \mathbf{A}, \quad \text{with } \mathbf{I} = \delta_{ij} (\mathbf{e}_i \otimes \mathbf{e}_j). \quad (\text{A.15})$$

The 3rd-order fundamental tensor (or *Ricci* permutation tensor) $\overset{3}{\mathbf{E}}$ is defined as follows:

$$\mathbf{u} \times \mathbf{v} = \overset{3}{\mathbf{E}} (\mathbf{u} \otimes \mathbf{v}), \quad \text{with } \overset{3}{\mathbf{E}} := e_{ijk} (\mathbf{e}_i \otimes \mathbf{e}_j \otimes \mathbf{e}_k). \quad (\text{A.16})$$

Here, e_{ijk} is the permutation symbol, which is expressed as

$$e_{ijk} \begin{cases} e_{123} = e_{231} = e_{312} = 1, \\ e_{321} = e_{213} = e_{132} = -1, \\ 0 \text{ for all remaining } e_{ijk}. \end{cases} \quad (\text{A.17})$$

Three different forms of the 4th-order fundamental tensor can be defined. They are built by a dyadic product and independent transpositions of 2nd-order identity tensors, viz.:

$$\begin{aligned} \text{identical map : } \overset{4}{\mathbf{I}} &:= (\mathbf{I} \otimes \mathbf{I})^T \quad \longleftrightarrow \quad \overset{4}{\mathbf{I}} \mathbf{A} = \mathbf{A}, \\ \text{'transposing' map : } \overset{4}{\mathbf{I}}_T &:= (\mathbf{I} \otimes \mathbf{I})^T \quad \longleftrightarrow \quad \overset{4}{\mathbf{I}}_T \mathbf{A} = \mathbf{A}^T, \\ \text{'tracing' map : } \overset{4}{\mathbf{I}}_{\text{tr}} &:= \mathbf{I} \otimes \mathbf{I} \quad \longleftrightarrow \quad \overset{4}{\mathbf{I}}_{\text{tr}} \mathbf{A} = (\text{tr } \mathbf{A}) \mathbf{I}. \end{aligned} \quad (\text{A.18})$$

A.1.3 The Eigenvalue Problem and Invariants of 2nd -Order Tensors

For an arbitrary 2nd-order tensor \mathbf{A} , the eigenvalue problem can be expressed as

$$(\mathbf{A} - \gamma_A \mathbf{I}) \mathbf{a} = \mathbf{0}, \quad \text{with} \quad \begin{cases} \gamma_A & : \text{ eigenvalues,} \\ \mathbf{a} & : \text{ eigenvectors.} \end{cases} \quad (\text{A.19})$$

Herein, a non-trivial solution for \mathbf{a} requires that $\det(\mathbf{A} - \gamma_A \mathbf{I}) = 0$ (the characteristic equation be fulfilled). In particular, the characteristic equation yields

$$\begin{aligned} \det(\mathbf{A} - \gamma_A \mathbf{I}) &= \det \mathbf{A} - \gamma_A \frac{1}{2} (\mathbf{A} \otimes \mathbf{A}) \cdot \mathbf{I} + \gamma_A^2 \frac{1}{2} \mathbf{A} \cdot (\mathbf{I} \otimes \mathbf{I}) - \gamma_A^3 \det \mathbf{I} \\ &= \mathbb{I}_A - \gamma_A \mathbb{II}_A + \gamma_A^2 \mathbb{I}_A - \gamma_A^3 = 0. \end{aligned} \quad (\text{A.20})$$

In the above equation, \mathbb{I}_A , \mathbb{II}_A and \mathbb{III}_A are the three scalar principal invariants of the tensor \mathbf{A} , which might be given in details as

$$\begin{aligned} \mathbb{I}_A &= \frac{1}{2} (\mathbf{A} \otimes \mathbf{I}) \cdot \mathbf{I} = \text{tr} \mathbf{A}, \\ \mathbb{II}_A &= \frac{1}{2} (\mathbf{A} \otimes \mathbf{A}) \cdot \mathbf{I} = \frac{1}{2} [(\text{tr} \mathbf{A})^2 - \text{tr}(\mathbf{A} \mathbf{A})], \\ \mathbb{III}_A &= \frac{1}{6} (\mathbf{A} \otimes \mathbf{A}) \cdot \mathbf{A} = \det \mathbf{A}. \end{aligned} \quad (\text{A.21})$$

A.1.4 Collected Operators and Rules

Applying the gradient, divergence, rotation and *Laplace* operators to a field function (\cdot) :

$$\begin{aligned} \text{Gradient increases the order of } (\cdot) \text{ by one: } \quad \text{grad } \alpha(\mathbf{x}) &= \frac{d\alpha(\mathbf{x})}{d\mathbf{x}} =: \mathbf{a}(\mathbf{x}), \\ \text{Divergence decreases the order of } (\cdot) \text{ by one: } \quad \text{div } \mathbf{T}(\mathbf{x}) &= [\text{grad } \mathbf{T}(\mathbf{x})] \mathbf{I} =: \mathbf{a}(\mathbf{x}), \\ \text{Rotation operator preserves the order of } (\cdot): \quad \text{rot } \mathbf{v}(\mathbf{x}) &= \mathbf{E}^3 [\text{grad } \mathbf{v}(\mathbf{x})]^T =: \mathbf{a}(\mathbf{x}), \\ \text{Laplace operator preserves the order of } (\cdot): \quad \Delta(\cdot) &:= \text{div grad } (\cdot). \end{aligned} \quad (\text{A.22})$$

Following this, a number of rules for the above operators are introduced:

$$\begin{aligned} \text{grad } (\alpha \beta) &= \alpha \text{ grad } \beta + \beta \text{ grad } \alpha, & \text{grad } (\alpha \mathbf{v}) &= \mathbf{v} \otimes \text{grad } \alpha + \alpha \text{ grad } \mathbf{v}, \\ \text{grad } (\alpha \mathbf{T}) &= \mathbf{T} \otimes \text{grad } \alpha + \alpha \text{ grad } \mathbf{T}, & \text{grad } (\mathbf{u} \cdot \mathbf{v}) &= (\text{grad } \mathbf{u})^T \mathbf{v} + (\text{grad } \mathbf{v})^T \mathbf{u}, \\ \text{grad } (\mathbf{u} \times \mathbf{v}) &= \mathbf{u} \times \text{grad } \mathbf{v} + \text{grad } \mathbf{u} \times \mathbf{v}, & \text{grad div } \mathbf{v} &= \text{div } (\text{grad } \mathbf{v})^T, \\ \text{div } (\alpha \mathbf{v}) &= \mathbf{v} \cdot \text{grad } \alpha + \alpha \text{ div } \mathbf{v}, & \text{div } (\alpha \mathbf{T}) &= \mathbf{T} \text{ grad } \alpha + \alpha \text{ div } \mathbf{T}, \\ \text{div } (\mathbf{T} \mathbf{v}) &= (\text{div } \mathbf{T}^T) \cdot \mathbf{v} + \mathbf{T}^T \cdot \text{grad } \mathbf{v}, & \text{div } (\mathbf{v} \times \mathbf{T}) &= \mathbf{v} \times \text{div } \mathbf{T} + \text{grad } \mathbf{v} \times \mathbf{T}, \\ \text{div rot } \mathbf{v} &= 0, & \text{rot grad } \alpha &= \mathbf{0}. \end{aligned} \quad (\text{A.23})$$

Appendix B:

Triaxial Test and Material Parameters

The material parameters that enter the elasto-viscoplastic model have been identified based on triaxial experiments, conducted at the Institut of Applied Mechanics, University of Stuttgart. For details about the different experiments and the parameter identification and optimisation strategies, the reader is referred to the works by, e. g. Müllerschön [134], Ehlers & Scholz [64], Scholz [155] and Ehlers & Avci [60].

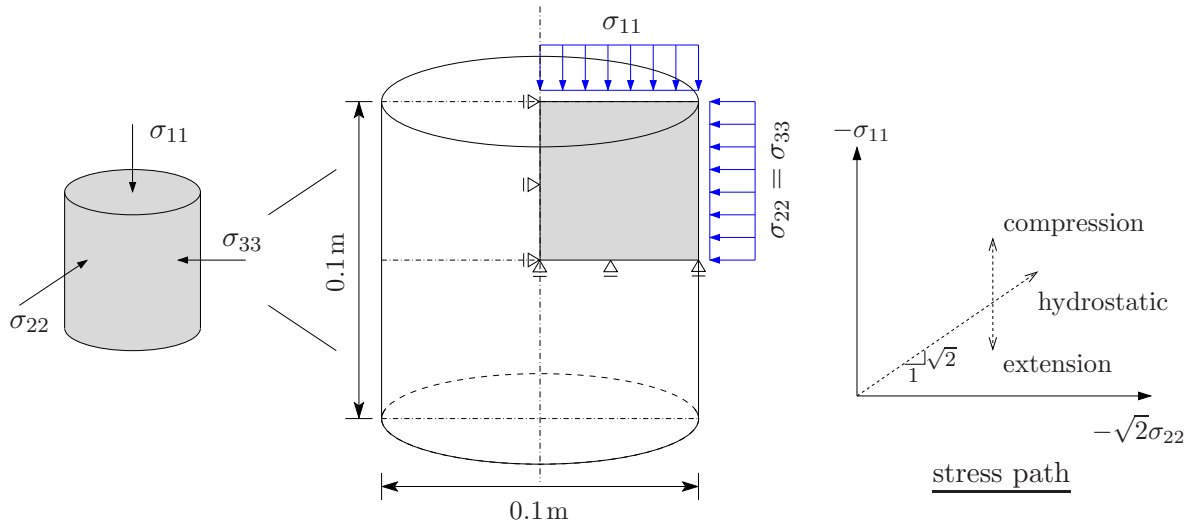


Figure B.1: Boundary conditions and applied loads of the triaxial test, three-dimensional to axisymmetric two-dimensional problem

Parameter	Symbol	Value	SI unit
1st <i>Lamé</i> constant of solid skeleton	μ^S	150×10^6	N/m ²
2nd <i>Lamé</i> constant of solid skeleton	λ^S	100×10^6	N/m ²
effective density of dense solid	ρ^{SR}	1550	kg/m ³
effective density of pore fluid	ρ^{FR}	1000	kg/m ³
initial volume fraction of solid	n_{0S}^S	0.585	–
maximum volume fraction of solid	n_{\max}^S	0.595	–

Table B.1: Material parameters of the hyperelastic solid matrix, cf. Avci & Ehlers [5]

Parameter	Symbol	Value (1) (Chapter 5)	Value (2) (Problem 6.4)	SI unit
initial values of the hardening/softening plasticity parameters	δ_0	0.01×10^{-6}	0.008×10^{-6}	m^2/N
	ϵ_0	0.0805×10^{-6}	0.01×10^{-6}	m^2/N
	β_0	0.105	0.11	-
	γ_0	0.0	0.0	-
final values of the hardening/softening plasticity parameters	δ^*	0.005×10^{-6}	0.005×10^{-6}	m^2/N
	ϵ^*	0.008×10^{-6}	0.0135×10^{-6}	m^2/N
	β^*	0.263	0.0	-
	γ^*	1.6	1.6	-
volumetric isotropic hardening parameters	C_δ^V	-100×10^{-6}	-90×10^{-6}	m^2/N
	C_ϵ^V	-300×10^{-6}	-300×10^{-6}	m^2/N
	C_β^V	-58	-58	-
	C_γ^V	-10	-10	-
deviatoric isotropic hardening parameters	C_δ^D	25×10^{-6}	15.9×10^{-6}	m^2/N
	C_ϵ^D	300×10^{-6}	300×10^{-6}	m^2/N
	C_β^D	350	350	-
	C_γ^D	35	35	-
additional viscoplasticity parameters	α	0.01	0.01	m^2/N
	κ	0.1×10^3	2.0×10^3	N/m^2
	m	0.5454	0.5454	-
	η_r	10^{-3}	10^{-3}	s
	r	1.5	1.5	-
	σ_0	0.1×10^3	2.0×10^3	N/m^2
additional plastic potential parameters	ψ_1	0.97	0.4 / 0.5	-
	ψ_2	0.48	0.1 / 0.3	-

Table B.2: Parameters for the viscoplasticity behaviour and the isotropic hardening

Bibliography

- [1] Abed, A.: *Numerical Modeling of Expansive Soil Behavior*. Dissertation, Mitteilung Nr. 56, Institut für Geotechnik, Universität Stuttgart 2008.
- [2] Akiyoshi, T.; Sun, X. & Fuchida, K.: General absorbing boundary conditions for dynamic analysis of fluid-saturated porous media. *Soil Dynamics and Earthquake Engineering* **17** (1998), 397–406.
- [3] Arnold, D. N.: Mixed finite element methods for elliptic problems. *Computer Methods in Applied Mechanics and Engineering* **82** (1990), 281–300.
- [4] Ascher, U. M. & Petzold, L. R.: *Computer Methods for Ordinary Differential Equations and Differential–Algebraic Equations*. Society for Industrial & Applied Mathematics, U. S. 1998.
- [5] Avci, O. & Ehlers, W.: Stress-dependent failure surface of granular materials. *Proceedings in Applied Mathematics and Mechanics* **8** (2010), 10401–10402.
- [6] Bachmann, H.: *Erdbebensicherung von Bauwerken*. Birkhäuser Verlag, Basel, Boston, Berlin 1995.
- [7] Bank, R. E.; Coughran, W. M.; JR.; Fichtner, W.; Grosse, E. H. & Rose, D. J.: Transient simulation of silicon devices and circuits. *IEEE Transactions on Electron Devices* **32** (1985), 1992–2007.
- [8] Basu, U.: Explicit finite element perfectly matched layers for transient three-dimensional elastic waves. *Computer Methods in Applied Mechanics and Engineering* **77** (2009), 151–176.
- [9] Basu, U. & Chopra, A. K.: Perfectly matched layers for time-harmonic elastodynamics of unbounded domains: theory and finite-element implementation. *Computer Methods in Applied Mechanics and Engineering* **192** (2003), 1337–1375.
- [10] Bathe, K.-J. & Wilson, E.: *Numerical Methods in Finite Element Analysis*. Prentice-Hall, New Jersey 1976.
- [11] Benzi, M.; Golub, G. H. & Liesen, J.: Numerical solution of saddle point problems. *Acta Numerica* **14** (2005), 1–137.
- [12] Biot, M. A.: Theory of propagation of elastic waves in a fluid-saturated porous solid, I. low frequency range. *Journal of the Acoustical Society of America* **28** (1956), 168–178.
- [13] Biot, M. A.: Theory of propagation of elastic waves in a fluid-saturated porous solid, II. higher frequency range. *Journal of the Acoustical Society of America* **28** (1956), 179–191.

- [14] Bishop, A. W.: The effective stress principle. *Teknisk Ukeblad* **39** (1959), 859–863.
- [15] Bluhm, J.; de Boer, R. & Skolnik, J.: *Allgemeine Plastizitätstheorie für poröse Medien*. Forschungsberichte aus dem Fachbereich Bauwesen, Heft 73, Universität-GH-Essen 1996.
- [16] de Boer, R.: *Vektor- und Tensorrechnung für Ingenieure*. Springer-Verlag, Berlin 1982.
- [17] de Boer, R.: *Theory of Porous Media*. Springer-Verlag, Berlin 2000.
- [18] de Boer, R.: *Trends in continuum mechanics of porous media*, Vol. 18 of *Theory and applications of transport in porous media*. Springer, Dodrecht, The Netherlands 2005.
- [19] de Boer, R. & Brauns, W.: Kinematic hardening of granular materials. *Ingenieur-Archiv* **60** (1990), 463–480.
- [20] de Boer, R. & Ehlers, W.: *Theorie der Mehrkomponentenkontinua mit Anwendungen auf bodenmechanische Probleme*. Forschungsberichte aus dem Fachbereich Bauwesen, Heft 40, Universität-GH-Essen 1986.
- [21] de Boer, R. & Ehlers, W.: The development of the concept of effective stresses. *Acta Mechanica* **83** (1990), 77–92.
- [22] de Boer, R.; Ehlers, W. & Liu, Z.: One-dimensional wave propagation in fluid saturated incompressible porous media. *Archive of Applied Mechanics* **63** (1993), 59–72.
- [23] Borja, R. I.; Tamagnini, C. & Amorosi, A.: Coupling plasticity and energy-conserving elasticity models for clays. *ASCE: Journal of Geotechnical & Geoenvironmental Engineering* **123** (1997), 948–957.
- [24] Bowen, R. M.: Theory of mixtures. In *Continuum Physics, Volume III – Mixtures and EM Field Theories*, Eringen, A. C., ed., Academic Press, London 1976, pp. 1–127.
- [25] Bowen, R. M.: Incompressible porous media models by use of the theory of mixtures. *International Journal of Engineering Science* **18** (1980), 1129–1148.
- [26] Bowen, R. M.: Compressible porous media models by use of the theory of mixtures. *International Journal of Engineering Science* **20** (1982), 697–735.
- [27] Braess, D.: *Finite Elemente*. Springer-Verlag, Berlin 1997.
- [28] Brauns, W.: *Plastische Deformationen granularer Stoffe*. Dissertation, Universität-GH-Essen 1989.
- [29] Breuer, S.: Quasi-static and dynamic behavior of saturated porous media with incompressible constituents. *Transport in Porous Media* **34** (1999), 285–303.

- [30] Brezzi, F. & Fortin, M.: *Mixed and Hybrid Finite Element Methods*. Springer-Verlag, New York 1991.
- [31] Bussat, S.; Glaubitt, A. & Neisecke, J.: Development of reference-samples for ultrasonic-testing of concrete. *Proceedings of the international symposium on NDT in civil engineering, Berlin* (2003), URL www.ndt.net/article/ndtce03/papers/p052/p052.htm.
- [32] Butcher, J. C.: *The Numerical Analysis of Ordinary Differential Equations: Runge-Kutta and General Linear Methods*. Wiley, New York 1987.
- [33] Cartwright, J. H. E. & Piro, O.: The dynamics of Runge-Kutta methods. *International Journal of Bifurcations Chaos* **2** (1992), 427–449.
- [34] Castro, G.: On the behavior of soils during earthquakes, liquefaction. In *Soil Dynamics and Liquefaction*, Cakmak, A. S., ed., Elsevier Science Pub., Amsterdam 1987, pp. 169–204.
- [35] Chen, Z.; Steeb, H. & Diebels, S.: A time-discontinuous Galerkin method for the dynamical analysis of porous media. *International Journal for Numerical and Analytical Methods in Geomechanics* **30** (2006), 1113–1134.
- [36] Chen, Z.; Steeb, H. & Diebels, S.: A space-time discontinuous Galerkin method applied to single-phase flow in porous media. *Computational Geosciences* **12** (2008), 525–539.
- [37] Chorin, A. J.: A numerical method for solving incompressible viscous problems. *Journal of Applied Physics* **2** (1967), 12–26.
- [38] Collins, I. F.: Elastic/plastic models for soils and sand. *International Journal of Mechanical Sciences* **47** (2005), 493–508.
- [39] Courant, R.; Friedrichs, K. & Lewy, H.: Über die partiellen Differenzgleichungen der mathematischen Physik. *Mathematische Annalen* **100** (1928), 32–74.
- [40] Danilov, A.: *Numerical treatment of dynamics in porous media*. Master thesis, Institute of Applied Mechanics (CE), University of Stuttgart 2004.
- [41] Day, R. W.: *Geotechnical earthquake engineering handbook*. Mcgraw-Hill, New York 2002.
- [42] Deraemaeker, A.; Babuška, I. & Bouillard, P.: Dispersion and pollution of the FEM solution for the Helmholtz equation in one, two and three dimensions. *International Journal for Numerical Methods in Engineering* **46** (1999), 471–499.
- [43] Diebels, S.: *Mikropolare Zweiphasenmodelle: Formulierung auf der Basis der Theorie Poröser Medien*. Habilitation, Bericht Nr. II-7, Institut für Mechanik (Bauwesen), Universität Stuttgart 2000.

- [44] Diebels, S. & Ehlers, W.: Dynamic analysis of a fully saturated porous medium accounting for geometrical and material non-linearities. *International Journal for Numerical Methods in Engineering* **39** (1996), 81–97.
- [45] Diebels, S.; Ehlers, W. & Markert, B.: Neglect of the fluid extra stresses in volumetrically coupled solid-fluid problems. *ZAMM* **81** (2001), 521–522.
- [46] Diebels, S.; Ellsiepen, P. & Ehlers, W.: Error-controlled Runge-Kutta time integration of a viscoplastic hybrid two-phase model. *Technische Mechanik* **19** (1999), 19–27.
- [47] Drucker, D. C. & Prager, W.: Soil mechanics and plastic analysis of limit design. *Quarterly of Applied Mathematics* **10** (1952), 157–165.
- [48] Drumheller, D. S.: The theoretical treatment of a porous solid using a mixture theory. *International Journal of Solids and Structures* **14** (1978), 441–456.
- [49] Du, X. & Ostoja-Starzewski, M.: On the size of representative volume element for darcy law in random media. *Proceedings of the Royal Society* **462** (2006), 2949–2963.
- [50] Ehlers, W.: *Poröse Medien – ein kontinuumsmechanisches Modell auf der Basis der Mischungstheorie*. Habilitation, Forschungsberichte aus dem Fachbereich Bauwesen, Heft 47, Universität-GH-Essen 1989.
- [51] Ehlers, W.: Toward finite theories of liquid-saturated elasto-plastic porous media. *International Journal of Plasticity* **7** (1991), 443–475.
- [52] Ehlers, W.: An elastoplasticity model in porous media theories. *Transport in Porous Media* **9** (1992), 49–59.
- [53] Ehlers, W.: Constitutive equations for granular materials in geomechanical context. In *Continuum Mechanics in Environmental Sciences and Geophysics*, Hutter, K., ed., Springer-Verlag, Wien 1993, CISM Courses and Lecture Notes No. 337, pp. 313–402.
- [54] Ehlers, W.: A single-surface yield function for geomaterials. *Archive of Applied Mechanics* **65** (1995), 246–259.
- [55] Ehlers, W.: *Vector and Tensor Calculus: An Introduction*. Lecture Notes, Institute of Applied Mechanics (CE), University of Stuttgart 1995–2012, URL <http://www.mechbau.uni-stuttgart.de/lis2>.
- [56] Ehlers, W.: Grundlegende Konzepte in der Theorie Poröser Medien. *Technische Mechanik* **16** (1996), 63–76.
- [57] Ehlers, W.: Foundations of multiphase and porous materials. In *Porous Media: Theory, Experiments and Numerical Applications*, Ehlers, W. & Bluhm, J., eds., Springer-Verlag, Berlin 2002, pp. 3–86.

- [58] Ehlers, W.: Challenges of porous media models in geo- and biomechanical engineering including electro-chemically active polymers and gels. *International Journal of Advances in Engineering Sciences and Applied Mathematics* **1** (2009), 1–24.
- [59] Ehlers, W. & Acartürk, A.: The role of weakly imposed Dirichlet boundary conditions for numerically stable computations of swelling phenomena. *Computational Mechanics* **43** (2009), 545 – 557.
- [60] Ehlers, W. & Avci, O.: Stress-dependent hardening and failure surfaces of dry sand. *International Journal for Numerical and Analytical Methods in Geomechanics* (2011), DOI: 10.1002/nag.
- [61] Ehlers, W. & Ellsiepen, P.: Theoretical and numerical methods in environmental continuum mechanics based on the Theory of Porous Media. In *Environmental Geomechanics*, Schrefler, B. A., ed., Springer-Verlag, Wien 2001, CISM Courses and Lectures No. 417, pp. 1–81.
- [62] Ehlers, W.; Ellsiepen, P.; Blome, P.; Mahnkopf, D. & Markert, B.: *Theoretische und numerische Studien zur Lösung von Rand- und Anfangswertproblemen in der Theorie Poröser Medien, Abschlußbericht zum DFG-Forschungsvorhaben Eh 107/6*. Institut für Mechanik (Bauwesen), Universität Stuttgart 1999.
- [63] Ehlers, W.; Graf, T. & Ammann, M.: Deformation and localization analysis of partially saturated soil. *Computer Methods in Applied Mechanics and Engineering* **193** (2004), 2885–2910.
- [64] Ehlers, W. & Scholz, B.: An inverse algorithm for the identification and the sensitivity analysis of the parameters governing micropolar elasto-plastic granular material. *Archive of Applied Mechanics* **77** (2007), 911–931.
- [65] Eipper, G.: *Theorie und Numerik finiter elastischer Deformationen in flüidgesättigten porösen Festkörpern*. Dissertation, Bericht Nr. II-1, Institut für Mechanik (Bauwesen), Universität Stuttgart 1998.
- [66] Ellsiepen, P.: *Zeit- und ortsadaptive Verfahren angewandt auf Mehrphasenprobleme poröser Medien*. Dissertation, Bericht Nr. II-3, Institut für Mechanik (Bauwesen), Universität Stuttgart 1999.
- [67] Erxianga, S.; Zhiquana, Y. & Zongliana, Q.: Nonlinear dynamic analysis of saturated soil-structure interaction by FEM. In *Dynamic Soil-Structure Interaction: Current Research in China and Switzerland*, Chuhan, Z. & Wolf, J. P., eds., Elsevier, Amsterdam 1998, pp. 217–230.
- [68] von Estorff, O.: Dynamic response of elastic blocks by time domain BEM and FEM. *Computers & Structures* **38** (1991), 289–300.
- [69] von Estorff, O. & Firuziaan, M.: Coupled BEM/FEM approach for nonlinear soil/structure interaction. *Engineering Analysis With Boundary Elements* **24** (2000), 715–725.

- [70] Felippa, C. A.; Park, K. C. & Farhat, C.: Partitioned analysis of coupled mechanical systems. *Computer Methods in Applied Mechanics and Engineering* **190** (2001), 3247–3270.
- [71] Givoli, D.: *Numerical Methods for Problems in Infinite Domains*. Elsevier, Amsterdam 1992.
- [72] Goda, K.: A multiphase technique with implicit difference schemes for calculating two- or three-dimensional cavity flows. *Journal of Computational Physics* **30** (1979), 76–95.
- [73] Göktepe, S.: *Micro-Macro Approaches to Rubbery and Glassy Polymers: Predictive Micromechanically-Based Models and Simulations*. Dissertation, Report No. I-20, Institute of Applied Mechanics (CE), University of Stuttgart 2007.
- [74] Graf, T.: *Multiphase Flow Processes in Deformable Porous Media under Consideration of Fluid Phase Transitions*. Dissertation, Report No. II-17, Institute of Applied Mechanics (CE), University of Stuttgart 2008.
- [75] Gresho, P. M. & Sani, R. L.: *Incompressible Flow and the Finite Element Method, Volume Two*. Wiley, Chichester 2000, second corrected reprint of 1998.
- [76] de Groot, M. B.; Bolton, M. D.; Foray, P.; Meijers, P.; Palmer, A. C.; Sandven, R.; Sawicki, A. & Teh, T. C.: Physics of liquefaction phenomena around marine structures. *Journal of Waterway, Port, Coastal, and Ocean Engineering* **132** (2006), 227–243.
- [77] Guermond, J.-L. & Quartapelle, L.: On stability and convergence of projection methods based on pressure Poisson equation. *International Journal for Numerical Methods in Fluids* **26** (1998), 1039–1053.
- [78] Hadamard, J.: *Leçons sur la propagation des ondes et les équations de l'hydrodynamique*. Chelsea, New York 1949. Reprint of Herman, Paris 1903.
- [79] Haeggblad, B. & Nordgren, G.: Modelling nonlinear soil-structure interaction using interface elements, elastic-plastic soil elements and absorbing infinite elements. *Computers & Structures* **26** (1987), 307–324.
- [80] Hairer, E. & Wanner, G.: *Solving Ordinary Differential Equations, Vol. 2: Stiff and Differential-Algebraic Problems*. Springer-Verlag, Berlin 1991.
- [81] Hameyer, K.; Driesen, J.; Gersem, H. D. & Belmans, R.: The classification of coupled field problems. *IEEE Transactions on Magnetics* **35** (1999), 1618 – 1621.
- [82] Haupt, P.: On the concept of an intermediate configuration and its application to a representation of viscoelastic-plastic material behavior. *International Journal of Plasticity* **1** (1985), 303–316.

- [83] Haupt, P.: Foundation of continuum mechanics. In *Continuum Mechanics in Environmental Sciences and Geophysics*, Hutter, K., ed., Springer-Verlag, Wien 1993, CISM Courses and Lectures No. 337, pp. 1–77.
- [84] Haupt, P.: *Continuum Mechanics and Theory of Materials*, 2nd Edition. Springer-Verlag, Berlin 2002.
- [85] Heider, Y.: *Numerical Simulation of Wave Propagation in Saturated Porous Media*. Master thesis, Institute of Applied Mechanics (CE), University of Stuttgart 2007.
- [86] Heider, Y.; Markert, B. & Ehlers, W.: Coupled problems of wave propagation in materially incompressible saturated soil based on the theory of porous media. *Proceedings of the 2nd ECCOMAS Thematic Conference COMPDYN* (2009), CD182.
- [87] Heider, Y.; Markert, B. & Ehlers, W.: Dynamic wave propagation in infinite saturated porous media half spaces. *Computational Mechanics* **49** (2012), 319–336.
- [88] Hill, R.: Acceleration waves in solids. *Journal of the Mechanics and Physics of Solids* **10** (1962), 1–16.
- [89] Holbrow, C. H.; Lloyd, J. N.; Amato, J. C.; Galvez, E. & Parks, M. E.: *Modern Introductory Physics*, 2nd Edition. Springer, New York 2010.
- [90] Holzapfel, G. A.: *Nonlinear Solid Mechanics: A Continuum Approach for Engineering*. Wiley, Chichester 2000.
- [91] Hosea, M. E. & Shampine, L. F.: Analysis and implementation of TR-BDF2. *Applied Numerical Mathematics* **20** (1996), 21–37.
- [92] Houlsby, G. T. & Puzrin, M. A.: *Principles of Hyperplasticity: An Approach to Plasticity Theory Based on Thermodynamic Principles*. Springer-Verlag, London 2006.
- [93] Huang, M.; Wu, S. & Zienkiewicz, O. C.: Incompressible or nearly incompressible soil dynamic behaviour – a new staggered algorithm to circumvent restrictions of mixed formulation. *Soil Dynamics and Earthquake Engineering* **21** (2001), 169–179.
- [94] Huang, M.; Yue, Z. Q.; Tham, L. G. & Zienkiewicz, O. C.: On the stable finite element procedure for dynamic problems of saturated porous media. *International Journal for Numerical Methods in Engineering* **61** (2004), 1421–1450.
- [95] Hughes, T. J. R.: *The Finite Element Method*. Prentice-Hall, London 1987.
- [96] Humrickhouse: *Hyperelastic models for granular materials*. Ph.D. thesis, UWFD-1365, University of Wisconsin 2009.
- [97] Ishihara, K.: *Soil Behaviour in Earthquake Geotechnics*. Oxford University Press Inc., New York 1996.

- [98] Ishihara, K.; Tatsuoka, F. & Yasuda, S.: Undrained deformation and liquefaction of sand under cyclic stresses. *Solids and Foundations* **15** (1975), 29–44.
- [99] Jefferies, M. & Been, K.: *Soil Liquefaction: A critical state approach*. Taylor & Francis, London and New York 2006.
- [100] Jeremić, B.; Yang, Z.; Cheng, Z.; Jie, G.; Sett, K.; Taiebat, M.; Preisig, M. & Tafazoli, N.: *Computational Geomechanics: Inelastic Finite Elements for Pressure Sensitive Materials*. Lecture Notes, Department of Civil and Environmental Engineering, University of California, Davis 2009, URL <http://cee.engr.ucdavis.edu/>.
- [101] Karajan, N.: *An Extended Biphase Description of the Inhomogeneous and Anisotropic Intervertebral Disc*. Dissertation, Report No. II-19, Institute of Applied Mechanics (CE), University of Stuttgart 2009.
- [102] Khalili, N.; Yazdchi, M. & Valliappen, S.: Wave propagation analysis of two-phase saturated porous media using coupled finite-infinite element method. *Soil Dynamics and Earthquake Engineering* **18** (1999), 533–553.
- [103] Kim, D. & Yun, C.: Time-domain soil-structure interaction analysis in two-dimensional medium based on analytical frequency-dependent infinite elements. *International Journal for Numerical Methods in Engineering* **47** (2000), 1241–1261.
- [104] Kim, S. & Stewart, J. P.: Kinematic soil-structure interaction from strong motion recordings. *Journal of Geotechnical and Geoenvironmental Engineering ASCE* **129** (2003/4), 323–335.
- [105] Kimoto, S.; Oka, F. & Higo, Y.: Strain localization analysis of elasto-viscoplastic soil considering structural degradation. *Computer Methods in Applied Mechanics and Engineering* **193** (2004), 2845–2866.
- [106] Kolymbas, D.: An outline of hypoplasticity. *Archive of Applied Mechanics* **61** (1991), 143–151.
- [107] Kolymbas, D.: Behaviour of liquefied sand. *Philosophical Transactions of the Royal Society of London* **356 A** (1998), 2609–2622.
- [108] Kosinski, W.: *Field Singularities and Wave Analysis in Continuum Mechanics*. Ellis Horwood, Chichester 1986.
- [109] Kramer, S. L. & Elgamal, A. W.: *Modeling Soil Liquefaction Hazards for Performance-Based Earthquake Engineering*. A report on research, PEER 2001/13, The Pacific Earthquake Engineering Research Center (PEER) 2001.
- [110] Lade, P. V.: Effects of voids and volume changes on the behaviour of frictional materials. *International Journal for Numerical and Analytical Methods in Geomechanics* **12** (1988), 351–370.
- [111] Lade, P. V.: Static instability and liquefaction of loose fine sandy slopes. *Journal of Geotechnical Engineering* **118** (1992), 51–71.

- [112] Lade, P. V. & Inelb, S.: Rotational kinematic hardening model for sand. Part I concept of rotating yield and plastic potential surfaces. *Computers and Geotechnics* **21** (1997), 183–216.
- [113] Lee, Y. & Park, K. C.: Numerically generated tangent stiffness matrices for nonlinear structural analysis. *Computer Methods in Applied Mechanics and Engineering* **191** (2002), 5833–5846.
- [114] Lehmann, L.: *Wave Propagation in Infinite Domains: With Applications to Structure Interaction*. Lecture Notes in Applied and Computational Mechanics, Springer Verlag, Berlin, Wien, New York 2007.
- [115] Lewis, R. W. & Schrefler, B. A.: *The Finite Element Method in the Static and Dynamic Deformation and Consolidation of Porous Media*, 2nd Edition. Wiley, Chichester 1998.
- [116] Li, C.; Borja, R. I. & Regueiro, R. A.: Dynamics of porous media at finite strain. *Computer Methods in Applied Mechanics and Engineering* **193** (2004), 3837–3870.
- [117] Li, X.; Han, X. & Pastor, M.: An iterative stabilized fractional step algorithm for finite element analysis in saturated soil dynamics. *Computer Methods in Applied Mechanics and Engineering* **85** (2003), 67–94.
- [118] Ling, H. I.; Yue, D.; Kaliakin, V. N. & Themelis, N. J.: Anisotropic elastoplastic bounding surface model for cohesive soils. *Journal of Engineering Mechanics* **128** (2002), 748–758.
- [119] Lubliner, J.: A maximum-dissipation principle in generalized plasticity. *Acta Mechanica* **52** (1984), 225–237.
- [120] Lysmer, J. & Kuhlemeyer, R. L.: Finite dynamic model for infinite media. *ASCE: Journal of the Engineering Mechanics Division* **95** (1969), 859–877.
- [121] Mahnkopf, D.: *Lokalisierung fluidgesättigter poröser Festkörper bei finiten elastoplastischen Deformationen*. Dissertation, Bericht Nr. II-5, Institut für Mechanik (Bauwesen), Universität Stuttgart 2000.
- [122] Manzari, M. T. & Dafalias, Y. F.: A critical state two-surface plasticity model for sands. *Géotechnique* **47 B** (1997), 255–272.
- [123] Markert, B.: *Porous media viscoelasticity with application to polymeric foams*. Dissertation, Report No. II-12, Institute of Applied Mechanics (CE), University of Stuttgart 2005.
- [124] Markert, B.: A biphasic continuum approach for viscoelastic high-porosity foams: Comprehensive theory, numerics, and application. *Archives of Computational Methods in Engineering* **15** (2008), 371–446.

- [125] Markert, B.: *Weak or Strong: On Coupled Problems in Continuum Mechanics*. Habilitation, Report No. II-20, Institute of Applied Mechanics (CE), University of Stuttgart 2010, <http://elib.uni-stuttgart.de/opus/volltexte/2010/5453/>.
- [126] Markert, B.; Heider, Y. & Ehlers, W.: Comparison of monolithic and splitting solution schemes for dynamic porous media problem. *International Journal for Numerical Methods in Engineering* **82** (2010), 1341–1383.
- [127] Marques, J. M. M. C. & Owen, D. R. J.: Infinite elements in quasi-static materially nonlinear problems. *Computers & Structures* **18** (1984), 739–751.
- [128] Marsden, J. E. & Hughes, T. J. R.: *Mathematical Foundations of Elasticity*. Dover Publications 1994, reprint of Prentice-Hall, 1983.
- [129] Matthies, H. G.; Niekamp, R. & Steindorf, J.: Algorithms for strong coupling procedures. *Computer Methods in Applied Mechanics and Engineering* **195** (2006), 2028–2049.
- [130] Matthies, H. G. & Steindorf, J.: *Strong Coupling Methods*. Tech. Rep. Informatik-bericht Nr.: 2002-06, Institute of Scientific Computing, Technical University Braunschweig 2002.
- [131] Miehe, C.: *Computational Mechanics of Materials*. Lecture notes, University of Stuttgart 2006.
- [132] Mira, P.; Fernández-Merodo, J. A.; Pastor, M. & Tonni, L.: Seismic initiation mechanisms of fast granular flows. *Proceeding of WCCM8 and ECCOMAS 2008* (2008).
- [133] Möller, G.: *Geotechnik Bodenmechanik Bauingenieur-Praxis*. Ernst & Sohn, Berlin 2007.
- [134] Müllerschön, H.: *Spannungs-Verformungsverhalten granularer Materialien am Beispiel von Berliner Sand*. Dissertation, Bericht Nr. II-6, Institut für Mechanik (Bauwesen), Universität Stuttgart 2000.
- [135] Mylonakis, G.; Nikolaou, S. & Gazetas, G.: Footings under seismic loading: Analysis and design issues with emphasis on bridge foundations. *Soil Dynamics and Earthquake Engineering* **26** (2006), 824–853.
- [136] Nanning, M. & Schanz, M.: Infinite elements in a poroelastodynamic FEM. *International Journal for Numerical and Analytical Methods in Geomechanics* **35** (2011), 1774–1800.
- [137] Niemunis, A.: *Extended hypoplastic models for soils*. Habilitation, Report No. 34, Ruhr-Universität Bochum 2002.

- [138] Oberkampf, W. L.; Trucano, T. G. & Hirsch, C.: Verification, validation, and predictive capability in computational engineering and physics. *Proceedings in the Foundations for Verification and Validation in the 21st Century Workshop, Johns Hopkins University, Applied Physics Laboratory, Laurel, Maryland* (2002), 1–74.
- [139] Ogden, R. W.: *Nonlinear elastic deformations*. Ellis Harwood Ltd., New York 1984.
- [140] Oka, F.; Higo, Y. & Kimoto, S.: Effect of dilatancy on the strain localization of water-saturated elasto-viscoplastic soil. *International Journal of Solids and Structures* **39** (2002), 3625–3647.
- [141] Oskooi, A. F.; Zhang, L.; Avniel, Y. & Johnson, S. G.: The failure of perfectly matched layers, and towards their redemption by adiabatic absorbers. *Optics Express* **16** (2008), 11376–11392.
- [142] Pastor, M.; Zienkiewicz, . C. & Leung, K. H.: Simple model for transient soil loading in earthquake analysis. ii: Non-associative models for sands. *International Journal for Numerical and Analytical Methods in Geomechanics* **9** (1985), 477–498.
- [143] Perzyna, P.: Fundamental problems in viscoplasticity. *Advances in Applied Mechanics* **9** (1966), 243–377.
- [144] Prakash, S.: *Soil Dynamics*. Mcgraw-Hill, New York 1981.
- [145] Press, W. H.; Teukolsky, S. A.; Vetterling, W. T. & Flannery, B. P.: *Numerical Recipes in C*, 2nd Edition. Cambridge University Press 1999, corrected reprint of 1992.
- [146] Prohl, A.: *Projection and Quasi-Compressibility Methods for Solving the Incompressible Navier-Stokes Equations*. Teubner, Stuttgart 1997.
- [147] Quarteroni, A.; Sacco, R. & Saleri, F.: *Numerical Mathematics*. Springer-Verlag, New York, Berlin, Heidelberg 2000.
- [148] Quintal, B.; Steeb, H.; Frehner, M. & Schmalholz, S.: Quasi-static finite element modeling of seismic attenuation and velocity dispersion due to fluid flow in partially saturated rocks. *Journal of Geophysical Research, Solid Earth* **116** (2011), doi:10.1029/2010JB007475.
- [149] Ramm, E.: *Computational Mechanics of Structures*. Lecture notes, University of Stuttgart 2006.
- [150] Rannacher, R.: Finite element methods for the incompressible Navier-Stokes equations. In *Fundamental Directions in Mathematical Fluid Mechanics*, Galdi, P.; Heywood, J. & Rannacher, R., eds., Birkhäuser, Basel 2000, pp. 191–293.
- [151] Roscoe, K. H. & Burland, J. B.: On the generalized stress-strain behaviour of wet clay. In *Engineering Plasticity*, Heyman, J. & Leckie, F. A., eds., Cambridge University Press, Cambridge, U. K. 1968, pp. 535–609.

- [152] Savenco, V.; Hundsdorfer, W. & Verwer, J. G.: A multirate time stepping strategy for stiff ordinary differential equations. *BIT Numerical Mathematics* **47** (2007), 137–155.
- [153] Schanz, M.: *Wave Propagation in Viscoelastic and Poroelastic Continua*. Springer-Verlag, Berlin 2001.
- [154] Schanz, M. & Diebels, S.: A comparative study of Biot’s theory and the linear Theory of Porous Media for wave propagation problems. *Acta Mechanica* **161** (2003), 213–235.
- [155] Scholz, B.: *Application of a Microplar Model to the Localization Phenomena in Granular Materials*. Dissertation, Report No. II-15, Institute of Applied Mechanics (CE), University of Stuttgart 2007.
- [156] Schrefler, B. A. & Simoni, L.: Non-isothermal consolidation of unbounded porous media using mapped infinite elements. *Communications in Applied Numerical Methods* **3** (1987), 445–452.
- [157] Simo, J. & Hughes, T. J. R.: *Computational Inelasticity*. Springer-Verlag, Berlin 1998.
- [158] Simoni, L. & Schrefler, B. A.: Mapped infinite elements in soil consolidation. *International Journal for Numerical Methods in Engineering* **24** (1987), 513–527.
- [159] Steeb, H.: Ultrasound propagation in cancellous bone. *Archive of Applied Mechanics* **80** (2010), 489–502.
- [160] Steeb, H.; Frehner, M. & Schmalholz, S.: Waves in residual-saturated porous media. In *Mechanics of Generalized Continua: One Hundred Years after the Cosserats*, Maugin, G. A. & Metrikine, A. V., eds., Springer, New York, London 2010, pp. 179–190.
- [161] Strang, G.: *Mathematical Methods for Engineers II*. online courses, MIT Open Courseware 2010, <http://academicearth.org/courses/mathematical-methods-for-engineers-ii>.
- [162] Suter, S. P.: The history of Poiseuille’s law. *Annual Review of Fluid Mechanics* **25** (1993), 1–20.
- [163] Taiebat, M.: *Advanced Elastic-Plastic Constitutive and Numerical Modeling*. Lambert Academic Publishing, Köln 2009.
- [164] Truesdell, C.: *Rational Thermodynamics*, 2nd Edition. Springer-Verlag, New York 1984.
- [165] Truesdell, C. & Noll, W.: The nonlinear field theories of mechanics. In *Handbuch der Physik*, Band III/3, Flügge, S., ed., Springer-Verlag, Berlin 1965.

- [166] Truesdell, C. & Toupin, R. A.: The classical field theories. In *Handbuch der Physik*, Band III/1, Flügge, S., ed., Springer-Verlag, Berlin 1960, pp. 226–902.
- [167] Tsuji, T.; Tokuyama, H.; Pisani, P. C. & Moore, G.: Effective stress and pore pressure in the Nankai accretionary prism off the Muroto Peninsula, southwestern Japan. *Journal of Geophysical Research* **113** (2008), B11401.
- [168] Underwood, P. & Geers, T. L.: Double asymptotic boundary element analysis of dynamic soil structure interaction. *International Journal of Solids and Structures* **17** (1981), 687–697.
- [169] van Kan, J.: A second-order accurate pressure-correction scheme for viscous incompressible flow. *SIAM Journal of Scientific Computing* **7** (1986), 870–891.
- [170] Verdugo, R. & Ishihara, K.: The steady state of sandy soils. *Soils and Foundation* **36** (1996), 81–91.
- [171] Vermeer, P.: A double hardening model for sand. *Géotechnique* **28** (1978), 413–433.
- [172] Wall, W. A.: *Fluid–Struktur–Interaktion mit stabilisierten Finiten Elementen*. Dissertation, Band 31, Institut für Baustatik, Universität Stuttgart 1999.
- [173] Wang, G.; Chen, L. & Song, C.: Finite-infinite element for dynamic analysis of axisymmetrically saturated composite foundations. *International Journal for Numerical Methods in Engineering* **67** (2006), 916–932.
- [174] Wang, Z. L. & Dafalias, Y. F.: Simulation of post-liquefaction deformation of sand. *Proceedings of the 15th ASCE Engineering Mechanics Conference, Columbia University, New York* (2002).
- [175] Wilmański, K.: Waves in porous and granular materials. In *Kinetic and continuum theories of granular and porous media*, Springer, Wien 1999, pp. 131–185.
- [176] Wilmański, K. & Albers, B.: Acoustic waves in porous solid-fluid mixtures. In *Dynamic Response of Granular and Porous Materials under Large and Catastrophic Deformations*, Hutter, K. & Kirchner, N., eds., Springer, Berlin 2003, pp. 285–313.
- [177] Wolf, J. P.: *Dynamic Soil-Structure Interaction*. Prentice-Hall, INC., Englewood Cliffs, New Jersey 1985.
- [178] Wolf, J. P.: *Soil-Structure-Interaction Analysis in Time Domain*. Prentice-Hall, Inc. 1988.
- [179] Wolf, J. P. & Song, C.: Some cornerstones of dynamic soil-structure interaction. *Engineering Structures* **24** (2002), 13–28.
- [180] Wood, W. L.: *Practical Time Stepping Schemes*. Clarendon Press, Oxford 1990.
- [181] Wu, J.; Kammerer, A. M.; Riemer, M. F.; Seed, R. B. & Pestana, J. M.: Laboratory study of liquefaction triggering criteria. *Proceedings of the 13th World Conference on Earthquake Engineering, Vancouver, B.C., Canada* (2004).

- [182] Wunderlich, W.; Schäpertöns, B. & Temme, C.: Dynamic stability of non-linear shells of revolution under consideration of the fluid-soil-structure interaction. *International Journal for Numerical Methods in Engineering* **37** (1994), 2679–2697.
- [183] Yazdchi, M.; Khalili, N. & Valliappan, S.: Dynamic soil-structure interaction analysis via coupled finite-element-boundary-element method. *Earthquake Engineering & Structural Dynamics* **18** (1999), 499–517.
- [184] Zeghal, M. & Elgamal, A. W.: Analysis of site liquefaction using earthquake records. *ASCE: Journal of Geotechnical & Geoenvironmental Engineering* **120** (1994), 996–1017.
- [185] Zienkiewicz, O. C.; Chan, A. H. C.; Pastor, M.; Paul, D. K. & Shiomi, T.: Static and dynamic behaviour of soils: a rational approach to quantitative solutions. I. fully saturated problems. *Proceedings of the Royal Society of London* **429** (1990), 285–309.
- [186] Zienkiewicz, O. C.; Chan, A. H. C.; Pastor, M.; Schrefler, B. A. & Shiomi, T.: *Computational geomechanics with special reference to earthquake engineering*. Wiley, Chichester 1999.
- [187] Zienkiewicz, O. C.; Chang, C. T. & Hinton, E.: Non-linear seismic response and liquefaction. *International Journal for Numerical and Analytical Methods in Geomechanics* **2** (1978), 381–404.
- [188] Zienkiewicz, O. C.; Emson, C. & Bettess, P.: A novel boundary infinite element. *International Journal for Numerical Methods in Engineering* **19** (1983), 393–404.
- [189] Zienkiewicz, O. C.; Huang, M.; Wu, J. & Wu, S.: A new algorithm for coupled soil-pore fluid problem. *Shock and Vibration* **1** (1993), 3–14.
- [190] Zienkiewicz, O. C.; Qu, S.; L.Taylor, R. & Nakazawa, S.: The patch test for mixed formulations. *International Journal for Numerical Methods in Engineering* **23** (1986), 1873–1883.
- [191] Zienkiewicz, O. C. & Taylor, R. L.: *The Finite Element Method. Basic Formulation and Linear Problems*, 4th Edition, Vol. 1. McGraw-Hill, London 1989.
- [192] Zienkiewicz, O. C. & Taylor, R. L.: *The Finite Element Method: The Basis*, 5th Edition, Vol. 1. Butterworth Heinemann, Oxford 2000.
- [193] Zinatbakhsh, S.: *Coupled problems in the mechanics of multi-physics and multi-phase materials*. Milestone Report, SimTech Cluster of Excellence, Institute of Applied Mechanics (CE), Universität Stuttgart 2010.
- [194] Zinatbakhsh, S.; Markert, B. & Ehlers, W.: On the stability analysis of decoupled solution schemes. *Proceedings in Applied Mathematics and Mechanics* **11** (2011), 497–498.

Nomenclature

Following the works of *de Boer* [16] and *Ehlers* [55], the tensor calculus notations and conventions that are used in this monograph are introduced. Concerning the porous media theories and the constitutive modelling, the symbols are chosen in analogy to *Ehlers* [57] and the modern released publications of the Institute of Applied Mechanics (CE), University of Stuttgart.

Conventions

Basic conventions

(\cdot)	indicates to an arbitrary quantity
s, t, ε, \dots	scalars (0^{th} -order tensor)
$\mathbf{s}, \mathbf{t}, \dots$	vectors (1^{st} -order tensor)
$\mathbf{S}, \mathbf{T}, \boldsymbol{\varepsilon}$	2^{nd} -order tensor
$\overset{n}{\mathbf{S}}, \overset{n}{\mathbf{T}}, \dots$	n^{th} -order tensor

Index and suffix notations

i, j, k, l, \dots	super- or subscript indices that range from 1 to N, e. g., N=3 for 3-dimensional physical space
$(\cdot)_{\alpha}$	with $\alpha = \{S, F, \dots\}$ as a capital subscript indicates to a kinematical quantity of the constituent α ($\alpha = S$:solid; $\alpha = F$:pore-fluid; $\alpha = L$:pore-liquid; $\alpha = G$:Gas)
$(\cdot)^{\alpha}$	with α as a capital superscript indicates to a non-kinematical quantity that belongs to the constituent α
$(\cdot)'_{\alpha}$	material time derivative following the motion of α

Symbols

Symbol	Unit	Discription
α	[-]	constituent identifier (for biphasic material, $\alpha \in \{S, F\}$)
$\varphi, \varphi^{\alpha}$	[-]	refers to the mutliphasic continua and the constituents
n^{α}	[-]	volume fraction of φ^{α}
$\mathcal{B}, \mathcal{B}^{\alpha}$	[-]	overall aggregate and partial bodies
V, V^{α}	[m ³]	volumes of $\mathcal{B}, \mathcal{B}^{\alpha}$
dv, dv^{α}	[m ³]	total and partial volume elements

dm^α	[kg]	local mass of φ^α
ρ	[kg/m ³]	overall aggregate density (mixture density)
$\rho^{\alpha R}, \rho^\alpha$	[kg/m ³]	material and partial densities of φ^α
P^α	[-]	material point of φ^α
\mathbf{x}	[m]	position vector in the actual configuration
\mathbf{X}_α	[m]	position vector of P^α in the initial configuration
χ_α	[-]	motion (mapping) function of P^α
\mathbf{F}_α	[-]	material deformation gradient of φ^α
J_α	[-]	<i>Jacobian</i> , defined as determinant of \mathbf{F}_α
$\dot{\mathbf{x}}_\alpha$ or \mathbf{v}_α	[m/s]	constituent velocity vector
$\ddot{\mathbf{x}}_\alpha$ or $\dot{\mathbf{v}}_\alpha$	[m/s ²]	constituent acceleration vector
\mathbf{d}_α	[m/s]	diffusion velocity vector
Ψ, Ψ		scalar- and vector-valued functions
\mathbf{u}_S	[m]	solid displacement vector
\mathbf{v}_α	[m/s]	velocity vector of φ^α
\mathbf{w}_F	[m/s]	fluid seepage velocity vector
p	[N/m ²]	excess pore-fluid pressure
p^{FR}	[N/m ²]	effective pore-fluid pressure ($p^{FR} = p$)
\mathbf{I}	[-]	2nd-order identity tensor
\mathbf{R}_S	[-]	solid rotational tensor for the polar decomposition of \mathbf{F}_S
$\mathbf{U}_S, \mathbf{V}_S$	[-]	right and left solid stretch tensors
$\mathbf{C}_S, \mathbf{B}_S$	[-]	right and left <i>Cauchy-Green</i> solid deformation tensors
\mathbf{E}_S	[-]	<i>Green-Lagrangian</i> solid strain tensor
\mathbf{A}_S	[-]	<i>Almansi</i> solid strain tensor
$\boldsymbol{\varepsilon}_S$	[-]	infinitesimal (linearised) solid strain tensor
$\mathbf{b}, \mathbf{b}^\alpha$	[m/s ²]	mass-specific body force vector acting on $\mathcal{B}, \mathcal{B}^\alpha$
$\mathbf{t}, \mathbf{t}^\alpha$	[N/m ²]	surface traction vector action on $\mathcal{S}, \mathcal{S}^\alpha$
\mathbf{n}	[-]	outward oriented unit surface normal vector
\mathbf{T}	[N/m ²]	total <i>Cauchy</i> (true) stress tensor
$\mathbf{T}^\alpha, \mathbf{T}_E^\alpha$	[N/m ²]	partial and partial effective <i>Cauchy</i> stress tensor

$\boldsymbol{\tau}_E^S$	[N/m ²]	<i>Kirchhoff</i> stress tensor
\mathbf{S}_E^S	[N/m ²]	2nd- <i>Piola-Kirchhoff</i> stress
\mathbf{L}_α	[1/s]	spatial velocity gradient of φ^α
Ψ, Ψ^α	[·/m ³]	volume-specific densities of scalar mechanical quantities
$\hat{\Psi}, \hat{\Psi}^\alpha$	[·/m ³]	volume-specific production of scalar mechanical quantities
$\boldsymbol{\Psi}, \boldsymbol{\Psi}^\alpha$	[·/m ³]	volume-specific densities of vectorial mechanical quantities
$\hat{\boldsymbol{\Psi}}, \hat{\boldsymbol{\Psi}}^\alpha$	[·/m ³]	volume-specific productions of vectorial mechanical quantities
ϕ, ϕ^α		general vector-valued mechanical quantities
$\boldsymbol{\Phi}, \boldsymbol{\Phi}^\alpha$		general tensor-valued mechanical quantities
σ, σ^α		scalar-valued supply terms of mechanical quantities
$\boldsymbol{\sigma}, \boldsymbol{\sigma}^\alpha$		vector-valued supply terms of mechanical quantities
$\hat{\rho}^\alpha$	[kg/m ³ s]	volume-specific mass production of φ^α
$\hat{\mathbf{s}}^\alpha$	[N/m ³]	volume-specific total momentum production of φ^α
$\hat{\mathbf{p}}^\alpha, \hat{\mathbf{p}}_E^\alpha$	[N/m ³]	volume-specific direct and effective momentum productions of φ^α
$\hat{\mathbf{h}}^\alpha$	[N/m ²]	volume-specific total angular momentum productions of φ^α
$\mathbf{q}, \mathbf{q}^\alpha$	[J/m ² s]	heat influx vector of φ and φ^α
r, r^α	[J/kg s]	mass-specific external heat supply of φ and φ^α
$\varepsilon, \varepsilon^\alpha$	[J/kg]	mass-specific internal energy of φ and φ^α
$\hat{\varepsilon}^\alpha$	[J/m ³ s]	volume-specific total energy production of φ^α
$\hat{\varepsilon}^\alpha$	[J/m ³ s]	volume-specific direct energy production of φ^α
η, η^α	[J/K kg]	mass-specific entropy of φ and φ^α
$\boldsymbol{\phi}_\eta, \boldsymbol{\phi}_\eta^\alpha$	[J/K m ² s]	entropy efflux vectors of φ and φ^α
$\sigma_\eta, \sigma_\eta^\alpha$		volume-specific external entropy supply of φ and φ^α
$\hat{\eta}, \hat{\eta}^\alpha$	[J/K m ³ s]	volume-specific entropy production of φ and φ^α
$\hat{\zeta}^\alpha$	[J/K m ³ s]	volume-specific direct entropy production of φ^α
θ, θ^α	[K]	absolute <i>Kelvin's</i> temperature of φ and φ^α
ψ, ψ^α	[J/kg]	mass-specific <i>Helmholtz</i> free energy of φ and φ^α
$\mathcal{D}, \mathcal{D}_{loc}$	[J/m ³ s]	total and local volume-specific dissipation
\mathcal{P}	[N/m ²]	<i>Lagrangian</i> multiplier (identified as the fluid pressure)

\mathbf{D}^4	[N s/m ²]	fourth-order positive definite fluid viscosity tensor
\mathbf{D}_α	[1/s]	stretching or deformation rate tensor of φ^α
μ^F	[N s/m ²]	fluid dynamic viscosity
\mathbf{S}_v	[N s/m ⁴]	2nd-order permeability tensor
g	[m/s ²]	gravitational acceleration
γ^{FR}	[N/m ³]	effective fluid weight
k^F	[m/s]	hydraulic conductivity (<i>Darcy</i> permeability)
R	[J/K mol]	universal gas constant
M	[kg/mol]	molar mass of the compressible fluid
$\boldsymbol{\sigma}$	[N/m ²]	2 nd -order stress tensor for single-phase materials
$\mathbf{C}_e^4, \mathbf{D}_e^4$	[N/m ²]	4 th -order elasticity tensors
$\boldsymbol{\sigma}_E^S$	[N/m ²]	2 nd -order solid effective stress tensor of the linear theory
$\boldsymbol{\varepsilon}_{Se}, \boldsymbol{\varepsilon}_{Sp}$	[-]	2 nd -order solid elastic and plastic strain tensors
μ^S, λ^S	[N/m ²]	1 st and 2 nd macroscopic <i>Lamé</i> constants of the solid matrix
k_0^S, k_1^S	[N/m ²]	material constants of φ^S for the hyperelastic model
I_σ	[N/m ²]	1 st principle invariant of $\boldsymbol{\sigma}_E^S$
$\mathbb{II}_\sigma^D, \mathbb{III}_\sigma^D$	[N/m ²]	2 st and 3 rd principle invariants of $\boldsymbol{\sigma}_E^{SD}$
F, G	[N/m ²]	yield and potential functions
$\mathcal{S}_h, \mathcal{S}_d$	[-]	hydrostatic and deviatoric yield-surface parameter sets, i. e., $\mathcal{S}_h = \{\alpha, \beta, \delta, \epsilon, \kappa\}$ and $\mathcal{S}_d = \{\gamma, m\}$
ψ_1, ψ_2	[-]	potential function parameters
Dr	[%]	soil relative density
Λ	[s]	<i>Lagrangian</i> multiplier for <i>Perzyna</i> -type viscosity
η_r	[s]	viscoplastic relaxation time
r	[-]	viscoplastic exponent
σ_0	[N/m ²]	reference stress for <i>Perzyna</i> -type viscosity
p_i	[-]	parameter set for isotropic hardening/softening
p_i^*, p_{i0}	[-]	maximum and the initial values of the parameters p_i
C_{pi}^V, C_{pi}^D	[-]	volumetric and deviatoric parameters for isotropic hardening/softening

\mathbf{Y}^S	[N/m ²]	2 nd -order solid back-stress tensor (kinematic hardening)
$\bar{\boldsymbol{\sigma}}_E^S$	[N/m ²]	2 nd -order solid shifted effective stress tensor
\mathbf{t}_E^S	[N/m ²]	the stress state at a point of the principle stress space
$\bar{\mathbf{t}}_E^S$	[N/m ²]	the stress state at a point of the shifted principle stress subspace
\mathbf{y}_E^S	[N/m ²]	shifting vector of the principle stress space
c_1, c_2, ν, ξ	[-]	kinematic hardening parameters
Γ	[-]	Overall boundary
$\Gamma_{(\cdot)}$	[-]	<i>Neumann</i> or <i>Dirichlet</i> boundaries
Ω	[-]	Spatial domain
Ω_e	[-]	One finite element
\mathcal{I}	[-]	singularity surface (wave front surface)
$\mathbf{n}_{\mathcal{I}}$	[-]	the normal unit vector to \mathcal{I}
$\mathbf{w}_{\mathcal{I}\alpha}$	[m/s]	velocity in which the surface \mathcal{I} moves relative to the constituents φ^α
$\mathbf{x}_{\mathcal{I}}$	[m]	position vector in the actual configuration of the surface \mathcal{I}
$\mathbf{v}_{\mathcal{I}}$	[m/s]	velocity of \mathcal{I} in the actual configuration
$\boldsymbol{\xi}_\alpha$	[-]	amplitude vector of the discontinuity (cf. compatibility condition)
c_s, c_p	[m/s]	shear- and pressure-wave speed of propagation
p'	[N/m ²]	the mean effective stress ($p' := \frac{1}{3} \mathbf{I}_\sigma$)
\mathbf{e}, \mathbf{e}_c	[-]	the void ratio ($\mathbf{e} := n^F / (1 - n^F)$) and the critical void ratio
$r_{\mathbf{u}}$	[-]	Pore-pressure ratio; excess pore-pressure to the initial effective stress
$\mathbf{u}_i(t, \mathbf{x})$		a set of primary variables with $i = 1, 2, \dots$
\mathbf{q}, \mathbf{p}_i		sets of internal and the hardening variables, respectively
\mathbf{u}		a column vector that collects all primary unknowns
$\delta \mathbf{u}$		column vector of all test functions
$\mathcal{G}_{\mathbf{u}}$		a function vector of all weak formulations (global residuum)
$\mathcal{L}_{\mathbf{q}}$		a function vector of the viscoplastic and isotropic hardening relations (local residuum)
$\mathcal{S}_{\mathbf{u}}(t), \mathcal{T}_{\mathbf{u}}$		continuous trial and test spaces

$\mathcal{S}_u^h(t), \mathcal{T}_u^h$	discrete trial and test spaces
\mathbf{u}^h	a column vector that collects all degrees of freedom of the FE nodes
$(\cdot)^h$	represent quantities in the discrete space (cf. Section 4.1.3)
N_u, M_u	space-dependent global basis functions of the trial and test functions
M_{inf}	geometry mapping functions of the infinite element treatment
$\boldsymbol{\xi}$ or $\{\xi_i\}$	the natural coordinate system
K_g, w_k	number of <i>Gauß</i> integration points and the corresponding weights
U, V, P	interpolation functions corresponding to the nodal unknowns of the FE mesh $\mathbf{u}_S / \mathbf{v}_S, \mathbf{v}_F$, and \mathbf{p} , respectively
M, K	Global mass and stiffness matrices of the space-discrete coupled system
f	Global force vector of the space-discrete coupled system
\mathbf{y}	represents all nodal degrees of freedom of the FE mesh
M_{ij}, K_{ij}	mass and stiffness submatrices of M and K
$\Delta(\cdot)$	<i>Laplace</i> operator, i. e., $\Delta := \text{div grad}$
\mathbf{v}_α^* [m/s]	constituent intermediate velocities
$\mathbf{h}_1, \mathbf{h}_2$	auxiliary functions used for a compact representation
Δt_{cr} [s]	critical time-step size of the semi-explicit-implicit scheme
$\Delta x, \Delta y$ [m]	FE discrete-element dimensions in x and y directions
σ, τ [N/m ²]	damping forces for pressure and shear waves

Acronyms

Selected Acronym	Definition
BDF2	2 nd -order Backward Difference Formula
BE	Backward (Implicit) <i>Euler</i>
BT	Biot's Theory
CFD	Computational Fluid Dynamics
CFL	<i>Courant-Friedrichs-Lewy</i> condition

CD, CU	Consolidated Drained and Consolidated Undrained triaxial test
CSL	Critical State Line
CSSM	Critical State Soil Mechanics
DAE	Differential-Algebraic Equations
DG	Discontinuous <i>Galerkin</i> Method
DIRK	Diagonally Implicit <i>Runge-Kutta</i>
FEM	Finite Element Method
IBVP	Initial-Boundary-Value Problem
IEM	Infinite Element Method
LBB	<i>Ladyschenskaja-Babuška-Brezzi</i> condition
ODE	Ordinary-Differential Equations
OSM, MSM	One-Step Methods, Multi-Step Methods
PDE	Partial-Differential Equations
PMD	Principle of Maximum Dissipation
PTL	Phase Transformation Line
PVW	Principle of Virtual Work
REV	Representative Elementary Volume
SSI	Soil-Structure Interaction
TM	Theory of Mixtures
TPM	Theory of Porous Media
TR	Trapezoidal Rule
VDB	Viscous Damping Boundary

List of Figures

1.1	Earthquake features and liquefaction phenomena	1
1.2	Verification and validation of a numerical model	8
2.1	REV and homogenisation process within the TPM	12
2.2	Motion of biphasic solid-fluid aggregates	13
2.3	<i>Cauchy</i> stress theorem	19
3.1	Single-surface yield function	44
3.2	Geometrical interpretation of the back-stress	46
3.3	Porous body separated by a singular surface	48
4.1	Mixed FEM approach and geometrical mapping	57
4.2	Illustration of a one-dimensional infinite element	59
4.3	Geometric mapping of quadrilateral infinite elements	60
4.4	Sketch of the implicit monolithic time-integration methods	72
4.5	Predictor-corrector algorithm	79
4.6	Viscous damping boundary (VDB)	83
5.1	Contraction and dilation due to the rearrangement of grains	88
5.2	Liquefaction mechanism within the critical state concept	88
5.3	Soil liquefaction mechanism of saturated granular assemblage	89
5.4	Wildlife Refuge site and seismic measurements	91
5.5	Isotropic consolidation and deviatoric stress paths	93
5.6	Contractive, dilative, and neutral flow rules	94
5.7	Drained shear-compression triaxial test	96
5.8	Undrained triaxial shear-compression test	97
5.9	Effective stress and pore-pressure changes during CU test	97
5.10	Cyclic loading and pore-pressure build-up for loose sand	100
5.11	Mean effective stress and shear stress under cyclic loading for a loose sand	100
5.12	Cyclic loading and pore-pressure build-up for moderate-dense sand	101
5.13	Cyclic mean effective stress and shear stress for moderate-dense sand	101
5.14	Geometry and boundary conditions of a strain localisation problem	102
5.15	Classification of problems in accordance with the loading nature	103

5.16	Loading rate effect: dynamic loading applied to the strain localisation problem	103
5.17	Loading rate effect: quasi-static loading applied to the strain localisation problem	104
5.18	Boundary drainage effect: dynamic loading applied to the strain localisation problem	104
5.19	Influence of the microstructure: dynamic loading applied to the strain localisation problem	105
6.1	Saturated poroelastic column under harmonic loading	108
6.12	Geometry, boundary conditions, and loading path of the 2-d problem . . .	120
6.14	Propagation of longitudinal waves in an ultrasonic experiment of a concrete sample	121
6.29	Geometry, boundary conditions, and loading path of the elastic structure-soil Half Space problem	130
6.35	Soil-structure interaction under seismic excitation, 'control' point	135
6.36	Kinematic interaction and inertial interaction	136
6.37	Displacement and velocity time history of the Kobe earthquake	138
6.38	Acceleration time history of the Kobe earthquake, FUK station	139
6.39	Soil-structure interaction problem under seismic loading	139
6.40	Applied loads to the soil-structure interaction problem	140
B.1	Boundary conditions and applied loads of the triaxial test	155

List of Tables

2.1	Identified physical quantities of the master balance relations	22
3.1	Different elasticity classes	41
5.1	Sand with different initial densities	95
6.1	Abbreviations for the different governing equations and numerical schemes	107
6.2	Material parameters of saturated elastic soil	109
6.3	The considered time-step sizes for the splitting scheme and the number of nodal unknowns	110
6.4	Material parameters for the compressible pore fluid via ideal gas	114
6.5	Abbreviations related to the infinite domain modelling	115
6.6	Two considered cases with varying permeability and geometry of the infinite domain model	116
6.7	Mesh sizes and time steps for the problem in Section 6.2	121
6.8	Summary of the observed solution behaviour for the distinct test cases in Section 6.2	129
6.9	Material parameters of elastic concrete	131
B.1	Material parameters of the hyperelastic solid matrix	155
B.2	Parameters for the viscoplasticity behaviour and the isotropic hardening .	156

Curriculum Vitae

Personal Data:

Name: Yousef Heider
Date of birth: March 13, 1980
Place of birth: Tartous, Syria
Nationality: Syrian
Marital status: unmarried

University Education:

since 08/2007 doctoral candidate and research associate at the Institute of Applied Mechanics (Civil Engineering), University of Stuttgart, Germany
2005 – 2007 M.Sc. in Computational Mechanics of Materials and Structures (COMMAS), University of Stuttgart, Germany
2003 – 2004 diploma in Structural Engineering, Damascus University, Syria
1998 – 2003 B.Sc. in Civil Engineering, Damascus University, Syria

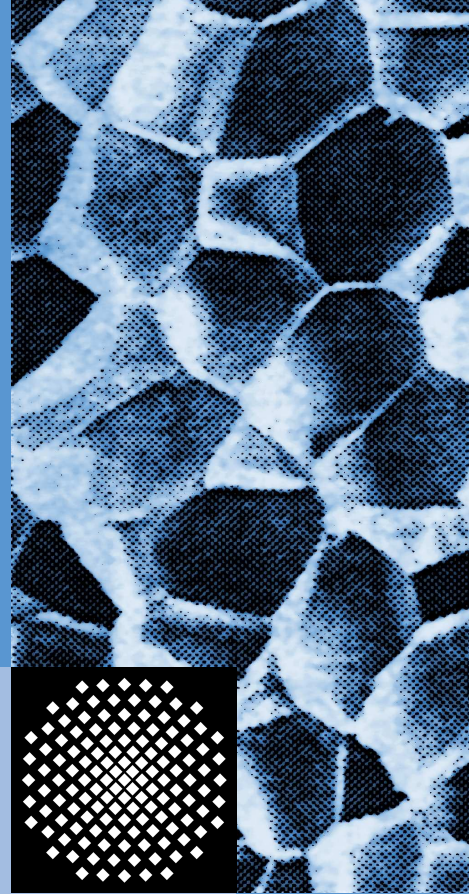
School Education:

1995 – 1998 Alsouda High School “scientific branch”, Tartous, Syria
1992 – 1995 Ali-Yousef Secondary School , Tartous, Syria
1986 – 1992 Bremanet-Raad Primary School, Tartous, Syria

Released Report Series

- II-1 Gernot Eipper: *Theorie und Numerik finiter elastischer Deformationen in fluid-gesättigten porösen Festkörpern*, 1998.
- II-2 Wolfram Volk: *Untersuchung des Lokalisierungsverhaltens mikropolarer poröser Medien mit Hilfe der Cosserat-Theorie*, 1999.
- II-3 Peter Ellsiepen: *Zeit- und ortsadaptive Verfahren angewandt auf Mehrphasenprobleme poröser Medien*, 1999.
- II-4 Stefan Diebels: *Mikropolare Zweiphasenmodelle: Formulierung auf der Basis der Theorie Poröser Medien*, 2000.
- II-5 Dirk Mahnkopf: *Lokalisierung fluidgesättigter poröser Festkörper bei finiten elasto-plastischen Deformationen*, 2000.
- II-6 Heiner Müllerschön: *Spannungs-Verformungsverhalten granularer Materialien am Beispiel von Berliner Sand*, 2000.
- II-7 Stefan Diebels (Ed.): *Zur Beschreibung komplexen Materialverhaltens: Beiträge anlässlich des 50. Geburtstages von Herrn Prof. Dr.-Ing. Wolfgang Ehlers*, 2001.
- II-8 Jack Widjajakusuma: *Quantitative Prediction of Effective Material Parameters of Heterogeneous Materials*, 2002.
- II-9 Alexander Droste: *Beschreibung und Anwendung eines elastisch-plastischen Materialmodells mit Schädigung für hochporöse Metallschäume*, 2002.
- II-10 Peter Blome: *Ein Mehrphasen-Stoffmodell für Böden mit Übergang auf Interface-Gesetze*, 2003.
- II-11 Martin Ammann: *Parallel Finite Element Simulations of Localization Phenomena in Porous Media*, 2005.
- II-12 Bernd Markert: *Porous Media Viscoelasticity with Application to Polymeric Foams*, 2005.
- II-13 Saeed Reza Ghadiani: *A Multiphase Continuum Mechanical Model for Design Investigations of an Effusion-Cooled Rocket Thrust Chamber*, 2005.
- II-14 Wolfgang Ehlers & Bernd Markert (Eds.): *Proceedings of the 1st GAMM Seminar on Continuum Biomechanics*, 2005.
- II-15 Bernd Scholz: *Application of a Micropolar Model to the Localization Phenomena in Granular Materials: General Model, Sensitivity Analysis and Parameter Optimization*, 2007.
- II-16 Wolfgang Ehlers & Nils Karajan (Eds.): *Proceedings of the 2nd GAMM Seminar on Continuum Biomechanics*, 2007.

- II-17 Tobias Graf: *Multiphasic Flow Processes in Deformable Porous Media under Consideration of Fluid Phase Transitions*, 2008.
- II-18 Ayhan Acartürk: *Simulation of Charged Hydrated Porous Materials*, 2009.
- II-19 Nils Karajan: *An Extended Biphasic Description of the Inhomogeneous and Anisotropic Intervertebral Disc*, 2009.
- II-20 Bernd Markert: *Weak or Strong – On Coupled Problems in Continuum Mechanics*, 2010.
- II-21 Wolfgang Ehlers & Bernd Markert (Eds.): *Proceedings of the 3rd GAMM Seminar on Continuum Biomechanics*, 2012.
- II-22 Wolfgang Ehlers: *Poröse Medien – ein kontinuumsmechanisches Modell auf der Basis der Mischungstheorie*, 2012. Nachdruck der Habilitationsschrift aus dem Jahr 1989 (Forschungsberichte aus dem Fachbereich Bauwesen der Universität-GH-Essen **47**, Essen 1989).
- II-23 Hans-Uwe Rempler: *Damage in Multi-Phasic Materials Computed with the Extended Finite-Element Method*, 2012.
- II-24 Irina Komarova: *Carbon-Dioxide Storage in the Subsurface: A Fully Coupled Analysis of Transport Phenomena and Solid Deformation*, 2012.
- II-25 Yousef Heider: *Saturated Porous Media Dynamics with Application to Earthquake Engineering*, 2012.



ISBN 3-937399-22-4
(D 93 – Dissertation, Universität Stuttgart)